Geotechnical site characterisation using seismic and resistivity geophysical techniques

Raad Mohammad Abd Alzahra Eissa

Submitted for the degree of Doctor of Philosophy

October 2019

Keele University

Abstract

Geotechnical site investigations are vital for any construction project in brownfield re-development and/or greenfield sites. Many non-invasive, near-surface geophysical techniques are used for site characterisation, with electrical resistivity and seismic methods being two of the most popular techniques.

Although electrical resistivity has been used to detect buried foundations in brownfield sites, there is still research needed to identify optimal survey parameters and electrode configurations. In this study, four of the most common resistivity arrays (Wenner, dipole-dipole, pole-dipole and pole-pole) were utilized, on profiles (0.25 m electrode spacing and 64 electrodes) at different orientations and distances from a scaled-model of a buried foundation wall (wall dimensions are 1.5 m long × 0.36 m wide × 0.48 m height). The Wenner and dipole-dipole arrays, with surveys oriented parallel to the foundation wall, were found to be optimal.

Integration of geophysical (seismic (using 24 geophones and 1 m geophone spacing), electrical resistivity (2, 3 and 4 m electrode spacing and 64 electrodes) and gravity) with conventional *in situ* CPT tests surveys allowed good site characterisation of a geologically heterogeneous site.

Seismic surveys are routinely conducted for shear wave velocity-depth profile site determinations. Train-induced vibrations have been shown to be used as passive seismic sources for site characterisation studies. In a Midlands glaciated valley site, passing train vibrations were collected using three-component seismic stations and 1D/2D array configurations. Linear arrays (115 m total length and 5 m geophone spacing), oriented parallel to the railway, were found to be optimal. Analysis of three (i.e. vertical and

horizontal) components revealed different shear wave velocities; however, it cannot be the case for the same site. Observing apparent wave velocities was the main interpretation for the differences in wave velocity. In addition, time-frequency analysis showed that potential Doppler shift was not noticeable on the observed train-induced vibrations.

Acknowledgement

An absolute gratitude and praise to Allah who is the most gracious, the most merciful and the omniscient for his countless favours on me.

I would like to thank the Higher Committee for Education Development in Iraq (HCED) for helping and providing funding for my doctorate.

A very special gratitude goes to my supervisory team, Dr. J. K. Pringle, Dr. I. G. Stimpson for their endless support during my PhD journey. Many thanks for Professor N.J. Cassidy (the first lead supervisor) for his significant support during my PhD, when he left Keele for Birmingham University. Without their support it would not be possible to do this work.

I am also grateful to Keele University to give me the opportunity to continue my education and doing my doctorate. Many thanks to the university staff for their help and support.

Thanks to Sam Toon and Ammar Bek for sharing their knowledge of Matlab which helped me to process seismic data.

Thanks to Dr. David Gunn of the British Geological Survey in Keyworth for his help to conduct fieldwork at Rugeley and for his time and knowledge to process the datasets.

I am also grateful to my forever interested, encouraging and always enthusiastic parents who have provided me through moral and emotional support in my life. Many thanks go to all my family members who have supported me along the way.

To all my friends, thanks a lot from the deepest part of my heart for the time that you spent with me, for being by my side, advice and always trying to spread happiness.

Contents

List of Figures

List of Tables

Chapter one: Introduction

1.1 Introduction to Site Investigation

Site investigation is a process to gather adequate geological, geotechnical and other relevant information for a proposed construction site and to recognise any potential ground problem that might be faced during or after construction. Site investigation, sometimes, are not undertaken correctly, and most failed structures have been due to lack of proper site investigations (Lancellotta, 2009).

The field of site investigation contains many disciplines: it can be undertaken by the site construction and building industry (Soupios et al., 2007; Mohamed et al., 2013), waste disposal sites (Yi et al., 2012). Önal et al. (2013) stated that groundwater pollution might have happened in the city of Tunceli, Turkey due to using an inappropriate site for solid waste disposal.

For civil constructions, site investigations are commonly undertaken to gather information about the site near-surface materials, groundwater conditions, collecting samples for laboratory tests, studying previously failed engineering cases, and to estimate ground works effects on safety of pre-existing structures (Smith and Smith, 1998; Craig, 2004). The main soil mechanical and physical parameters in site investigations are commonly soil density, grain size distribution, moisture content, permeability, pore water pressure, and soil effective stress, shear strength and stiffness (Simons et al., 2002).

To perform a successful site investigation, Gabriel (2001) states a common set of factors which any site investigation should be assessed on; these are summarized here:

1- Ground problems should be recognized;
2- Preparing an adequate plan for ground hazard management, the plan is continuously refined as work progresses;
3- Relevant, effective and good value information should be supplied.

These factors are important and the site should be studied with care, with accurate results when the earthworks (i.e. excavation) and construction are performed close to susceptible structures such as tunnels and historically important buildings (Mathew et al., 1997).

Generally, a site investigation contains four sequential steps, which are summarized below (Barnes, 2010):

1- Desk studies, in which any available information such as the geological/soil maps, borehole records, previous geotechnical reports, groundwater, etc., should be collected and studied; they should be the basis for the new investigation.
2- Site reconnaissance, includes initial site visits to verify desk study results to manage the next steps, and to better understand the site. Any additional information such as recent site changes, accessibility issues, etc. can be recorded.
3- Ground investigation, generally, can be focused following both the desk studies and reconnaissance stages, being designed based on each unique site and the specific project undertaken. It can be performed by many different *in situ* and laboratory tests; sampling methods (non-invasive and invasive), depth of investigation, cost and time all being potentially important issues. Sometimes, ground investigations are subdivided into two stages, preliminary investigations

and detailed investigations depending on the site complexity and if problems arise during construction (Lancellotta, 2009).

4- Final investigation report which includes all findings from the previous steps.

Site investigation methods are commonly undertaken by conventional methods such as trial pits and boreholes (Barnes, 2016). Direct methods refer to sampling, then the collected samples are tested in a soil mechanics laboratory, more details for site investigation and conventional soil tests are available in many soil mechanics textbooks (e.g., see Clayton et al., 1995, Simons et al., 2002 and Barnes, 2016).

1.2 Introduction to geotechnical geophysics

Geophysics is a main branch of geology, which is used to study the Earth's interior from the ground surface using basic physics. It can be subdivided into two main areas, pure geophysics and applied geophysics. Applied geophysics can be performed for many different applications (Reynolds, 1998, 2011); generally, applications of applied geophysics that have already been mentioned in the published literature can be summarized in Figure 1-1.

Near surface geophysics, which always applied for shallow investigations (tens of metres beneath the ground surface) (Everett, 2013), to hundreds of metres (Doll et al., 2012), has been applied for many studies including engineering studies (Doll et al., 2012). It has advantages that it can be in sub-metre-scaled studies (see for example Everett, 2013). There are powerful advantages of benchmarking the geophysical result against other complementary datasets, including borehole data, that allow the geophysical response to be extrapolated across a whole site.

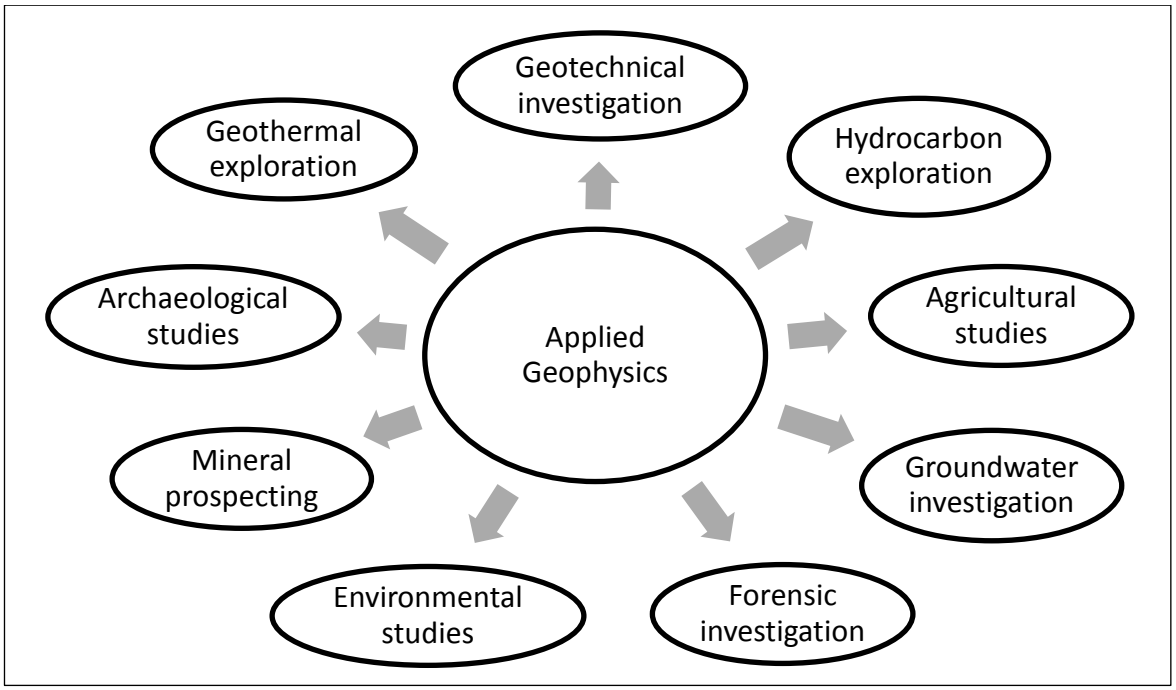

Figure 1-1: Main implementations of geophysical techniques, modified from Reynolds (2011).

Engineering site investigation and unseen hazards / ground problems can be studied by applied geophysics implementation; these kind of studies are called geotechnical geophysics (Keary et al., 2002). Geotechnical geophysics investigations can be performed beside/during conventional site investigations, and they can be compared and combined for better understanding and more accurate modelling (Reynolds, 2011).

Inadequate site investigations of heterogeneous sites can have many drawbacks and can lead to wide range of structural damage (Barnes, 2016). Therefore, and for more representative sampling investigations, saving time and cost, geophysical techniques have been used for initial site investigations to detect and characterise any site-specific issues prior to, as well as during invasive investigations (Hencher, 2012). Geotechnical geophysics are further subdivided into invasive and non-invasive techniques, invasive techniques include seismic down hole, up hole, and cross hole which requires a borehole

to be drilled first (Mathews et al., 2000). Non-invasive techniques work without boreholes such as seismic refraction (Hunter et al., 2002) and electrical resistivity method (Tabbagh et al., 2000). The geophysical techniques can be divided based on the nature of the source of the measured property, some of these methods work with external energy sources like electrical resistivity and refraction seismic, whilst others work without external sources, such as gravity and passive seismic methods.

Geophysical methods can also be utilized for different soil parameter determination. In fact, there is a link between the geophysical method used, the physics behind it and the required soil parameter. For example, electrical field and potential difference are sensitive physical quantities for water and material (e.g. clay minerals); therefore, electrical resistivity can be applied for ground water table determination and soil moisture content investigations (Samouelian et al., 2005).

Sometimes, two or more geophysical methods are used to investigate the same site. These kind of surveys are performed for more accurate identification for the underground situation. The two proposed methods cannot be chosen arbitrarily; they should be chosen to gain more information of the subsurface using joint analysis and interpretation (Cardarelli et al., 2010; Doll et al., 2012).

1.2.1 Introduction to the electrical resistivity method

The electrical resistivity method is one of the routinely-used, near-surface geophysical methods (Keary et al., 2002). Results from this method can be obtained after three steps, data collection, forward modelling and inversion. Collected data sets are obtained using different techniques; these differ depending on the aim of the survey. Due to subsurface complexity, 2D and 3D surveys are better for subsurface discrimination (Bentley and

Gharibi, 2004). These surveys are applied using different arrays or configurations of electrical probes (approximately one hundred electrode configurations); the most popular are Wenner and dipole-dipole arrays (Szalai and Szarka, 2008). Working out the optimal array is site-specific; each single array has a set of advantages and drawbacks.

The forward and inversion process are always undertaken together by computerized specialist software programs. The main benefit of the forward and inversion processes are to translate measured data to “true” subsurface resistivity. After that, results (i.e. models or curves) are interpreted for underground characterisation (see Narayan et al., 1994; Sharma and Verma, 2015).

Geophysicists perform the resistivity method to typically determine soil parameters for the construction industry (see for example Gunn et al., 2015a and Lysdahl et al., 2017). Soil moisture content is one of the physical parameters that governs soil mechanical behaviour as it affects soil shear strength and compressibility. This method helps civil engineers to determine the ground water table and soil moisture content variations in 1D, 2D and 3D, typically by vertical electrical sounding (VES), electrical 2D surveys, and volumetric surveys, respectively. In addition, the resistivity method is successfully used to investigate subsurface and determine location and size of voids (natural and man-made cavities) (see Cardarelli et al., 2010; Banham and Pringle, 2011), the bedrock - soil interface (Rao et al., 2004), and determining a competent layer for civil construction foundations (Soupios et al., 2007). Subsurface geological structures characterisation (e.g. anisotropy phenomena), (Ravindran, 2012; Lane et al., 1995; Asfahani, 2011), groundwater contamination and forensic investigations (e.g. old tombs detection), (Pringle and Jervis, 2010; Dick et al., 2015) are other resistivity method applications. It has

many advantages, such as being economic, fast, and more representative method in terms of sampling.

1.2.2 Introduction to the seismic method

The seismic method is another popular geophysical method that has been used for geotechnical applications. Soil particles are oscillated when seismic waves pass through the ground and apply very small strains (Mathews et al., 2000). Seismic wave velocity propagation is related to elastic constants of a medium; this makes seismic waves have an ability to determine soil mechanical parameter such as soil stiffness (Foti et al., 2015).

Any seismic event, natural event (e.g. earthquake) or man-made event (e.g. explosions, human daily activities), generates a train of seismic waves which contains two main groups, body waves (e.g. primary and secondary waves) and surface waves (e.g. Rayleigh and Love waves). Each wave type has specific physical properties, therefore, its effects, processing and applications differ between each other; for instance, secondary and surface waves are more suitable to determine soil shear strength and soil stiffness (Mathew et al., 1997; Mathews et al., 2000).

Seismic surveys for geotechnical purposes can be utilized using secondary waves and surface waves with different techniques. Surface waves are used in this project for geotechnical investigations. Seismic surface waves (i.e. ground roll) are generated from natural seismic and man-made events, and in both cases it can be used for geotechnical purposes (Foti et al., 2015). These surveys are usually a four step process: data collection, dispersion curve production, inversion process to determine shear wave velocity-depth profile, and soil shear modulus calculations (Lane, 2009). The last three steps are

computationally-intensive processes, and require implementation in either commercial software or the authorship of bespoke algorithms.

Surface wave data sets can be collected using linear or 2D geophone arrangements, different arrays shapes / size, and passive or active seismic sources have been applied with different techniques (Foti et al., 2015). Combined active and passive seismic source surveys are more effective than one type source, where wide range of wave's frequencies will be collected and shear wave velocity will be determined for bigger range of depth below ground level (Foti et al., 2015).

The refraction microtremor (ReMi) technique is used in this project. This method is used to collect seismic waves from passive sources (i.e. natural and human activities). The conventional ReMi is a linear array which was first proposed by Louie (2001). Standard refraction equipment, such as single geophone sensor, which is popular for most companies, institutions and geophysicists, is used for data collection. In addition, geophone spacing (i.e. geophone interval) is varied, and multicore cables can be used; in an urban environment, stand-alone recorders are more applicable and efficient to avoid lay out of long heavy cables and damage to cables (Louie, 2001). The conventional ReMi proposes all passive sources are equally distributed around the site and picking the subsequent dispersion curve should be taken with care (i.e. picking true wave velocity or the minimum apparent wave velocity). These two conditions are necessary for data processing otherwise erroneous results can be obtained. Strobbia et al. (2015) state that the 2D arrays (the geophones arrange in two dimensional geometries, for example, L-shape array, where the deployed array has the "L" letter shape) are better than linear (the geophones arrange in a straight line) with passive sources surveys, where the

dispersion curve can be extracted with more confidence. The ReMi method has been used for site characterisation in many projects (e.g. Cha et al., 2006; Gamal and Pullammanappallil, 2011). This method is compared with many methods to calibrate its results (e.g. Perez-Santisteban et al., 2011; Stephenson et al., 2005; Rosenblad and Li, 2009).

1.3 Thesis structure and aims

In this thesis, the electrical resistivity technique has firstly been tested for buried foundation determination and secondly some of the geophysical techniques (e.g. resistivity, seismic, microgravity) have been applied for combined site investigation as a case study. Finally, the seismic technique has been used using train-induced vibrations for site characterisation.

Empirical studies have evidenced the ability of the resistivity method to determine buried foundations. Buried foundations, especially those that are constructed of concrete, can show significant variations in resistivity from the host background. Thus, it is important to determine the optimal different configurations to locate buried foundations.

Some of geophysical techniques (electrical resistivity, passive and active seismic surveys) and direct tests (cone penetration test and sand-replacement density test) have been performed and combined for site characterisation as a case study. The electrical resistivity has been used to generate several 2D resistivity models for the underground. The seismic surveys have been used to produce 1D and 2D (cross section) shear wave velocity – depth profiles, these data sets were used to determine the material shear modulus. Results from these surveys were applied to relate the measured soil parameters.

Finally, train-induced seismic vibrations have been tested for shear wave velocity-depth profile determination. Therefore, testing the generated vibrations is important for near surface applications. In this thesis this has been undertaken using different geophone configurations and three components seismic stations for trains passing the studied site in both directions.

Therefore, the aims of this thesis are outlined below, with more detailed aims in the individual chapters.

1- To determine differences in resistivity models of different electrode configurations (arrays) for eliminating a target from the host background and to demonstrate the usefulness of local traffic-induced vibrations for site investigation.
2- To perform a multi-geophysical technique site investigation using active and passive geophysical techniques with *in-situ* direct tests.
3- To test the usefulness of train-induced vibrations for seismic surveys to characterise a site in three dimensions.

To achieve these aims, and to put the case study chapters in context, a review of the literature was conducted. Moreover, in the last chapter, the thesis results are discussed; conclusions and limitations being also presented. The main content of the thesis chapters are summarized:

- Chapter 2 shows the basics of electrical resistivity, passive and active seismic, microgravity, cone penetration test (CPT), train-induced vibrations and soil

mechanics. The chapter represents the applications of these techniques for near surface and site characterisation.

- Chapter 3 details the electrical resistivity technique for buried foundation determination of four electrode configurations. The results are compared with the target dimensions to determine which is the optimal electrode array for determining a buried foundation. Then, results of two different inversion techniques are compared to state which inversion method is optimal. In addition, traffic-induced vibrations are observed to produce shear wave velocity-depth profiles from different seismic components. The results are used to find the range of the effective investigated depth.
- Chapter 4 details the results for geophysical surveys of a case study and combined with the *in situ* direct tests for site characterisation as a case study and provides a background for the feasibility study of train-induced vibrations.
- Chapter 5 details the passive seismic surveys that were used for train-induced vibration collection and processing. The results of different arrays and seismic components are presented and compared to find out the seismic components and survey parameters differences. To constrain the results of the train-generated vibrations, it is compared with microgravity surveys which were conducted at the same place and time.
- Chapter 6 discusses the main thesis results and gives limitations of the conducted studies.
- Chapter 7 concludes, suggests further research and possible applications.

Chapter two: Theoretical background

In this chapter published literature for the geophysical methods and direct soil tests used in this thesis will be briefly reviewed. Within each reviewed method, the emphasis on its application for site characterisation is given. For more details, text books are suggested at the end of each section.

2.1 Resistivity method

2.1.1 Introduction to electrical geophysical methods

The “Electrical method” is one of the most popular geophysical methods that is used for sub-surface investigation. The resistivity method is an active one and it is widely used in engineering, mining, geotechnical and hydrogeological applications to investigate the shallow subsurface geology (McDowell et al., 2002; Reynolds, 2011; Everett, 2013). It can also be a useful investigation tool for ore and environmental studies (Milsom and Eriksen, 2011; Everett, 2013).

As with many other geophysical methods, resistivity is a non-invasive technique that is cheaper than invasive drilling (Hencher, 2012). Resistivity has the advantage in that it is an indirect method that can used to investigate sub-surface targets that contain some variation and/or contrast in their bulk resistivity properties, when compared to background values (Keary et al., 2002).

However, the resistivity method has some limitations, namely, the ambiguity of interpretation or non-uniqueness of the results (McDowell et al., 2002). That is, any individual apparent resistivity profile or data set can be produced from a number of equally valid sub-surface ‘models’ of resistivity. The true model can only be determined with direct investigation of the ground (so-called ground truthing) (McCann et al., 1997)

or by proxy investigation through other geophysical methods (Cardarelli et al., 2010). The properties of deeper structures are also less accurately determined, when compared to shallow structures, due to the influence of surface topography and the dominating effects of near-surface resistivity variations (Keary et al., 2002). Electrode spacing and the maximum electrical power of the measuring instrument also limit the depth of current penetration and, therefore, the depth of investigation (Milsom, 2003). The physical restraints of long cables and extensive electrode arrays can make collecting surveys in rural ground, significant topography variation and urban ground difficult and time-consuming (Telford et al., 1990; Metwaly et al., 2009; Reynolds, 2011). Despite these limitations, the resistivity method has become one of the most popular techniques for imaging the sub-surface and has been used for many applications.

2.1.2 Electrical resistivity theory

The basics of the electrical resistivity method depend upon the fundamentals of electrical physics. The premise is to inject an electrical current into the ground, via a pair of electrodes, and then measure the difference in the voltage across another pair of electrodes. For most surveys, the current source utilizes two current electrodes (A & B or C1 & C2) and the difference in potential is measured across two other electrodes, i.e. the two potential electrodes M & N or P1 & P2 (Keller and Frischknecht, 1966). The injected current, by a single surface electrode, will flow in the soil and the pattern of flow in three dimensions will have a generally semi-circular shape, whilst the equipotential lines are perpendicular on it (see Figure 2-1).

The resistivity method depends on the principle of Ohm's law with soil, as well as any other conducting material, obeying law under direct current (or DC) condition (Milsom and Eriksen, 2011). In simple terms, the electrical resistance R (in Ohms) of a conductor is defined as:

$$R = \frac{\Delta V}{I} \qquad (2-1)$$

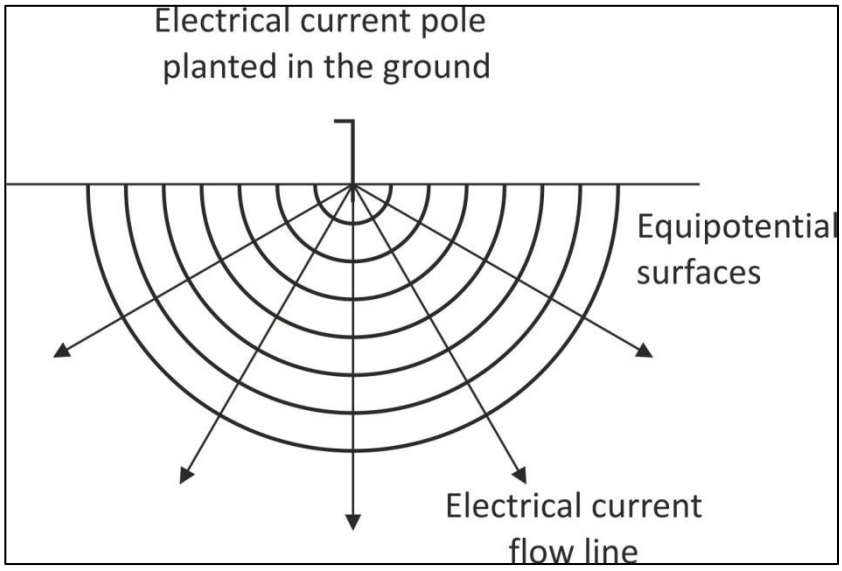

Figure 2-1: Pattern of electrical current flowing in the ground and equipotential lines, (modified from Keary et al., 2002).

where ΔV (in volts) is the potential difference between two points and I (in Amps) is the electrical current (Milsom and Eriksen, 2011).

The resistance, R, of a conductor, is proportional to its length L (m) and inversely proportional to its cross-sectional area A (m^2):

$$R = \frac{\rho L}{A} \qquad (2-2)$$

where ρ is the resistivity of the conductor (Ohm.m). From Equation 1 and 2 the resistivity can be expressed by the following equation (Reynolds, 2011):

$$\rho = \frac{\Delta V}{I}\frac{A}{L} \qquad (2-3)$$

With a single electrode acting as the current source in an infinite, homogeneous and uniform resistivity half-space, the current distribution will be hemispherical in shape with the current electrode at the centre of the hemisphere (Keary et al., 2002).

Any point at a specific distance from the current source, the following equation can be used to determine the resistance R, if the distance, r, and the surface area of the equipotential surface $2\pi r^2$ is known:

$$R = \rho\frac{r}{2\pi r^2} = \frac{\rho}{2\pi r} \qquad (2-4)$$

From Equation 1:

$$\Delta V = IR = I\frac{\rho}{2\pi r} \qquad (2-5)$$

Most resistivity surveys use two electrodes to measure the potential difference between two points, and the potential difference between them is given as:

$$\Delta V = V_{P1} - V_{P2} = \left(\frac{I\rho}{2\pi r1} - \frac{I\rho}{2\pi r2}\right) - \left(\frac{I\rho}{2\pi r3} - \frac{I\rho}{2\pi r4}\right) \qquad (2-6)$$

$$\Delta V = \frac{I\rho}{2\pi}\left(\frac{1}{r1} - \frac{1}{r2} - \frac{1}{r3} + \frac{1}{r4}\right) \qquad (2-7)$$

From Equation 7, the resistivity can be determined from:

$$\rho = \frac{2\pi}{\left(\frac{1}{r1} - \frac{1}{r2} - \frac{1}{r3} + \frac{1}{r4}\right)}\frac{\Delta V}{I} = K\frac{\Delta V}{I} \qquad (2-8)$$

where K is a geometric factor relating to each specific electrode configuration. The geometric factor depends on the arrangement of the four electrodes spatially. Using equation 8 above, the potential can be determined by any configuration of array with four electrodes over a homogeneous half space, (Reynolds, 2011). The resultant measured resistivity should be constant in a homogeneous medium and does not depend on the spacing of the electrodes and surface location (Keary et al., 2002).

In fact, almost all the geomaterials can be considered as not uniform at the survey scale and therefore, the apparent resistivity and true resistivity will be non-uniform in x-y-z space. By using the measured current, I, and potential values ΔV, the apparent resistivity, ρ_a, is calculated by the following formula, (Reynolds, 2011).

$$\rho_a = \mathrm{k}\frac{\Delta \mathrm{V}}{\mathrm{I}} \qquad (2-9)$$

This measured 'apparent' resistivity value relates to the bulk resistivity of the ground measured by the instrument, and not necessarily is the true resistivity of the individual components of the materials in the sub-surface. The relationship between the true and apparent resistivity is complex and requires an inversion procedure to determine the true subsurface resistivity values for the subsurface from the apparent resistivity measured at the survey array (Loke, 2015).

2.1.3 Electrical conduction in sub-surface materials

Electrical current flows through materials in three ways: electronic conduction, electrolytic conduction and dielectric conduction (Lowrie, 2007; Reynolds, 2011). Electronic conduction takes place by the movement of free electrons, with metals being the most electronically conductive materials (Lowrie, 2007). Electrolytic conduction is the

principal conduction phenomenon that occurs in soil and rocks that contain suitable amounts of pore water. In this case the current flow is caused by the movement of free ions in the water volume (Lowrie, 2007).

For “DC” resistivity techniques in sub-surface materials, dielectric conduction effects are minor in comparison to electronic conduction and electrolytic conduction (Lowrie, 2007). As such, resistivity is predominantly controlled by the two former conduction mechanisms. Geomaterials with a portion of clay minerals have a specific current conduction mechanism. Electrical current conduction in clay mineral is due to the ions at their crystal surfaces (Salem, 2001). In general, pore water has dissolved ions and clay mineral crystals which try to make electrical charge balance by adsorbing dissolved ions at their surfaces; this phenomenon leads to build up of a layer of ions called a double layer (Murthy, 2002). Clay minerals have an influence on current conduction due to the double layer effects. Surface electric current conduction by clay minerals is affected by the amount and type of the clay minerals (Salem, 2001).

2.1.4 The electrical properties of sub-surface materials

Geomaterials have a wide range of electrical resistivity values which are distributed from under 10^{-2} to more than $10^{8}\ \Omega.\mathrm{m}$ (Dobrin and Savit, 1988). In general, igneous and metamorphic rocks have the highest resistivity values because these materials are less porous and contain smaller pore fluids when compared to sedimentary rocks and soils. Sedimentary rocks have commonly lower resistivity values than Igneous and Metamorphic rocks (Reynolds, 2011). The resistivity values of sedimentary rocks are controlled by the porosity and the concentration of dissolved salt and other ions in the groundwater, plus the presence of clay minerals in the rock matrix (Reynolds, 2011; Lowrie, 2007).

Soils and unconsolidated sediments generally have resistivity values much less than rocks. The resistivity of a soil depends on the porosity, degree of saturation and clay content (Reynolds, 2011). Figure 2-2 represents the typical range of resistivity values for different types of rocks and soil, and the overlap in the individual values in this figure shows the variety and broad range of apparent resistivity that can be expected in each material.

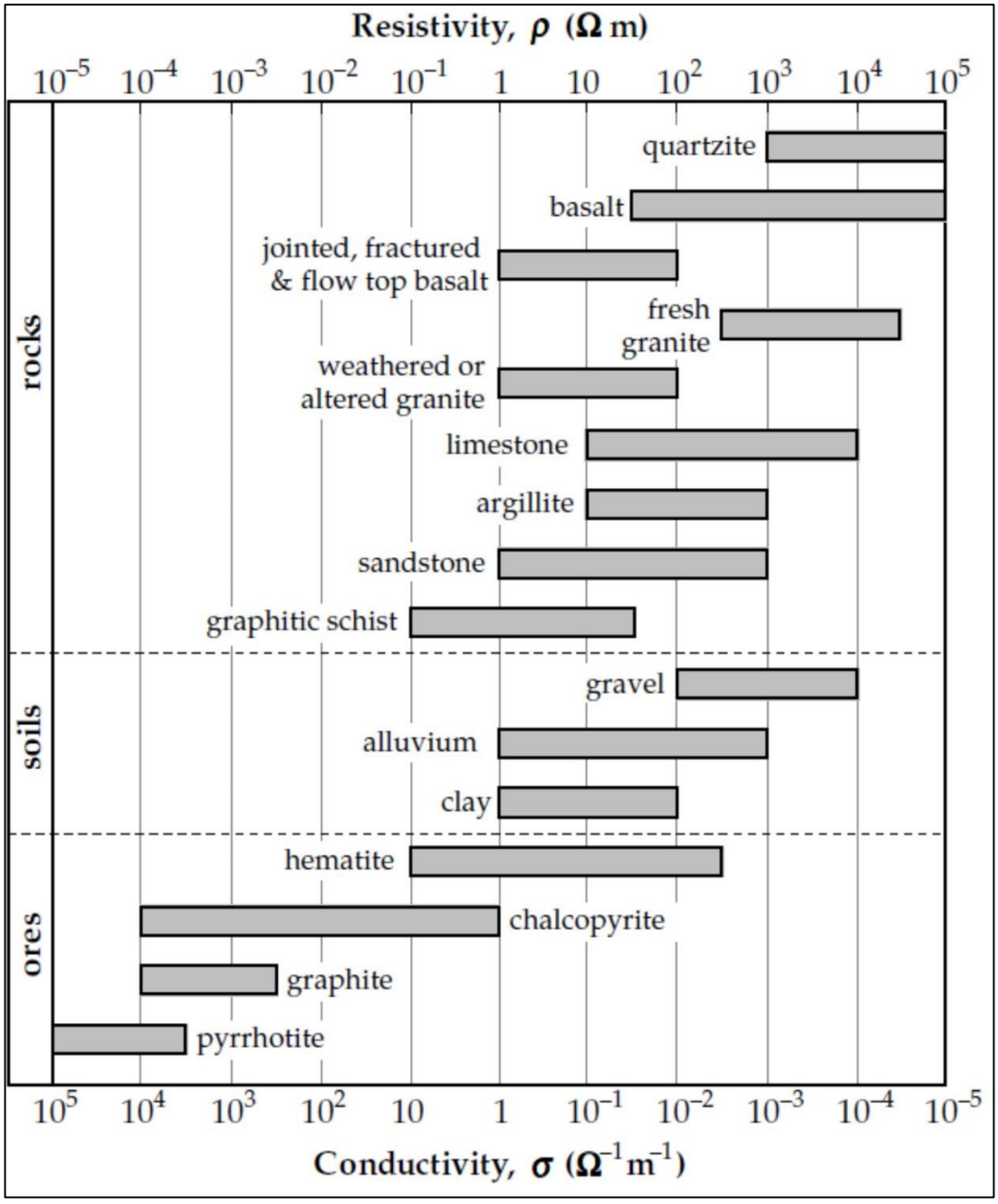

Figure 2-2: Electric resistivity values for different types of rocks, soils and ores (Lowrie, 2007).

2.1.5 Potential errors with data

The data collected in a survey sometimes contains errors, or has a high degree of noise, as a result of measurement or survey problems. Loke (2015) states that this so-called 'bad' or noisy data can be divided into two broad categories; those from systematic error effects and those associated with random noise. Systematic noise comes from failure(s) during the survey such as weak soil-electrode contacts, damaged cables, instrument problems and mistakes during the system operation and data collection process (Loke, 2015). Additionally, increasing electrode separation can lead to reduced data quality (Milsom and Eriksen, 2011).

Random noise has different causes (e.g., powerlines) with telluric currents (natural sub-surface currents) may be the most important of these as they vary with time (Milsom and Eriksen, 2011). Arrays with very large geometric factors are more affected by the random noise than narrow separation surveys (Milsom and Eriksen, 2011).

2.1.6 Electrode array configurations

About one hundred independent geoelectrical array configurations have been found in the geophysical literature (Szalai and Szarka, 2008). However, only a few of them are commonly used (Keary et al., 2002). Choosing the most practical array for any field survey depends on the type of structure that the researcher is investigating, the sensitivity of the resistivity meter being used and the ambient noise level at the site. Horizontal data coverage (the ability of an array to measure more resistivity readings in the horizontal direction, with increasingly investigated depth) all have to be considered when selecting an array (Loke, 2015).

2.1.6.1 The Wenner array

The Wenner array has a simple configuration where the current and potential electrodes are laid out with equal spacing *a* (Keary et al., 2002). Three different configurations are available; they are called alpha, beta and gamma (Carpenter and Habberjam, 1956). A Wenner alpha array needs four electrodes (Figure 2-3-a), with the outer two electrodes used for current injection and the inner two electrodes for measuring the difference in potential (Dobrin and Savit, 1988).

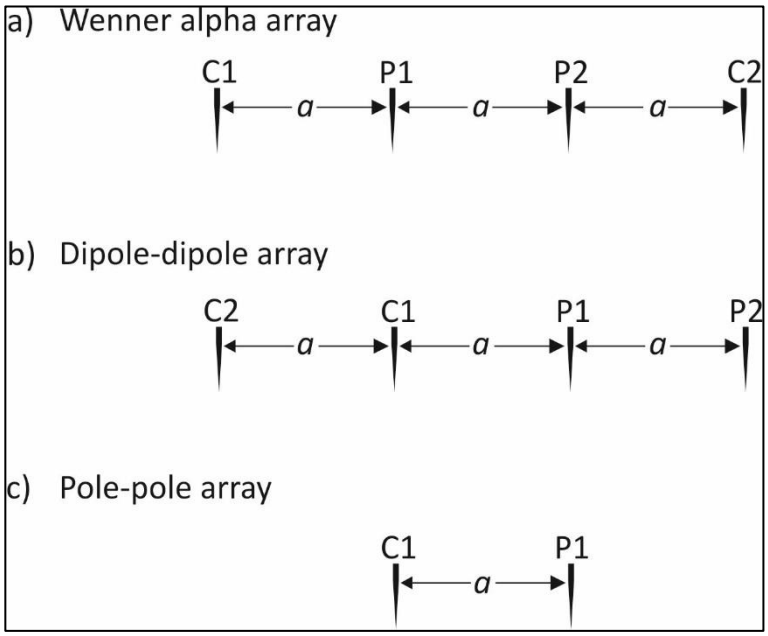

Figure 2-3: Common arrays used in resistivity surveys, C1 & C2 are current electrodes, P1 & P2 are potential electrodes, *a* is electrode spacing (modified from Loke, 2015).

2.1.6.2 Dipole-dipole array

For this array type, the current electrodes are placed adjacent to each other next to the pair of potential electrodes, in a similar way to the Wenner Beta array (see Figure 2-3-b) (Loke, 2015). The spacing *a* between the pair of current/potential electrodes is fixed during the initial survey, whilst the distance between the electrodes pairs (C1-C2 and P1-P2) is increased gradually to increase the investigated depth, the *n* factor (Milsom, 2003).

2.1.6.3 Pole-pole array

With this array, four electrodes are used but two are placed away from the main survey region. The pole-pole array has the advantage of providing a greater investigated depth for a given electrode spacing and more horizontal coverage (see Figure 2-3-c) (Loke, 2015).

Its disadvantage is the comparatively poorer resolution in comparison with other arrays. In addition, placing two remote electrodes make it more susceptible to the effects of telluric noise, more extended cables are required, and the presence of subsurface significant inhomogeneity(s) may effect current field which reduces data quality (Dahlin and Zhou, 2004; Okpoli, 2013).

2.1.6.4 Pole-dipole array

With this type of array, four electrodes are used but one current electrode (C2) has to be placed remotely from the survey area whilst the other (C1) and the two potential electrodes (P1 and P2) are within the survey line (Figure 2-4), (Loke, 2015). Because of this form of electrode separation, pole-dipole arrays are inherently asymmetrical. As such, when collecting data over symmetrical target structures, the apparent resistivity anomalies in the 2D pseudosections or 3D cube are also asymmetrical (Milsom and Eriksen, 2011). To overcome this problem, forward and reverse surveys have to be collected. The forward and reverse surveys are then combined to give a single data set for inversion and interpretation. In this way any asymmetrical bias in the measured data would be minimized (see Figure 2-4), (Loke, 2015).

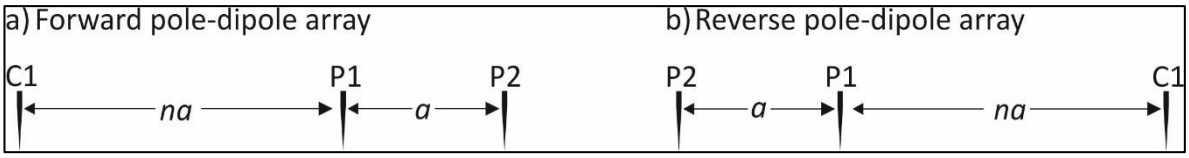

Figure 2-4 Forward and reverse configurations for pole-dipole array, C1 is current electrode, C2 is a remote current electrode and it does not appear in the figure, P1 & P2 are potential electrodes, *a* is electrode spacing, and *n* is the *n* factor (modified from Loke, 2015).

2.1.7 Geoelectrical resistivity surveys types

In general, electrical resistivity surveys can be divided into four types; 1D electrical vertical sounding (VES) surveys, 2D constant separation traverse (CST) surveys, 2D 'pseudo-section' surveys and fully 3D volumetric surveys (Okpoli, 2013).

Subsurface anomalies usually have 3D distributions, therefore, 2D surveys only give an approximate characterisation for the subsurface. Two dimensional imaging can be obtained by integrating sounding and profiling techniques to determine vertical and lateral subsurface variation by using a range of different electrodes spacing along an array (Aizebeokhai, 2010). Two dimensional surveys assume that the variations of the subsurface resistivity are occurring vertically and horizontally along the survey line, but are constant in a perpendicular direction, therefore, 3D surveying gives the most accurate understanding for subsurface anomalies, especially with complex ones. Closer electrode spacing helps to resolve more details whilst large crossline spacing helps to reduce survey time (Bentley and Gharibi, 2004).

2.1.8 Inversion theory

More sophisticated interpretation methods use inversion as a tool to produce a 2D section or 3D volume of true resistivity values from the measured apparent resistivity

data. The main aim of inversion theory is to produce a true resistivity model of the sub-surface, that provides simulated measured apparent resistivity values that are a best match/fit to the actual measured apparent resistivity (Loke and Barker 1995).

The forward modelling programme (the simulated data) is based on a finite-difference or finite-element method, and then the inversion technique is used to iteratively change the model until the simulated data matches the collected data as a least-squares best fit (Dahlin, 2001). The difference between simulated and collected data is measured and presented as root mean square (RMS) error (Loke and Dahlin, 2002). Note, however, that the inversion result is non-unique, because the subsurface is inherently variable in three dimensions and many causes lead to non-uniqueness, therefore, inversion of a set of data may produce two or more different models (Griffith and Kings, 1981; Roy, 2008).

2.1.9 Electrical resistivity method applications

The electrical resistivity method has been used in many near surface applications. It has been applied for forensic investigation (Matias et al., 2006; Pringle and Jervis, 2010; Pringle et al., 2016; Rubio-Melendi et al., 2018), archaeology (Imai et al., 1987; Osella et al., 2005), agricultural studies (Michot et al., 2003; Ravindran and Prabhu, 2012; Beff et al., 2013; Dick et al., 2018), natural underground cavities (Nyquist and Roth, 2005; Deceuster et al., 2006; Cardarelli et al., 2010; Zhu et al., 2011), man-made underground cavities (Chambers et al., 2007; Cardarelli et al., 2010; Banham and Pringle 2011; Orfanos and Apostolopoulos, 2011) and for groundwater studies (Metwaly et al., 2009; Kumar et al., 2014; Akawwi et al., 2014; Ofomola, 2018). The method is also widely used for moisture content determination (see, for instance, Dannowski and Yaramanci 1999;

Turesson, 2006; Brunet el at., 2010; Celano et al., 2011; Yan et al., 2012; Bazin and Pfaffhuber, 2013; Chrétien et al., 2014).

For civil engineering purposes, resistivity surveys have been used to characterise sites, for example, pre-installation ground assessments (Soupios et al., 2007), investigation of existing foundations (e.g. Cardarelli et al., 2007; Arjwech et al., 2013), monitoring of ground stabilisation procedures (e.g. Fischanger et al., 2013; Apuani et al., 2015) and to monitor active soil landslides (Crawford and Bryson, 2018). Resistivity imaging has been used to Earth-filled dam (Cardarelli et al., 2014) and to assess railway embankment conditions (Donohue et al., 2011; Gunn et al., 2015a), (see Figure 2-5).

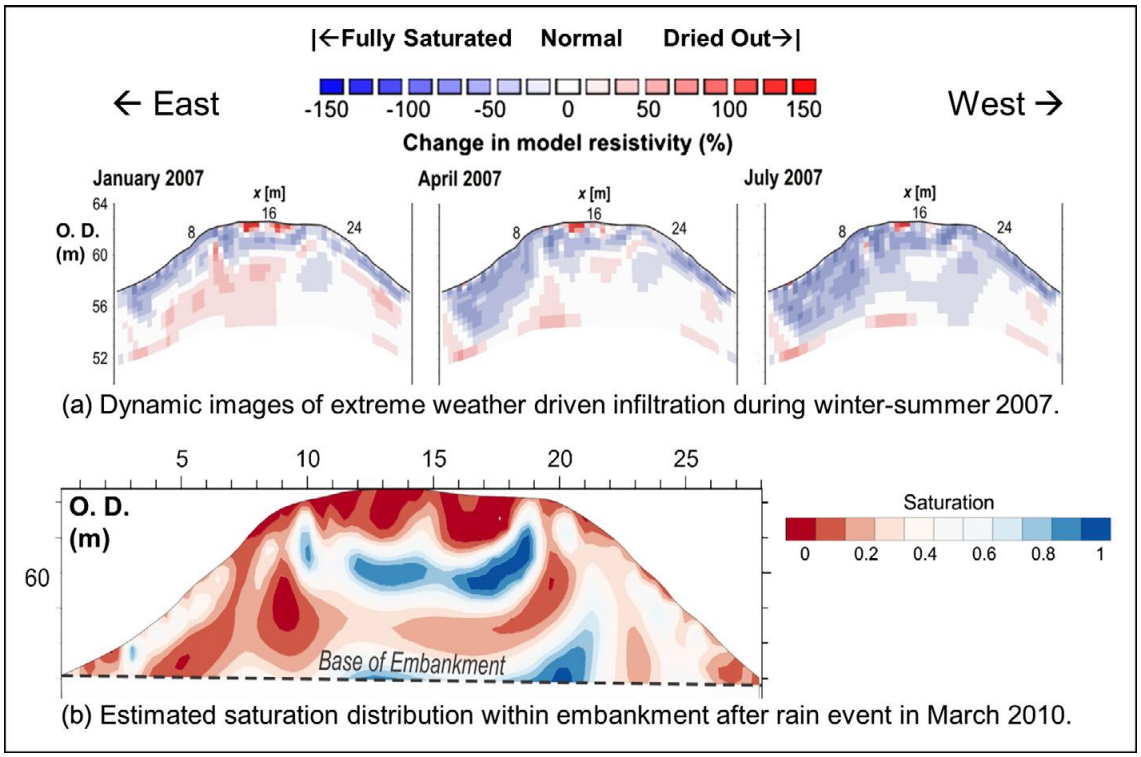

Figure 2-5: An electrical resistivity image showing moisture movement and moisture conditions cross an embankment (Gunn et al., 2015a).

Archie (1942) showed the relationship between sandstone moisture content and its resistivity for the petroleum industry, but it can also be applied for moisture content determination in soils. Resistivity imaging is commonly used as a reconnaissance method to detect natural aggregate (sand and gravel), commonly confirmed by intrusive drilling results, as it shows an effective indicator for coarse aggregate existence, and the thickness and the subsurface distribution can also be determined (Beresnev et al., 2002). Sudha et al. (2009) also demonstrates the ability of electrical resistivity to determine soil strength. Fallah-Safari et al. (2013) undertook an experimental test to determine the relationship between different clays and soils electrical properties and their geotechnical tests, results showed a reasonable correlation between geotechnical parameters such as water content, void ratio, and compressive strength with electrical resistivity. Figure 2-6 represent the relationship between moisture content and resistivity of a bentonite clay sample, it shows a noticeable decreasing in resistivity from about 35 Ohm.m at about 0.22% moisture content to about 5 Ohm.m at 0.37% moisture content.

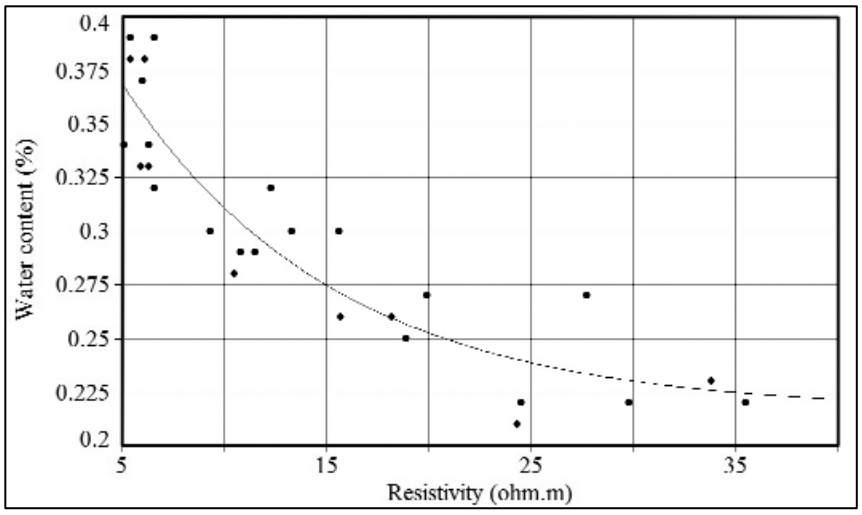

Figure 2-6: Water content-resistivity relationship of a bentonite clay sample (Fallah-Safari et al., 2013).

Chrétien et al. (2014) stated that the resistivity method is an adequate method to determine seasonal water content variations to understand soil deformation on a construction site. Cosenza et al. (2006) also demonstrated that electrical resistivity showed a good indirect predictor of water content for geotechnical tests. It employed to determine buried karst features (location and dimensions) for highways and municipal roadways extension in Florida, US, results matched data from soil boring (Garman and Purcell, 2004).

2.2 Seismic method

2.2.1 Introduction to seismic geophysical method

The “Seismic method” is one of the geophysical methods has been used since the 1920s (Keary et al., 2002). This method includes many techniques and all of them are dependent on the physics of the mechanical wave. Seismic techniques are divided into two types depending on the nature of seismic source (i.e., the source of seismic waves), passive techniques are natural seismic sources (e.g. refraction microtremor technique); whilst active techniques depend on active seismic sources (e.g. multichannel analysis of surface waves).

Disadvantages of the seismic methods include, for example, sensitivity to cultural noise; surface waves are regarded as noise when primary or secondary waves are of use, and vice versa, (Mathews et al., 2000; Everett, 2013). Moreover, seismic surveys can be classified into invasive and non-invasive techniques. Invasive techniques include cross-hole, down-hole, and up-hole where a borehole(s) is required, whilst non-invasive techniques contain refraction, reflection and surface wave techniques (Foti et al., 2015).

2.2.2 Overview of seismic surface waves

In general, seismic waves can be classified into two main groups, body waves and surface waves, and these are further classified according to the wave propagation. Body waves contain two main types of seismic waves: primary and secondary waves (see Telford et al., 1990 for more details). Seismic waves propagate through different materials can have different wave velocities. Figure 2-7 represents the typical wave velocities for different types of rocks and soils.

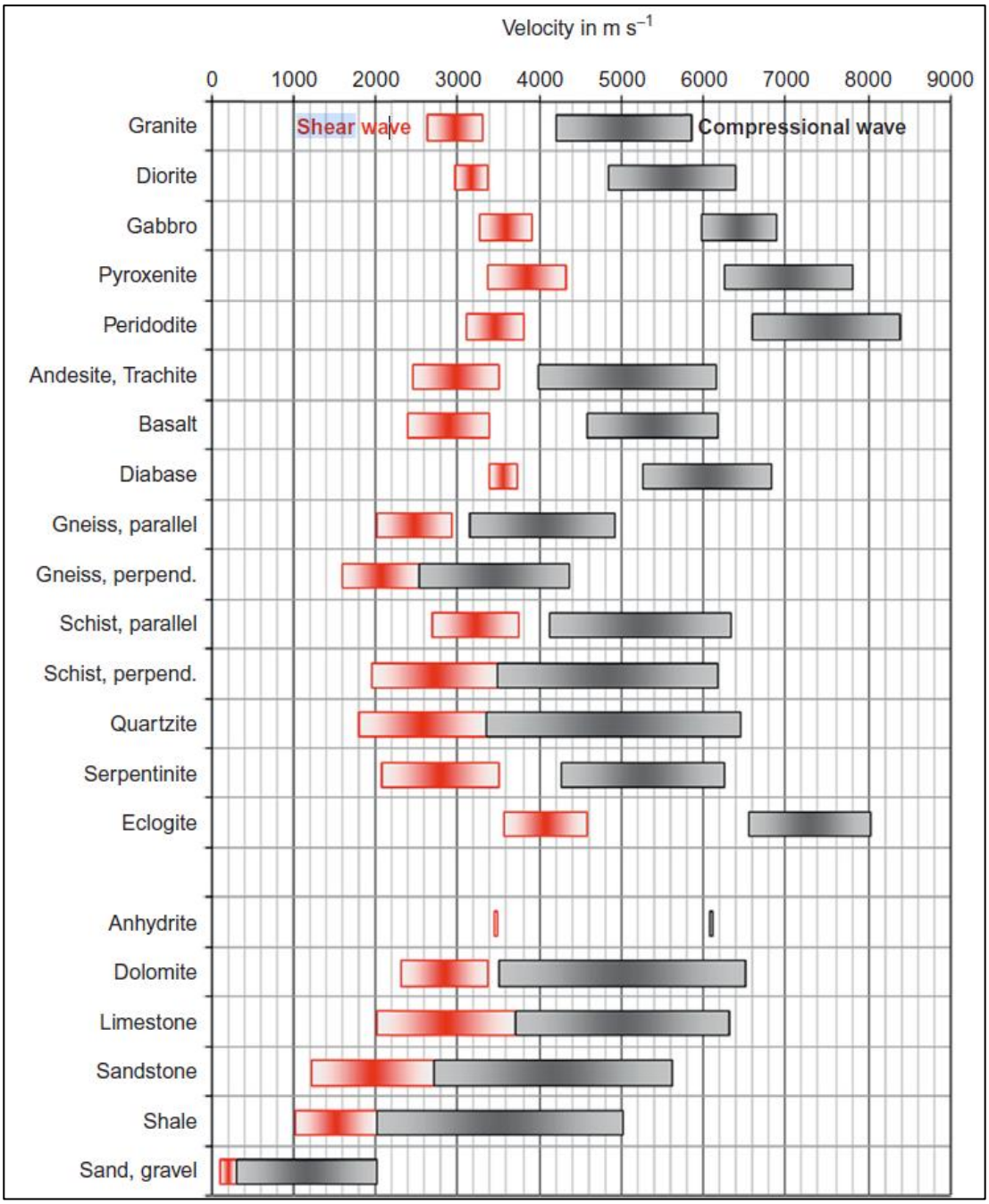

Figure 2-7: Compressional (grey) and shear (red) wave velocities for different types of rocks and soils (Schön, 2015).

Surface waves generally propagate at the ground surface or close to it, generate in a bounded elastic medium and travel at the surface of this medium (Keary et al., 2002). Surface waves can be divided into two types:

1. Rayleigh waves: They propagate along free surface or along separate boundaries between two different solid media (Keary et al., 2002). During the passage of these waves, particles move in a retrograde and vertically-oriented major axis elliptical path (Lowrie, 2007; Telford et al., 1990), (see Figure 2-8- a). Although Rayleigh waves move on a free surface, particle movements are not restricted to the medium. Particles that lie below the surface are affected by this wave. The amplitude of these waves decreases exponentially with depth (Lowrie, 2007).
2. Love waves: These are the second type of surface wave, its generation related to the medium properties, where the shear waves propagate through layered medium and the velocity of shear wave in a layer close to the surface is less than that in deeper ones. Love wave propagation lad to particle vibration in horizontal motion and transverse to the direction of wave propagation (Keary et al., 2002), (see Figure 2-8- b).

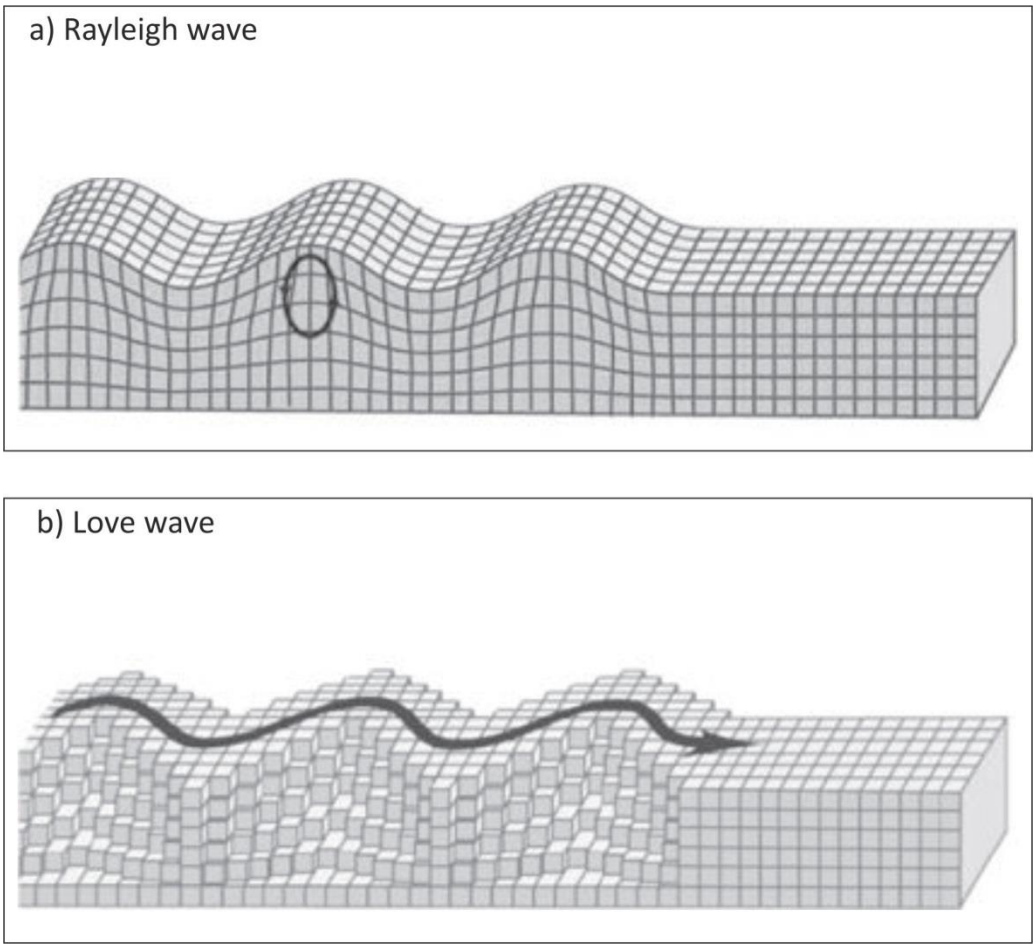

Figure 2-8 Propagation of surface waves (a) Rayleigh wave and (b) Love wave (Everett, 2013).

Seismic surface waves have another property of propagation, whereby during its travel through inhomogeneous medium (e.g. soil), it suffers from frequency changes (Foti et al., 2015). Surface waves propagate slower than body waves and their propagation velocity is highly frequency dependent (Shearer, 2009). Surface wave velocity can be explained by two components; phase velocity and group velocity. Phase velocity is a velocity of each single phase that propagates within a wave packet, whilst group velocity is a velocity for whole of the wave packet (i.e. all the propagated frequencies), (see Figure 2-9), (Everett, 2013; Foti et al., 2015).

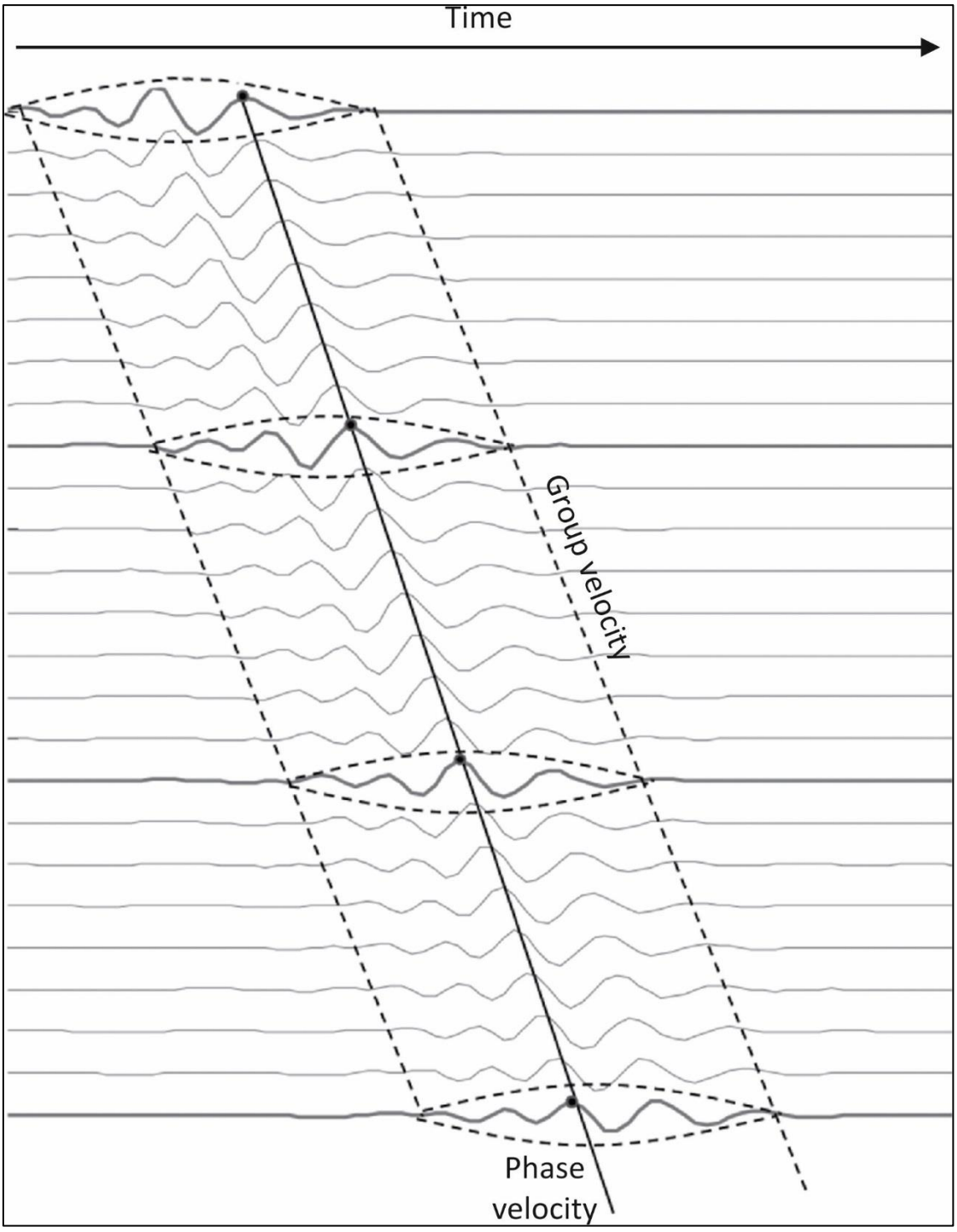

Figure 2-9: Group velocity and phase velocity for surface waves (Foti et al., 2015).

2.2.3 Dispersion

When the wave disturbance happened, many frequencies start to travel away from the source of the disturbance. If the all frequencies have the same velocity and the relationship among them is constant, the wave packet (i.e., sometime called envelope) has the same shape each time and it has the same velocity. Otherwise, when the propagated frequencies have different velocities, which led to the wave packet has different velocity from that of frequencies, (Fleisch and Kinnaman, 2015). In other words, the Rayleigh wave's phase velocity is frequency dependent (Foti et al., 2015; Shearer, 2009). This dispersion concept is an inherent property of surface waves, which is employed to extract information of particle motion. Dispersion property is employed to draw a dispersion curve; a dispersion curve is a curve which can be plotted by a set of points for phase velocity against wavelength for each single frequency (Mathews et al., 1996). Dispersion curves have many frequencies and each one penetrates the ground with a certain depth. The frequency is related to its wavelength, therefore, a phase velocity-depth profile can be determined (Lane, 2009).

2.2.4 Seismic Inversion

Seismic inversion is a final step in processing of seismic data, and it is a mathematical process whereby shear wave velocity profiles can be obtained from dispersion curves (Foti et al., 2015). It is an iterative process, by which, theoretical and measured dispersion curves are matched between each other as much as possible; *a priori* information is required about the investigated site material, such as Poisson's ratio and the geomaterial density (Milsom and Eriksen, 2011). Without more information about the surveyed site and its material, many well-fitting inversion models can be obtained (Foti et al., 2015).

Xia et al. (1999) state that the Rayleigh wave phase velocity is affected by geomaterial properties such as shear wave velocity, primary wave velocity, geomaterial density and thicknesses of layers, where shear wave velocity effects are initially put on a dispersion curve in frequencies more than 5 Hz. Note that material density has limited effect on modelled shear wave velocity profiles.

2.2.5 Theory of elasticity

Seismic wave propagation through a geomaterial depends on elasticity theory. Applying a force on the external faces of a solid body can lead to a change of shape and/or size of a solid body (Telford et al., 1990). When the external forces are removed the body will return to the original situation without any permanent deformation, this property is called elasticity (Telford et al., 1990). According to this theory, materials will be divided into four types:

Elastic material: the material that return to the original shape after the applied forces have been removed (i.e., no more permanent deformation).

Plastic material: the material that have a permanent deformation after the applied forces have been removed.

Brittle material: the material that ruptured or failed suddenly within the elastic range.

Anelastic material: this material has a different stress-strain relationship, when this material is subjected to a specific stress it does not represent the strain at the same time, but it takes more time where the strain increased gradually (Lowrie, 2007).

Passing a train of seismic waves through the earth creates a very short elastic disturbance, typically over a short period (i.e., typically few seconds to minutes). Materials may have different behaviours with short term stress (e.g. passing of seismic waves) than they have due to long term stress (a building load). Time, temperature and hydrostatic confining pressure are factors that affect the response stress of a geomaterial. Therefore, material behaviour (elastic, anelastic and plastic) is governed by the depth of material. Petrophysical properties of the geomaterial are the main factors for anelastic behaviour. Seismic waves that pass through not perfectly elastic material will lose a part of their energy (e.g. by frictional heating), then, a gradual decreasing in the wave amplitude with increasing in distance from the source occurs, this phenomenon is known as attenuation (Lowrie, 2007).

2.2.5.1 Stress and strain

According to the elasticity theory, the effects of any applied forces are represented by the variation of the shape and size of the effected object. Stress and strain concepts show the applied force and the effected object relationships (Telford et al., 1990).

A. **Stress**: is defined as the ratio of applied force to unit area, and it can be divided into two types:

1- Normal stress, when the force applied in a perpendicular direction to the face (area) of an object.

2- Shear stress, when the force applied in a tangential manner to the face (area) of an object (Telford et al., 1990).

B. **Strain**: is defined as the variations in the shape and/or the size of the medium (an object) due to subjected stress(s) (Telford et al., 1990).

Various elastic moduli have been found to state the linear stress-strain relationships for any specific material, each one of them has determined a ratio of a particular stress to the strain that was caused by it (Keary et al., 2002).

1. **Young's modulus**: is the ratio of longitudinal stress to longitudinal strain, since strain is a dimensionless amount, then Young's modulus is measured by a stress unit only, so its units are in Pascals:

$$\epsilon = \frac{longitudinal\ stress\ F/A}{longitudinal\ strain\ \Delta L/L} \qquad (2-10)$$

2. **Bulk modulus**: is the ratio of volume stress to volume strain, measured by pressure units (Pascals).

$$K = \frac{volume\ stress\ P}{volume\ strain\ \Delta v/V} \qquad (2-11)$$

3. **Shear modulus**: is the ratio of shear stress to resultant shear strain tan ϑ, measured by pressure units (Pascals).

$$Go = \frac{shear\ stress\ \tau}{shear\ strain \tan\vartheta} \qquad (2-12)$$

4. **Axial modulus**: is the ratio of longitudinal stress to longitudinal strain (in case with absence of lateral strain).

$$\varphi = \frac{longitudinal\ stress\ F/A}{longitudinal\ strain\ (unaxial)\ \Delta L/L} \qquad (2-13)$$

2.2.6 Seismic surface wave methods

The need for a rapid, cost effective and reliable investigation technique has led to many indirect methods to be developed. Seismic surface wave methods have been developed and used for soil geotechnical investigation (Mathews et al., 2000; Clayton, 2011).

Depending on the nature of the source of the surface waves, surface waves methods are divided into two groups: active surface methods and passive surface methods.

2.2.6.1 Active seismic methods

These methods depend on any seismic source device or tool that release energy into the ground by generating seismic waves. In surface waves, the seismic source should generate sufficient amount of energy in order to obtain high signal-to-noise ratios (SNR). To investigate deeper the wide range of wave frequencies are required, where the low frequency waves have ability to propagate deeper into the ground. Many active seismic sources have been employed to generate active seismic waves (e.g. sledge hammer, explosives or electro-mechanical vibrators). Site preparation, cost, source repeatability, time difference between two shots, environmental damage, safety requirements, and the need for authorization are important aspects in terms of seismic source reliability (Foti et al., 2015).

The surface waves, as other seismic waves, can be recorded on land using specific tools (e.g. geophones). The geophones can be laid down in linear and 2D geometries (e.g. L-shape, triangle, and square arrays). In linear array surveys, the geophones are set out in a straight line away from the active seismic source. Data acquisition parameters should be decided to resolve the target that the survey is being collected for (e.g. penetration depth and resolution required), these parameters are typically the length of the array *La*, the receivers spacing Δx, the time sampling and the source offset (see Figure 2-10), (Foti et al., 2015).

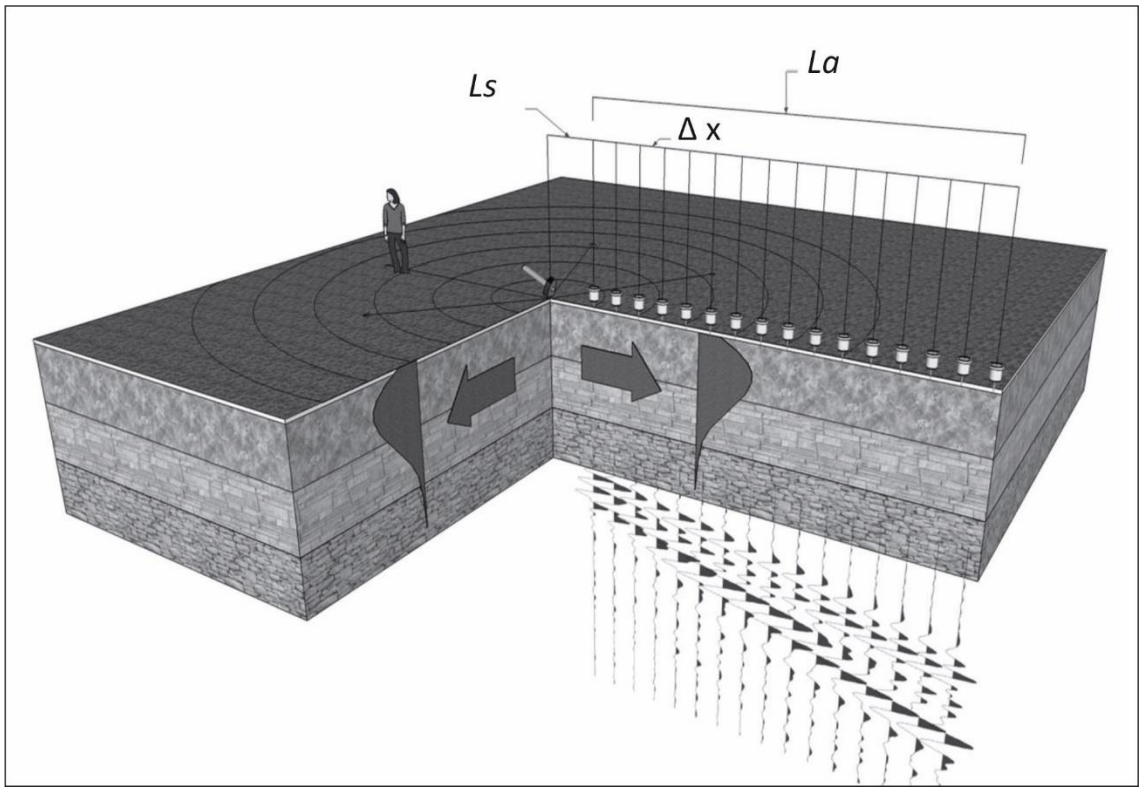

Figure 2-10: Schematic design showing the active seismic source and the distributed geophone receivers on a survey line (Foti et al., 2015).

Depending upon the geophones configuration and the active seismic source, active methods include different techniques, for instance, spectral analysis of surface waves (SASW), continuous surface wave (CSW), and multichannel analysis of surface wave (MASW). For more detail see Okada, (2003); Rix, (2005); Foti et al., (2015); Moro, (2015).

Park et al. (1999) introduced the Multichannel analysis of surface waves (MASW) method to overcome some weaknesses of SASW method. Increasing the number of geophone receivers has some advantages; for example, it helps in increasing production rate in the field. A set of receivers (usually twelve or more) are used in a linear configuration, with an active seismic source to collect seismic surface waves (Figure 2-10) (Foti et al., 2015), and then dispersion and inversion processes are undertaken to generate a shear wave velocity-depth profile. Using many geophone receivers (multi-channel) helps in

investigating all the required depths below ground level, by one or a few surface wave repeats without rearranging the receiver's configuration, this makes MASW method much faster than the SASW method (Park et al., 1997). The second advantage is that noise sources (e.g. P-waves) that are recorded at the same time with Rayleigh wavefields, can be easily recognized from the seismic record by its frequency content. Finally the reduction of noise helps in enhanced signal-noise ratios (SNR) for Rayleigh waves, when then helps in better dispersion curve estimations (Everett, 2013).

The method has been used for site and earthwork evaluation, to assess geotechnical parameters for a wind farm site (Pegah and Liu, 2016); to assess aged railway embankment, (Gunn et al., 2018); and for site response to earthquakes, (Amoroso et al., 2018; Karabulut, 2018; Rahman et al., 2018).

2.2.6.2 Passive seismic methods

Passive seismic methods depend on passive seismic sources, these sources can be natural sources, for example wind effects (Mucciarelli et al., 2005; Gassenmeier et al., 2015), ocean waves or changes in atmospheric pressure, or human daily activities near or around the site (e.g. traffic, drilling and so on) (Cha et al., 2006; Behm et al., 2014). Natural sources generate low frequency waves (i.e., below 1 Hz), whilst, high frequencies, more than 1 Hz, are almost all generated by human activities. Because of the absence of active sources, the techniques based on ambient noise are called passive. Ambient noise is sometimes called microtremors (Okada, 2003). The nature of these types of waves make them useful in surface wave testing. Ambient noise, generally, is predominated by surface waves (i.e., Rayleigh and Love waves), body waves have limited contribution in ambient noise generation (Foti et al., 2015).

In low frequency ranges, the ambient noise has more low frequencies than that generated by light active seismic sources at the ground surface (e.g., small sledgehammer). Therefore, passive methods have an advantage to use ambient noise. Otherwise, in near surface applications, it is more effective to combine passive and active methods to get higher frequencies and investigate shallower depths (Foti et al., 2015).

Ambient noise can be recorded by 1D (Louie, 2001) or 2D (Strobbia and Cassiani, 2011) configurations. Some of the common 2D configurations applied for passive seismic waves collection are L-shape, T-shaped, square and circle configurations (Foti et al., 2015), (Figure 2-11).

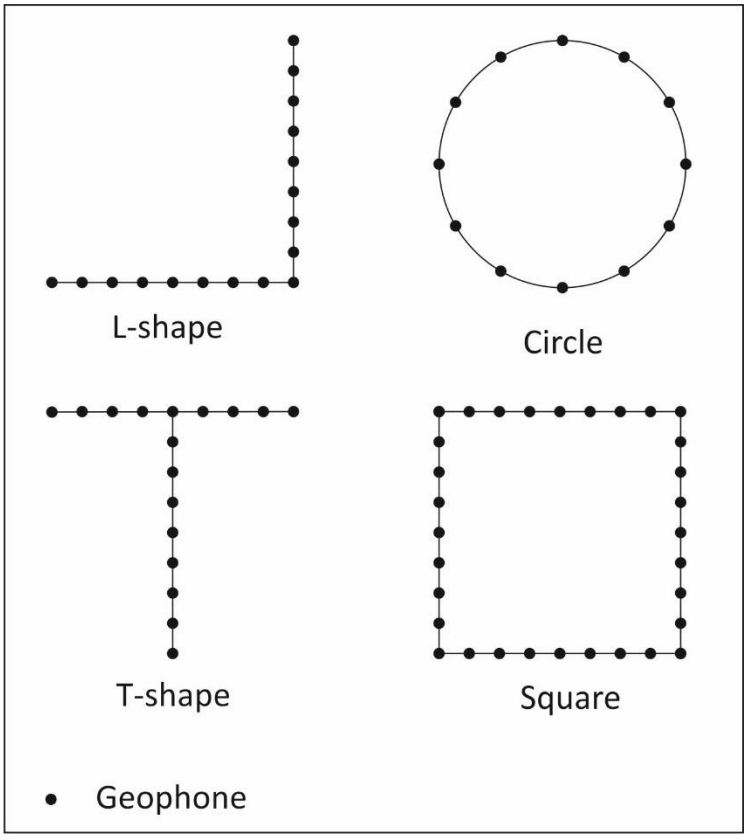

Figure 2-11: Common 2D geophone configurations for passive waves collection, modified from (Foti et al., 2015).

The refraction microtremor method (ReMi) was developed by Louie (2001), and it works with standard seismic refraction equipment. This method tries to collect microtremor (ambient noise) by a technique similar to shallow P-wave refraction surveys and using the same equipment. Noisy urban sites are more suitable than quiet rural sites, because the latter do not produce refraction microtremor results that are easy to interpret (Louie, 2001). Urban microtremors have surface waves with broad ranges of frequency, this helps in shallow depth investigations (Stephenson et al., 2005). Sometimes ambient noise lacks high frequencies, and in this case, an active seismic source (e.g. hammer hits) can be used to increase the high frequency waves. Moreover, thin layers can be determined using small geophone spacing and high frequency waves (Gamal and Pullammanappallil, 2011).

The ReMi method works with little field work according to two essential factors; the use of a single geophone sensor and a linear spread with 12 or more geophones (Louie, 2001). Because this method depends on a linear array, oblique waves may be recorded and apparent phase velocities may be picked (Louie, 2001; Stephenson et al., 2005). Strobbia et al. (2015) state that the use of two orthogonal linear arrays helps to overcome the limitations of the ReMi method and the true velocity (i.e., true propagation direction) can be identified.

Louie (2001) states that the collected data by the ReMi method can be processed by using slant-stack transform (tau-*p*), where dispersion curves can be determined clearly and easily. Slant-stack transformation is used to decompose a wavefield due to its plane wave components, and it is initially applied for reflection and refraction seismic data processing (Yilmaz, 2001).

Cha et al. (2006) applied the ReMi method to evaluate a rock mass shear wave velocity for a railway tunnel project. Raines et al. (2011) applied it to determine 1D shear wave velocity – depth profile and a 2D cross section which was used to predict a backfilled mineshaft position. Gouveia et al. (2018) performed active (MASW) and passive (ReMi) seismic surveys to obtain a site's shear wave velocity to estimate site seismic response and to determine soil – bedrock interface depth at the site.

For more details see Reynolds, (1998, 2011); Dobrin and Savit, (1988); Keary et al., (2002); Okada, (2003); Foti et al., (2015).

2.3 Train-induced vibrations

Moving trains generate a set of wave frequencies (i.e. vibrations) that can propagate through the ground, the vibrations have been understood as the weakness of railways (Thompson, 2009). One of the sources of train-induced vibration is the roughness of the trains' wheels and the rail track surfaces. This roughness makes the wheel and the rails vibrate relatively to each other and generate vibrations, and these vibrations/sound can be propagated in the air and into the ground (Wu and Thompson, 2001; Yang and Hung, 2009) (Figure 2-12). The train as a moving load (the train's weight) can be another vibration source (Yang and Hung, 2009; Yang et al., 2003).

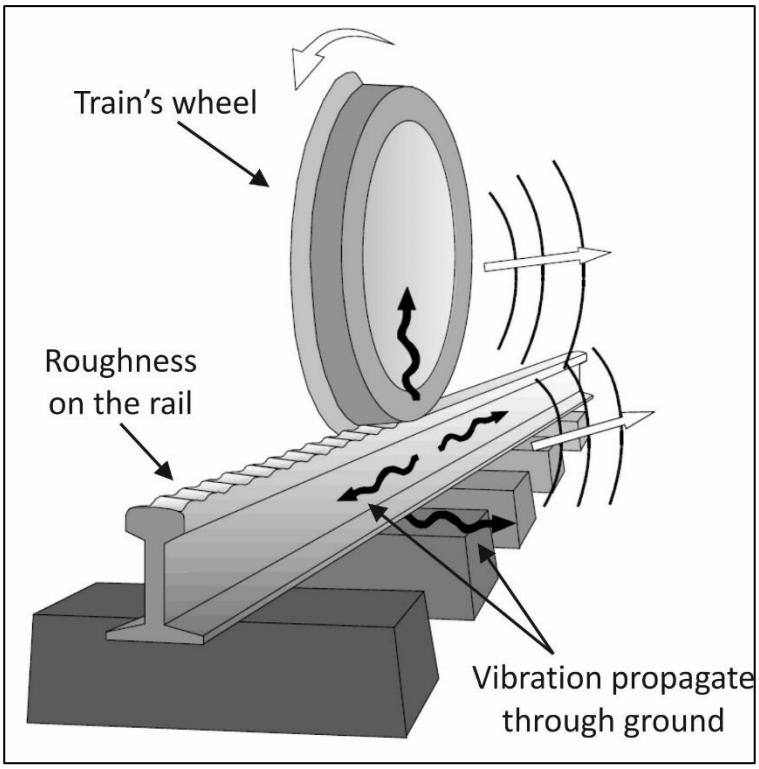

Figure 2-12: Train-induced vibrations generated by roughness on wheels and sleepers, adopted from (Thompson, 2009).

Railway noise collected at Gunma, Japan, provided evidence that the most energetic part of the vibrations lay in the range of 12-16 Hz (Nakata et al., 2011). The induced vibrations span a range of frequencies from about 5 Hz to 50 Hz, the maximum amplitude occurs between 5-20 Hz (Quiros et al., 2016). Collected data from different passenger trains show that the frequency range can be between 10 Hz to about 40 Hz (Fuchs et al., 2017).

Moving trains generate vibrations that are mainly composed of the Rayleigh wave (Kim and Lee, 2000; Kouroussis et al., 2014). Different soils have different soil Rayleigh wave velocities, the soil Rayleigh wave velocity depends on the geomaterial parameter, for instance, the soil density. The train-induced vibrations intensity is related to train speed, therefore increasing the train speed leads to increasing vibration intensity. The soil

Rayleigh wave velocity is therefore a critical velocity in the vibration-ground system (Krylov, 2001). Connolly et al. (2014) tested the train-induced vibrations at three different earthwork profiles (i.e. when the railway was on the track, on an embankment, and in an earthwork cutting). The earthwork configuration seemed to have an effect of the collected noise that was already generated from a moving train. The cutting earthwork generated higher vibrations in 3 components than the vibration generating from surface and in an embankment earthworks. In contrast, vibrations generated on the embankment and on the surface had similar vibration levels. These findings were not consistent with US Federal railroad administrations report in 2012 (see Hanson et al. (2012), which suggested that the earthwork cutting might be reducing the vibration level.

Because the train-induced vibrations generate from moving trains, the generated vibrations would be expected to be affected by the Doppler Effect; when the train is approaching or travelling away from the sensors (Chen et al., 2004; Quiros et al., 2016). However, Fuchs et al. (2017) state there was no clear evidence for this in their study.

Nakata et al. (2011) collected train vibrations and applied a cross-coherence method using seismic interferometry to record body and surface waves. A transverse component of the retrieved surface wave (Love wave) was used, as a demonstration, to determine shear wave velocity-depth profile down to about 300 m bgl.

Quiros et al. (2016) recorded a vertical component of train-induced vibrations. The studied site is about 10 miles southwest Belen within the Rio Grande rift in southern New Mexico. The collected data was processed using seismic interferometry to retrieve body and surface waves (i.e. Rayleigh waves). The generated surface waves could then be applied for shear wave velocity-depth profile determination through an inversion process

of their generated dispersion curve. A 1D shear wave velocity-depth profile was calculated down to about 180 m below ground level (bgl) for the studied site (Figure 2-13).

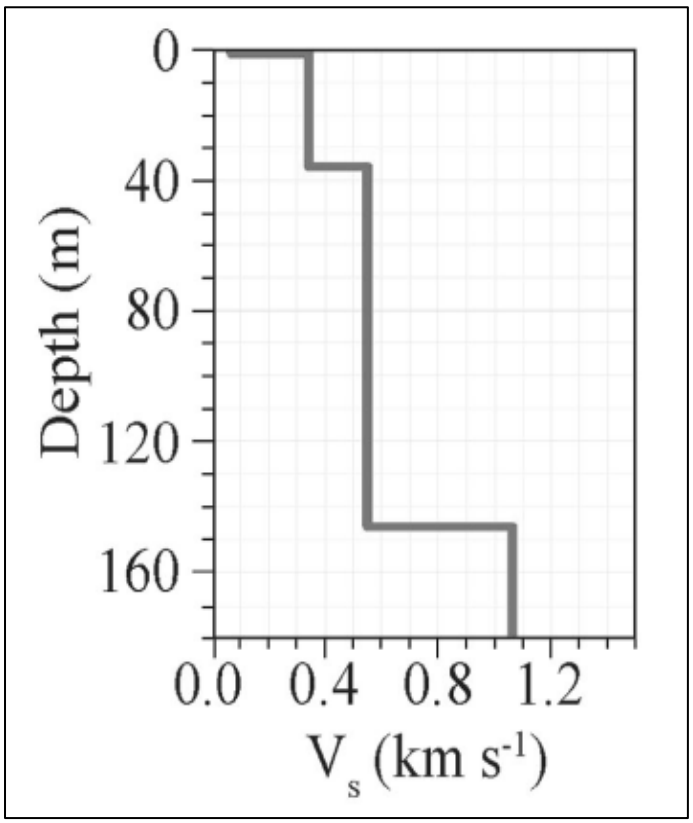

Figure 2-13: A 1D shear wave velocity – depth profile obtained from the inversion of train-induced vibrations in the frequency range 0-8 Hz, adopted from (Quiros et al., 2016).

The moving trains can be a good passive seismic source for surface waves. The generated vibrations can also be used to estimate shear wave velocity for shallow depths bgl and could be applied for a range of near surface applications (such as site investigation) and shallow subsurface imaging (Chen et al., 2004; Nakata et al., 2011; Quiros et al., 2016; Fuchs et al., 2017). For more details see Yang and Hung (2009), Thompson (2009).

2.4 Microgravity method

2.4.1 Introduction to microgravity method

The microgravity method can be applied to near surface geophysical applications (Nabighian et al., 2005). Physically the method depends on gravitational theory which was described by Isaac Newton in the seventeenth century (Reynolds, 1998, 2011). During a gravity survey, the relative variations in gravitational attraction can be measured between two or more adjacent points (Emsley and Bishop, 1997). The variations in measured gravity values are dependent upon many variables, for example, site latitude/longitude, diurnal/instrument drift, regional and local ground material density, as well as terrain and above-ground materials to be considered (Mussett and Khan, 2000).

Gravity is measured in *Gal* unit (*1 cm/s*^{2}) or *mGal*. Modern, highly sensitive microgravity instruments measure very small differences in material gravities, it can measure down to 10 parts per 10^6 (Reynolds, 2011). The value of gravity at the ground surface is 9.8 ms^{-2}; but lateral variations in the material density can be in order of 100μms^{-2} (Keary et al., 2002).

2.4.2 The density of subsurface materials

In sedimentary rocks, variation in porosity is the dominant reason for the density changing. Igneous and metamorphic rocks densities are highly affected by mineral composition. Typically, acidic rocks have lower densities than basic and ultrabasic rocks, (Keary et al., 2002). The higher porosity of the material the lower the relative density. Material lying progressively beneath the ground surface would be expected to have higher densities due to compaction (Reynolds, 2011). Table 2-1 represents the typical densities for different types of rocks and soils.

Table 2-1: Densities of different types of rocks and soils (Milsom and Eriksen, 2011).

Rock type	Density (Mg/m^3)
Top soil	1.2-1.8
Dry sand	1.4-1.65
Wet sand	1.95-2.05
Gravel	1.5-1.8
Clay	1.5-2.2
Salt	2.1-2.4
Siltstone	2.1-2.6
Sandstone	2.15-2.65
Chalk	1.9-2.1
Limestone	2.6-2.7
Slate	2.6-2.8
Quartzite	2.6-2.7
Gneiss	2.6-2.9
Granite	2.5-2.7
Basalt	2.7-3.1
Gabbro	2.7-3.3

2.4.3 Gravity correction

Microgravity data can be affected by the variation in the earth gravitational field which is not related to the variation in density of subsurface material, therefore, before any interpretation from microgravity results, the data has to be corrected. Sometimes, this correction is called microgravity reduction (Keary et al., 2002).

2.4.3.1 Drift correction

Due to the elastic creep of the gravimeter's spring, gravity readings suffer from changing with time even when readings are taken at the same location. The drift correction can be determined by taking several readings at a fixed location but at different times. Then the difference between successive readings, plotted with time, generate a *drift curve* (Figure 2-14). The observed readings can be corrected by subtracting the drift using the drift curve (Keary et al., 2002).

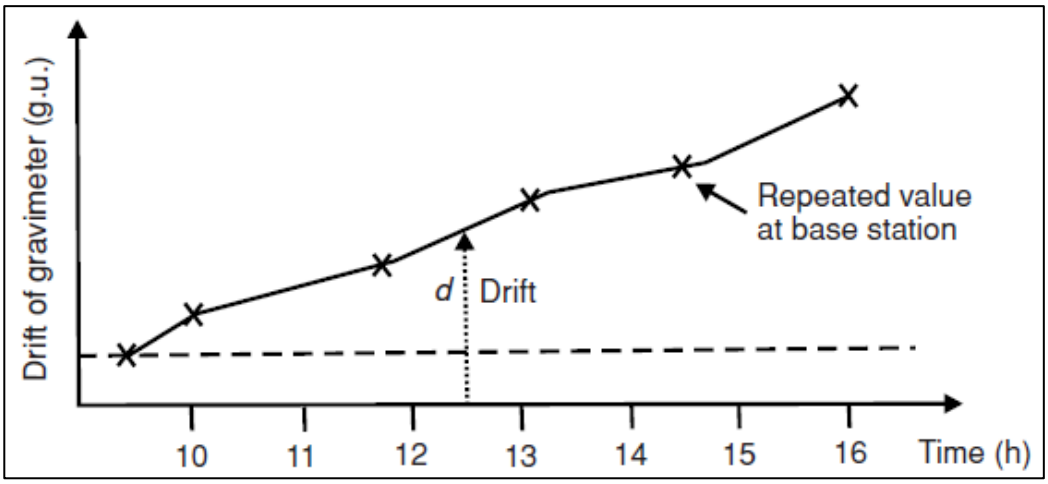

Figure 2-14: Drift curve generated from repeated readings at the same station and at different times (Reynolds, 2011).

2.4.3.2 Latitude correction

This correction can be made by subtracting a theoretical gravity reading, which is determined from the international gravity formula, from the observed gravity reading (Reynolds, 2011).

2.4.3.3 Elevation correction

This correction can be made by performing two corrections, the free-air correction and Bouguer correction. The free-air correction compensates the decrease in the observed readings due to the increasing in the distance between the gravimeter and the centre of the Earth. Bouguer correction takes into account the gravity of the rock mass between the gravimeter and sea-level. For land surveys, the correction removes the overestimation caused by the rock mass from the observed readings (Keary et al., 2002).

2.4.3.4 Terrain correction

The elevation correction (free-air and Bouguer corrections) does not take in consideration the variation in topography; therefore, terrain correction is necessary due to the variation

of topography on the observed readings. For a gravity station beside a hill, the presence of extra rock mass (i.e. the hill) will apply an upward attraction on the gravimeter and reduce the observed gravity reading. For a gravity station beside a valley, the missing rock mass, results in underestimation of the observed gravity. In both cases (the hill and/or the valley) terrain correction has to be undertaken to remove the effects of the topography variations (Reynolds, 2011).

2.4.3.5 Bouguer anomaly

The final result of the gravity correction is the Bouguer anomaly which represents only the variation in density of the subsurface materials. It is the observed gravity after subtracting the summation of all the reductions (Reynolds, 2011).

2.4.4 Microgravity surveys and applications

Gravity surveys are commonly undertaken on 2D or grid profiles, with measurement station spacings depending on the target size and gravity variation (Keary et al., 2002). The microgravity method, sometimes, can be used alongside with other geophysical survey method(s). In this integrated survey approach, the results obtained can be constrained with each other helping in better ground truthing process. For example, Mochales et al. (2008) collected gravity, magnetic and ground penetrating radar data to delineate a filled cavity from the background material.

The microgravity method has been applied for many near surface geophysical investigations. The method has been used for underground cavity and tunnel detection (Butler, 1984; Elawadi et al., 2001; Styles et al., 2005; Mochales et al., 2008; Kaufmann et al., 2011). It can be a useful indirect method for archaeological investigations (PadÍn et al., 2012). It has also been used for site investigations; for example, Ardestani (2013) used

gravity surveys to detect underground voids at a construction site. The expected problematic spots (i.e. low density) are represented by residual negative anomalies in the microgravity map of the studied site (Figure 2-15). It has been applied with seismic reflection surveys for deep groundwater aquifer characterisation (i.e. subsurface extent) (Khazri and Gabtni, 2018). For more details see Reynolds, (1998, 2011); Dobrin and Savit, (1988); Keary et al., (2002).

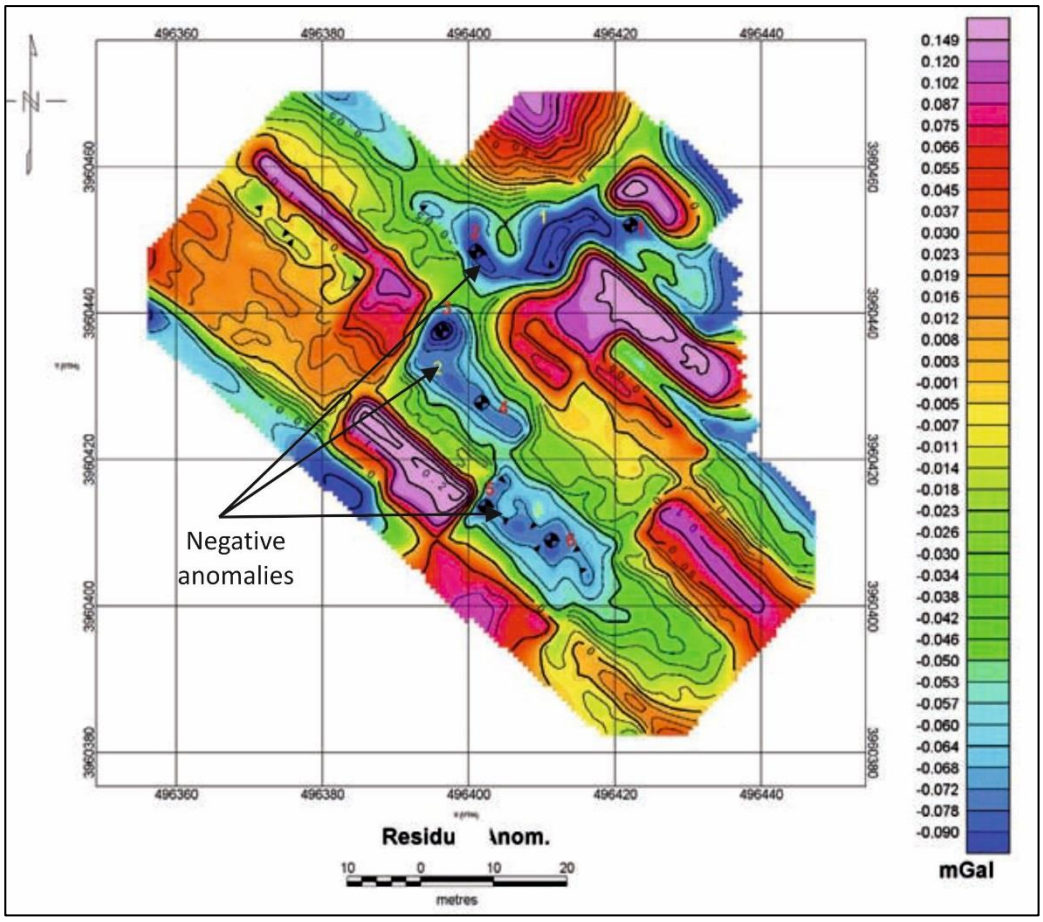

Figure 2-15: Microgravity map showing low density (negative anomalies) spots in a construction site, (Ardestani, 2013).

2.5 Soil mechanics

2.5.1 Introduction

Soil has many definitions dependent on the discipline of science, in civil engineering and geotechnical engineering communities, soil is defined as a natural occurring or it is a man-made material (Barnes, 2010 and 2016). It contains separated and uncemented particles (Das, 2006). Soil as a material has a wide range of physical, chemical and mechanical properties. Solid particles have many different shapes, from nearly spherical bulky grains to thin, flat plates or long, slender needles. Particle size, as well as its shape, has a wide variety, ranging from very small (i.e., clay particle size which is 0.002 millimetre or less) to gravel (2 millimetres or more), (Murthy, 2002).

Civil constructions are on the ground surface or built underground (i.e., tunnels or excavation works) and building foundations should have a suitable layer to carry the load; therefore, civil and geotechnical engineering communities investigate deeper than others, i.e., agricultural engineers (Smith, 2006). Many problems come from inadequate site investigations; problems within the structure itself (e.g., crack(s) to complete collapse), financial (e.g., over-running costs) and administrative problems (e.g., longer construction period) (Barnes, 2010). Therefore, soil mechanics and site investigations are highly important in civil and geotechnical engineering work.

2.5.2 Soil physical parameters

Soil physical parameters refer to soils in natural condition and without human impacts (i.e., load of building, excavations, etc). These parameters include soil phases, moisture content, solid particles arrangement, particle size distribution, soil density, porosity, etc. (Wilun and Starzewski, 1975).

2.5.2.1 Soil phases

Any soil sample contains solid particles and voids; the voids may be filled with fluid (usually water with dissolved ions) or empty (filled by air) (Miyazaki, 2006). A soil sample has to match one of three conditions: 1) three-phase soil, which contains solid particles, have part of pores space filled by water and the rest volume filled by air (i.e. unsaturated soil), (Figure 2-16- a), 2) if the soil pores are filled by water, the soil is in saturated conditions (Figure 2-16- b); and 3) when the soil voids are filled by air, the soil is in dry conditions (Figure 2-16- c) (Craig, 2004).

Soil phases are not constant in terms of time, but they do continuously change (e.g. rain/irrigation lead to a change in moisture content and a dry soil may change to be saturated) (Yong and Warkentin, 1975). Soil phases are related to depth, where soil below the water table is always saturated (Smith, 2006).

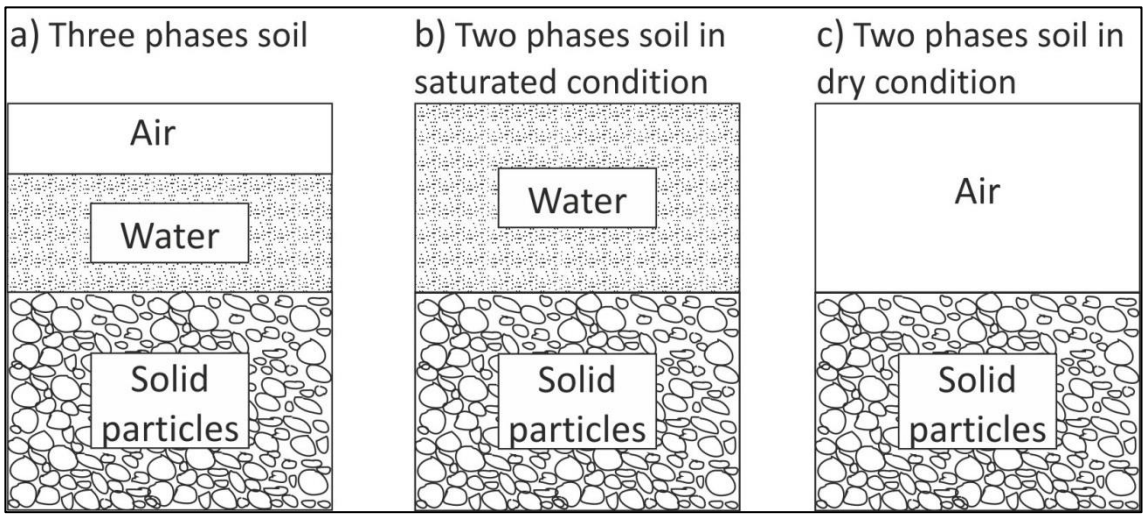

Figure 2-16: Soil phases, a) three phases of soil, b) two phase soil in saturation condition, and c) two phases of soil in day condition, modified from (Das, 2006).

2.5.2.2 Moisture content

Moisture content of a soil can be defined as the ratio of the mass of water contained in the pores to the mass of solid particles, (Craig, 1997). It is one of soil properties that has a wide range from zero (completely dry soil) to a hundred percent (saturated soil); sometimes percentage goes up to 500% or more (e.g. soil rich with bentonite clay minerals), (Murthy, 2002). It is given by the following equation:

$$w = \frac{M_w}{M_s} \times 100 \qquad (2-14)$$

Where w is water content, M_w is water mass in the pores, and M_s is solid particle mass.

Water is present in soil pores by different mechanisms; it is in the form of free or gravitational water, capillary water and adsorbed water (Wilun and Starzewski, 1975). Water content within the same soil sample may change due to different water percentages in pores or changing pore volumes (Yong and Warkentin, 1975). Moreover, the moisture content of different soil samples may vary with variation in solid particle minerology, it can be 5% for a dry sand to about several hundred % for a peat soil or soils rich in montmorillonite clay mineral, (Barnes, 2016).

The basic method for water content determination in civil engineering is the oven drying method; where the soil sample is first weighed and then heated up to 105-110 ^{o}C until all free water is evaporated and weighed again. This method has some drawbacks, as it is time consuming, taking 24 hours approximately. Coarse grained (e.g., sand), high organic (e.g., peat) soils that are sampled from below the water table can lose some of their moisture content by gravitational force; in this case, the results will represent a partially drained soil moisture content (Barnes, 2010). The small volume of soil that are typically

used, usually less than 50 cm^3, may not be a representative sample, and thus may lead to a serious error in water content measurement (Yong and Warkentin, 1975; Wilun and Starzewski, 1975).

Geophysical methods can overcome some of these limitations; they can sample larger areas and can even be applied in 3D/4D methods. Among these, electromagnetic induction (Sherlock and McDonnell, 2003), ground penetrating radar (Topp et al., 1980), and electrical resistivity (Samouelian et al., 2005) are used. Electrical resistivity is the most common because soil moisture is the dominant factor of soil resistivity, i.e. through electrolytic conduction. Moreover, soil resistivity is affected by its clay content (Samouelian et al., 2005). It can also investigate a big soil volume depending on the electrode spacing and the survey profile length.

2.5.3 Mechanical soil parameters

Mechanical soil parameters are those related to the movement of soil particles' such as, slope soil movement, sudden movement with failures, settlement, consolidation, swelling and shrinkage. The main aim of geotechnical engineering is to prevent or to reduce such movement (Atkinson, 2014). Soil deformation caused by building load is a function of soil properties, the applied load and time. Therefore, soil resistance for deformation (i.e., soil deformation) is a result of the interaction of all these factors. Soil resistance acts with accurate civil and design engineering works for building stability and safety (Yong and Warkentin, 1975).

2.5.3.1 Soil stiffness

Soil stiffness can be defined as resistance of a body to a deformation against applied force (Clayton, 2011). It is a relationship that relates strain increment changes to stress

increment changes (Wood, 2004), and is a geotechnical parameter can be utilized for solving soil-structure interaction problems (Heymann, 1998). The relationship of stress-strain for hard rock is linear, whilst it is strongly non-linear for soil and weak rock, (Mathews et al., 1997). Although many developments in instrumentation and laboratory techniques, laboratory measurements reveal a noticeable difference from that measured *in situ*. In addition, limited sampling, sample discontinuities, soil fabric and variation in soil composition all add complexities for stiffness measurements (Mathews et al., 2000).

Laboratory or *in-situ* stiffness measurements should be carefully undertaken, factors such as strain, very small strains (0.001% and less) stiffness behaves without noticeable changes (Figure 2-17), other issues such as void ratios, grain size/shape, particle arrangement and effective stress are also important (Clayton, 2011).

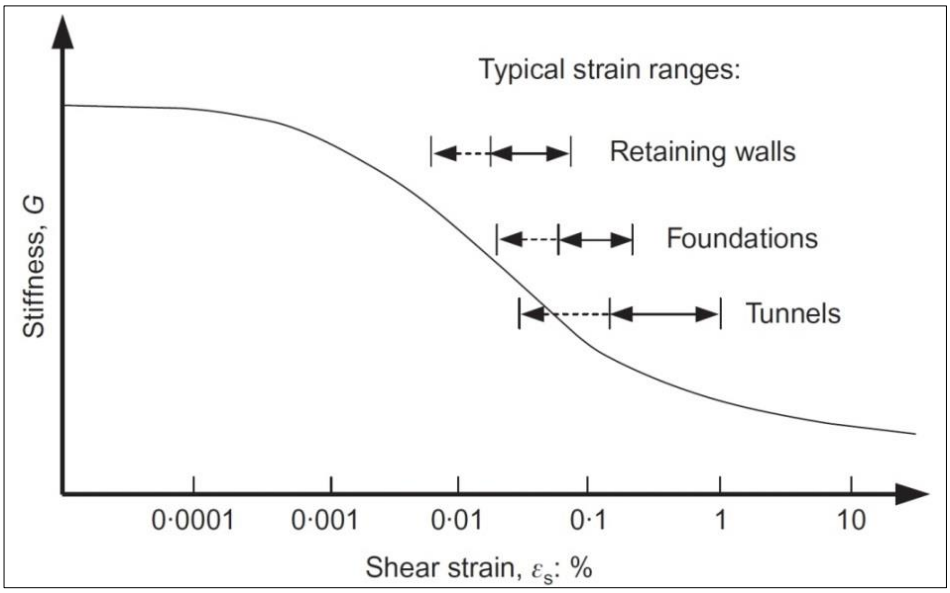

Figure 2-17: Stiffness variations with a range of strain variations (Clayton, 2011).

Bishop and Hight (1977) stated that the geomaterials are anisotropic or it can have transversely isotropic behaviour. Practically, a geomaterial assumed to have isotropic linear elasticity and two from four parameters (i.e. Young's modulus, bulk modulus, shear modulus and Poisson's ratio) are required to characterise such material (Clayton, 2011). In addition, for soil stiffness determination, drained and undrained cases should be taken in consideration and the shear modulus has the same values in undrained and drained cases where only changes in shape are considered in shear modulus (Clayton, 2011).

Soil shear modulus is one of the soil parameters that are needed to determine soil stiffness, under dynamic loading (Aggour et al., 1987). Soil shear modulus depends upon many factors, for instance, soil type, degree of saturation and number of load cycles (Hardin and black, 1968).

Propagated seismic waves (the shear wave) produce very small strains (10^{-6}-10^{-4}%) (Mathews et al., 2000), and generate changes in shape rather than in volume (Clayton, 2011). In addition, shear wave velocity is a function of shear stiffness and the measured stiffness is not affected by the saturation condition of the tested material. In the case of transversely isotropic material, shear modulus can be determined from shear wave velocity distortion in the vertical and in the horizontal planes (Clayton, 2011). Moreover, field seismic techniques allow determination of soil stiffness which are more representative of ground volume and can be applied *in-situ*. Therefore, geophysical seismic methods have been provided and utilized for soil and weak rock stiffness measurement using different active (for example, up-hole and down-hole methods) and passive (for example, refraction microtremor and multichannel analysis of surface waves) seismic methods.

2.6 Cone penetration test (CPT)

The CPT test is a field soil test. It is widely applied for soft soils, with modern equipment; it can be performed for stiff to very stiff soils (Robertson and Cabal, 2015). Many shapes and sizes of the CPT have been used, the most popular is a cone with an apex of 60˚ with 10 cm^2 base area (Figure 2-18). The cone connects to a set of rods, a metre length for each piece of rod, and pushed in the ground. The CPT can be run mechanically by an operator or electrically by a loading cell (Murthy, 2002). This test can be mainly applied for sub-surface stratigraphy and material identification, and for geotechnical parameter determination, for instance, determining soil shear modulus (Lunne et al., 1997). In addition, the test is applied for groundwater and environmental studies, (Robertson and Cabal, 2015).

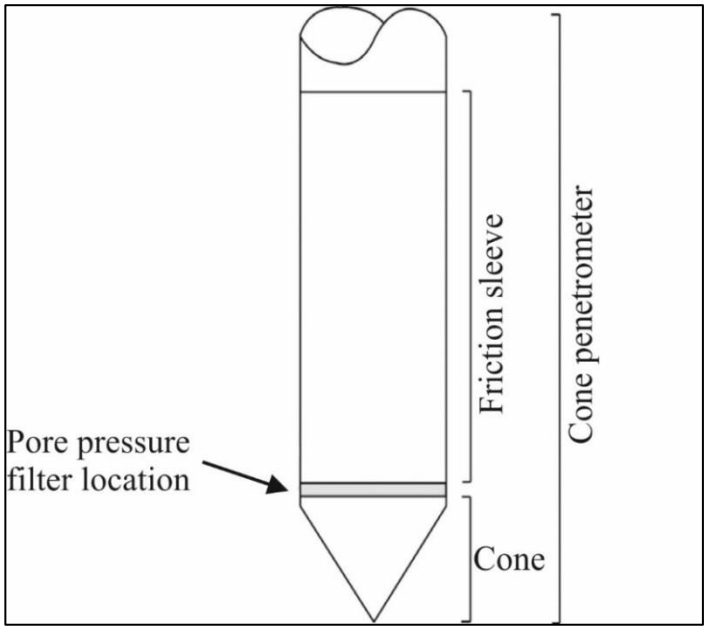

Figure 2-18: A Cone Penetrometer Test (CPT) schematic design (Robertson and Cabal, 2015).

The CPT has some advantages, it is fast and gives continuous soundings, does not depend on the operator and is repeatable, and it has strong theoretical background for data interpretation. The main limitation of the test is depth restricted and not applicable in some soil types, for example, in gravel soils (Robertson and Cabal, 2015).

The CPT test can be used on dry land and land covered by water, and can be performed in difficult environments such as soft ground. Many intrusive push rods have been developed and can even be carried on heavy vehicles, for instance, trucks, mounted track, and anchored drill-rigs that can sample up to 250 m a day (Luune et al., 1997).

Figure 2-19: A CPT unit carried on a mounted track (Robertson and Cabal, 2015).

Over water, the equipment used depends upon water depth; floating barges are used for shallow water (<30m), deeper depths use a seabed system, or using down-hole equipment from a borehole (Luune et al., 1997; Robertson and Cabal, 2015).

In the published literature, the CPT test can be carried out alone or with another(s) test for two reasons: (1) to constrain other tests results or, (2) to investigate shallow depths. Oyedele and Olorode (2010) apply the CPT test with an electrical resistivity survey as an integrated site investigation, to find the reason for several buildings having differential settlement. Integrated results from the CPT and the resistivity surveys show good agreement. At the investigated site, a clayey soil layer of low shear strength and high compressibility potential was identified as the reason for the differential settlement. Adewoyin et al. (2017) investigated a proposed construction site using the CPT test alongside with 2D resistivity survey. The obtained results represent a weak geomaterial layer from the ground surface to 7 m depth. This layer was identified as the main reason for water retention near to the ground surface. Based on the results, soil improvement work or pile foundation was suggested to reduce the site's hazard on the construction foundations. Boncio et al. (2018) applied CPTu and other stratigraphic and geotechnical tests to define a fine-grained site susceptibility to liquefaction in Italy. For more details see Lunne et al. (1997), Mayne (2007) and Robertson and Cabal (2015).

2.7 Summary

Geophysical methods have been shown as good indirect tools for looking into the ground for near-surface investigations, for example, geotechnical site investigation (McCann et al., 1997). It involves many different methods, for example, the seismic, electrical resistivity and microgravity methods; each method depends on certain physical basis and each technique can be performed alone or alongside another(s) technique. It plays an important role during site reconnaissance surveys, during and after a construction stage. Each geophysical method has advantages and limitations, in general, the geophysical methods are fast, relatively cheap and more representative than the conventional tests. The non-uniqueness of the most geophysical techniques might be one of the most important limitations.

Choosing a geophysical technique for a certain site investigation should be related to the physical basis of the method and the target that the surveys are looking for. In addition, site accessibility, budget, time and, most importantly, the technique's performance criteria (e.g. vertical and lateral resolution and signal-to-noise ratio) should be taken in consideration.

For buried foundation surveys, the electrical resistivity method has been successfully used by utilizing different electrode configurations; however, there is a need for studies to determine the optimal electrode configuration(s).

Results from different geophysical surveys can be combined into an integrated interpretation for better ground truthing, each technique might overcome the limitation of another. Geophysical surveys can also be performed alongside conventional site

investigation techniques (e.g. trial pits and/or borehole data), which helps to constrain the geophysical datasets and more accurate modelling of a study site.

Train-induced vibrations have been observed and demonstrated to generate shear wave velocity-depth profile in a few previous studies. In all these studies, the train-induced vibrations have been collected using single component geophones, and almost always, using seismic interferometry technique. The vibrations have been provided to be consistent with Rayleigh waves and, in general, the observed frequency range was about 5 Hz – 50 Hz. Doppler Effect analysis shows that the vibrations generated by a moving train will be slightly changed.

Chapter three: Electrical resistivity tomography array comparisons to detect cleared-wall-foundation in brownfield sites - Keele test site

Finding buried targets (i.e. foundations) is a main goal of any site investigation for brownfield site development (Reynolds, 2011) and indeed in archaeological studies (Vargemezis et al., 2013). For instance, about 493,000 unknown bridge foundations are stated in the United States of America. Geophysical methods can be applied to both locate and characterise buried foundations (i.e. to figure out the foundation size, type and condition - see Arneson et al., 2012). Buried foundations cause a discontinuity in the host material which can be imaged in resistivity data as a resistive anomaly (Khan et al., 2012).

The electrical resistivity technique has been widely used for near surface investigations and to delineate underground targets (see for instance, Cosenza et al., 2006; al Hagrey and Peterson, 2011; Chrétien et al., 2014; Lysdahl et al., 2017). The method has been applied for buried foundation detection in many case studies (Cardarelli et al., 2007; Khan et al., 2012; Vargemezis et al., 2013; Arjwech et al., 2013; Lysdahl et al., 2017). In most of these studies, dipole-dipole electrode configurations were used for data collection, although, in the literature, there have been about 100 different electrode configurations used (Szalai and Szarka, 2008).

In addition to the resistivity surveys, a passive seismic experiment was performed at the same site. This experiment was conducted for local traffic-induced vibrations testing as passive seismic waves. Traffic-induced vibrations have been used as passive seismic waves in many case studies (see, Nakata et al., 2011; Behm et al., 2014).

Therefore, this study aims to (1) evaluate, using the most popular electrode configurations (i.e. Wenner, dipole-dipole, pole-dipole and pole-pole) and two inversion algorithms (the least-square smoothness-constrained and robust inversion algorithms), ERT surveys to detect a scaled-model of a simulated buried cleared-wall foundation, (2) determine their appropriate survey parameters and (3) collect local traffic-induced vibrations, using three-component seismic stations, to determine shear wave velocity-depth profiles and to test the usefulness of the local traffic-induced vibrations for site investigation.

Study objectives, for the resistivity study, will therefore be to: (1) collect multiple 2D ERT datasets over a scaled model of a buried cleared-wall foundation on Keele's test site; (2) repeat the surveys using the four most commonly-used array configurations (Wenner, dipole-dipole, pole-dipole, and pole-pole); (3) combine the 2D datasets into pseudo-3D datasets, (4) invert all the datasets with the two commonly-used least-squares and robust inversion methods; (5) determine the best array type and inversion method for the 2D and pseudo-3D datasets respectively and finally; (6) the collected resistivity data will be used to find the site moisture content.

Study objectives, for the passive seismic study, will therefore be to: (1) collect a series of ReMi datasets using local traffic-induced vibrations, as passive seismic waves, (2) collection of three component ground motions (vertical component (V), horizontal and orientated in north-south component (HNS), and horizontal and orientated in an east-west component (HEW)), (3) determine shear wave velocity-depth profile and the range of the effective investigated depth for each seismic component.

3.1 Site information

3.1.1 Site selection criteria

The main consideration to select the Keele test site in this project is the already-present test facility, comprising of an excavated and refilled shallow pit, containing a buried brick wall target, which forms a geotechnical/archaeological target (see Cassidy, 2001). Therefore, the test site can be good simulation for a cleared-wall brownfield site over which geophysical surveys can be collected.

3.1.2 Site location

Keele University is located close to Keele village, about 3 miles to the west of Newcastle-under-Lyme in Staffordshire, United Kingdom. The site is located on Keele University campus close to the William Smith Building (see Figure 3-1 and Figure 3-2).

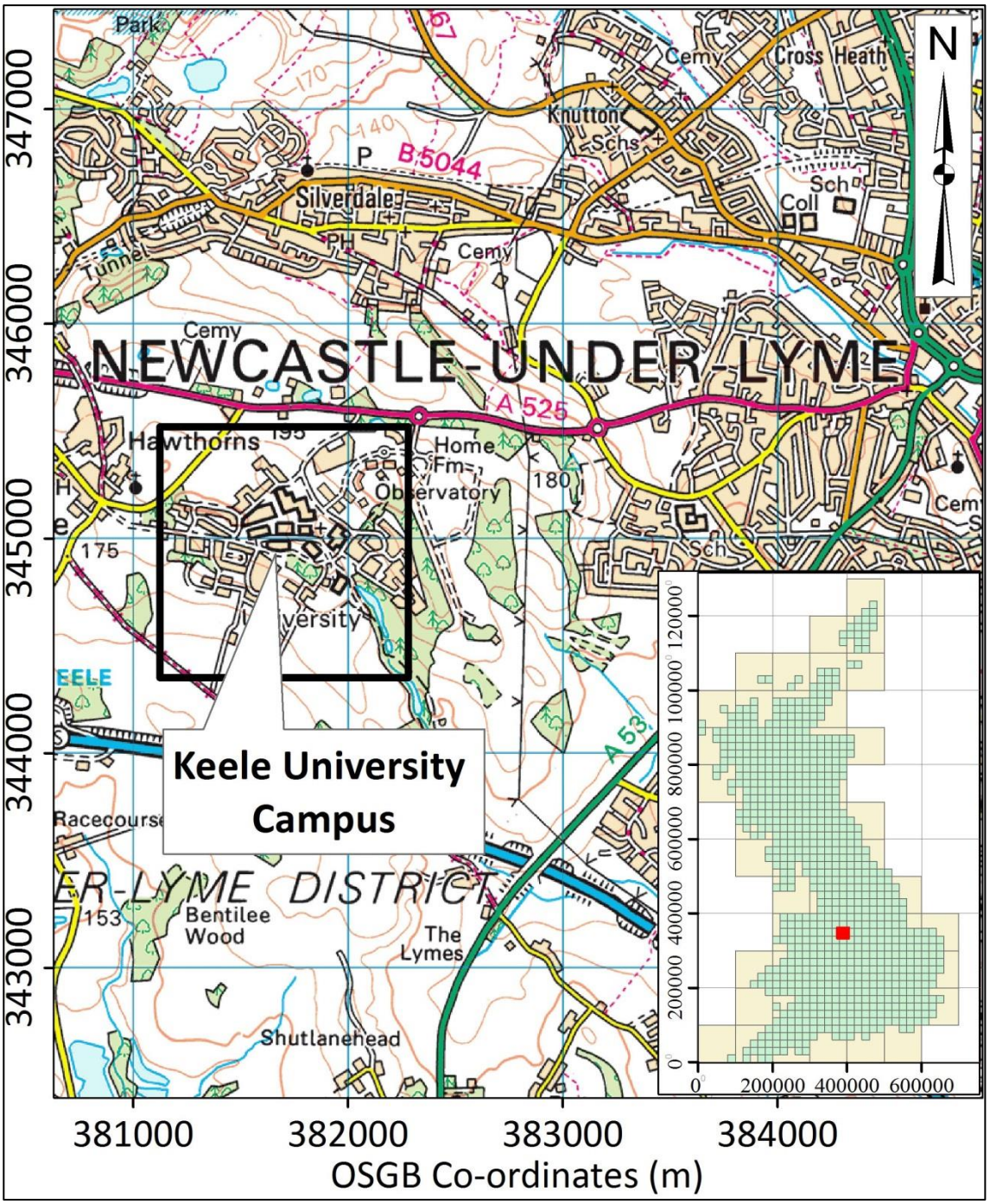

Figure 3-1: Location map of the Keele University study site with (inset) UK location map. Images supplied courtesy of Ordnance Survey/EDINA, 2012.

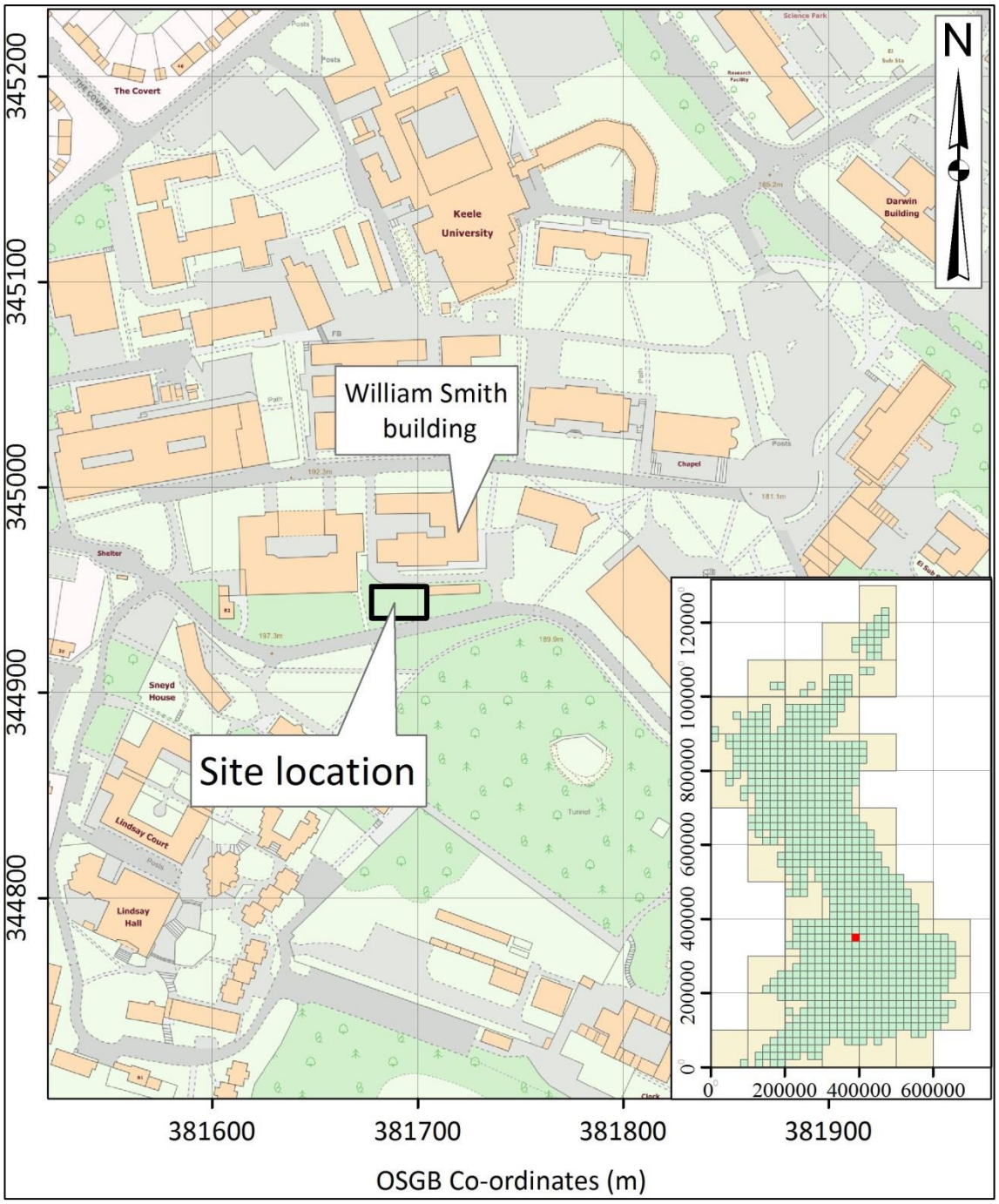

Figure 3-2: Keele University campus map shows the site location (labelled) with (inset) UK location map. Images supplied courtesy of Ordnance Survey/EDINA, 2016.

3.1.3 Local geology of the site

Generally, the geology underneath Keele campus is dominated by two clastic sedimentary rocks formations; these belong to the Carboniferous Halesowen and Butterton Formations. The test facility lies over the Butterton Formation which consists predominantly of sand and gravel detrital materials, with finer silt and clay (Figure 3-3), thought to deposited in ancient river channels (Cassidy, 2001; EDINA Digimap, 2013).

Overlying superficial deposits are dominated by Quaternary deposits, which consist of glacial sand and gravel deposits. However, the superficial deposit map does not show any at the test site (Figure 3-4).

Cassidy (2001) states the depth of the rock-soil interface is less than 1.2 m below ground level, with shallow, uniform soil horizons and a topsoil horizon thickness of approximately 0.2 m; the ground water table is at a depth of approximately 3 m - 4 m. Analysed soil samples (i.e. a grain size distribution curve) show the site soil is a clayey sand soil type.

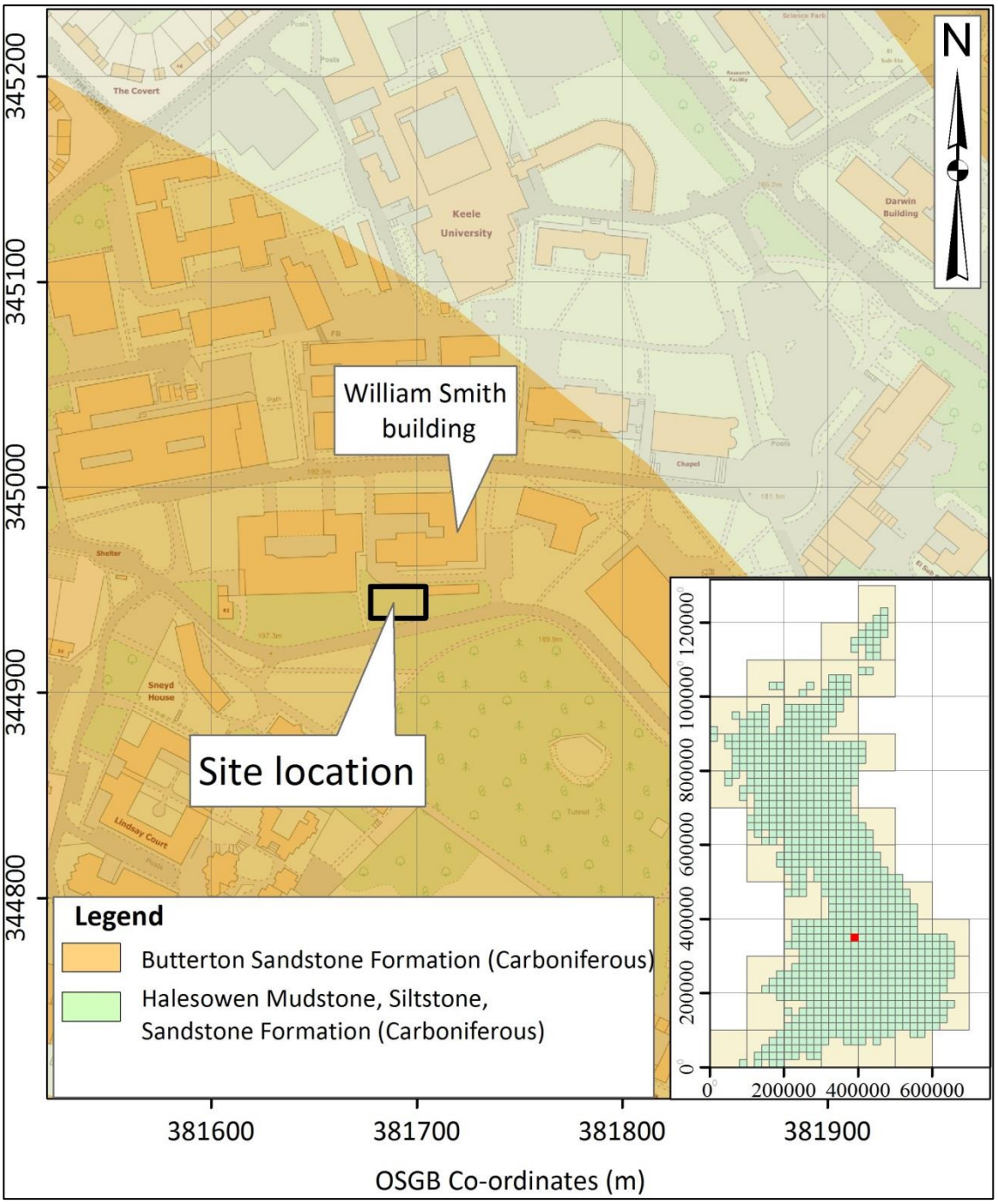

Figure 3-3: Bedrock lithology map at Keele University campus, with (inset) UK location map. Images supplied courtesy of Ordnance Survey/EDINA, 2013.

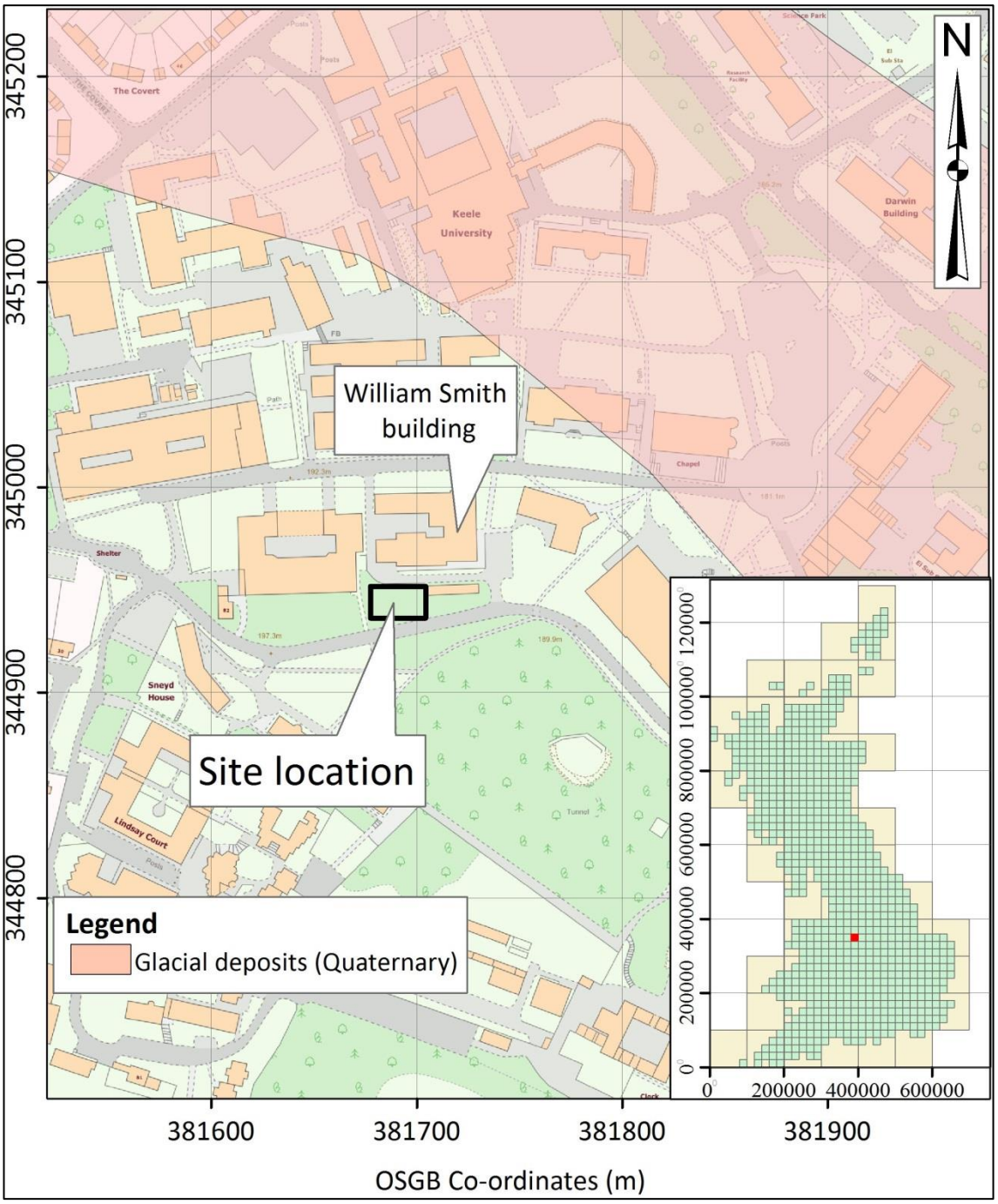

Figure 3-4: Superficial deposits map at Keele University campus, the map does not show superficial deposits at the test site; with (inset) UK location map. Images supplied courtesy of Ordnance Survey/EDINA, 2013.

3.1.4 Test facility site

An excavated and back-filled pit with dimensions of 0.8 m deep x 3 m long x 2.9 m wide constitutes the test site facility, with a Victorian brick wall target of 1.5 m long × 0.36 m wide × 0.48 m height being constructed in its centre, being orientated in an East-West long axis direction (Figure 3-6). The vertical edges of the pit were covered by an impermeable membrane and a drainage system was added to facilitate water filling/drainage. The pit was then back-filled with clay-free, well-sorted, 4 mm quartz gravel, and with porosity of about 42%, to a depth of 0.56 m. The final 0.24 m was refilled by using the re-cycled, compacted top soil and the pit levelled (Figure 3-5 and Figure 3-6), (see Cassidy, 2001). The test site facility was constructed in 2001 to simulate buried building foundations for site investigation studies and will be used here as a cleared-wall foundation for comparing different electrical resistivity configurations.

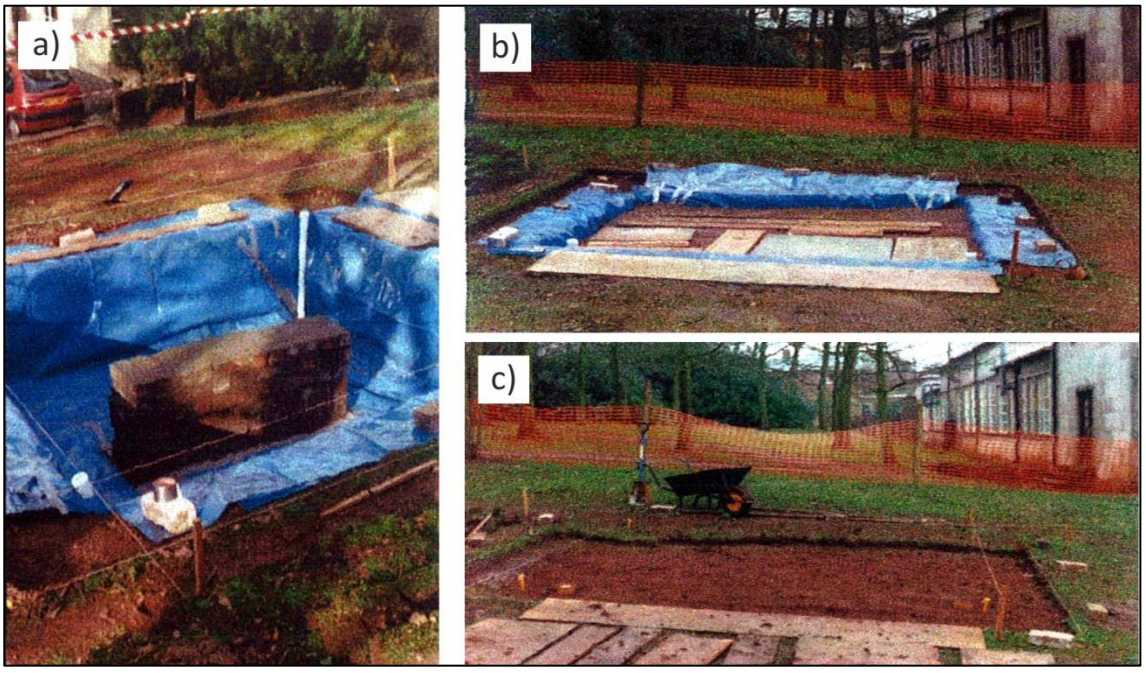

Figure 3-5: Three stages of the pit 'test site' construction, a) brick wall and impermeable membrane, b) gravel fill stage, and c) backfilling of soil before ground surface levelling (adopted from Cassidy, 2001).

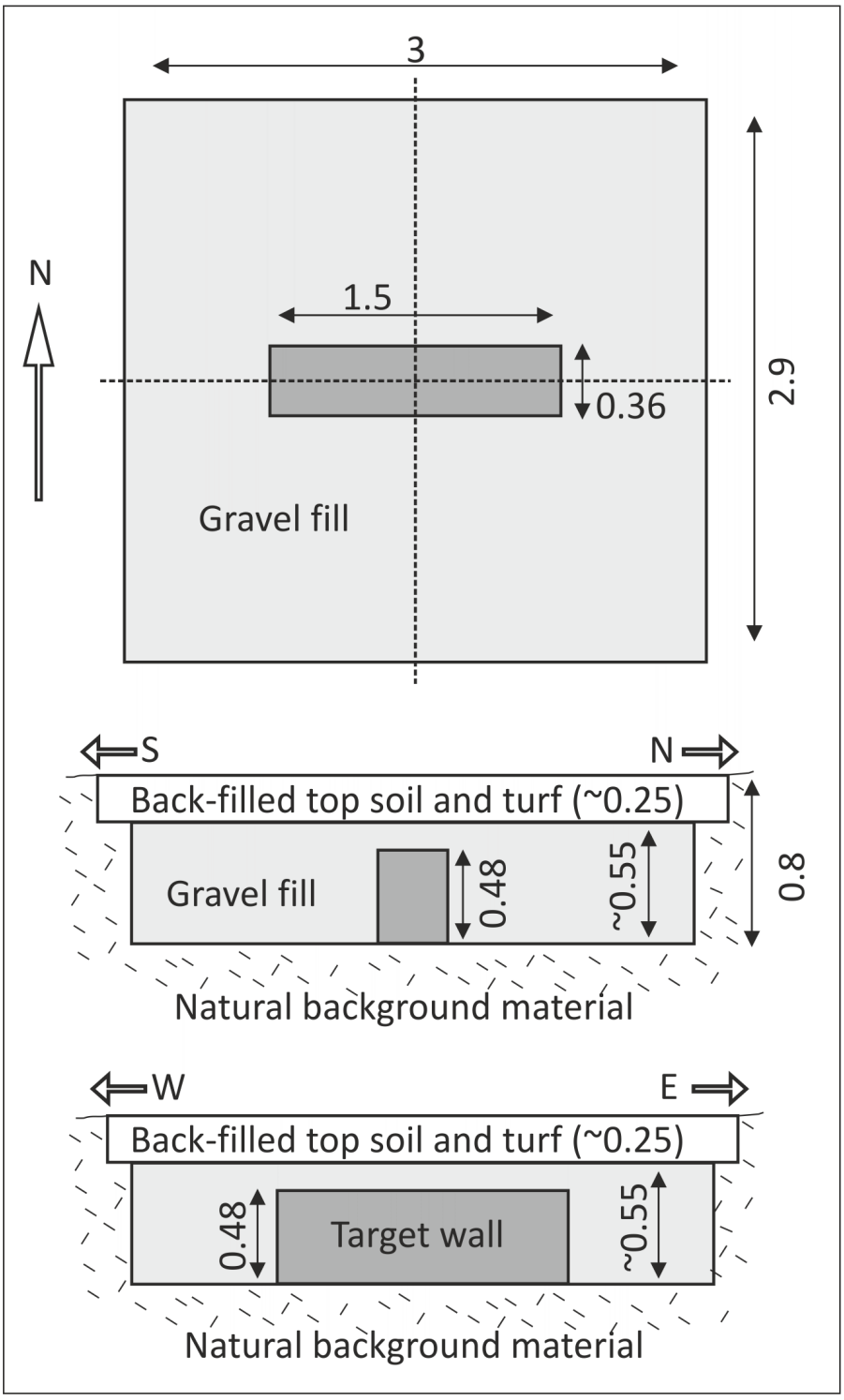

Figure 3-6: Top (plan view) and two (side views) of the buried cleared-wall foundation (dark grey), test site gravel infill (light grey) and top soil fill (marked) within the test site, with measurement in metres, (modified from Cassidy, 2001).

3.2 Methodology

3.2.1 Resistivity methodology

3.2.1.1 Survey consideration

For any resistivity survey, it is important to consider how to get the survey objective(s) (i.e. the most representative model for the sub-surface situation) in the most efficient length of time (Loke et al., 2010). Taking high-resolution, multiple geometry measurements in multiple surveys lines, increases the size of the required computer memory and time needed for processing (including checking data quality and the inversion process). Such an approach does not necessarily improve the resultant model and, therefore, it is important that the distribution of the measurements positions across the target is considered carefully in both two and three dimensions (see Loke et al. 2014). In terms of horizontal coverage, Loke (2015) states that each electrode configuration has specific advantages/disadvantages for both 2D & 3D surveys. For 2D surveys, Wenner, Schlumberger, dipole-dipole, pole-dipole and pole-pole are the most common configuration (Loke et al., 2010) whilst Pole-pole, dipole-dipole, pole-dipole arrays are usually employed for 3D surveys (Milsom and Eriksen, 2011).

Ultimately, the sub-surface geology (or any resistive target) has 3D variations and, as such, 3D resistivity surveys are better at solving these complex subsurface variations, allowing for a more accurate model of the subsurface to be developed (Bentley and Gharibi, 2004). Due to instrument limitations, inversion software constraints and data collection time issues, 3D data sets were developed by combining the results of parallel sets of 2D in-line profiles in one direction, i.e., by combining 2D profiles (see Loke, 2015).

Usually a combination of two groups of perpendicular survey lines (one group in the 'x' direction and the other in the 'y' direction) are used to avoid any directional bias in the collected data (Bentley and Gharibi, 2004). Note that each array type has specific sensitivity in a direction perpendicular to the array (Table 3-1) and this property governs profile spacing for these pseudo-3D surveys. The groups trending North-South, and East-West directions were used in this research to prepare pseudo-3D models.

Table 3-1: Arrays sensitivity in direction perpendicular to its trend (Loke, 2015).

Array type	Sensitivity amount in perpendicular direction for array trend.
Pole-pole	Slightly over a half of the electrodes spacing
Pole-dipole	1.6 times the electrodes spacing
Dipole-dipole	1.8 times the electrodes spacing
Wenner	1.7 times the electrodes spacing

The quality of the measured resistivity values not only depend on the electrodes/array configuration but also on the electrical properties of the active source, such as the amount of injected current into the ground (Allied associates geophysical Ltd., 2006). The injected current is distributed in the subsurface as an expanding half space with increasing current electrode separation. As such, the current field will distribute over a bigger half space until there is insufficient energy to provide a measurable voltage difference at the two potential electrodes. Therefore, the injected current should be increased with depth to compensate for this effect. The Imager Pro 2006 program (version 1.1.4, Campus international products Ltd) was set up to inject 0.5 Amps with the first few depth levels, and then the current was increased gradually to 5 Amps for the last level of investigation following standard approaches (see Reynolds, 2011).

Note that at any pair of current electrodes, the electrical charge will accumulate during the injection cycle (the electrode polarisation effect) and, therefore, the current electrodes cannot be used immediately as potential electrodes for the next reading (otherwise erroneous results will occur). The best way to avoid this problem is to use alternating positive-negative cycles of current injection at each electrode point and then swap all four electrodes for the next reading to give the electrodes some time to allow the electrical charge to dissipate (see Dahlin, 2000 for more information). In this project, the Campus™ Tigre acquisition equipment was set up to collect each repeat reading across 3 cycles of alternating current injection polarity with a 'time-off' period of 0.5 second and a 'time-on' period of 1 second. In addition, each subsequent reading used an adjacent set of four electrodes from its previous measurement.

3.2.1.2 Inline 2D array data collection (field deployment)

Using a range of array types in combination helps avoid the disadvantages of using a singular specific array (such as limitations in the depth of investigation, array sensitivities to vertical and/or horizontal variations and the variable ability to detect directional discontinuities respectively), (see Milsom and Eriksen, 2011 for more information). As the intention of this chapter is to determine the best resistivity configuration, the most popular Wenner, dipole-dipole, pole-pole, and pole-dipole arrays were all employed to; a) allow visual data comparisons and b) determine the most appropriate configuration for the target, the cleared-wall buried foundation in this case.

Two groups of resistivity surveys were collected across the test site, the first were orientated north-south, whilst the second trended east-west (Figure 3-7). Each group consisted of 3 parallel lines of 64 electrodes, with an electrodes spacing of 0.25 m, thus

creating a 16 m total length 2D profile line. Each line was separated by 0.75 m except for NS3 and EW3 lines which acted as control and were located away from the target area (Figure 3-7). The survey lines in group one (north-south trending) were parallel to the test site width and normal to its length whilst the survey lines in the second group (east-west trending) were parallel to the test site length and normal to its width. Wenner, pole-pole, dipole-dipole, and pole-dipole (repeatedly collected forward and reverse surveys) array configurations were collected at each single 2D profile line (Figure 3-7).

Within the first group (N-S orientation), the first line (NS 1) passed over the centre point of the test site and the buried brick wall (Figure 3-7, and Figure 3-9 a). The second line (NS 2) extended 0.75 m to the east away from the centre point of the test site; at this distance the line passed over the brick wall - quartz gravel interface (Figure 3-7, Figure 3-8, and Figure 3-9 b). The third line (NS 3) passed 2.5 m to the east of the centre point of the test site (Figure 3-7, Figure 3-8, and Figure 3-9 c). In the E-W orientated group, the first line (EW 1) was laid over the centre point of the test site and the buried brick wall, the second (EW 2) at 0.75 m to the north and the third (EW 3), 4 m to the north. The EW 2 line passed over the quartz gravel and away from brick wall by 0.56 m (Figure 3-7, Figure 3-8, and Figure 3-10 a, b, and c).

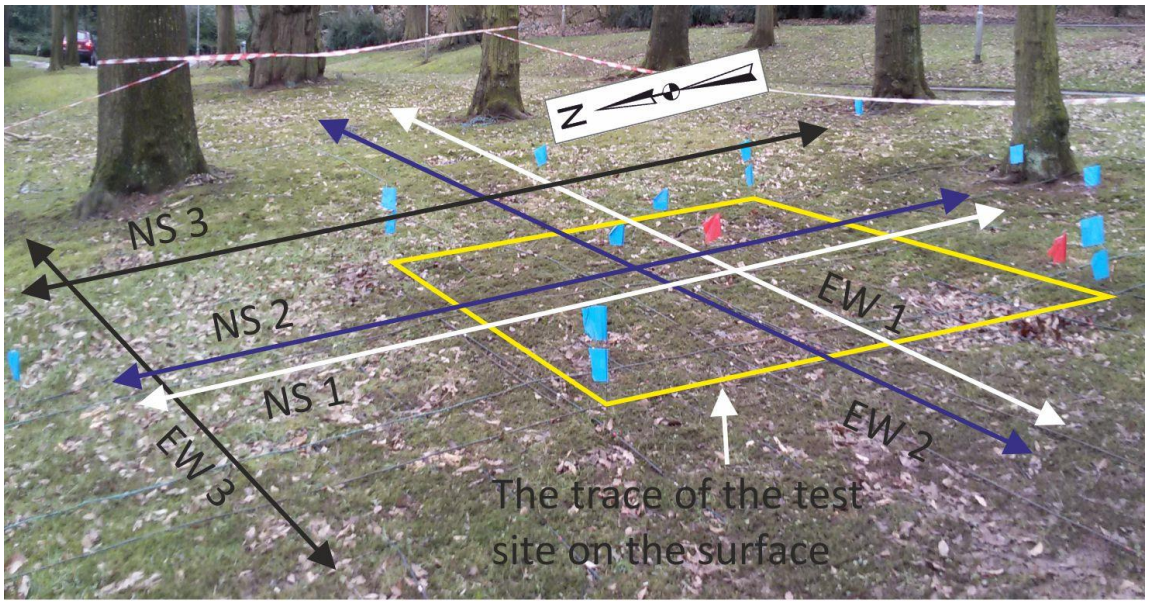

Figure 3-7: Test site facility with the orientation of the survey lines. The white lines are the first line in each group and pass over the centre point of the test site. The cross point of the white colour lines is over the centre point of the test site and brick wall target. The blue lines are the second line in each group and they pass at 0.75m from the centre point of the test site. The black lines are the third line in each group and lie away from the test site target area. The yellow tetragon is the pit 'test site' trace. Photograph direction is south-east.

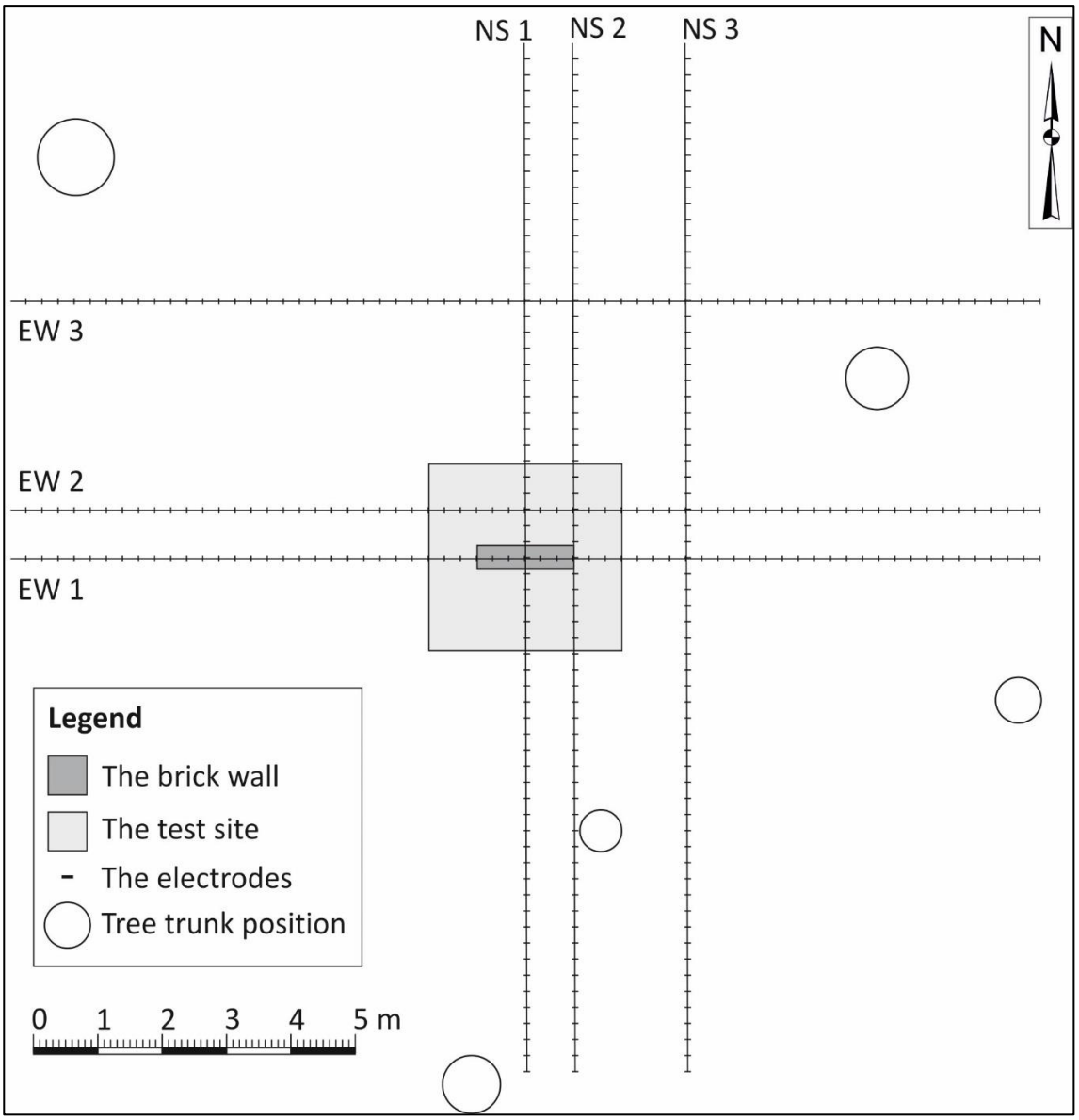

Figure 3-8: Schematic diagram showing the geophysical survey positions on the test site.

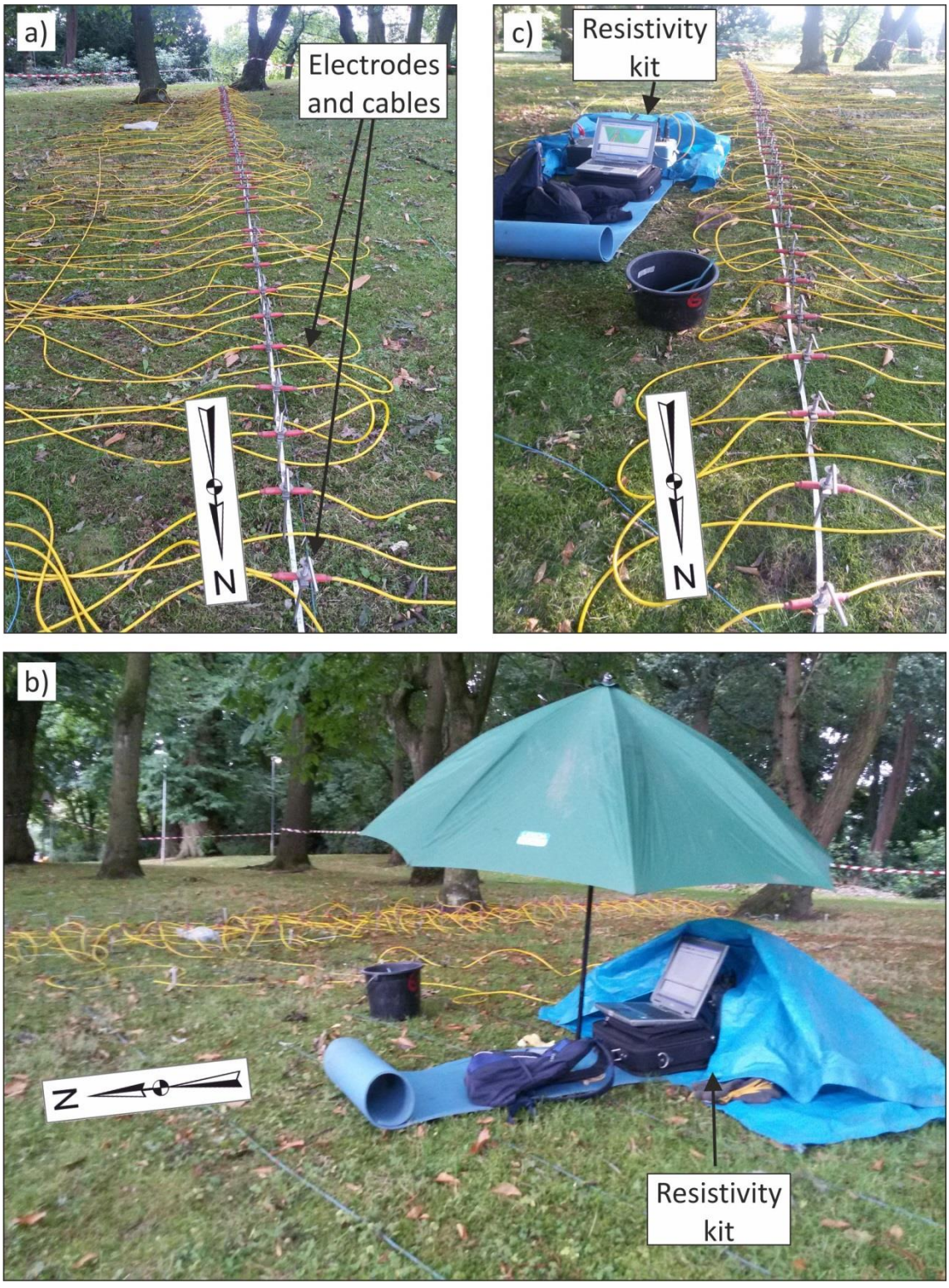

Figure 3-9: Group one survey lines. a) line NS 1, photograph direction is south. b) line NS 2, photograph direction is south. c) line NS 3, photograph direction is south-east.

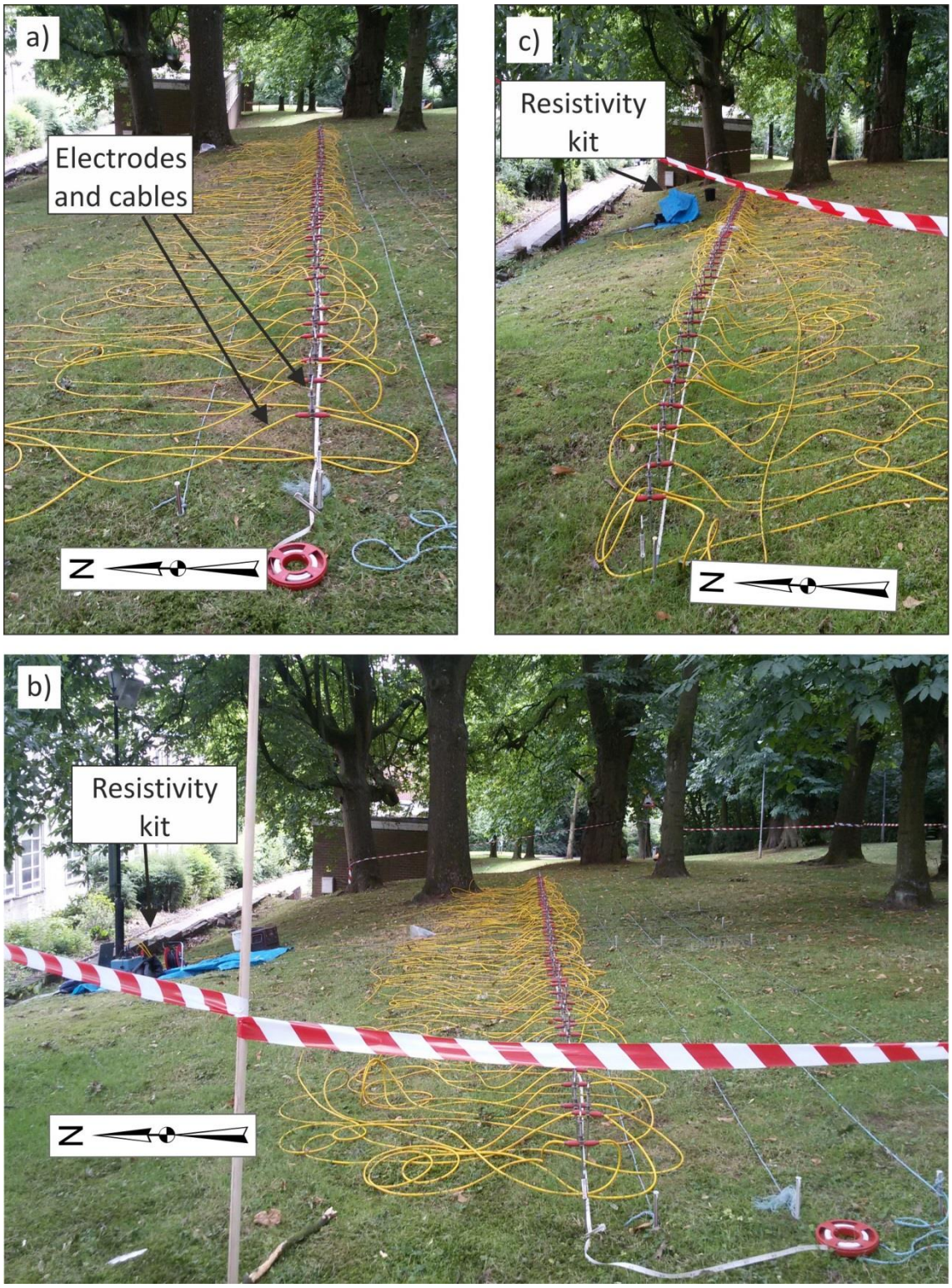

Figure 3-10: Group two survey lines. a) line EW 1, photograph direction is east. b) line EW 2, photograph direction is east. c) EW 3, photograph direction is east.

With inline electrode configurations, when the electrodes spacing increases to investigate relatively deeper readings, one reading at each edge is lost, resulting in reduction in penetration depth at the respective ends of the array (see Griffiths and Barker, 1993 for background). Therefore, a total survey line length of 16 m was used to avoid this disadvantage and to increase the breadth/depth of investigation to the site bedrock. With these survey parameters, the cleared-wall buried foundation target, the test site itself, the bedrock underneath it and the surrounding ground (soil) are all investigated with the main 'central' part of the array.

In each survey, the resistivity system collects data with the smallest electrode spacing '*a*' of 0.25 m, i.e., the minimum electrode spacing and first level of investigation. To investigate deeper depths, the system automatically increases the spacing factor *n* to be *n*=2 and the new electrode spacing will be 0.50 m ($n \times a$, or $2a$). After collecting all possible data from each single level, the procedure repeats itself and the *n* factor increases at 0.25 m intervals (i.e., the third level will be 0.75 m, or $3a$, the fourth level 1.0 m, or $4a$, and so on). The maximum spacing (the deepest level) depends on the array type chosen with the Wenner array, for instance, has a maximum spacing interval of $21a$.

3.2.2 Passive seismic methodology

3.2.2.1 Survey considerations

The studied site at Keele University campus receives passive waves from different passive seismic sources, such as people walking or running close to the site, cars and vehicles along the nearby M6 and, most importantly, the buses and cars using Keele hall road which is close to site and can be assumed as the main passive seismic source.

Passive seismic surveys, using refraction microtremor (ReMi), was performed using L-shape array configurations. The 2D arrays are more practical, where the true velocity for any obliquely incident waves can be determined using trigonometric functions. Apparent velocity for obliquely incident waves is the main drawback for the linear array (Strobbia *et al.*, 2015).

Although microtremor waves penetrate into the ground depending upon its wavelength, the investigated point is not located at the maximum penetrated depth; Rayleigh waves lose energy with depth (Mathews et al. 1996). Wavelength (λ) to depth (z) ratio (λ/z) cannot determined accurately but a ratio of 2 can be used (Abbiss, 1981).

From the pit design, the maximum depth of the pit is 0.8 m (Cassidy, 2001), and to investigate deeper to determine ground properties beneath the pit, the interested depth range was, therefore, from the ground surface down to about 2 m. Based on the ratio (λ/z) is 2, the interested wavelength range can be from 3 m and less, therefore, the array length was defined to be 3 m.

3.2.2.2 Field deployment

One L-shape array was used at the study site; one side of the array was oriented in a north-south direction and the second side was oriented in a east-west direction (Figure 3-11 and Figure 3-12. The array had 7 three-component seismic stations using 1 m geophone spacing and a set geophone frequency of 4.5 Hz. Seismic records were collected during week days where many passive sources (especially buses and cars using the Keele hall road) were more available, for the survey parameters see Table 3-2.

Table 3-2: Survey parameters for the L-shape seismic array at the Keele facility test site.

Survey parameter	Amount
Number of seismic stations	7
Number of components	3
Survey type	Passive, ReMi
Stations spacing (m)	1
Seismic recorder	The Geode
Sample interval (m sec)	1
Record length (sec)	60
Delay (sec)	0

Figure 3-11 shows the L-shape array deployment at the Keele facility test site. Louie (2001) stated that the vertical geophones give accurate results with 20^{o} off vertical direction. The vertical geophones were planted nearly vertically (i.e. within 5^{o} off the vertical axis) and manually checked using a clinometer. In addition, horizontal geophones in N-S and E-W directions were oriented using a Silva compass for accurate directions. The L-shape array bounds the pit from the north and west sides and the L-shape corner was not kept over the pit's centre, (Figure 3-11 and Figure 3-12).

Figure 3-11: Field deployment using L-shape seismic array at the Keele test site, photograph direction is south-west.

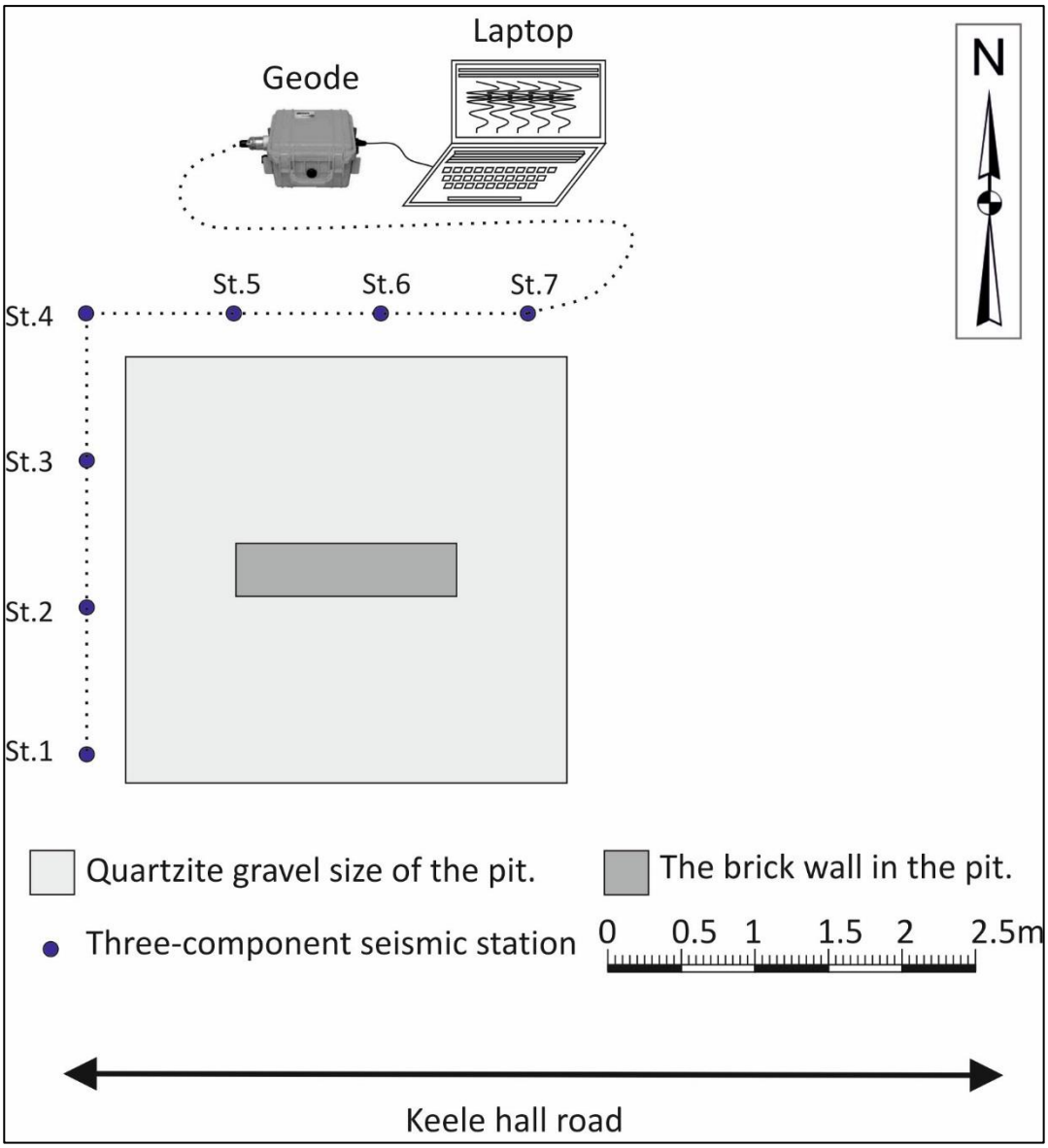

Figure 3-12: L-shape seismic array and its position relative to the pit's location at Keele test site.

3.3 Results

3.3.1 Data preparation

3.3.1.1 Resistivity data preparation

Before processing, the collected resistivity data was checked for consistency and quality, any bad data points were removed or interpolated in Res2Dinv v. 4.3 (Geotomo™ software) and Surfer v. 8.04 software. Bad data points were identified as being either anomalously low or high, when compared with adjacent readings, or indeed recorded as zero values. These can be easily visualised as a spike in the profile in the Res2Dinv program, and then removed. To avoid deleting many bad data points, Surfer™ v. 8.04 was also used to determine an average of readings surrounding the bad data points. Every 2D profile was then inverted in Res2Dinv following standard procedures (see Geotomo™ Software, 2004).

The number of collected and corrected data points are detailed in (Table 3-3). All resistivity surveys investigated deeper than the bottom of the target wall foundation, but the pole-pole data sets had a significant number of zero readings recorded, therefore, just the target section was selected and processed to generate 2D resistivity models.

As the 2D ERT profiles were collected using all four array configurations (Table 3-3), pseudo-3D ERT model datasets were also created using the same Geotomo™ Res2Dinv v.4.3 software, allowing resistivity values to vary in 3D during inversion (without limiting cutoffs), to produce six horizontal resistivity slices for visualisation purposes (see Loke et al., 2003 for background). Respective pseudo-3D datasets had 3,600 data points (Wenner), 5,238 data points (dipole-dipole), 5,454 data points (pole-dipole) and 2,730 data points (pole-pole) respectively.

Table 3-3: Summary statistics of each ERT profile, array type, data points collected/inverted and depth 'n' levels (see Reynolds, 2011 for details). Figure 3-8 for profiles locations.

ERT Profile	Array	No. of collected data points	No. of corrected data points	Data 'n' levels
NS 1	Wenner	600	7	15
	Dipole-dipole	873	0	18
	Pole-dipole	909	1	18
	Pole-pole	455	1	13
NS 2	Wenner	600	1	15
	Dipole-dipole	873	0	18
	Pole-dipole	909	0	18
	Pole-pole	455	1	13
NS 3	Wenner	600	20	15
	Dipole-dipole	873	72	18
	Pole-dipole	909	0	18
	Pole-pole	455	6	13
EW 1	Wenner	600	0	15
	Dipole-dipole	873	0	18
	Pole-dipole	909	0	18
	Pole-pole	455	3	13
EW 2	Wenner	600	2	15
	Dipole-dipole	873	13	18
	Pole-dipole	909	1	18
	Pole-pole	455	1	13
EW 3	Wenner	600	0	15
	Dipole-dipole	873	1	18
	Pole-dipole	909	1	18
	Pole-pole	455	2	13

3.3.1.2 Seismic data preparation

The collected data was prepared using the ReflexW^{TM} v.8.1 (Sandmeier geophysical research) software. The software was used for trace extraction to separate the three seismic components (V, HNS, and HEW). Particle motions plots were prepared to check the collected data consistency with Rayleigh waves (Figure 3-13); where x axis represents the east-west direction (i.e. parallel to the Keele hall road at the site), y axis is in north-south direction (i.e. orthogonal to the Keele hall road), and z is the vertical direction.

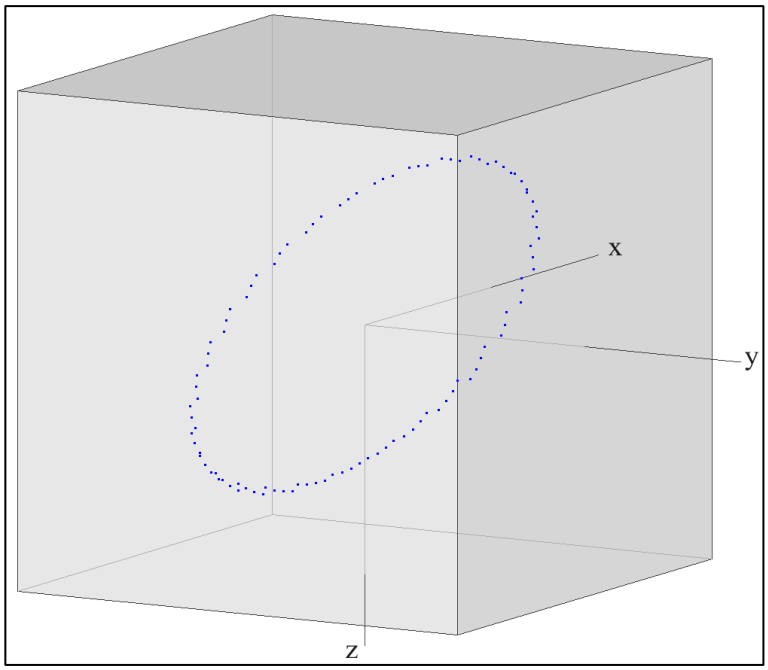

Figure 3-13: Particle motion plot, data used was collected using the L-shape array, x axis is in east-west direction, y axis is in north-south direction (see text). 100 samples were used to generate the plot.

3.3.2 Resistivity data results

Respective ERT array datasets were then finite-difference inverted (the finite difference method is a discretization method by which the subsurface can be subdivided in many rectangular cells, each cell can have a certain resistivity value), using first the non-linear, least-squares optimization algorithm and secondly using robust inversion algorithms. These two inversion algorithms represent a subsurface target in two different ways. The least-square smoothness-constrained inversion algorithm represents underground interfaces smoothly increasing/decreasing in resistivity; this algorithm smooths sharp boundaries like soil-bedrock. The robust inversion represents the sharp interfaces, like soil-bedrock, as rapid changes in resistivity values and whole block of each material (soil or rock) can has a certain resistivity value. Normal mesh and damping factor were used with the least-square smoothness-constrained inversion. The robust inversion was carried

out using respective 0.05 data and 0.01 model constrain cutoffs, for comparison, within Geotomo™ Res2Dinv v.4.3 software (see Loke & Barker, 1995; Geotomo™ Software, 2004). The 5th model iteration and a common logarithmic, colour-contoured interval was used throughout for consistency. The software set the depth of 'n' level 1 at ~0.5 electrode spacing (*a*) for the Wenner, ~0.3*a* for dipole-dipole, 0.6*a* for pole-dipole and 0.9*a* for pole-pole array configurations respectively based on Edwards (1977).

3.3.2.1 2D resistivity models

Data collected from North-South trending profiles will be presented first and then the data from East-West trend profiles. Just the target section of all the survey profiles for each group will be presented for comparison purposes; the whole 2D resistivity models of the least-square inversion are presented in appendix A and of the robust inversion are presented in appendix B.

Note that the pole-dipole array is an asymmetrical array; symmetrical targets can be represented as asymmetrical anomalies (see Loke, 2015). To avoid the limitation of this configuration, two sets of pole-dipole data were collected on every profile reversing the direction of collection.

In the constrained resistivity model inversions, Res2Dinv was set up with a limited value (to ignore very small and very large resistivity readings) of true resistivity values (upper/lower limit factors were 10 and 0.1 respectively), and user-defined logarithmic contour intervals were applied to the data for consistency of display purposes. The minimum/maximum threshold values were chosen from the range of resistivities expected in the test site area (from previous surveys) of ~100-~10,000 Ω.m.

3.3.2.1.1 First group (North-South trending surveys)

The NS line 1 generates a 2D model more informative than the second and third profiles for the test site, mainly because the line passes over the centre point of the test site and the brick wall. Figure 3-14 shows the resistivity models obtained from the least-square smoothness-constrained inversion of Wenner, dipole-dipole, pole-dipole, and pole-pole arrays focused in the area of the test site for the three profiles.

As the depth and construction design of the test site are well known (see Figure 3-6), an accurate comparison, between the real depth and extent of the test site and the resistivity models can be obtained. The Wenner and dipole-dipole arrays clearly show the lateral change/extent of the test site, with clear lateral interfaces at the edges where the test site should be. Pole-dipole configuration shows an asymmetrical shape for the test site. The Wenner array results show the anomaly to be sharper and more vertically defined at the edges, in comparison to the dipole-dipole array (which is contrary to perception that the Wenner is poor at lateral target discrimination). In addition, both arrays are reasonably good at defining the extent of the test site but the dipole-dipole data is better constrained and slightly more accurate with regard to its true depth.

The Wenner and dipole-dipole arrays pick up the internal brick foundation target as a higher resistivity anomaly, whilst pole-dipole and pole-pole they do not. The depth to the top of the foundation is better on the dipole-dipole data but the depth to the bottom is better on the Wenner.

Despite the individual drawbacks of the Wenner and dipole-dipole arrays to determine the actual depth of the test site and the cleared-wall foundation, on balance, both provide well-constrained, good-resolution models overall. Clear resistivity contrasts can

be identified between the manmade and natural materials with the brick wall (at the centre of the model) having high resistivity values (2000 Ω.m and more) in comparison with the surrounding gravel (1000-2000 Ω.m), whilst on pole-dipole and pole-pole models there is no clear contrast for the brick wall. In addition, for all the arrays, the test site has a noticeably different range of resistivity values from the surrounding soil (100-500 Ω.m) allowing the test site to be easily recognized; as mentioned above Wenner and dipole-dipole are more accurate for the test site extent.

The whole 2D ERT models (see the appendix A) reveal another important property of these arrays. In comparison to the Wenner, pole-dipole, and pole-pole arrays, the dipole-dipole array has improved lateral coverage in the deeper corners of the model. This helps provide a broader picture of the sub-surface at extended depths and therefore a more representative/appropriate model within geometrically constrained surveys (i.e. where lateral space is restricted).

For pole-pole array is the highest array for telluric noise in terms of sensitivity, (Loke, 2015). The collected data using pole-pole array shows many bad data points which might be effect the RMS error of the resistivity models to be 9.3 % for pole-pole. The bad data points can be generated by the telluric noise sources at the site. The RMS error for Wenner, dipole-dipole, and pole-dipole are 5.0 %, 5.0 %, and 4.1 % respectively.

The thin top soil level of relatively lower resistivity is well constrained and nearly has the same resistivity response on all the resistivity models.

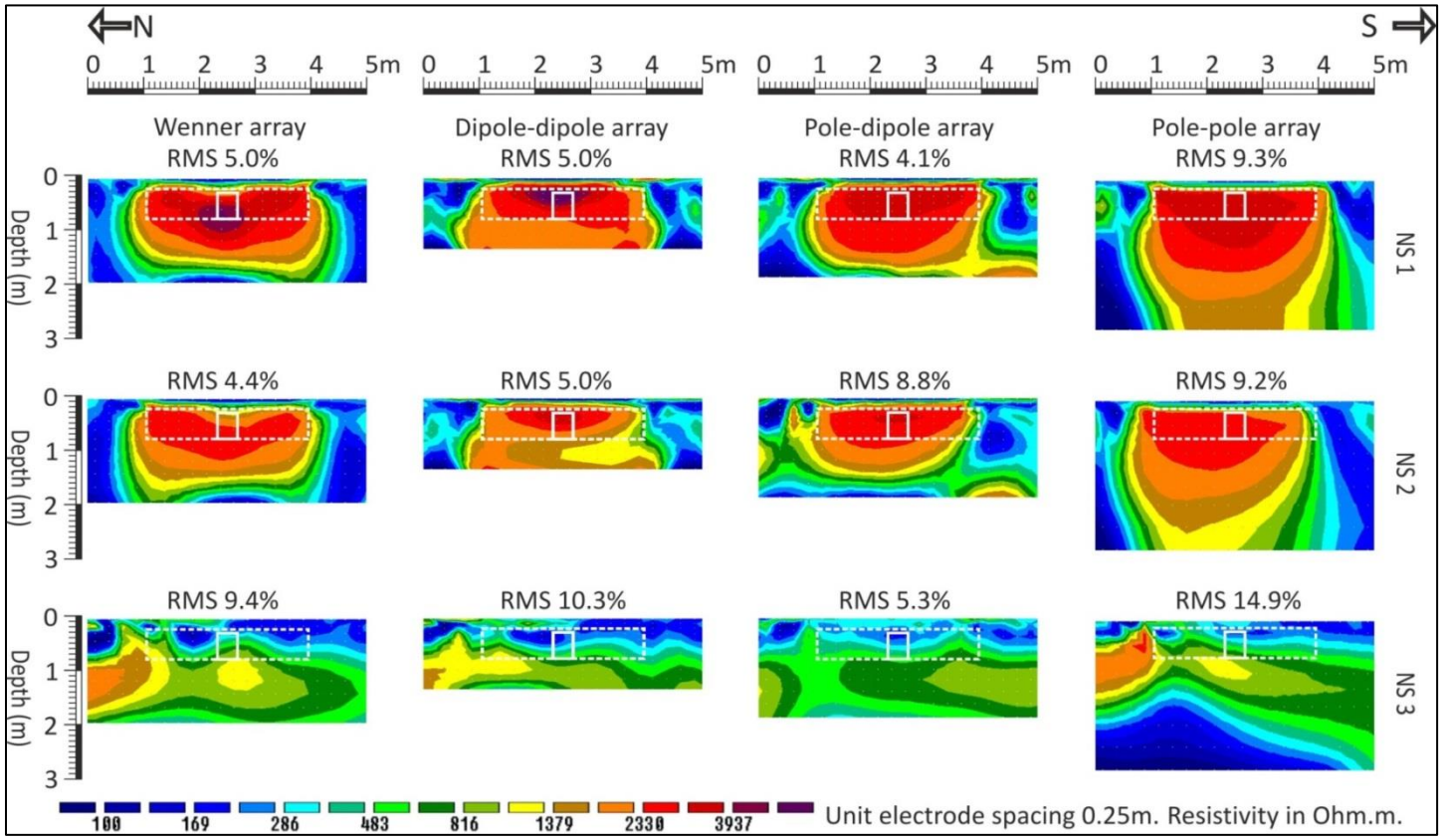

Figure 3-14: ERT 2D profile sections in N-S direction using least-square smoothness-constraint inversion with Wenner, dipole-dipole, pole-dipole, and pole-pole array configurations (see Figure 3-7 and Figure 3-8 for location). White boxes indicate cleared-wall foundation (solid line) and surrounding test site (dotted line) positions respectively. Pole-dipole data shown is merged from data collected in both directions on each profile (see text). Inversion iteration 5 results shown throughout.

The second profile survey was laid at 0.75 m eastwards from the centre point of the test site and shows less information about the target, but nearly similar characteristics to line NS 1. All the arrays still discriminate the test site as a high resistive target (i.e. resistivity range 1000 Ω.m and more) from the surrounded natural soil (relatively low resistivity 100-500 Ω.m). Wenner and dipole-dipole configurations are more accurate than pole-dipole and pole-pole for the test site's extent and represent the test site in good agreement with the real design. Pole-dipole represents the test site in an asymmetrical shape (Figure 3-14).

The dipole-dipole data is more accurate than the Wenner, pole-dipole, and pole-pole in terms of discriminating the buried wall foundation because it has the ability to investigate about 1.8 times minimum electrodes spacing in a direction normal to the array trend (Figure 3-14).

The obtained resistivity models for all arrays from the second profiles show different RMS errors. Pole-pole has the biggest RMS which is 9.2 %, whilst for Wenner, dipole-dipole, and pole-dipole are 4.4 %, 5.0 %, and 8.8 % respectively.

The third survey profile was laid at a distance of 2.5 m to the east of the centre point of the test site and over the natural background geology. The data illustrates the soil (100-300 Ω.m) and bedrock (300-800 Ω.m) resistivities and it's interface at approximately 0.8-1 m deep. There is no identifiable features that can be related to the test site's contrasting higher resisitivities of 2000 Ω.m or more. Pole-pole array still has high RMS error about 14.9%, for the whole resistivity models see the appendix A.

The robust inverted profiles produce similar results, although it was harder to differentiate the cleared-wall foundation (i.e. the brick wall) from the test site (Figure 3-15). However, the robust inversion imaged more accurately the test site extent and depths in the inverted profiles, compared the least-squared inversion profile (Figure 3-14).

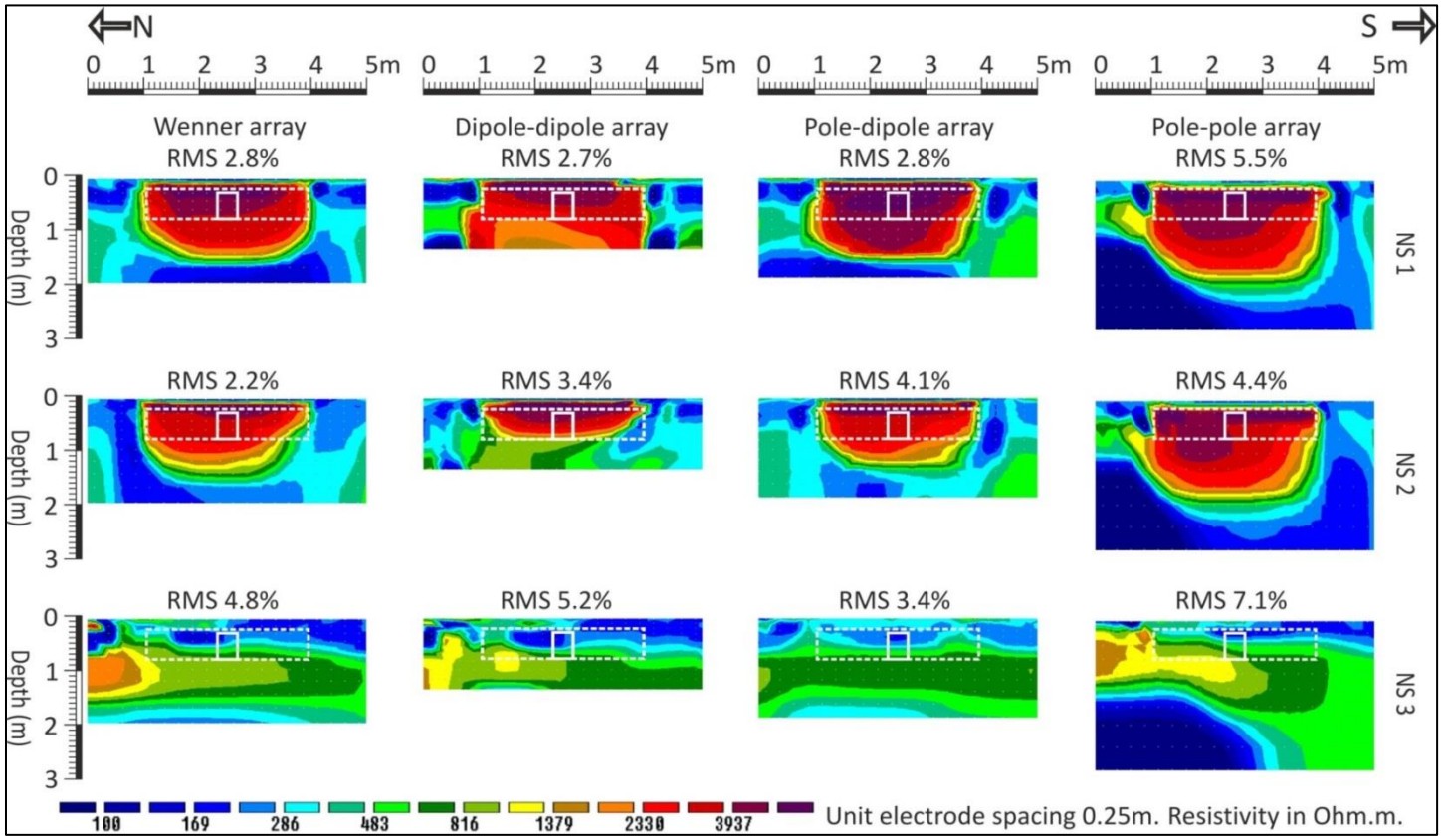

Figure 3-15: ERT 2D profile sections in N-S direction using robust inversion with Wenner, dipole-dipole, pole-dipole, and pole-pole array configurations (see Figure 3-7 and Figure 3-8 for location). White boxes indicate cleared-wall foundation (solid line) and surrounding test site (dotted line) positions respectively. Pole-dipole data shown is merged from data collected in both directions on each profile (see text). Inversion iteration 5 results shown throughout.

3.3.2.1.2 Second group (East-West trending)

For the profile survey 1, the least-squared smoothness-constrained inversion, of all the applied arrays show a good level of detection and discrimination for the test site and the cleared-wall foundation. For pole-dipole and pole-pole arrays in east-west direction can be more informative than surveys in north-south direction. The models look similar to those obtained from line NS 1 in the first group, (Figure 3-16).

Wenner and dipole-dipole arrays represent well-constrained, lateral discrimination for the test site from surrounded soil with the cleared-wall foundation clearly evident as a high resistivity anomaly. Pole-dipole and pole-pole arrays discriminate the test site from the surrounding soil and the cleared-wall foundation inside the test site. The Wenner and dipole-dipole, as in the NS 1 profile, are sensitive to the bottom and to the top of the cleared-wall foundation, respectively (Figure 3-16).

The pole-dipole is more accurate to the top of the clear-wall foundation, whilst the pole-pole is more accurate to the bottom. The data shows the cleared-wall foundation anomaly as being wider in comparison with the models obtained from line NS 1 due to survey line being parallel to the length of the foundation. In comparison, the dipole-dipole array is more accurate at defining this wider feature, (Figure 3-16).

The thin, low resistivity top soil is approximately equally delineated from the test site by all the used arrays. The RMS error of the data sets of this profile is 5.0 %, 6.4 %, 6.8 % and 12.7 % for Wenner, dipole-dipole, pole-dipole, and pole-pole respectively.

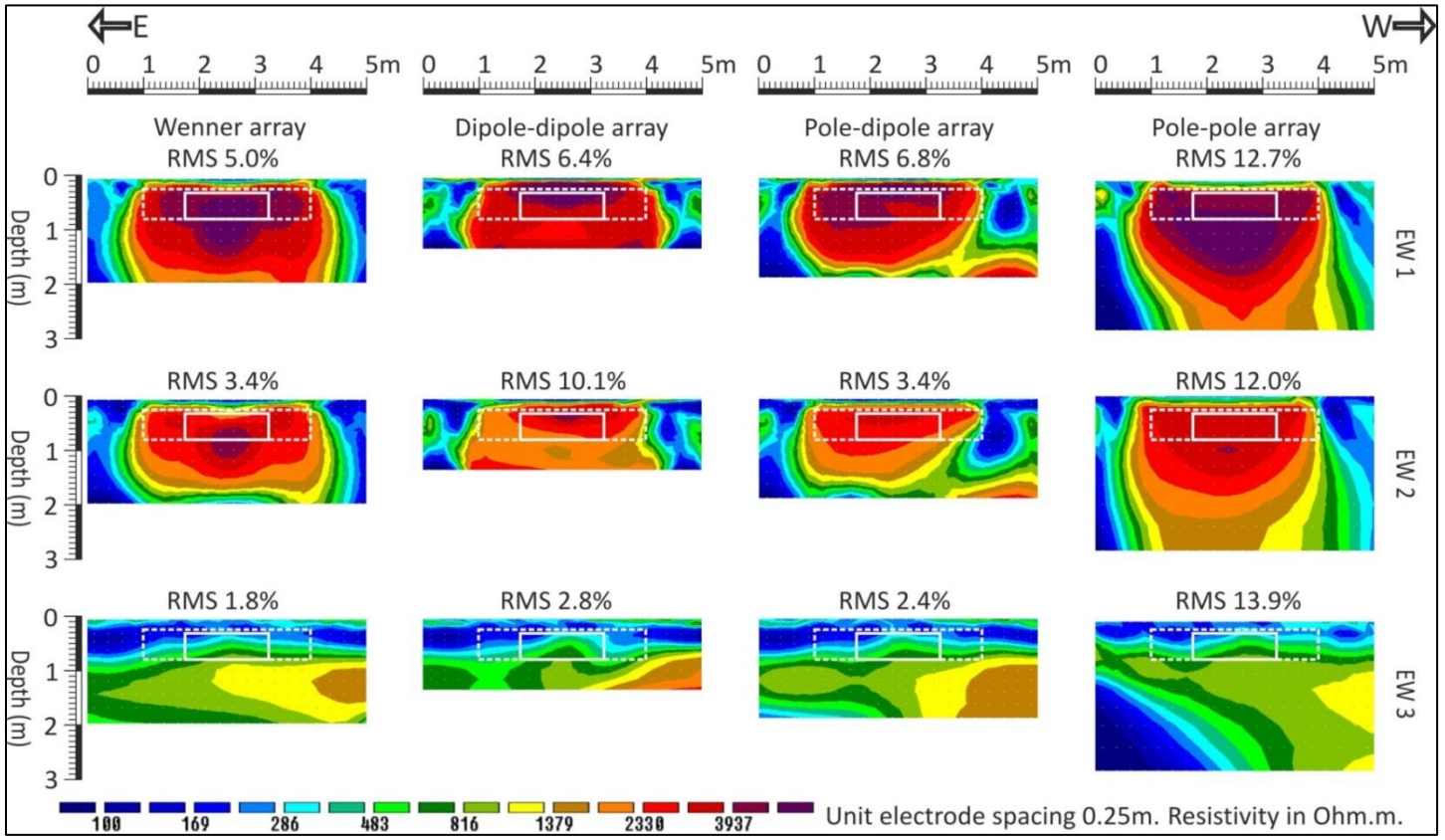

Figure 3-16: ERT 2D profile sections in E-W direction using least-square smoothness-constraint inversion with Wenner, dipole-dipole, pole-dipole, and pole-pole array configurations (see Figure 3-7 and Figure 3-8 for location). White boxes indicate cleared-wall foundation (solid line) and surrounding test site (dotted line) positions respectively. Pole-dipole data shown is merged from data collected in both directions on each profile (see text). Inversion iteration 5 results shown throughout.

The second line is less informative than the first one mainly due to its position which is 0.75 m from the centre point of the test site (i.e. from EW 1 survey profile). Both of the test site and the cleared-wall foundation are detected by all the arrays (i.e. the Wenner, dipole-dipole, pole-dipole and pole-pole) and the anomalies are well discriminated from each other-(Figure 3-16). The Wenner and dipole-dipole are good for the test site's extent.

The dipole-dipole and the pole-dipole are better at delineating the top of the cleared-wall foundation. As before, the Wenner is better for identifying the basal interface. Even the pole-pole show the cleared-wall foundation much deeper than the real depth, but it looks more sensitive for the bottom of it. In comparison to the equivalent line in the first group's survey, line NS 2, the Wenner array data shows the influence of the cleared-wall foundation due to its increased cross sectional area. The pole-pole array has the highest RMS error which is 12.0 %, 3.4 % for Wenner, 10.1 % for dipole-dipole, and 3.4% for pole-dipole.

The third survey profile lies 4 m to the north of the test site across the natural geology. As with the profile NS 3, the soil-bedrock interface is noticeable; therefore, the model can be used to understand the geology of the site in a direction that orthogonal to the previous lines of group 1. As previous, pole-pole array still has the highest RMS error (13.9 %), and all the four arrays data do not detect the presence of the test site, for the whole resistivity models of the third profile see the appendix A.

The robust inversion of the E-W survey generates similar characteristics to those of the NS survey. The wall foundation was not clearly delineated (Figure 3-17). The robust inversion imaged the test site extend more accurately than the least-square inversion (Figure 3-16).

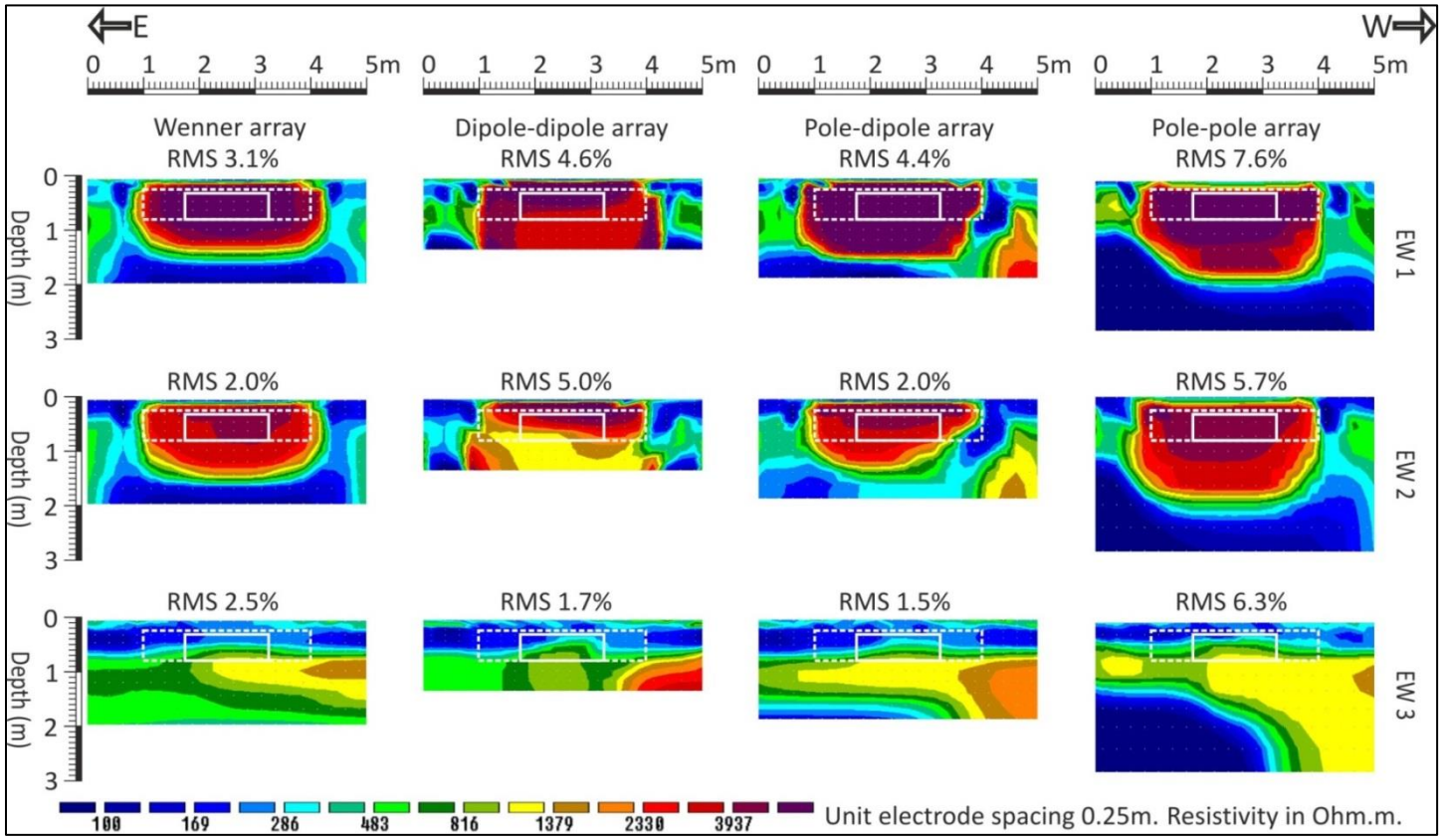

Figure 3-17: ERT 2D profile sections in E-W direction using robust inversion with Wenner, dipole-dipole, pole-dipole, and pole-pole array configurations (see Figure 3-7 and Figure 3-8 for location). White boxes indicate cleared-wall foundation (solid line) and surrounding test site (dotted line) positions respectively. Pole-dipole data shown was merged from data collected in both directions on each profile (see text). Inversion iteration 5 results shown throughout.

3.3.2.2 Pseudo-3D models

As subsurface anomalies vary in three dimensions, 3D surveys have the ability to provide more accurate models of the buried features. The collected data for all the used arrays were combined into pseudo-3D data sets and inverted to provide 3D models using the Res3Dinv program.

The actual depths and dimensions of the test site are already known so a quick comparison with the pseudo-3D models can be done. Each single electrode configurations of the pseudo-3D data sets can be inverted and represented by six horizontal slices with different depths.

For the pseudo-3D models, all data showed the surrounding test site from background, in the least-square inversion data this became more circular with depth but less so for the robust inversion data (Figure 3-18). The robust inversion data resistances were also higher at shallower depths, compared to the least-squares inversion data (Figure 3-19).

The pseudo-3D models did not resolve the cleared-wall foundation target, (Figure 3-18 and Figure 3-19).

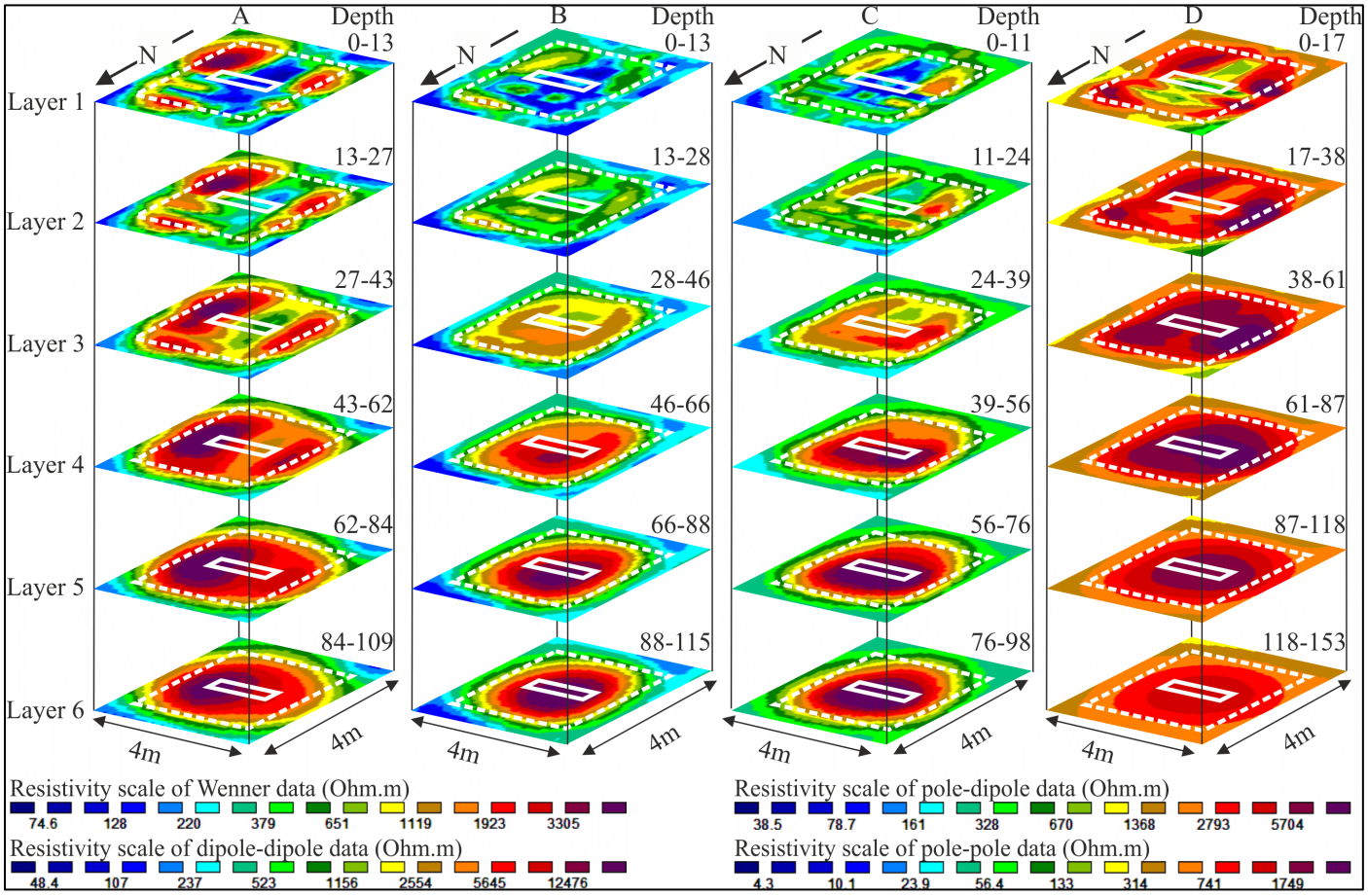

Figure 3-18: Horizontal depth slices of pseudo-3D ERT datasets generated for (A) Wenner, (B) dipole-dipole, (C) pole-dipole, and (D) pole-pole array surveys from the 2D ERT profiles, using least-square smoothness-constraint inversion. White boxes indicate cleared-wall foundation (solid line) and surrounding test site (dotted line) positions respectively. Depth in centimetres.

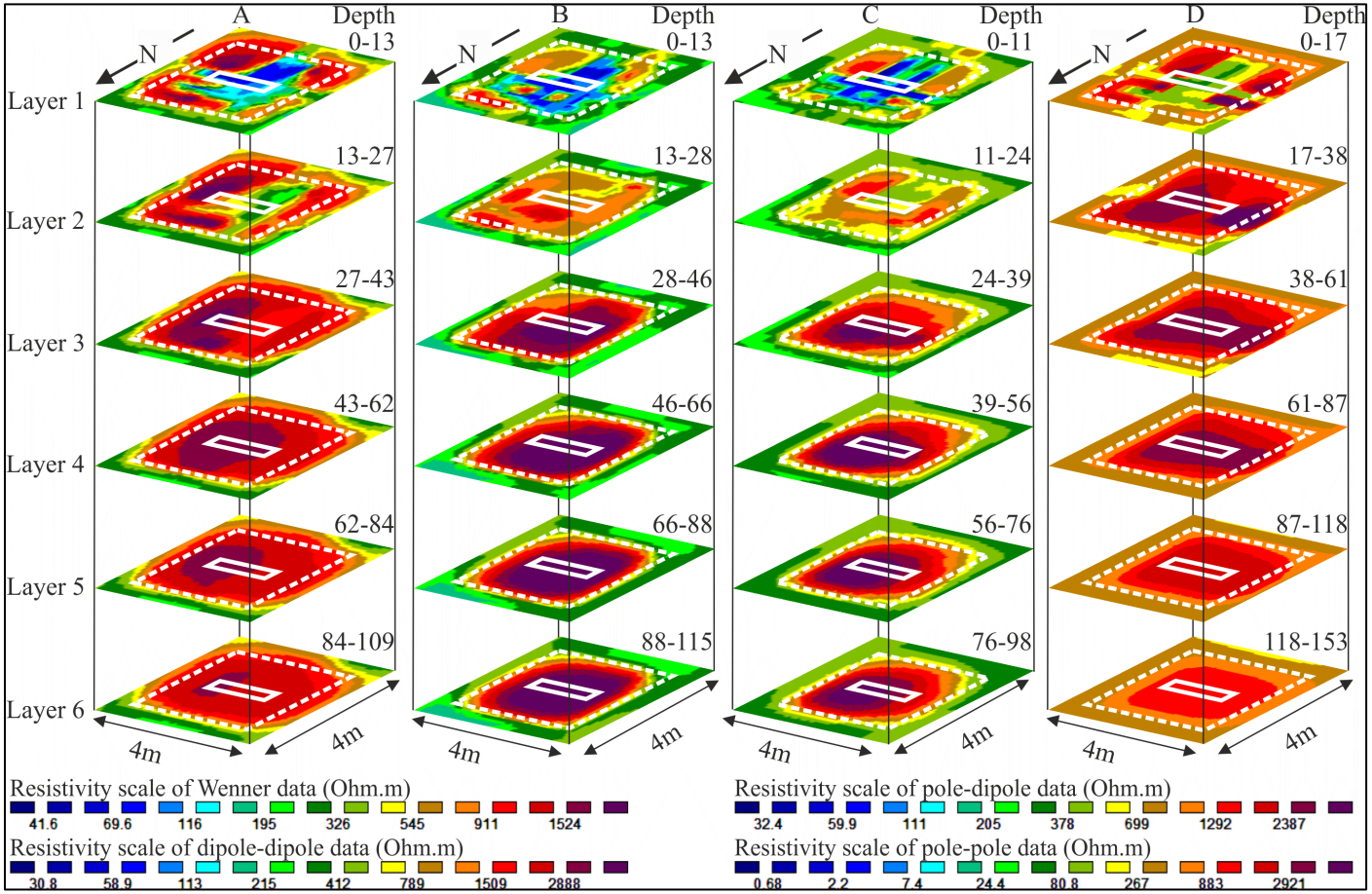

Figure 3-19: Horizontal depth slices of pseudo-3D ERT datasets generated for (A) Wenner, (B) dipole-dipole, (C) pole-dipole, and (D) pole-pole array surveys from the 2D ERT profiles, using robust inversion. White boxes indicate cleared-wall foundation (solid line) and surrounding test site (dotted line) positions respectively. Depth in centimetres.

Based on the comparing the different electrode configurations, these 2D resistivity models were then qualitatively assessed based on two parameters: 1) the successful imaging of the cleared-brick wall foundation (i.e. which array could detect and discriminate the foundation from the gravel-fill) and 2) the cleared-brick wall foundation accurate positioning (i.e. to what extent the brick wall position could be accurately located by the different array types). The assessment contained three rankings: it was ranked *Good* for when the resistivity model (i.e. of a certain electrode configuration) achieved the two assessment parameters, *Moderate* for when the model achieved one of the two assessment parameters and ranked *Poor* for when the model did not achieved any parameters, the imaging rating detailed in (Table 3-4) for the least-square smoothness-constrained and for the robust inversion methods.

For the least-square inverted data profiles (Figure 3-14 and Figure 3-16), the Wenner and dipole-dipole arrays gave generally *Good* results, whilst the pole-dipole and pole-pole array gave generally *Moderate* to *Poor* results (Table 3-4). Note that the target appeared to be spatially wider on EW profiles, when compared to the NS profiles (cf. Figure 3-14 and Figure 3-16), as the EW profiles were parallel to the buried target and thus had a larger sampling area (Figure 3-8).

For the robust inverted data profiles (Figure 3-15 and Figure 3-17), the Wenner and dipole-dipole arrays gave generally *Moderate* results, whilst the pole-dipole and pole-pole arrays gave generally *Poor* results (Table 3-4). With these inversions, it was also harder to differentiate the cleared-wall foundation from the test site materials (cf. Figure 3-15 and Figure 3-17).

Table 3-4: ERT 2D profiles (both least-squares and robust inversions) were qualitatively assessed based on the accuracy of the cleared-wall foundation position and being successfully imaged. Images were ranked *Good* for when the model achieved this, *Moderate* for when the model only achieved one and ranked *Poor* when the model did not achieve any parameters (see text). Model RMS inversion percentages also included, * indicated relatively high model errors.

2D Profile number (see Figure 3-8) and array type	Least-square Inverted model, , RMS % error misfit	Cleared-wall foundation well defined	Robust Inverted model, RMS % error misfit	Cleared-wall foundation well defined
NS 1, Wenner	5.0	Good	2.8	Moderate
NS 1, Dipole-dipole	5.0	Good	2.7	Moderate
NS 1, Pole-dipole	4.1	Poor	2.8	Poor
NS 1, Pole-pole	9.3	Poor	5.5	Poor
NS 2, Wenner	4.4	Moderate	2.2	Poor
NS 2, Dipole-dipole	5.0	Moderate	3.4	Poor
NS 2, Pole-dipole	8.8	Poor	4.1	Poor
NS 2, Pole-pole	9.2	Poor	4.4	Poor
NS 3, Wenner	9.4	N/A (off axis)	4.8	N/A (off axis)
NS 3, Dipole-dipole	10.3	N/A (off axis)	5.2	N/A (off axis)
NS 3, Pole-dipole	5.3	N/A (off axis)	3.4	N/A (off axis)
NS 3, Pole-pole	14.9*	N/A (off axis)	7.1	N/A (off axis)
EW 1, Wenner	5.0	Good	3.1	Moderate
EW 1, Dipole-dipole	6.4	Good	4.6	Moderate
EW 1, Pole-dipole	6.8	Moderate	4.4	Poor
EW 1, Pole-pole	12.7*	Poor	7.6*	Poor
EW 2, Wenner	3.4	Good	2.0	Moderate
EW 2, Dipole-dipole	10.1	Good	5.0	Moderate
EW 2, Pole-dipole	3.4	Moderate	2.0	Moderate
EW 2, Pole-pole	12.0*	Poor	5.7	Poor
EW 3, Wenner	1.8	N/A (off axis)	2.5	N/A (off axis)
EW 3, Dipole-dipole	2.8	N/A (off axis)	1.7	N/A (off axis)
EW 3, Pole-dipole	2.4	N/A (off axis)	1.5	N/A (off axis)
EW 3, Pole-pole	13.9*	N/A (off axis)	6.3	N/A (off axis)

3.3.3 Grain size distribution curve

The grain size distribution of the site soil was determined using dry sieve analysis and laser diffraction method; in this work the Beckman Coulter LS230 Laser Diffraction Particle Size Analyzer was used. The laser diffraction gives more accurate and detailed measurements of particle size of fine grains, particle size range can be between 0.04 µm - 2 mm. It is faster than traditional sedimentation methods (i.e. pipette or hydrometer methods), and less affected by workers or their laboratory experience, therefore, it was used (see Beckman Coulter, 2011 for more information). The soil sample was prepared and cleaned from organic material and sieved using the dry sieve technique to find out any possible soil particles larger than 2 mm (see BS 1377-2:1990 for more details). The dry sieve showed that the soil was finer than 2 mm. The soil was then immersed in a chemical dispersion solution as a dispersive agent overnight, the dispersive agent used to dissipate soil particles (i.e. clay particles) during sedimentation and testing. In this work Sodium Hexametaphosphate was used with 1% concentration as a dispersive agent, and then, the soil sample was tested using the laser diffraction analyzer.

The results obtained of the grain size analysis were represented by a grain size distribution curve (Figure 3-20). The grain size distribution curve could then be used for soil classification and for estimating the clay content in the soil. Based on the grain size distribution curve, the tested soil can be characterized as a clayey sand soil. The soil has a very small clay fraction (i.e. less than 2%).

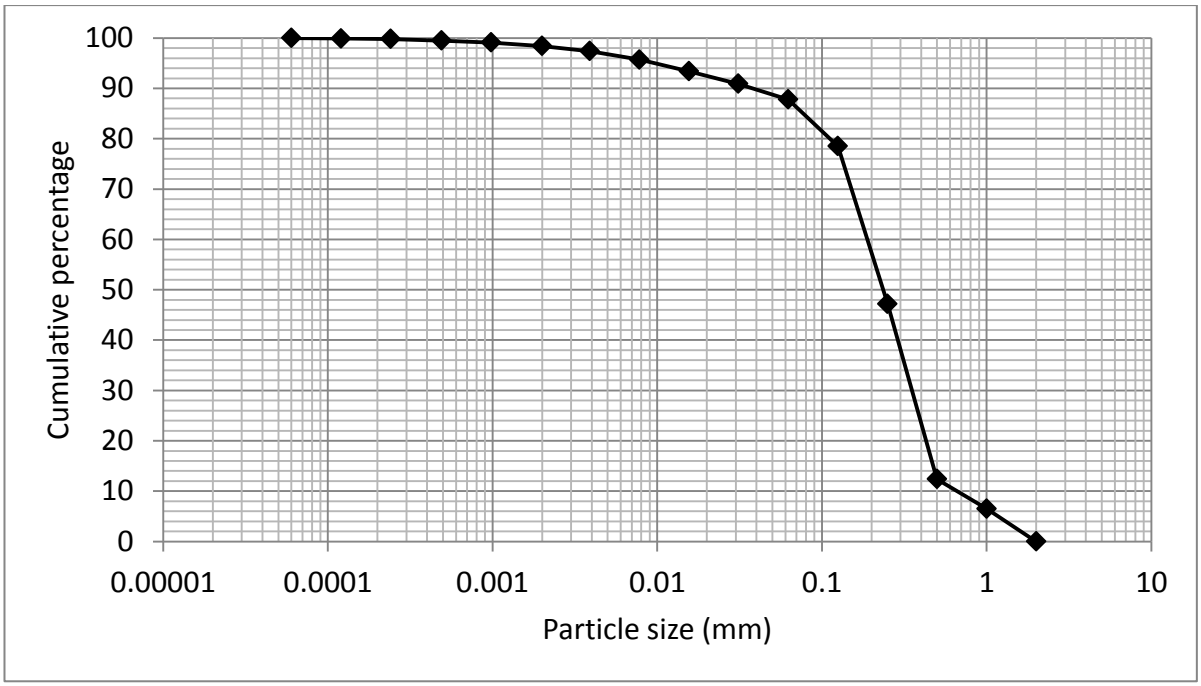

Figure 3-20: Grain size distribution curve of Keele test site soil using dry sieve and laser diffraction methods.

3.3.4 Moisture content determination:

Archie (1942) found an empirical formula that related resistivity measurements (i.e. resistivity of porous media to resistivity of fluid in pores which is called the formation factor) to clean sandstone porosity. The formula has been used and developed to estimate soil moisture content for different kinds of soils and rocks. Archie's law can be applied for moisture content as a geotechnical parameter for site characterisation. Soil volumetric moisture content for different geomaterial has been found using electrical resistivity data (see, for example, Turesson, 2006; Calamita et al., 2012; Beff et al., 2013; Brillante et al., 2015). Finding moisture content using the resistivity data is detailed in the following subsections.

3.3.4.1 Observed moisture content

The collected resistivity data should be correlated to measured moisture content to determine regression coefficients. Therefore, during resistivity data collection, observed moisture content readings were taken using a delta-T probe soil moisture sensor (Table 3-5). The observed moisture content readings were taken along the array (i.e. the array of resistivity data); readings spacing was every 1 m. Observed moisture content readings could then be used to estimate the regression coefficients. In addition, these parameters were assumed to be constant across the investigated cross section.

Table 3-5: Observed soil moisture content using delta- probe sensor at Keele facility site, with the standard deviation in parentheses.

Number of readings	Observed moisture content using delta-T probe %
1	19.4
2	21.9
3	20.5
4	20.7
5	19.3
6	17.5
7	19.2
8	20.5
9	20.3
10	19.7
11	18.4
12	19.6
13	18.3
14	18.1
Average	19.5 (SD = ± 1.2)

3.3.4.2 Estimated moisture content

The investigated site consists of two different materials: natural material (i.e. top soil and sandstone bedrock) and man-made material (i.e. the test site) as presented in the site information section 3.1.

In this work for natural ground material, volumetric moisture content was quantified based on the linear dependence of electrical resistivity on soil moisture content (equation 1), as mentioned in Calamita et al. (2012).

$$w = a + b\rho \qquad (3-1)$$

where w is the moisture content, ρ is resistivity data, and a and b are the regression coefficients.

To estimate the regression coefficients of the model, the first level of the resistivity data of pole-dipole array in E-W direction was used where each four adjacent resistivity readings were averaged, and the average of resistivity readings with the observed moisture content readings were applied in regression analysis for the regression coefficients determination (see Figure 3-21). The regression coefficients were assumed to be constant for all the investigated sections of the site and the resistivity reading were used without temperature corrections.

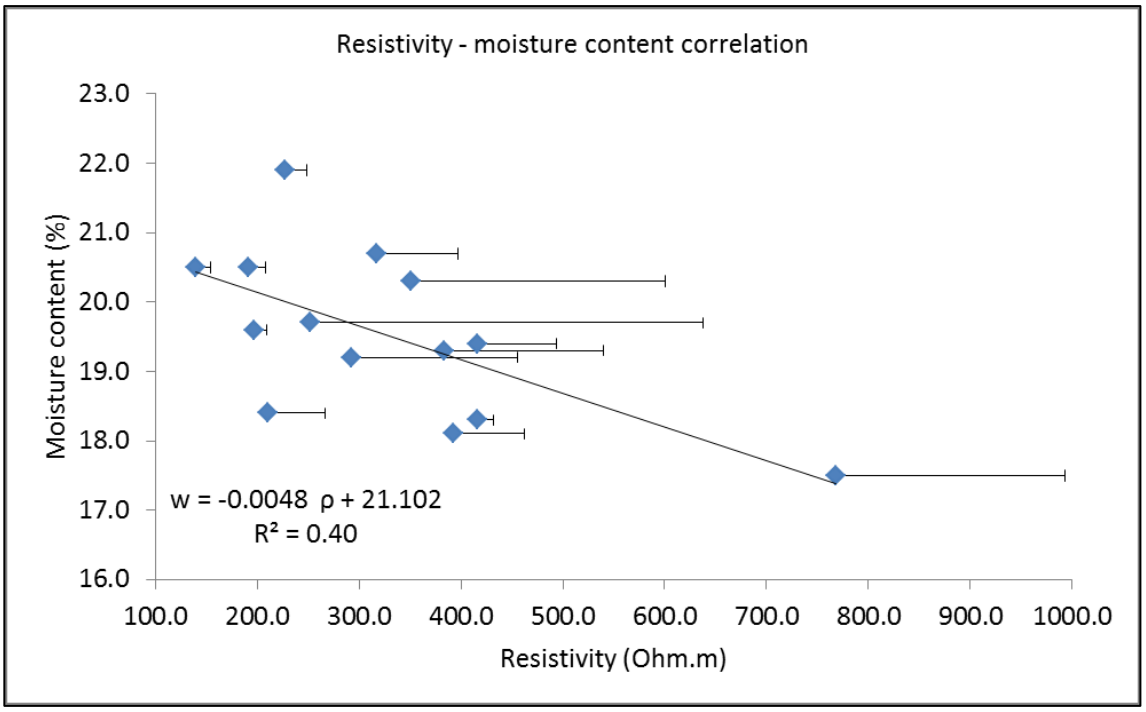

Figure 3-21: Regression coefficients determination of the resistivity-moisture content, w is the volumetric moisture content, and ρ is averaged resistivity readings.

The resistivity data yields estimated water content not considerably differs from the observed moisture content using the delta-T probe. Table 3-6 shows the absolute differences between the estimated (Mce) and the observed (Mco) moisture contents which is in a range of 0.0 – 1.9. A detailed uncertainty analysis for the observed and estimated moisture content was not possible; only one dataset of moisture content was available. The standard deviation of the observed and estimated moisture content was ± 1.2 and ± 0.8 respectively. Adding and/or subtracting the standard deviation to their relative moisture content values show an overlapped range of the moisture content which indicate that the obtained moisture content readings were consistent.

Table 3-6: Estimated (using electrical resistivity data), observed (by delta-T probe) and the absolute difference of the volumetric moisture contents of Keele test site (see text), with the standard deviation in parentheses.

Number of readings	Estimated volumetric moisture content using resistivity data (Mce) %	Observed moisture content using delta-T probe (Mco) %	Absolute difference between (Mce) and (Mco) %
1	19.1	19.4	0.3
2	20.0	21.9	1.9
3	20.2	20.5	0.3
4	19.6	20.7	1.1
5	19.3	19.3	0.0
6	17.4	17.5	0.1
7	19.7	19.2	0.5
8	20.4	20.5	0.1
9	19.4	20.3	0.9
10	19.9	19.7	0.2
11	20.1	18.4	1.7
12	20.2	19.6	0.6
13	19.1	18.3	0.8
14	19.2	18.1	1.1
Average	19.5 (SD = ± 0.8)	19.5 (SD = ± 1.2)	0.0

For the quartzite volume of the pit (i.e. clean, well sorted, 4 mm gravel, with porosity of about 42% and shallower than the ground water table), moisture content determination can be a special case where the Archie's law basics do not match the test site 'the pit' circumstances. The gravel volume was neither saturated nor partially saturated, and was expected to be just wet. In this case, Archie's law cannot be useful for moisture content determination due to the significance of percolation effects (see Martys, 1999; Khalil and Santos, 2009).

The test site is buried and covered by 0.24 m of natural soil of the site. Therefore, the gravel part of the test site cannot be completely dry but, it can be assumed to be damp by a thin film of moisture that covers the gravel particles. The bulk estimated volumetric

moisture content of the site using resistivity data is represented in Figure 3-22. The estimated moisture content was assumed to be constant for each material of the site (i.e. soil, bedrock and the test site).

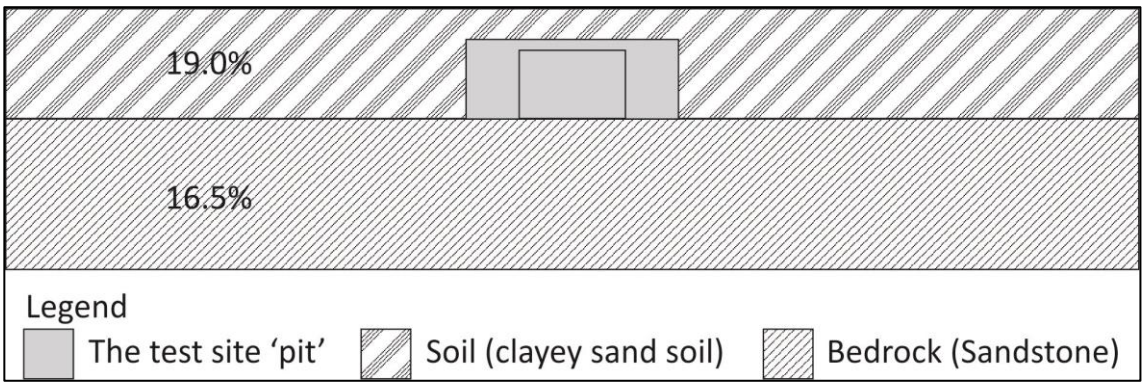

Figure 3-22: Bulk volumetric moisture content of Keele test site using resistivity data (i.e. pole – dipole array, E-W direction), the model used for moisture content determination is $w = a + b\rho$, where w is moisture content, ρ is resistivity, a and b are regression coefficients; a=21.102, and b= -0.0048 using regression analysis.

All the investigated section of the site is shallower than the groundwater table, with high porosity material, i.e. sandstone bedrock and quartzite gravel of the test site. Therefore, the investigated section cannot be expected to have a high moisture content. The natural soil layer at the site also has a higher moisture content than the bedrock moisture content. It is worthwhile mentioning here that the soil clay content helps to absorb more water and keep it saturated.

3.3.5 Seismic data results

The prepared datasets were processed using SeisImager/SW software, version 5.2.1.3 Geometrics Inc., to determine dispersion curves using the integrated SPAC technique, and then the dispersion curves were inverted using least squares inversion algorithm to produce shear wave velocity-depth profiles. The SeisImager/SW picks the dispersion curve automatically but, sometimes, SeisImager/SW miss some frequencies, therefore, the missed frequencies were picked manually.

The obtained results and the shear wave velocity-depth profiles for the three seismic components will be presented in the following sections:

3.3.5.1 Vertical component

The shear wave velocity-depth profile of the vertical component is shown in Figure 3-23. The figure shows the range of the effective investigated depth which is shown by the dark grey area and is about 4 m -11 m.

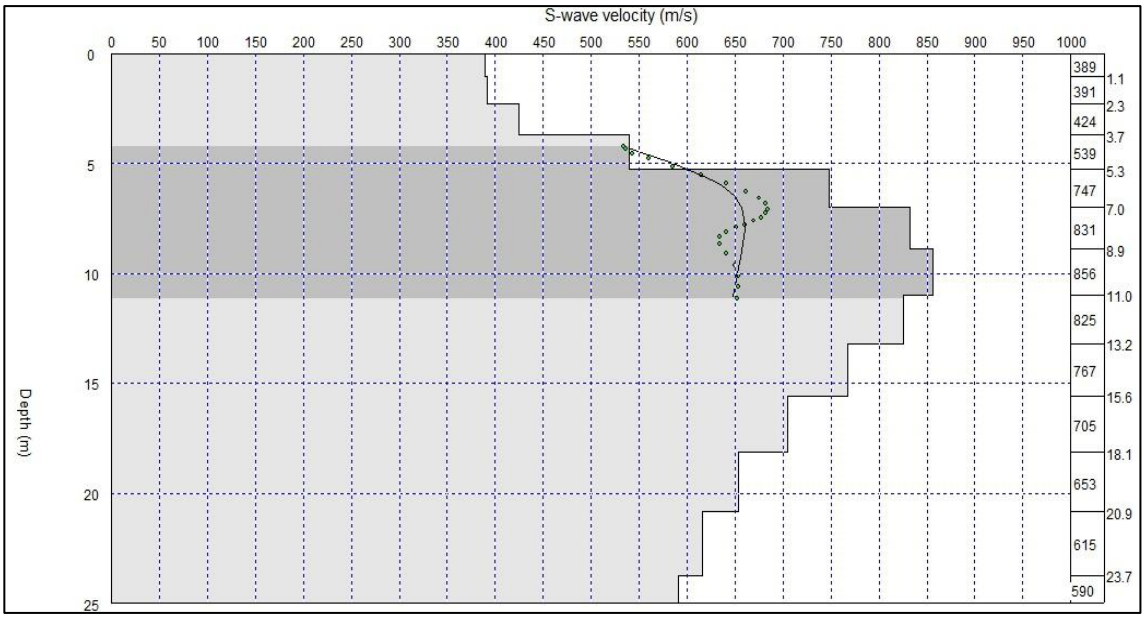

Figure 3-23: Shear wave velocity-depth profile of the vertical component, L shape array was used for data collection. The first column on the right side of the figure shows the shear wave velocity of each single layer and the second column shows the depth of each layer. The dots show the actual penetrated depth using the 1/3 wavelength method.

3.3.5.2 Horizontal north-south component

Shear wave velocity-depth profile of the component is shown in Figure 3-24. The range of the effective investigated depth is about 3 m - 11 m.

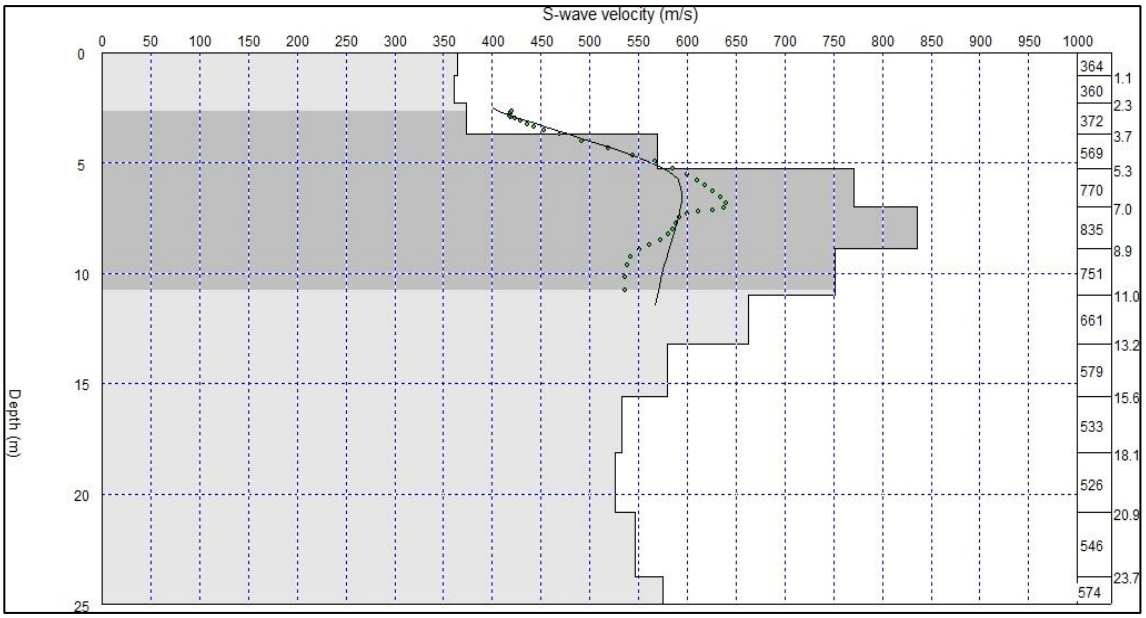

Figure 3-24: Shear wave velocity-depth profile of the horizontal north-south component, L shape array was used for data collection. The first column on the right side of the figure shows the shear wave velocity of each single layer and the second column shows the depth of each layer. The dots show the actual penetrated depth using the 1/3 wavelength method.

3.3.5.3 Horizontal east-west component

Shear wave velocity-depth profile of the component is shown in Figure 3-25. Effective investigated depth range about 3 m - 12 m.

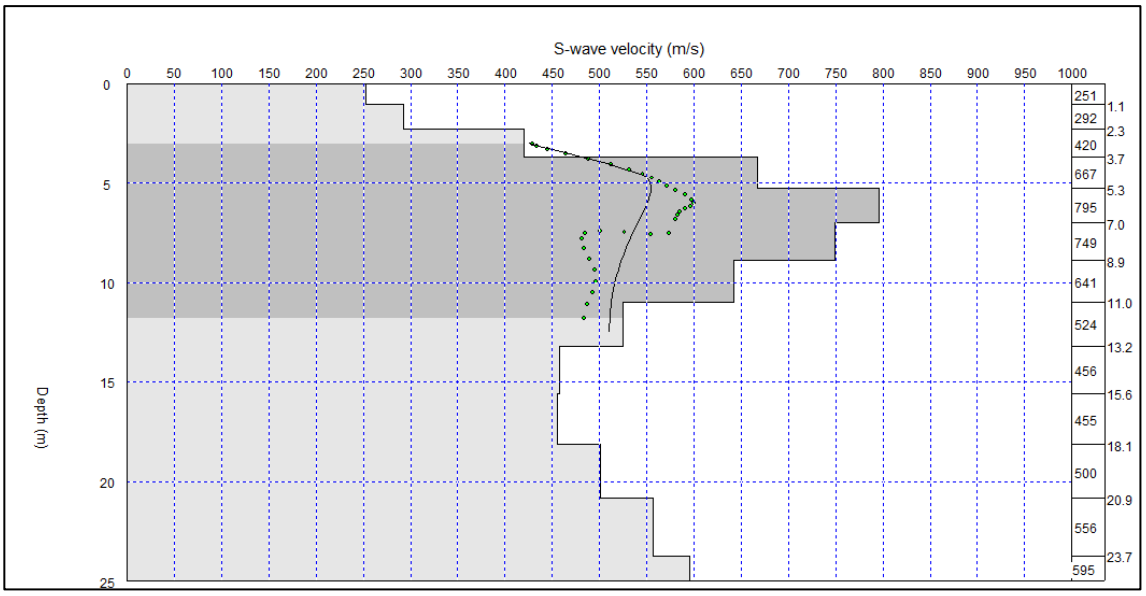

Figure 3-25: Shear wave velocity-depth profile of the horizontal east-west component, L shape array was used for data collection. The first column on the right side of the figure shows the shear wave velocity of each single layer and the second column shows the depth of each layer. The dots show the actual penetrated depth using the 1/3 wavelength method.

In general, the range of the effective investigated depth was from about 3 m to about 11 m; taking in consideration the size of the deployed array. There is no response from depths deeper or shallower than the effective investigated depths. The effective investigated depth range was deeper than the imaged cross section from the resistivity surveys and deeper than the bottom of the facility test (i.e. the pit) therefore; the geophysical surveys at the site (i.e. passive seismic and resistivity surveys) cannot be performed for joint interpretation for a better ground model.

3.4 Summary

The resistivity surveys have been conducted to compare four popular electrode configurations (Wenner, dipole-dipole, pole-dipole and pole-pole) and two inversion algorithms (the least-square smoothness-constrained and robust) using a constant electrode spacing of 0.25 m for detecting a cleared-wall foundation. The cleared-wall foundation was imaged by multiple resistivity profiles, being oriented parallel and perpendicular to the foundation length. The resistivity datasets were then separately inverted using the least-square smoothness-constrained and robust algorithms.

Using the least-square algorithm, the Wenner and dipole-dipole were found to be the best arrays for determining the cleared-wall foundation over all the four used arrays, the Wenner array was found to be better to detect the bottom of the wall, whilst dipole-dipole array was found to be better for the wall top. The pole-pole array was the poorest array to detect the wall and that was interpreted due to its sensitivity to the electrical noise at the site. The least-square inversion best represents the studied target in smooth variation in the resistivity changes and being more informative than the robust inversion.

Surveys, taken in parallel to the target, imaged the target better than perpendicular survey profiles, presumably due to the increased target size. The Wenner and dipole-dipole arrays imaged the cleared-wall foundation in perpendicular profiles. Array type was deemed just as, or even more important than, electrode spacing when designing electrical resistivity surveys due to different sensitivities to buried targets.

Alongside the resistivity surveys, passive seismic surveys were utilized to generate shear wave velocity-depth profiles of the studied site. The effective investigated depth range was about 3 m – 11 m, too deep to image the buried wall.

Chapter four: Characterising a potential HS2 site by geophysical techniques and direct tests: case study – Rugeley, Staffordshire, UK

Site ground characterisation has to be carried out for most construction projects (Clayton et al., 1995). For this, all available and relevant information about the site or the surrounding area should be collected (Simons et al., 2002). Site investigation processes should estimate the stability, serviceability and construction of the proposed site, laboratory analysis of field samples or indeed with *in situ* field tests (Barnes 2016). Some of the *in situ* field tests can be performed by geophysical methods, for example, seismic methods which are indirect, relatively cheap and fast methods (Simons et al., 2002). Seismic surface waves have been applied for site investigation in many studies (see, for example, Cha et al., 2006; Behm et al., 2014). Resistivity and microgravity methods have been performed for site characterisation(for resistivity method see, for example, Sudha et al., 2009; Vargemezis et al., 2015; Yalcinkaya et al., 2016; Osinowo and Falufosi, 2018 and for the microgravity method see, for example, Tuckwell et al., 2008; Mantlík et al., 2009; Pringle et al., 2012; Ardestani and Ashena, 2018).

In this chapter, geophysical and direct test datasets were collected and utilized to assess the geotechnical properties of a site in Rugeley, Staffordshire (see Figure 4-1 for location). Moreover, this case study provides a site (already subjected to many geophysical surveys and direct conventional tests) to perform a feasibility study of train-induced vibrations.

The main aims of the study were to (1) assess the stratigraphy of the site, (2) to determine the physical and geotechnical properties of the site, where the proposed route for the HS2 (High Speed 2) is close to the site and to compare the determined datasets

qualitatively and quantitatively. The study objectives, therefore, are to (1) acquire multi-geophysical data (i.e. seismic, resistivity and microgravity); (2) perform conventional geotechnical *in situ* tests (i.e. cone penetration test, sand replacement test and grain size distribution analysis); (3) process all the collected datasets (i.e. the geophysical and the conventional datasets) and finally (4) determine, any possible, physical and the geotechnical site characteristics.

The surveys at Rugeley site (in terms of survey considerations and arrays parameters) were designed to investigate the site from the ground surface down to about 40 m (the required depth for most construction projects), (see Simons et al., 2002 for background). In addition, for all the surveys (electrodes position, geophones position, CPT soundings and deposits samples), the coordinates defining the position on the ground surface were collected to prepare relevant maps.

4.1 Site information

4.1.1 Location

The studied site is situated about two miles to the south-east of Rugeley town centre in Staffordshire, United Kingdom. The site is located close to the West Coast Main Line railway crossing over the River Trent, between the towns of Rugeley and Lichfield in Staffordshire. The railway embankment divides the site into two areas, east and west of the railway line. The River Trent at the site flows in a NW to SE direction, with a now-closed coal power station situated about 1 mile to the WNW (Figure 4-1).

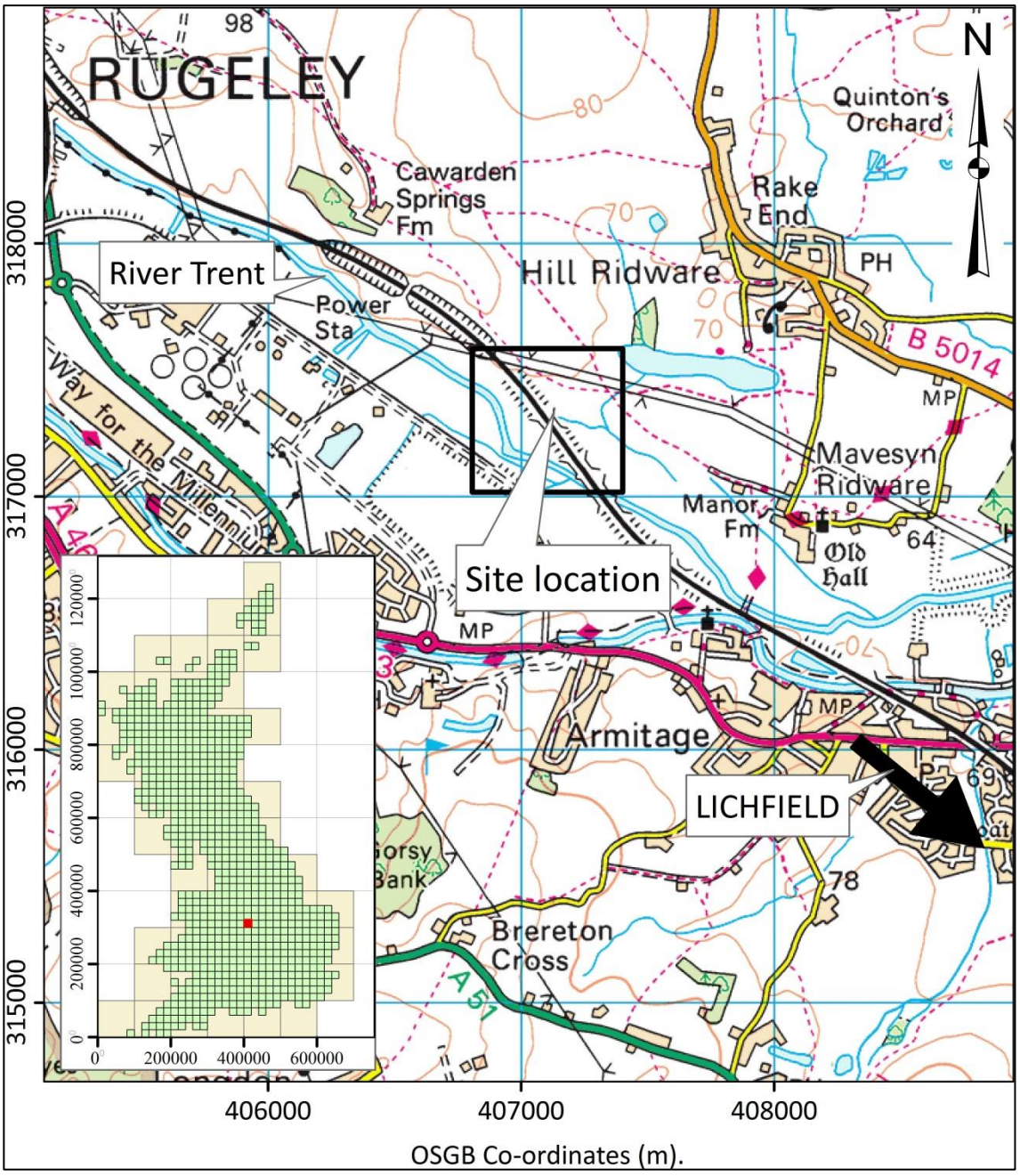

Figure 4-1: Location map of the Rugeley study site with (inset) UK location map. Images supplied courtesy of Ordnance Survey/EDINA, 2016.

4.1.2 Local geology of the site

Nearby borehole records (BGS Geoindex, 2018), presented in Table 4-1, indicate that the bedrock is the Triassic Chester and Helsby Sandstone Formations, consisting of brown, red and grey interbedded pebbly sandstones, siltstones and mudstones. Mercia

Mudstone Group crops out just to the north of the site. Overlying these are unconsolidated Quaternary and Recent sedimentary deposits linked to the last glaciation and the modern River Trent. Towards the end of the last glaciation, meltwater over-deepened the river valley which was then backfilled with glacial outwash sediments. These are topped with post-glacial and recent river terrace and alluvium deposits from the River Trent (Figure 4-2, Figure 4-3 and Figure 4-4). The railway runs to the northeast of the deepest part of the river channel. The channel sediment thickness was estimated using a microgravity survey (see section 4.6) and borehole data.

Table 4-1: The closest available boreholes near the Rugeley study site (BGS Geoindex, 2018).

No.	Borehole number (BH.NO.)	Coordinates		Drilling date	depth	Water table depth at drilling time
		Easting	Northing			
1	SK01NE29	406936	317531	1960	187.75m	9.1m
2	SK01NE21	407300	317510	1960	451.1m	/
3	SK01NE32	407291	317292	1960	165.2m	4.26m
4	SK01NE27	406962	316968	1959	149.3M	6.0m

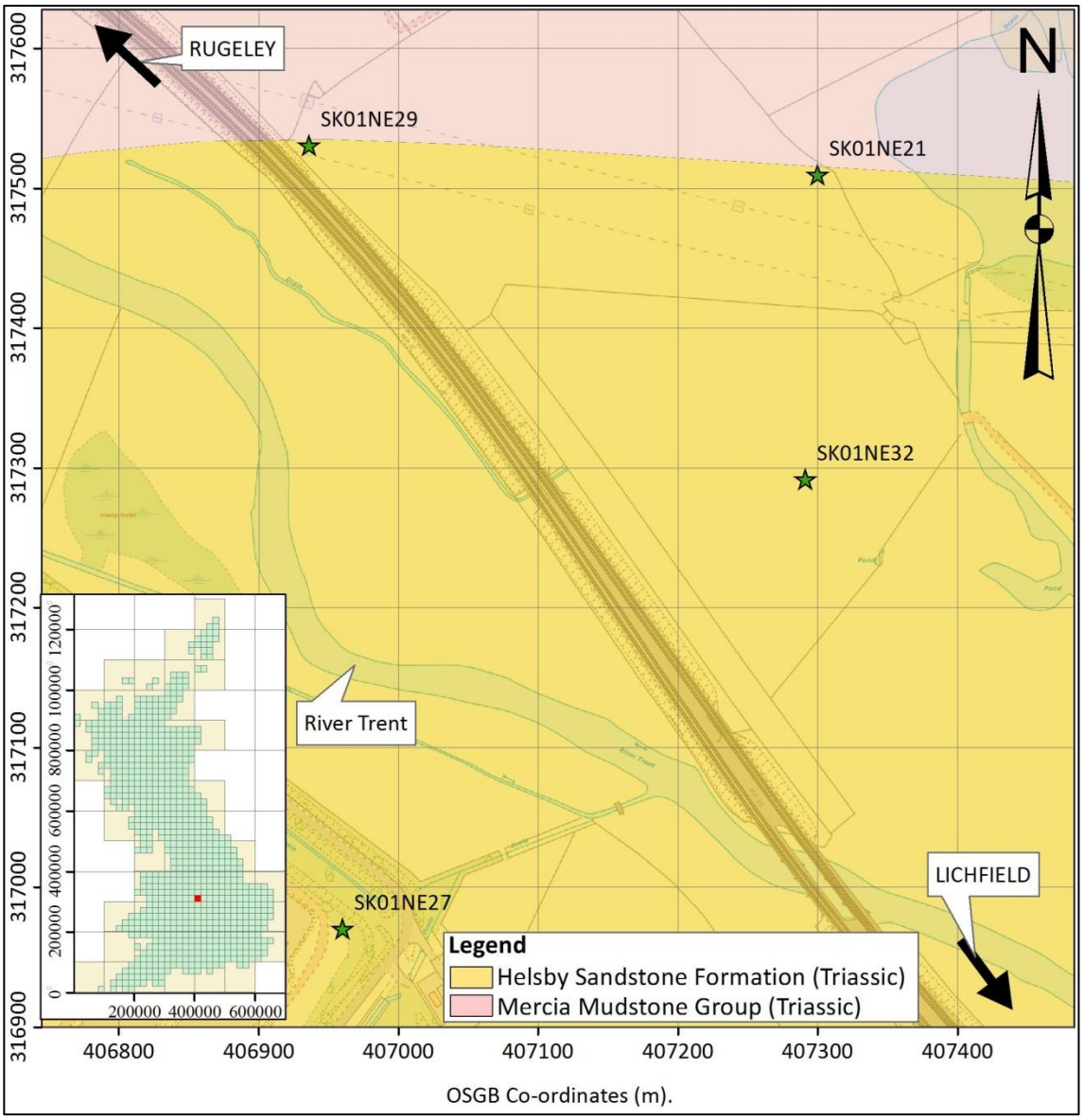

Figure 4-2: Rugeley study site map shows the site's bedrock geology with (inset) UK location map. Borehole information (green stars denote location) shown in Figure 4-4. Images supplied courtesy of Ordnance Survey/EDINA, 2016.

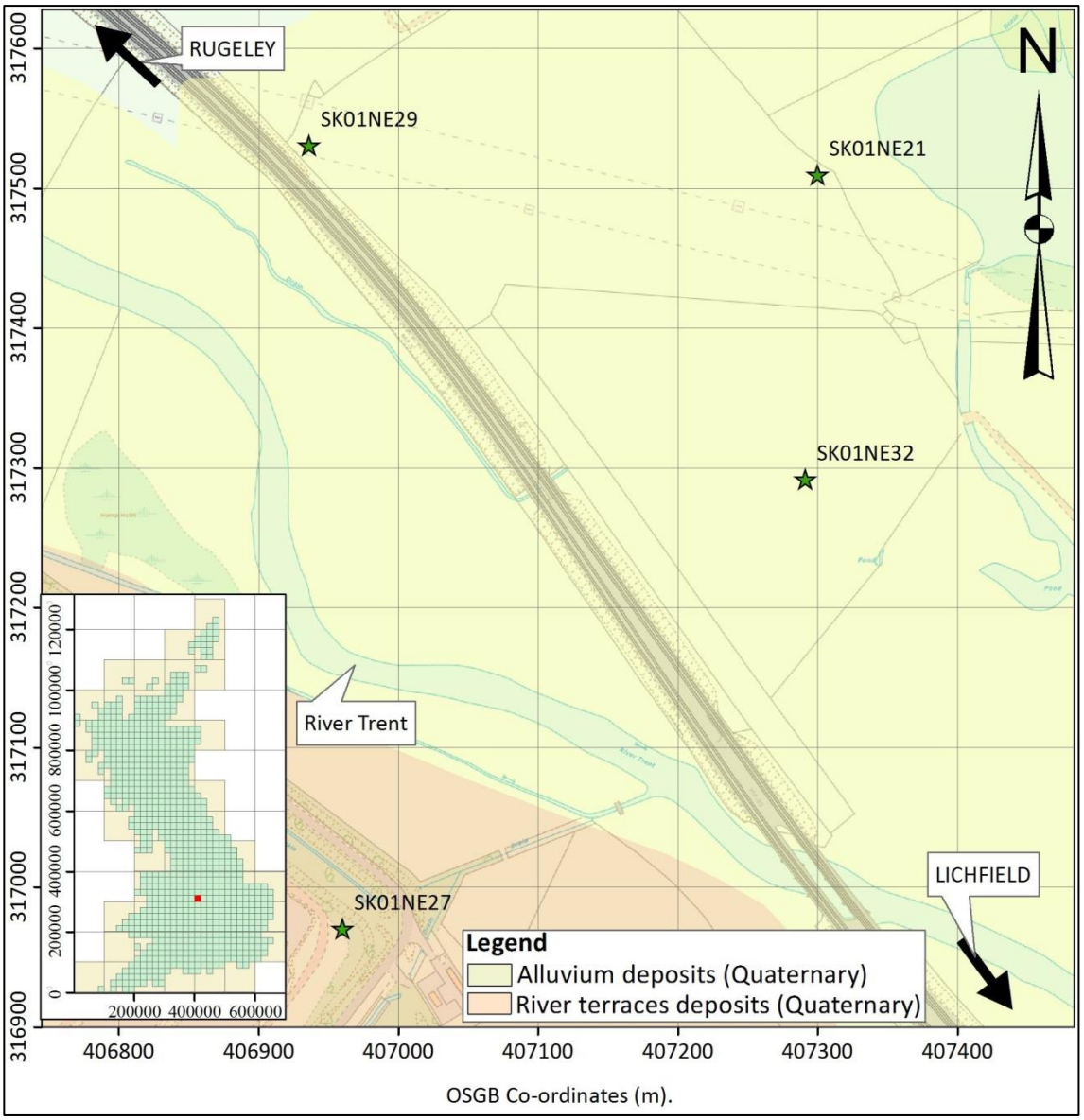

Figure 4-3: Rugeley study site map shows the unconsolidated deposits (alluvium and river terraces) at the site with (inset) UK location map. Borehole information (green stars denote location) shown in Figure 4-4. Images supplied courtesy of Ordnance Survey/EDINA, 2016.

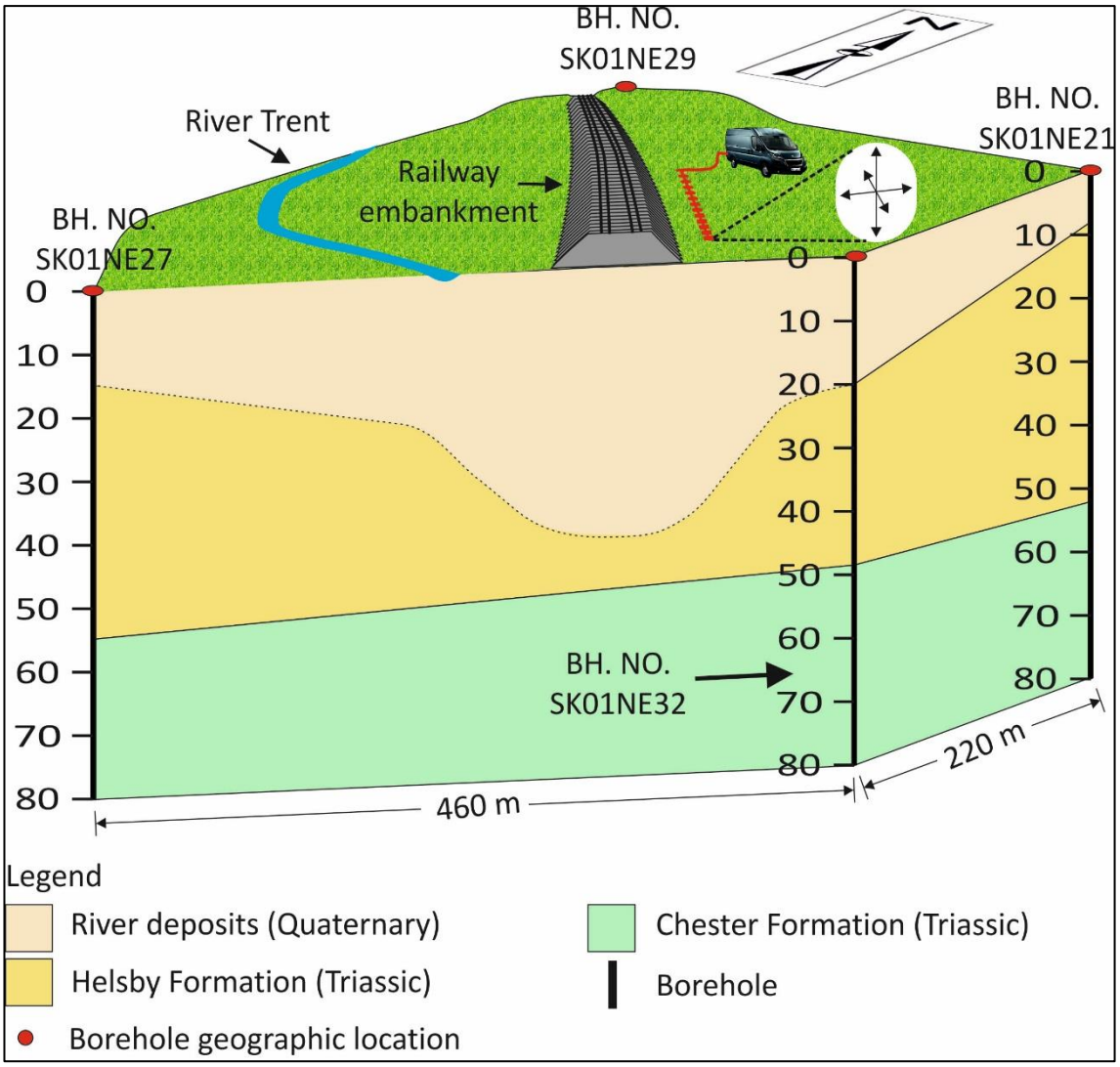

Figure 4-4: Schematic 3D geological figure of the Rugeley study site, showing superficial deposits and the underlying bedrock, generated from British Geological Survey borehole logs and microgravity surveys. See Figure 4-2 and 4-3 for named borehole (BH) locations. Vertical scale is in metres. Dotted line shows the expected glacially over-deepened River Trent channel.

The site's hydrological system has also changed during the last two centuries as a result of human activities. These changes can be noticed clearly from historical site maps, the oldest available historical map for the site was plotted during 1846-1899. These show two mill leetes flowing from the river Trent to the east and south east directions (Figure 4-5). Later on, the leetes became disused, and small ditches and a small water pond remain

and can be recognized as the leete's remnants. These changes can affect geophysical data from the site; therefore, these can be helpful for result interpretation.

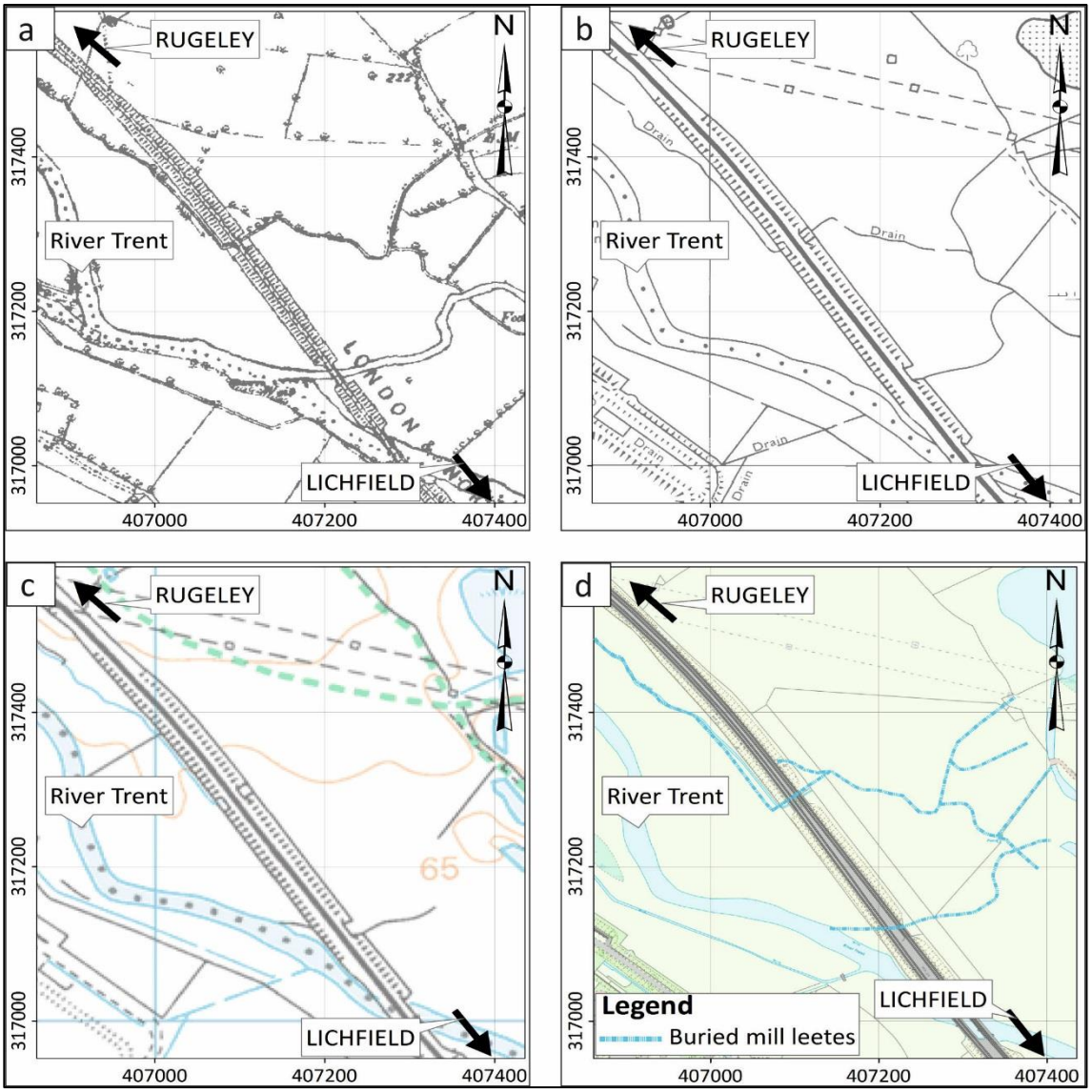

Figure 4-5: Rugeley study site historical maps show the leetes that ran from the River Trent to the east and south east directions, a) plotted during 1846-1899, b) plotted during 1958-1996, c) a contemporary map, and d) shows position of remnant leetes. Images supplied courtesy of Ordnance Survey/EDINA.

4.1.3 Site topography

The topography of the site is dominated by a flat area (i.e. the Trent Valley flood plain). The railway embankment (Figure 4-6) is the main manmade change in the landscape of the site, which runs in a NW-SE direction; it is about 40 m wide, and about 5 m high. Moreover, at the north and north-west of the site, the landforms are governed by gentle sloped hills; they are higher than the flat area by about 5 m, the contour map of the site is represented in Figure 4-7.

Figure 4-6: Rugeley study site photograph showing the raised railway embankment and a passing Pendolino passenger train. Photograph direction is south-west.

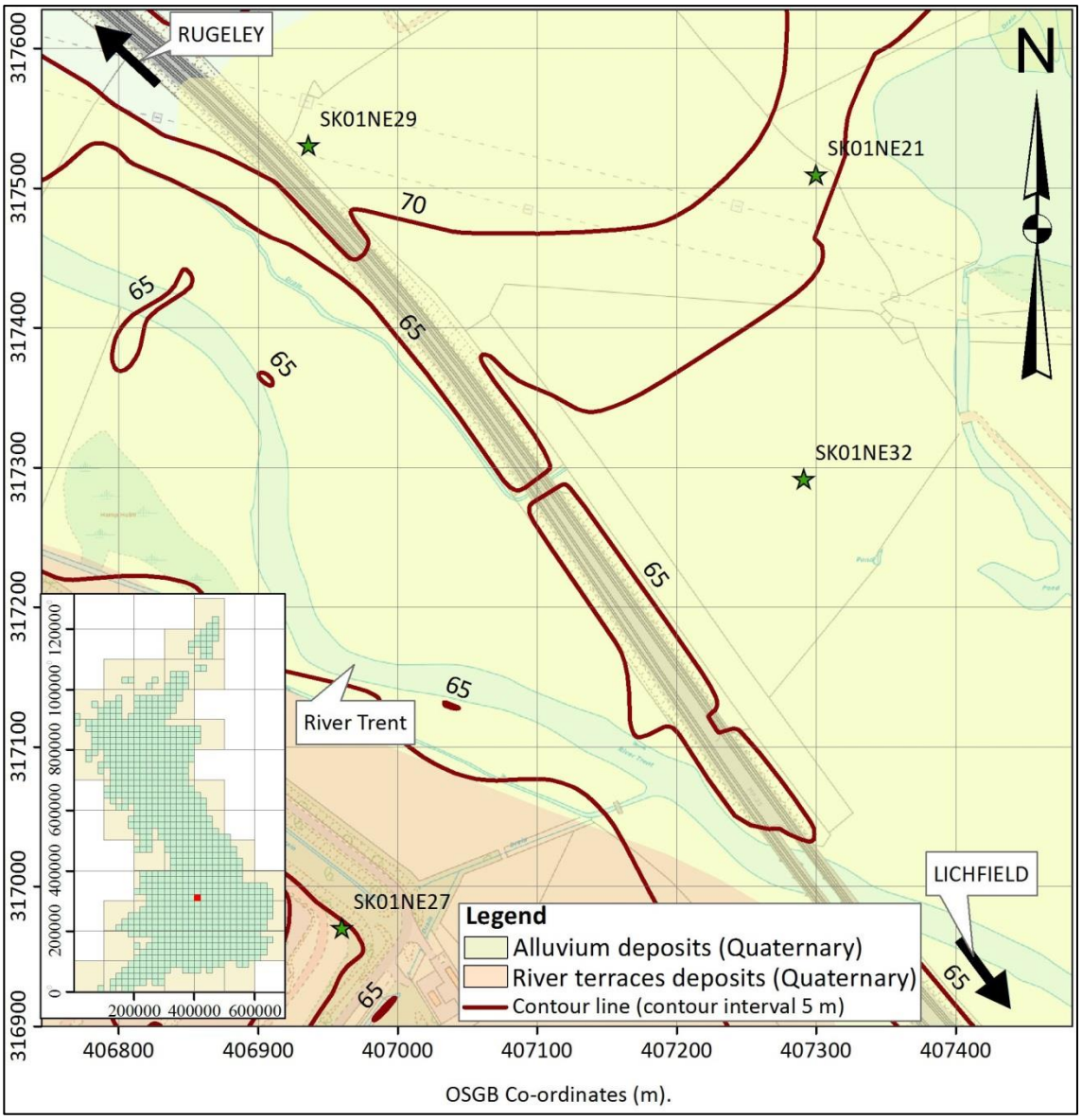

Figure 4-7: Rugeley study site contour topography map showing the relative changes in elevation in metres above sea level, with (inset) UK location map. Borehole information (green stars denote location) shown in Figure 4-4. Images supplied by Ordnance Survey/EDINA, 2016.

4.2 Grain size analysis

Grain size analysis was undertaken at 14 positions (i.e. 14 deposit samples) on the Rugeley study site (see Figure 4-12 for locations). The deposit samples were tested by two methods: mechanical sieving (wet and dry sieving) and by the sedimentation method using the X-ray SediGraph. The wet sieving was used for the separation of the cohesive and fine sediments whilst the dry sieving was used for the coarse fraction (sand and gravel) analysis. The X-ray SediGraph was utilized for the size distribution of the particles finer than 63 μm. Then, the outcomes of the sieving and X-ray procedures were combined to produce a continuous grain size distribution curve for each collected sample (Figure 4-8), following standard procedures (for sieve analysis see Barnes, 2016; BS 1377-2:1990 and for the X-ray SediGraph analysis background see Coakley and Syvitski, 1991). The grain size distribution curves are summarized in a histogram for each sample (i.e. showing the main percentages for the deposits gravel, sand, silt and clay grain sizes), and the average of all the tested samples (Figure 4-9). For all the grain size distribution curves, see appendix C.

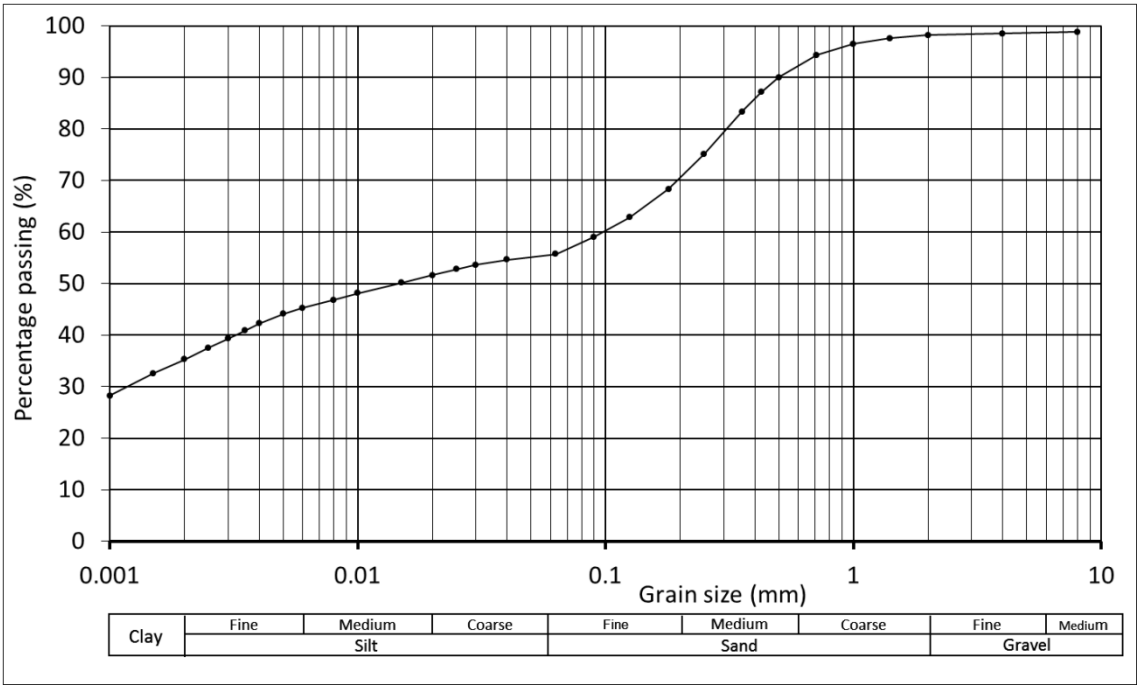

Figure 4-8: Example of a grain size distribution curve from sample 1, see (Figure 4-12) for sample location.

Samples 6-9 and 14 evidence that the coarse material (i.e. sand and gravel) is the dominant grain size which matches with the high interpreted resistivity results (see Figure 4-18 and Figure 4-23). Therefore, river deposits are expected to cover most the northern and northeast parts of the site. Samples at the south part of the studied site, samples 1-4, evidence that the fine material (i.e. clay and silt) is the dominant grain size.

Figure 4-10 shows the borehole SK01NE32 data down to about 38 m bgl. The borehole data shows variation in grain size with depth, which ranges from clay – pebble sized grains. The first 10 m of the deposit has a wide range of grain size from clays to pebbles. From 10 m to about 20 m bgl, the borehole data shows clean fine - coarse sand particles. From 20 m to 37 m, clean fine to medium sandstone (bedrock) is the dominant grain size.

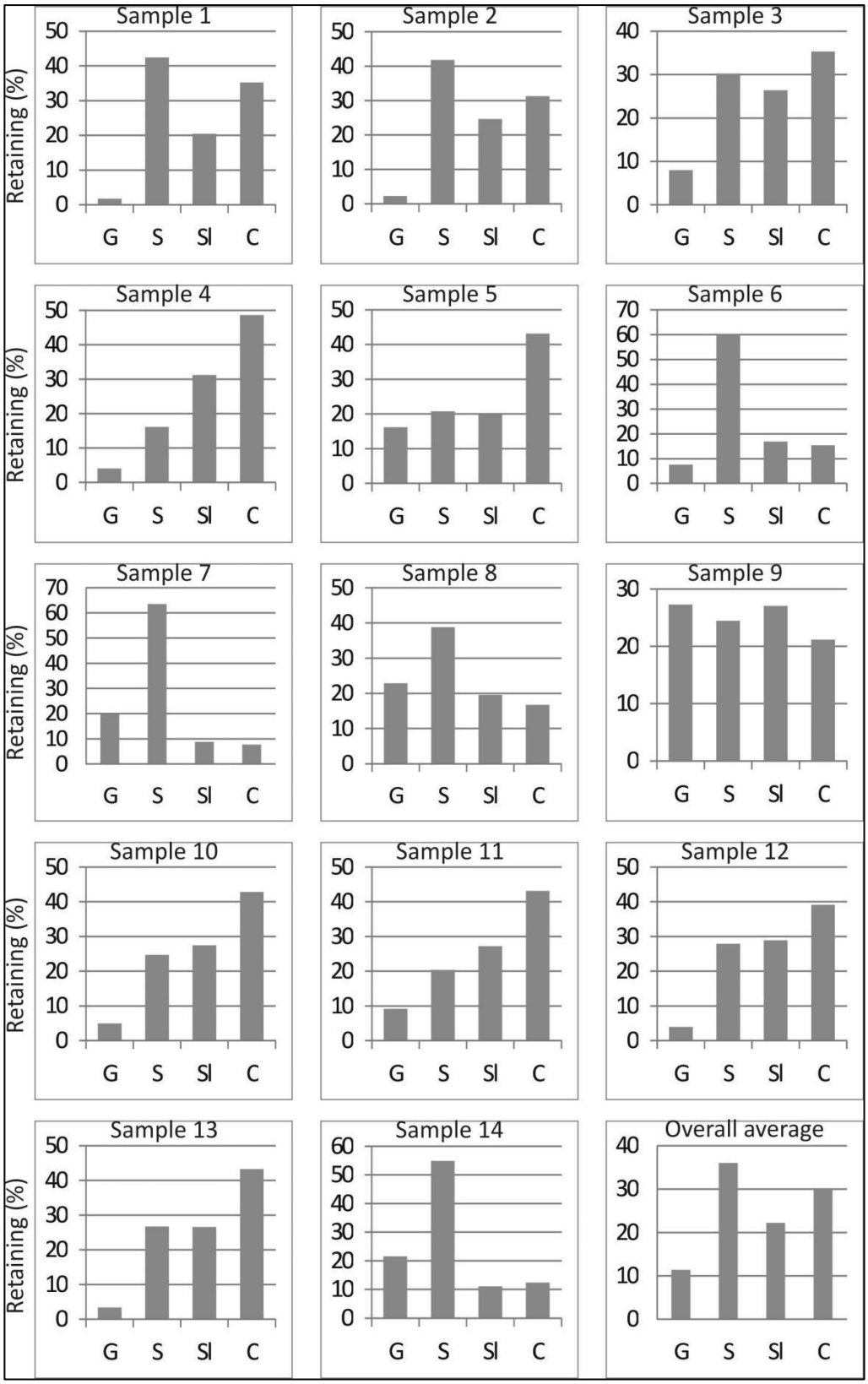

Figure 4-9: Grain size distribution histograms for the 14 deposit samples and the average for all samples. G (gravel), S (sand), Sl (silt) and C (clay), for the sample locations see (Figure 4-12).

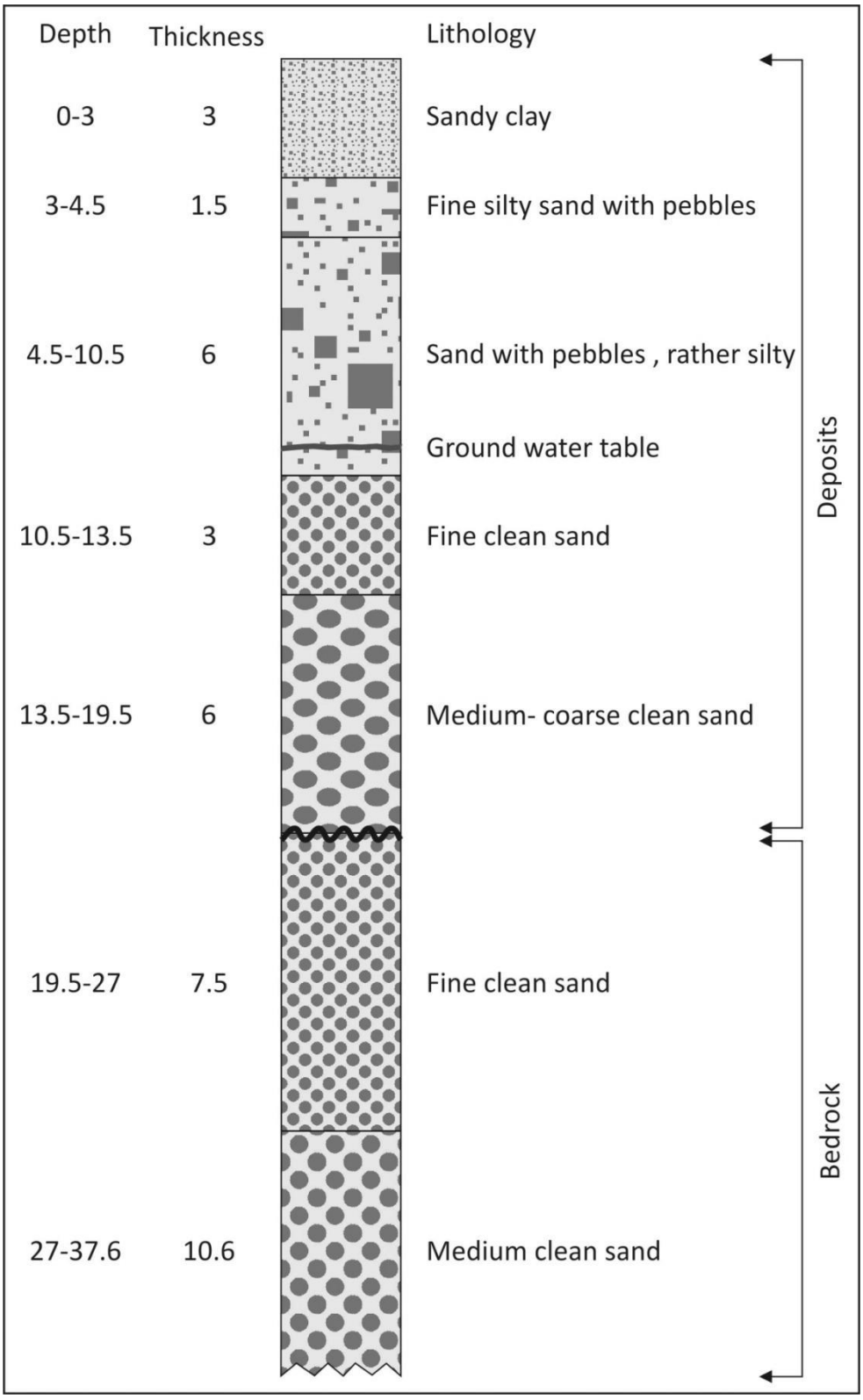

Figure 4-10: Borehole SK01NE32 (see Figure 4-12 for location) data shows the grain size variation with depth. Depth and thickness are measured in metres.

4.3 Electrical resistivity surveys

4.3.1 Methodology

4.3.1.1 Survey consideration

Mains overhead electrical power lines pass close to the site, as well as those associated with the electrified railway, which makes the site a noisy area electrically (i.e. a telluric current that may cause geophysical interference) (Figure 4-11).

Figure 4-11: Telluric electrical current sources during resistivity surveys at Rugeley site, a) photograph direction is south-west; b) photograph direction is north-west.

Therefore, for the electrical resistivity surveys, a Wenner array was utilised as it has the smallest geometric factor among other arrays used for resistivity surveys and it has strongest signal strength, and as the array experienced for surveys in electrically noisy area at Keele University campus for buried foundation determination.

The site has a relatively simple geology, consisting of Quaternary drift deposits which overlie clastic sedimentary (Triassic Chester and Helsby Sandstone Formations) bedrock (see section 4.1). Therefore, the Wenner array is effective for a site like this; it is more sensitive for vertical changes detection (Loke, 2015) and for horizontal changes, as founded from the resistivity surveys for buried-wall foundation detection, see chapter three. On the other hand, the Wenner array has poor horizontal coverage which is an inherent drawback and loss readings at both ends of the deployed array with depth, as can be seen on the resistivity 2D cross sections from the buried foundation detection surveys, see, the appendices A and B. The horizontal coverage issue is settled by extending the survey lines as long as possible such as lines 6 and 7; whilst with long lines such as 1 and 2 overlapped surveys were used.

4.3.1.2 Electrical resistivity survey parameter

The resistivity surveys (i.e. 8 2D ERT profiles) were collected (see Figure 4-12 and Figure 4-13 for respective locations) using the Campus™ Tigre acquisition equipment, with different electrode spacing and different number of electrodes depending on site accessibility, see Table 4-2.

Table 4-2: Electrode spacing and number of electrodes for each resistivity profile used for data collection at Rugeley site.

Survey line number	Electrode spacing (m)	Number of profiles/electrodes
1	3	2 profiles with 64 electrodes and a profile with 32 electrodes
2	2	2 profiles with 64 electrodes
3	3	One profile with 64 electrodes
4	3	One profile with 49 electrodes
5	3	3 profiles with 64 electrodes
6	2	One profile with 38 electrodes
7	2	One profile 63 electrodes
8	4	One profile with 64 electrodes

In this case study, the Campus™ Tigre acquisition equipment was set up to collect each reading across 3 cycles of alternating current injection polarity with a 'time-off' period of 0.5 second and a 'time-on' period of 1 second, in order to calculate the potential difference over these three cycles. In addition, each subsequent reading used an adjacent set of four electrodes from its previous measurement to give the electrode some time to allow the electrical charge to dissipate (Dahlin, 2000).

4.3.1.3 Field deployment

Resistivity profiles were positioned to cover the different Quaternary deposits (based on the available geological information) and to be close and adjacent to the railway embankment. The following subsections briefly describe the field deployment for the resistivity profiles. The available system has 64 electrodes with 3 m electrode spacing, therefore the system does not cover a long profile. Therefore, for long lines (i.e. lines 1, 2, and 5) the data was collected using multiple profiles and then combining the data in a final overall profile. For the resistivity profiles position, orientation and location to the superficial and bedrock lithology are represented in Figure 4-12 and Figure 4-13.

Figure 4-14 shows the equipment used for data collection and Figure 4-15 represents the fieldwork deployment.

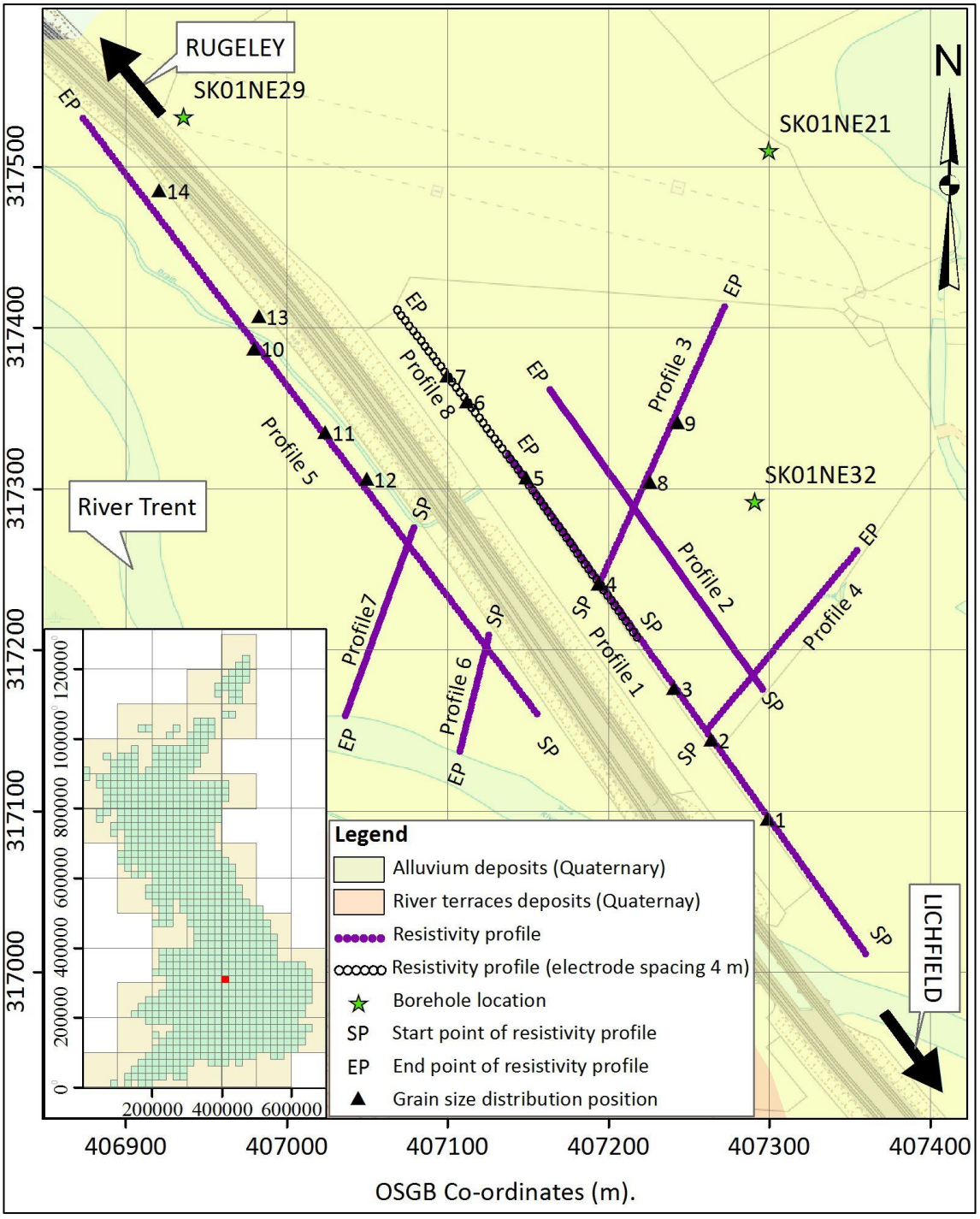

Figure 4-12: The location of the resistivity survey profiles relative to superficial deposits is shown (see key) at the Rugeley site with (inset) UK location map. Grain size measurement positions are also shown (see key). Images supplied courtesy of Ordnance Survey/EDINA, 2016.

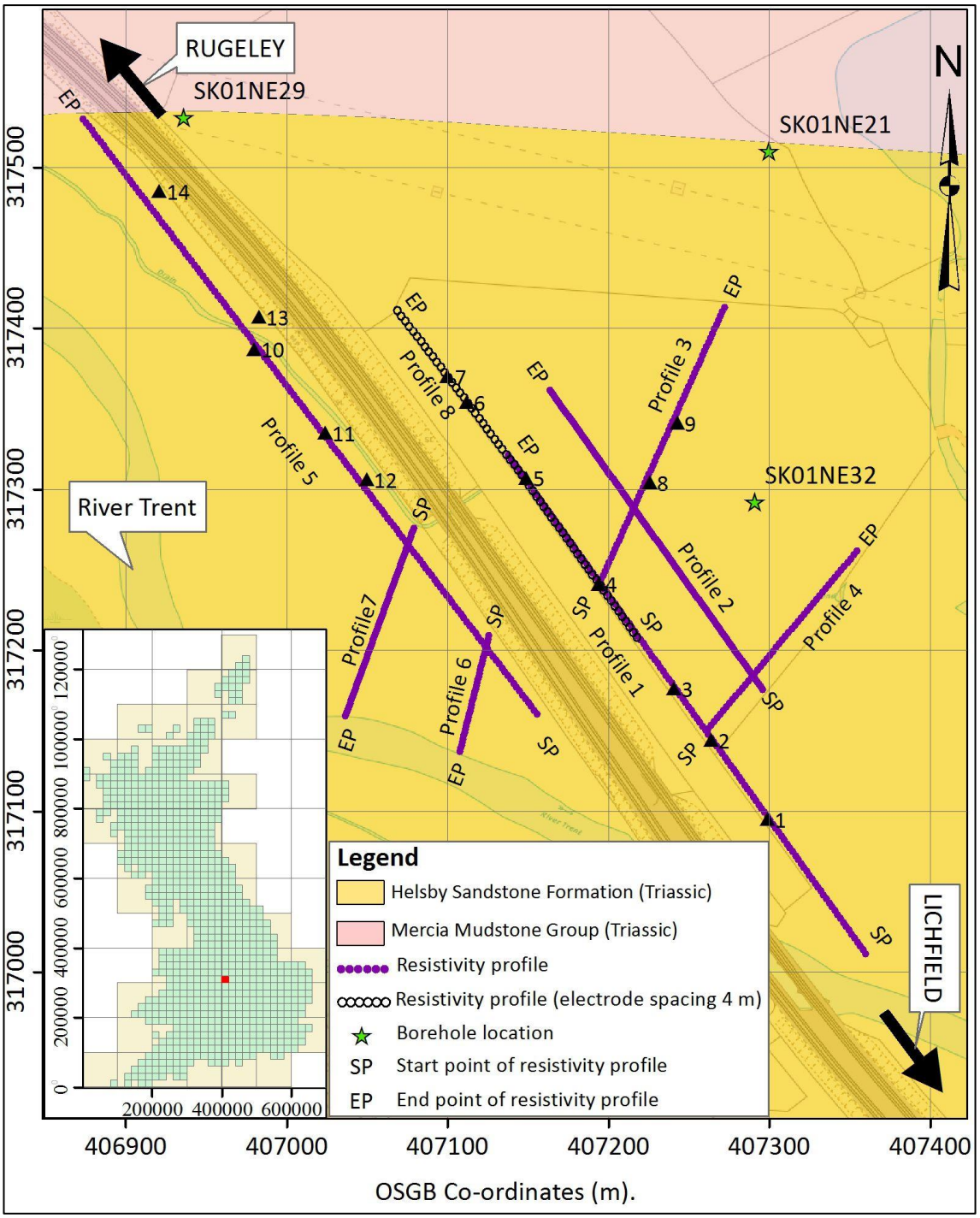

Figure 4-13: The location of the resistivity survey profiles relative to bedrock is shown, at the Rugeley site with (inset) UK location map. Grain size measurement positions are also shown (see key). Images supplied courtesy of Ordnance Survey/EDINA, 2016.

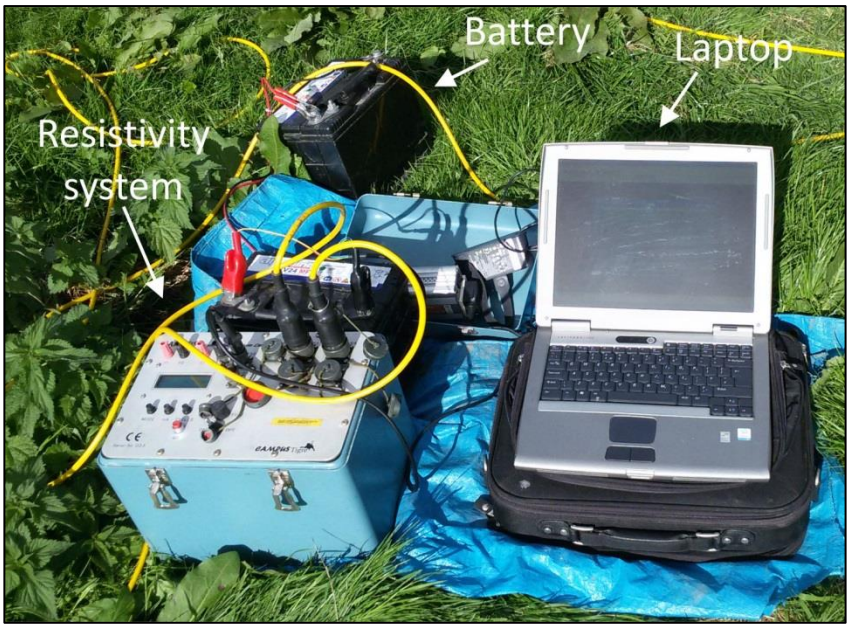

Figure 4-14: Campus ^{TM} Tigre electrical resistivity ERT system used for data acquisition at the Rugeley site, Staffordshire, UK.

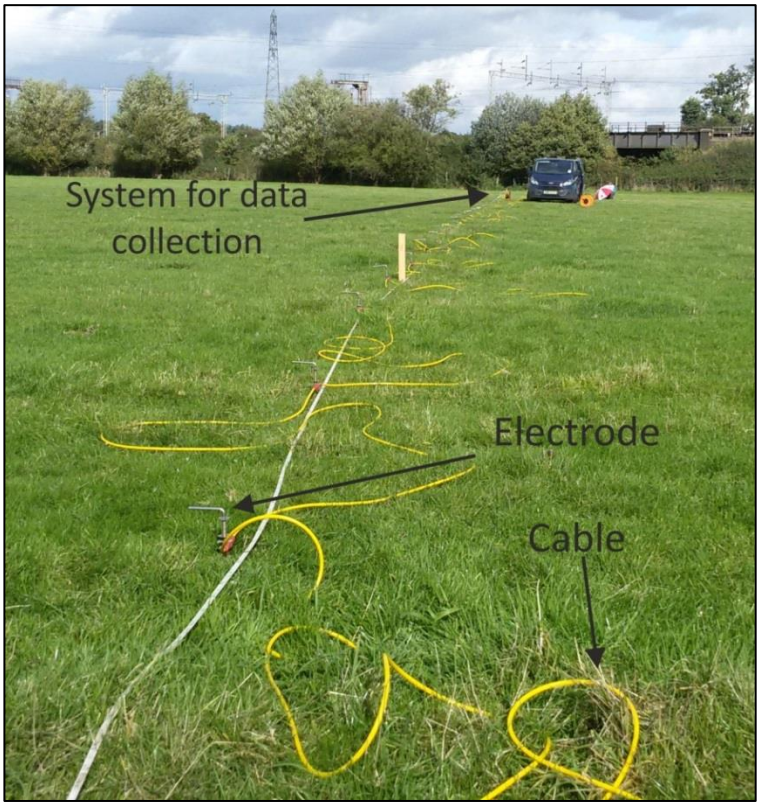

Figure 4-15: Field deployment of resistivity surveys field deployment at the Rugeley site, represents resistivity profile no.7, electrode spacing 2 m (see Figure 4-12 and Figure 4-13 for locations). Photograph direction is north-east.

4.3.2 Resistivity data preparation

The collected resistivity 2D data profiles were checked and bad data point(s) was manipulated to be in context with adjacent data points. The Res2Dinv v. 4.3 (Geotomo™ Software) and Surfer v.8.04 software were used for data checking and the Res2Dinv software was used for data processing and to produce 2D resistivity models (see Geotomo™ Software, 2004, for background).

To attain profiling survey and to minimize the horizontal coverage limitation of the Wenner array (see Loke, 2015), any new profile was laid with specific overlap at the end of the previous profile. Data points from overlapped parts were deleted from one survey and data from the second one was used in the final dataset. Any gap(s) between two adjacent profiles were filled using resistivity values which are appropriate within the same level and levels above and below it.

4.3.3 Resistivity data results

The Res2Dinv v.4.3 (Geotomo™ Software) software was used for data processing, importing each 2D profile separately. The data processing options used were 4 nodes for unit electrode spacing, the robust model inversion algorithm, with robust constrain cutoff factor of 0.05, and severe reduce effect of the side blocks. The finite difference element method and normal mesh option were used for the forward numerical modelling. The 2D resistivity models were finally displayed using the user-defined, linear colour contour interval with minimum limit of 40 Ω.m and contour spacing of 20 Ω.m, (see Geotomo™ Software, 2004, for more details).

4.3.3.1 Profile no.1

This profile was performed in three sub profiles a, b and c (see Figure 4-12 and Figure 4-13 for the profile position). The overall resistivity model for the profile (i.e. the three sub-profiles were combined in a long profile) is illustrated in Figure 4-16, with RMS error 4.4% and inversion iteration 5 results shown.

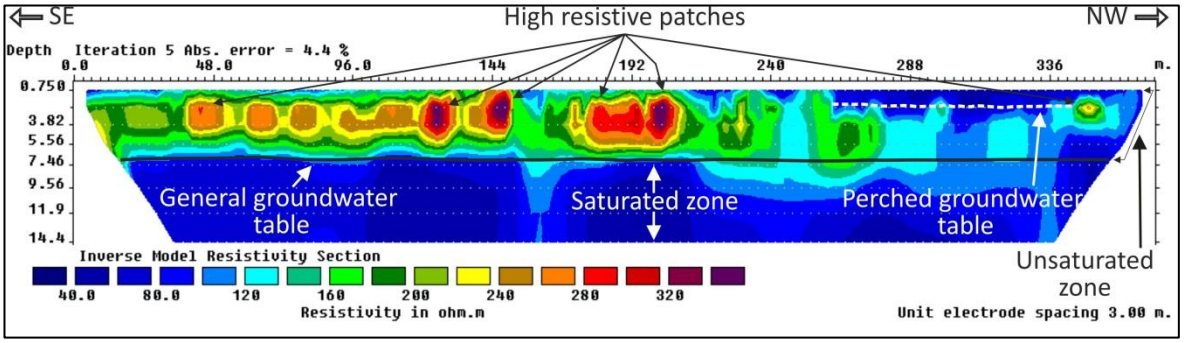

Figure 4-16: The overall resistivity model of profile no.1 from the Rugeley site (Figure 4-12 and Figure 4-13 for location), the solid black line shows the ground water table bgl at the site, and the dashed white line shows the interpreted perched groundwater table level.

4.3.3.2 Profile no.2

Two sub-profiles were applied to survey the total length of the profile. Is located at 45 m to the east of the first profile in NW-SE direction. The overall resistivity model of the profile is represented in Figure 4-17, with RMS error 3.3% and inversion iteration 5 results shown.

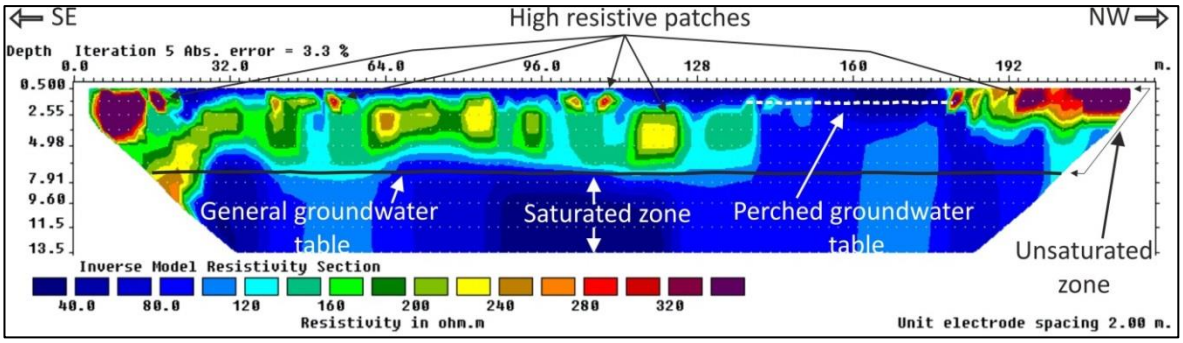

Figure 4-17: The overall resistivity model of the second resistivity profile from the Rugeley site (see Figure 4-12 and Figure 4-13 for location), the solid black line shows the ground water table bgl at the site, and the dashed white line shows the interpreted perched groundwater table.

4.3.3.3 Profile no.3

The resistivity model of the profile is illustrated in Figure 4-18, with RMS error 3.7% and inversion iteration 5 results shown.

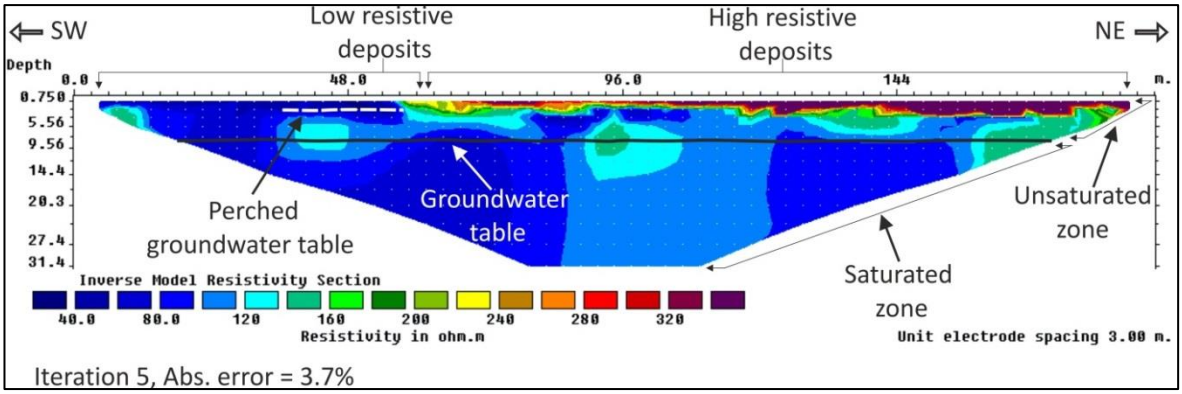

Figure 4-18: Resistivity model of profile no.3 from the Rugeley site (see Figure 4-12 and Figure 4-13 for location), the solid black line shows the ground water table bgl at the site, and the dashed white line shows the interpreted perched groundwater table.

4.3.3.4 Profile no.4

Figure 4-19 shows the resistivity model of profile no. 4, with RMS error 3.7% and inversion iteration 5 results shown.

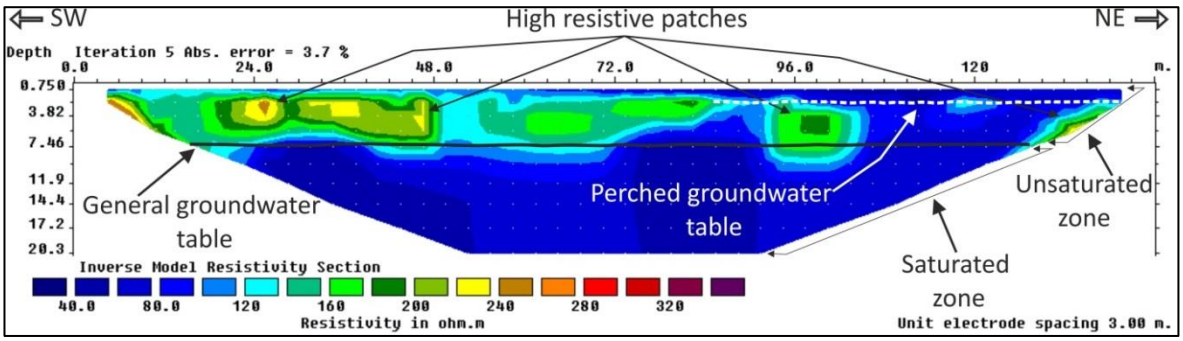

Figure 4-19: Resistivity model of profile no.4 from the Rugeley site (see Figure 4-12 and Figure 4-13 for location), the solid black line shows the ground water table bgl at the site, and the dashed white line shows the interpreted perched groundwater table bgl respectively.

4.3.3.5 Profile no.5

The profile consists of 3 sub-profiles a, b and c, the overall resistivity model of the profile is represented in Figure 4-20, with RMS error 5.3% and inversion iteration 5 results shown.

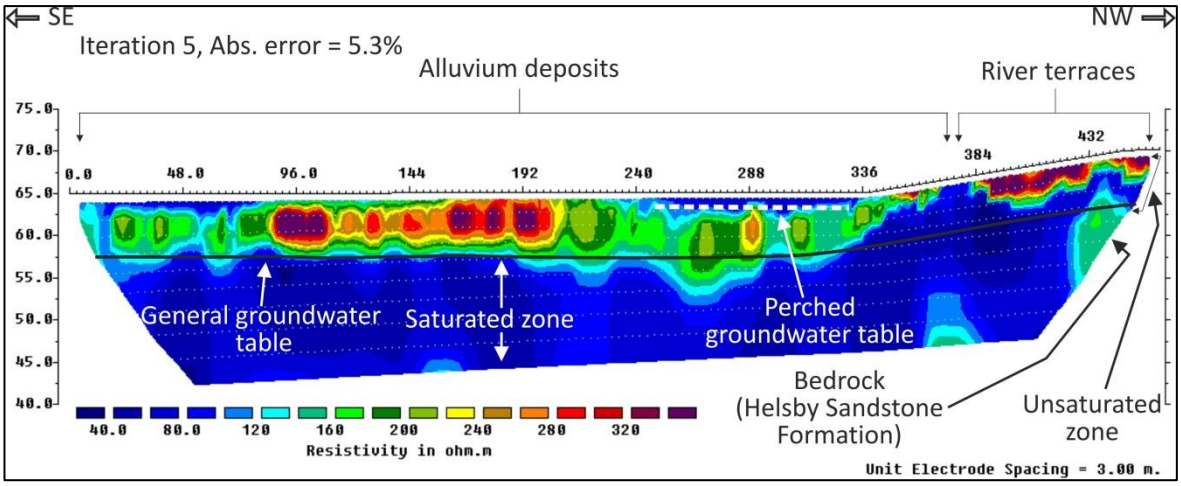

Figure 4-20: The overall resistivity model of profile no.5 from the Rugeley site (see Figure 4-12 and Figure 4-13 for location), the solid black line shows the ground water table bgl at the site, and the dashed white line shows the perched groundwater table bgl.

4.3.3.6 Profile no.6

Profile 6 is the shortest one; it runs in a NE-SW direction to the west of the railway. Its length is 74 m. The resistivity model of the profile is represented in Figure 4-21, with RMS error 2.4% and inversion iteration 5 results shown.

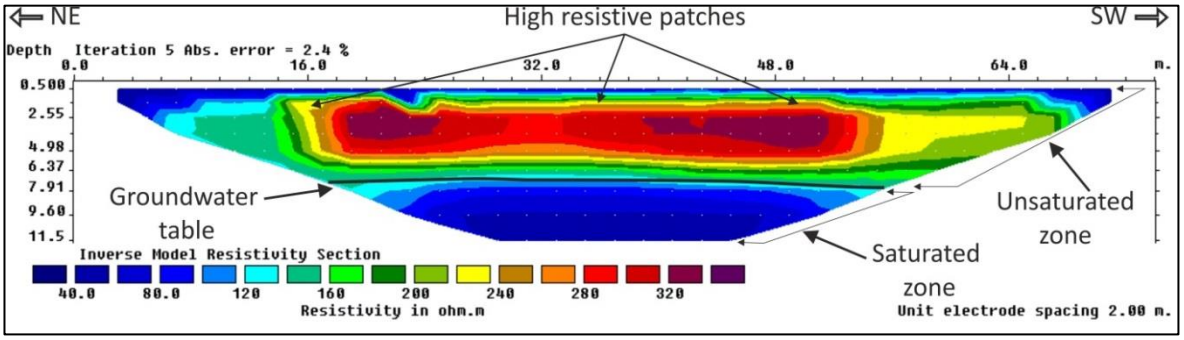

Figure 4-21: Resistivity model of profile no.6 from the Rugeley site (see Figure 4-12 and Figure 4-13 for location), the solid black line shows the ground water table bgl at the site.

4.3.3.7 Profile no.7

Resistivity model of the profile is illustrated in Figure 4-22, with RMS error 3.5% and inversion iteration 5 results shown.

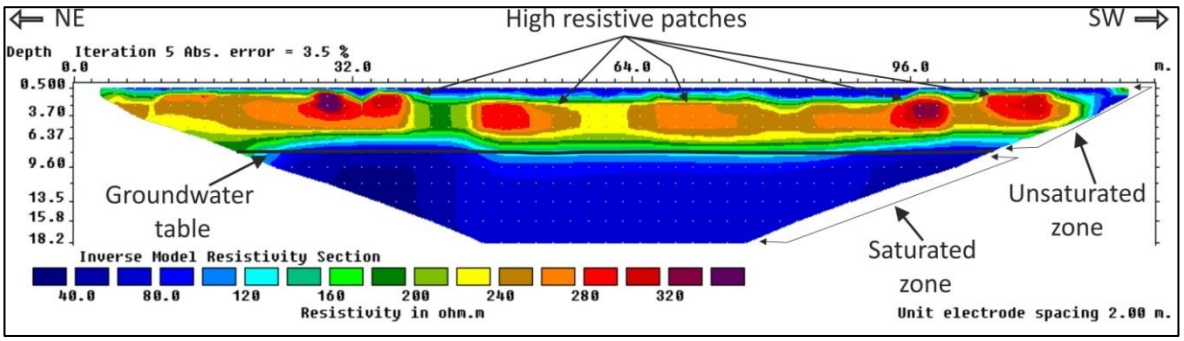

Figure 4-22: Resistivity model of profile no.7 from the Rugeley site (see Figure 4-12 and Figure 4-13 for location), the solid black line shows the ground water table bgl at the site.

4.3.3.8 Profile no.8

The survey was performed with 4 m electrode spacing in order to investigate deeper than the other previous profiles. The 2D model of the profile is represented in Figure 4-23, with RMS error 3.1% and inversion iteration 4 results shown.

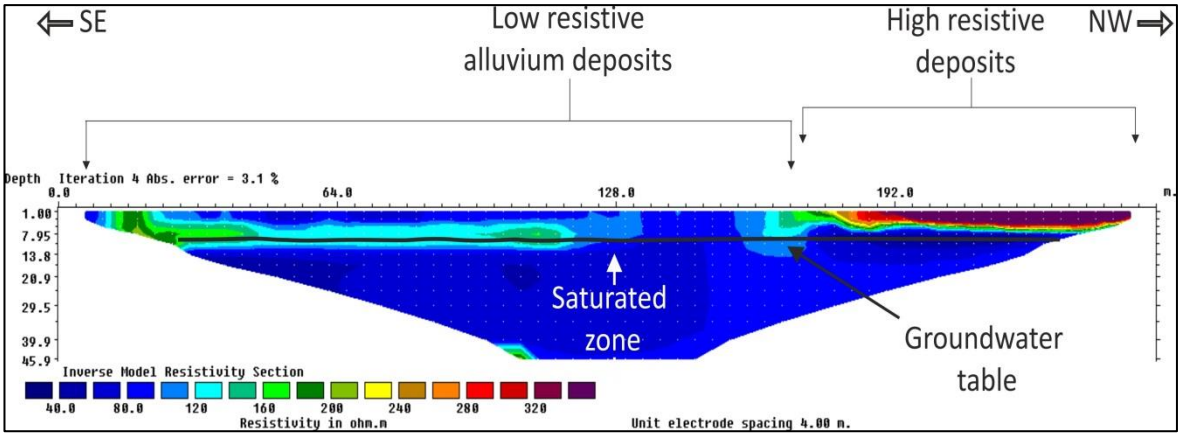

Figure 4-23: Resistivity model of profile no.8 from the Rugeley site (see Figure 4-12 and Figure 4-13 for location), the solid black line shows the ground water table bgl at the site.

4.3.4 Resistivity survey findings

4.3.4.1 Site stratigraphy

The resistivity results represent noticeable variations on the investigated profiles acquired over the site. Most of the resistivity profiles show a high resistivity layer from close to the ground surface down to about 7 m bgl, (see, for example, Figure 4-22). This high resistive layer is expected to be shallower than the groundwater table and can be confirmed by comparison to the exposed gravelly layer at the river Trent bank that is present onsite (Figure 4-24). The gravelly layer is expected to cover most of the site.

Figure 4-24: The gravelly layer which produced the high resistive layer on the 2D ERT cross sections. Photograph direction is north – north east.

The horizontal distribution of the Quaternary deposits can be predicted using the resistivity results. The northwest part of the profiles 2 and 8 and the northeast part of the profile 3 show high resistive deposits at the ground surface which is expected to be recent river deposits. The grain size distribution analysis (see Figure 4-12 for the analysis points

locations) can confirm this partly, which show high sand content at the northern parts of the studied site and high clay material content at the southern parts. The boundary appears to follow the mill leetes (i.e. the existing surface depression at the site), see the historical map (Figure 4-5) for the mill leetes location.

In addition, the resistivity results show low resistivity patches at the ground surface which is close to the buried streams location (Figure 4-23). Therefore, it can be interpreted as the low resistivity material (clay rich fine deposits) which is replaced in the streams. See the historical map (Figure 4-5) for the mill leetes location.

4.3.4.2 Groundwater table determination

The ground water table position can be interpreted from the resistivity data. The sharp decrease of the resistivity data at about 7 m depth on most the 2D cross sections (i.e. 1, 2, 4, 5, 6, 7 and 8) can be a good indicator of the regional groundwater table position.

The 2D resistivity profiles image the ground at the mill leetes positions as low resistive anomaly (see, profile no.1, profile no.2, profile no.3, profile no.4, profile no.5 and profile no.8). Salehin et al. (2004) stated that the streambeds tend to have horizontal structures; therefore, the buried streams are highly expected to have a specific local sediment types and sediment architecture conditions. Weissmann and Fogg (1999) state that the horizontal layered structure of the streambeds expected to cause less downward movement of the water. In addition, river deposits could contain different particles sizes (i.e. clay – gravel) and each facies can have specific hydraulic characteristics. Consequently, the horizontal layered structure and the obstructed vertical water conductivity could be expected to create a local perched groundwater table (see, for example, Rassam et al., 2006; Park, Y. et al., 2007; Massoud et al., 2016).

The low resistivity pits at the mill leetes position are therefore, interpreted as a shallow local perched groundwater table. Moreover, during resistivity data collection, several water ponds were noticed in those trenches. See the historical map (Figure 4-5) for the mill leetes location.

4.4 Active seismic survey using the multichannel analysis surface waves method (MASW)

To investigate shallower depths (i.e. less than the investigated depth by passive seismic surveys of ~3 m bgl) and to investigate bigger representative 2D cross sections, an active seismic survey, using the multichannel analysis seismic survey technique (MASW), was performed at the Rugeley test site (Figure 4-25 and Figure 4-26).

The survey was undertaken using a land streamer, a sledgehammer (to provide the active source) and a metal plate for seismic wave generation (Figure 4-27). The shot points were kept at the opposite end to the recording system (i.e. the car in Figure 4-27). A profiling technique (i.e. a linear spread with numerous shot points) was applied to investigate long profiles and to generate 2D cross sections (Figure 4-28). The survey parameters are detailed in Table 4-3 and follow standard procedures (Geometrics, Inc.: SeisImager/SW^{TM}).

Table 4-3: Active seismic survey parameters at Rugeley site using multichannel analysis surface waves method (MASW).

Survey parameter	Duration amount
Geophone spacing	1 m
Shot point spacing	5 m
Near offset	2 m
Number of geophones	24 (all active)
Spread length	23 m
Record length	800 mSec

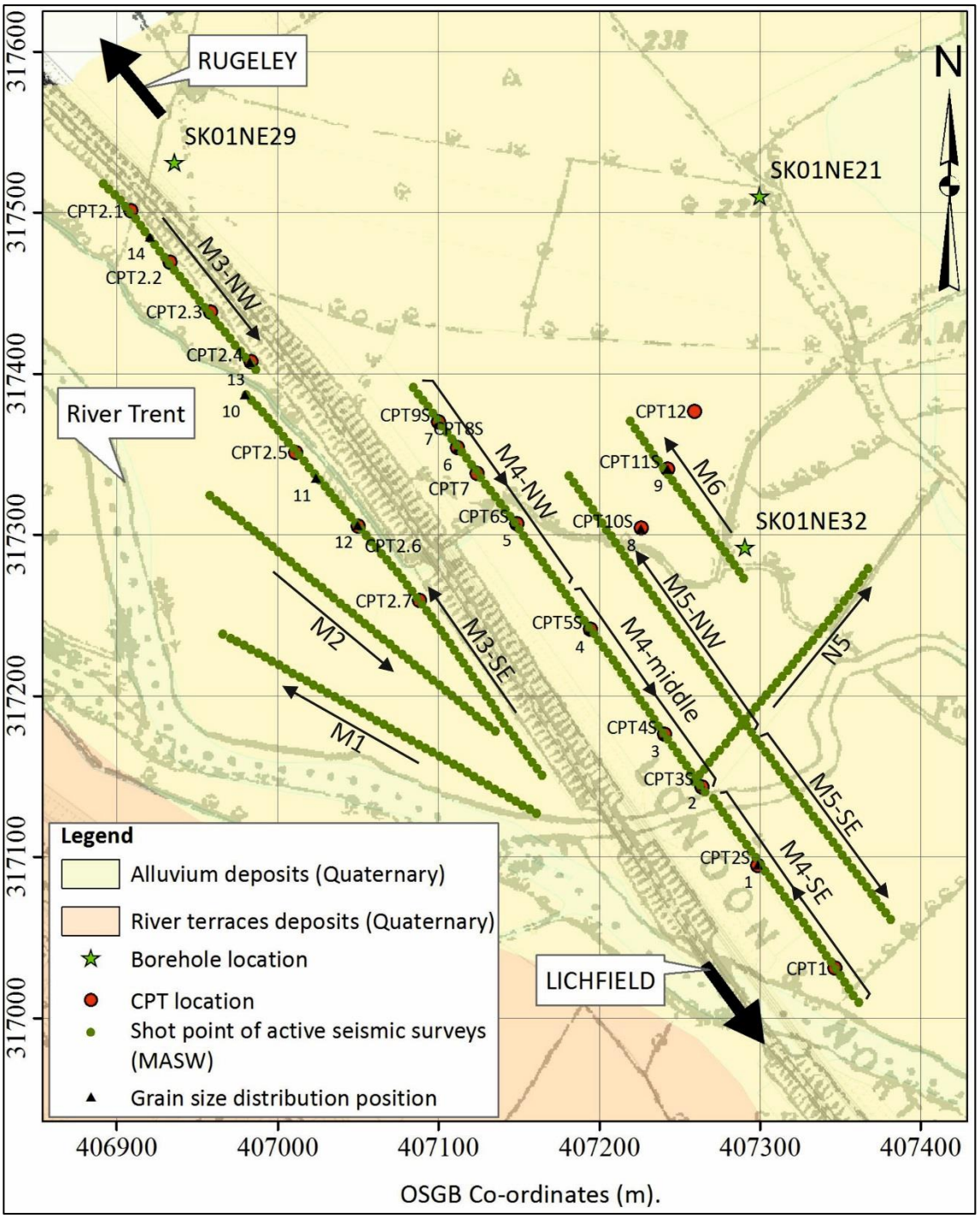

Figure 4-25: Active seismic surveys (MASW) at Rugeley site, showing the distribution of Quaternary deposits and the position of shot points, the black arrows show the survey direction (i.e. the first shot point and the last shot point). Images supplied courtesy of Ordnance Survey/EDINA, 2016.

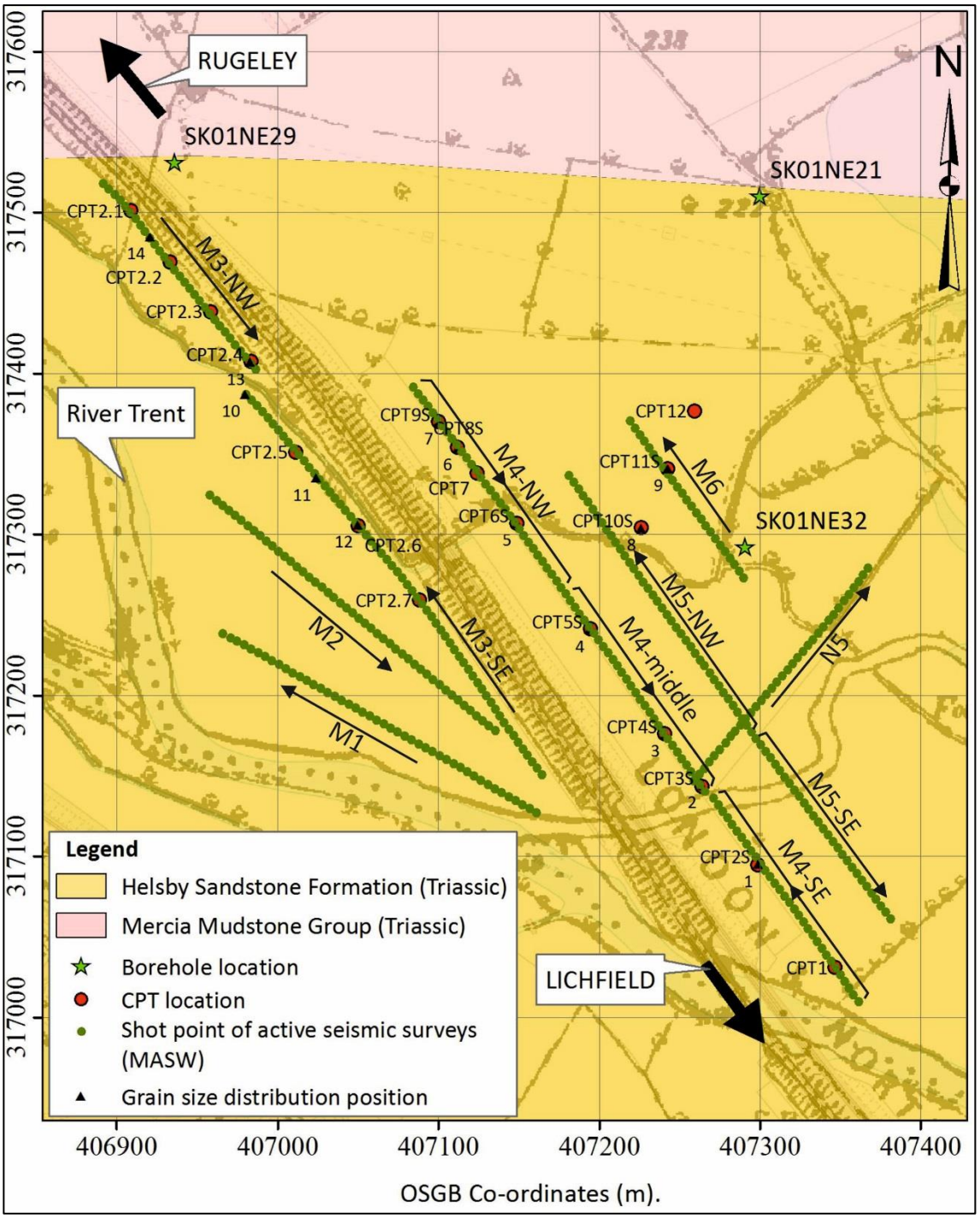

Figure 4-26: Active seismic surveys (MASW) at Rugeley site, showing bedrock distribution and position of shot points, the black arrows showing the survey direction (i.e. the first shot point and the last shot point). Images supplied courtesy of Ordnance Survey/EDINA, 2016.

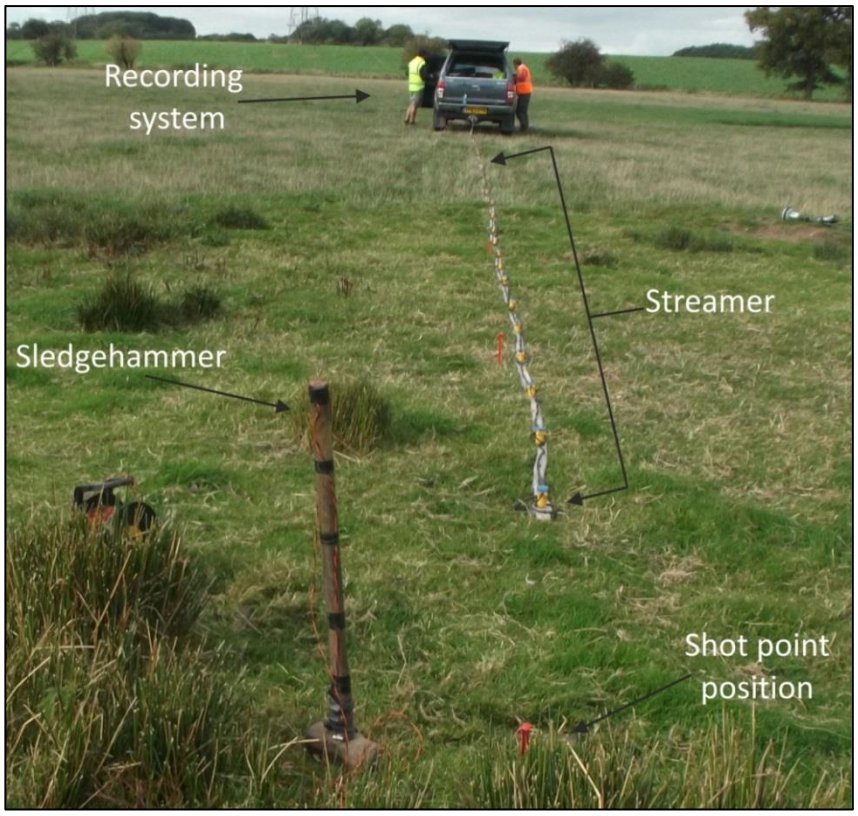

Figure 4-27: Active seismic (MASW) field work at the Rugeley site showing the equipment deployment that was used for data collection.

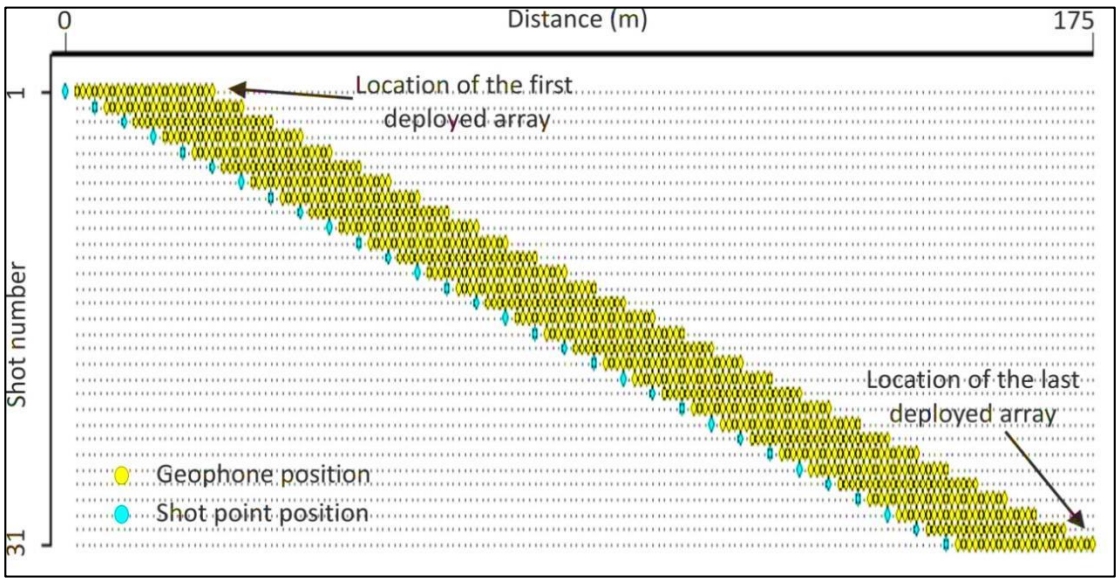

Figure 4-28: A map of the 2D MASW geometry survey showing shot point position and the geophone position (i.e. the streamer) for each record of all the surveyed profile.

The collected data was processed using the SeisImager/SW version 5.2.1.3, Geometrics Inc. The pickwin package set up the source-receiver geometry of a surveyed profile using the source and first receiver coordinates and the receiver spacing for each single shot (see Figure 4-28). The imported traces assembled into CMP gathers through cross-correlations process between any two adjacent seismic traces in each record. Then the dispersion curve can be calculated through phase velocity-frequency transformation and picking the maximum amplitude.

Here, all the dispersion curves are transformed to WaveEq package, which can be utilized to delete the higher mode and the low quality data points, to invert the dispersion curveand determining the shear wave velocity – depth cross section. After that, the determined 2D shear wave velocity – depth transferred to the GeoPlot package to be visualized into 2D cross sections. In this project, the contour interval was chosen manually, the minimum wave velocity is 50 m/sec and the contour interval is 25 m/sec (for more details see Geometrics, Inc.: SeisImager/SW^{TM} manual). All the surveyed profiles were processed and 2D cross sections graphically prepared, see appendix D.

All the 2D cross sections show increasing shear wave velocity with depth. Some also evidence low shear wave velocity from the ground surface down to about 3 m, with higher wave velocity places determined from about 8 m+. In addition, the position of the mill leetes can be determined by the 2D cross section, as low shear wave velocity patches comparing with the surrounding background material (see Figure 4-29). The position was compared with the available historical, presented in Figure 4-5, and with the field notes (i.e. ditches in the field) and they agreed. High shear wave velocity patch comparing with hosting background, on the 2D cross section, can be observed and interpreted as a gravel

deposit patch (Figure 4-29). The 2D cross sections show the horizontal and the vertical variations in the deposits properties (i.e. shear wave velocity and ultimately shear modulus).

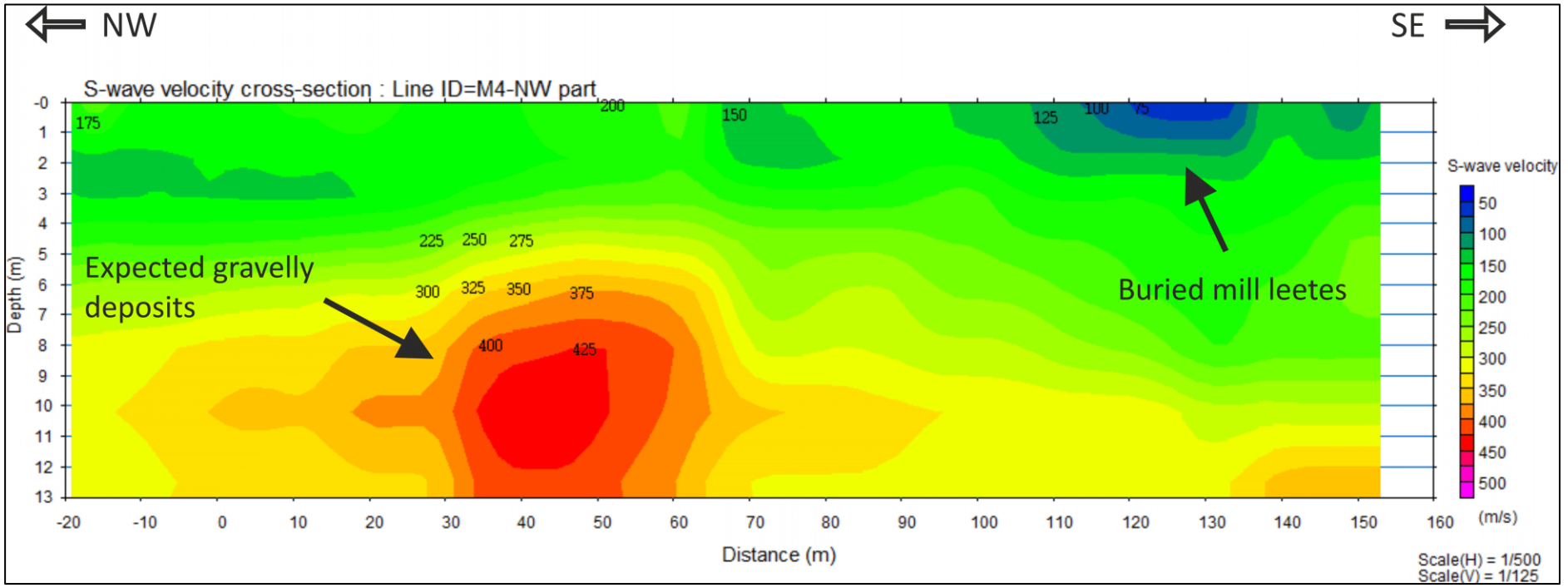

Figure 4-29: Shear wave velocity 2D cross section of profile M4 – the NW part shows shear wave velocity contours with depth and the position of the mill leetes.

4.5 Cone penetration test (CPT)

CPT tests were undertaken at the site using a Panda 2 apparatus to determine shear modulus for the penetrated depths (i.e. ground surface – 4 m bgl) and to investigate the deposits stratigraphy at the site (Figure 4-30). The test was done at 19 points distributed over the site; the CPT soundings were performed at the same location as the geophysical surveys (i.e. active and passive seismic, electrical resistivity and microgravity). The location of the CPT soundings is presented in Figure 4-31 and Figure 4-32 for the superficial deposits and bed rock, respectively.

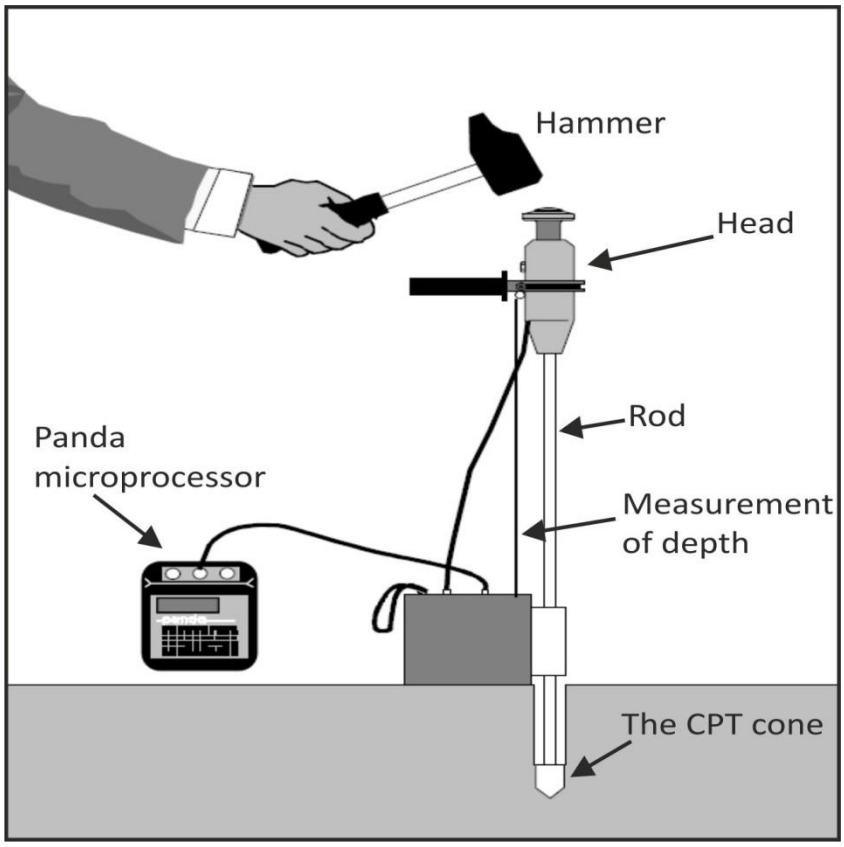

Figure 4-30: The Panda 2 instrument components and its setup in the field for data collection (modified from Langton, 1999).

The CPT was performed to different depths according to the underground situation where the maximum penetrated depth was about 4 m for most of the soundings. Although the available Panda 2 can sound down to 4 m, which can be seen in some cores, some soundings penetrate down to even less than 1 m. For those soundings where it was hard to push the cone further into the ground, a second sounding near to the first one was tried but it still difficult to investigate deeper than the sounding was stopped.

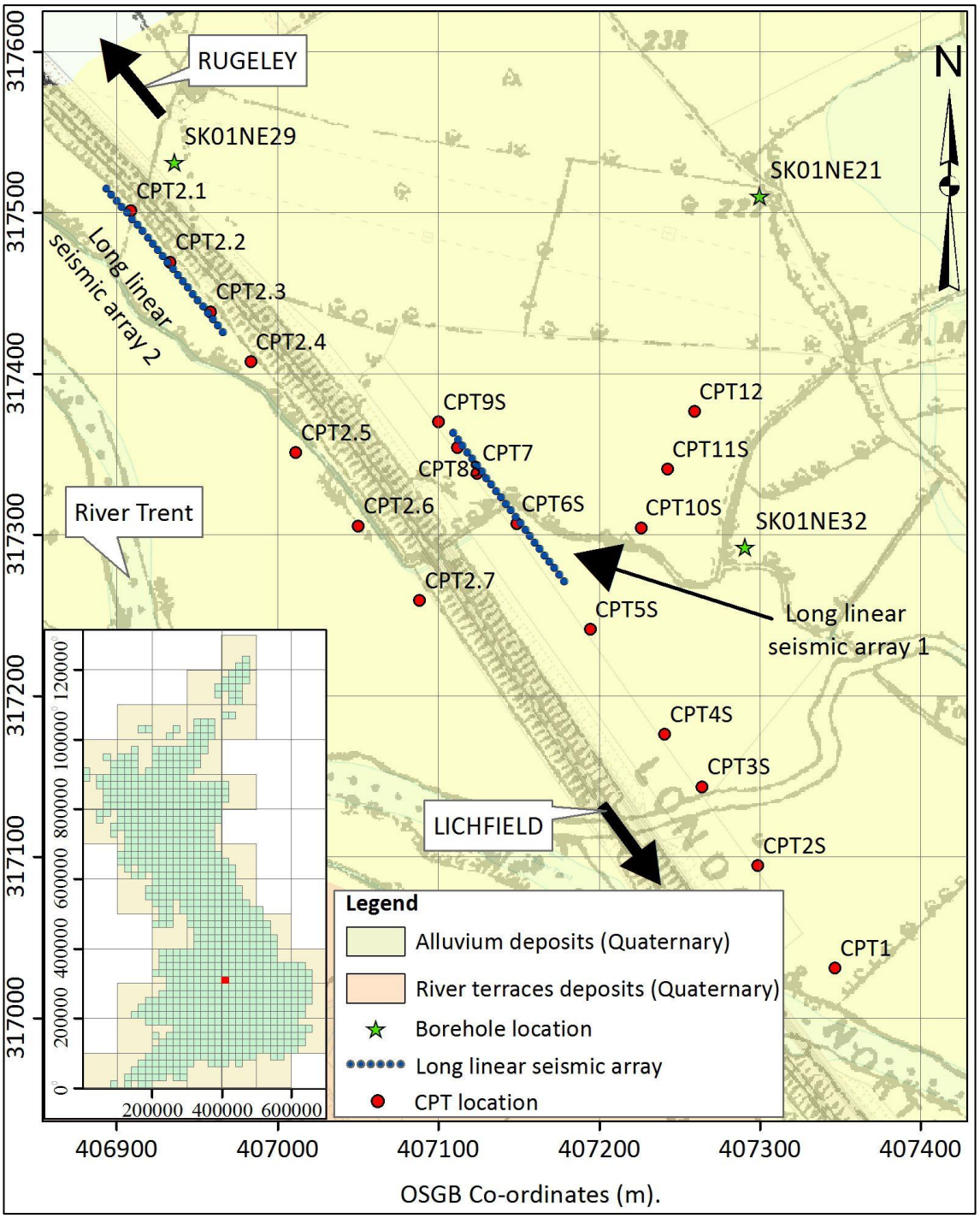

Figure 4-31: Cone penetration test (CPT) locations with superficial deposits underlain at the Rugeley site with (inset) UK location map. The three borehole positions (green stars) are also shown. Images supplied courtesy of Ordnance Survey/EDINA, 2016.

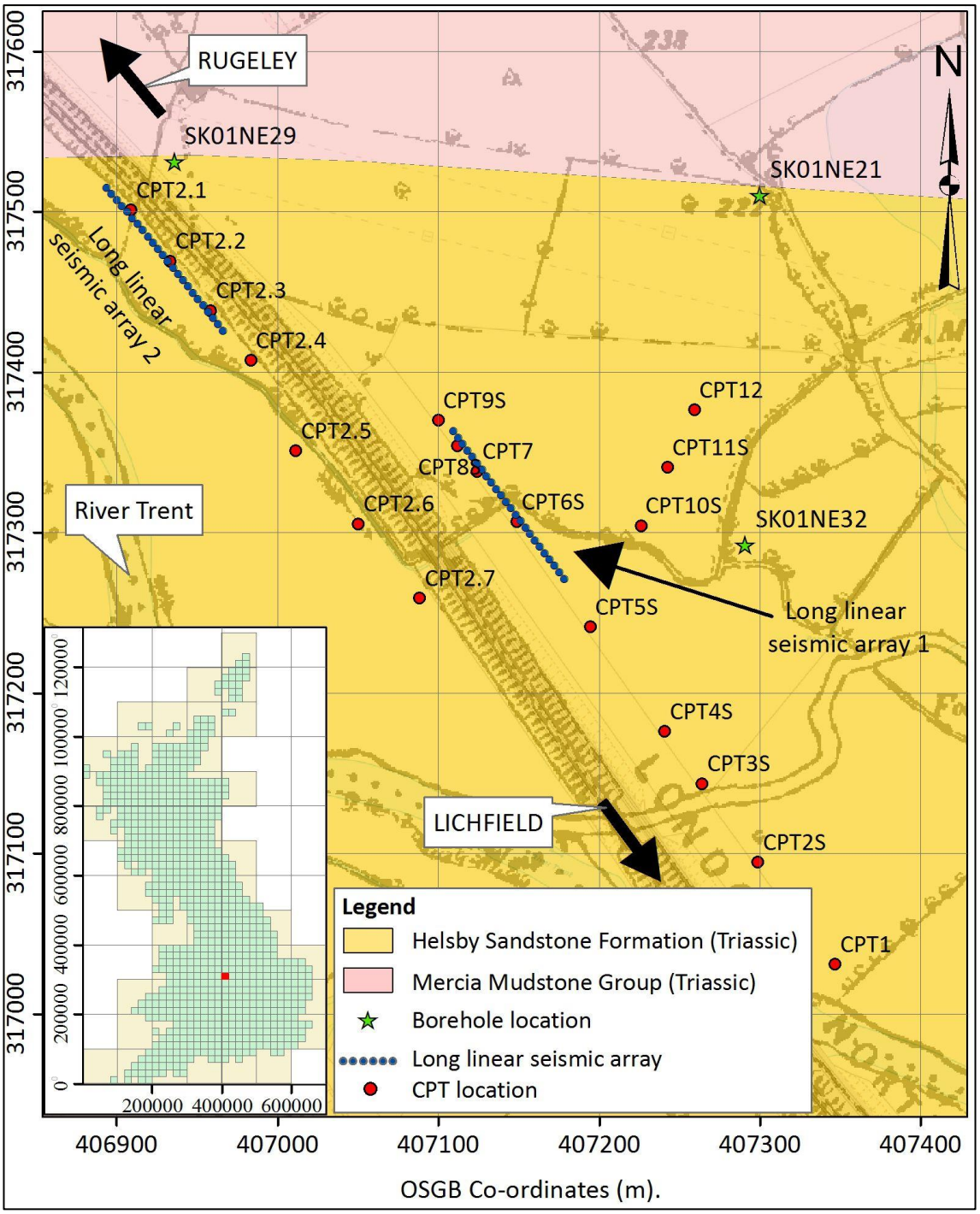

Figure 4-32: Cone penetrating test (CPT) locations with bedrock underlain at Rugeley site with (inset) UK location map. The three borehole positions (green stars) are also shown. Images supplied courtesy of Ordnance Survey/EDINA, 2016.

Because the Panda 2 produces only cone resistance (q_c) at the sampled depth(s) (Figure 4-33), then the CPT data interpretation and determining shear modulus is not a straightforward process. Chai and Roslie (1998) developed a formula (see equation 4-1) to relate deposits elastic modulus to cone resistance determined from a cone penetration test. The formula developed can be applied for elastic modulus determination of coarse and sandy coarse deposits.

$$\varepsilon = 17.6 * q_c^{0.64} \qquad (4-1)$$

Where ε is the elastic modulus and q_c is the cone resistance.

Then the shear modulus G_o can be calculated using the determined elastic modulus (Robertson, 2009), using the equation below:

$$\varepsilon \approx 2.5\ G_o \qquad (4-2)$$

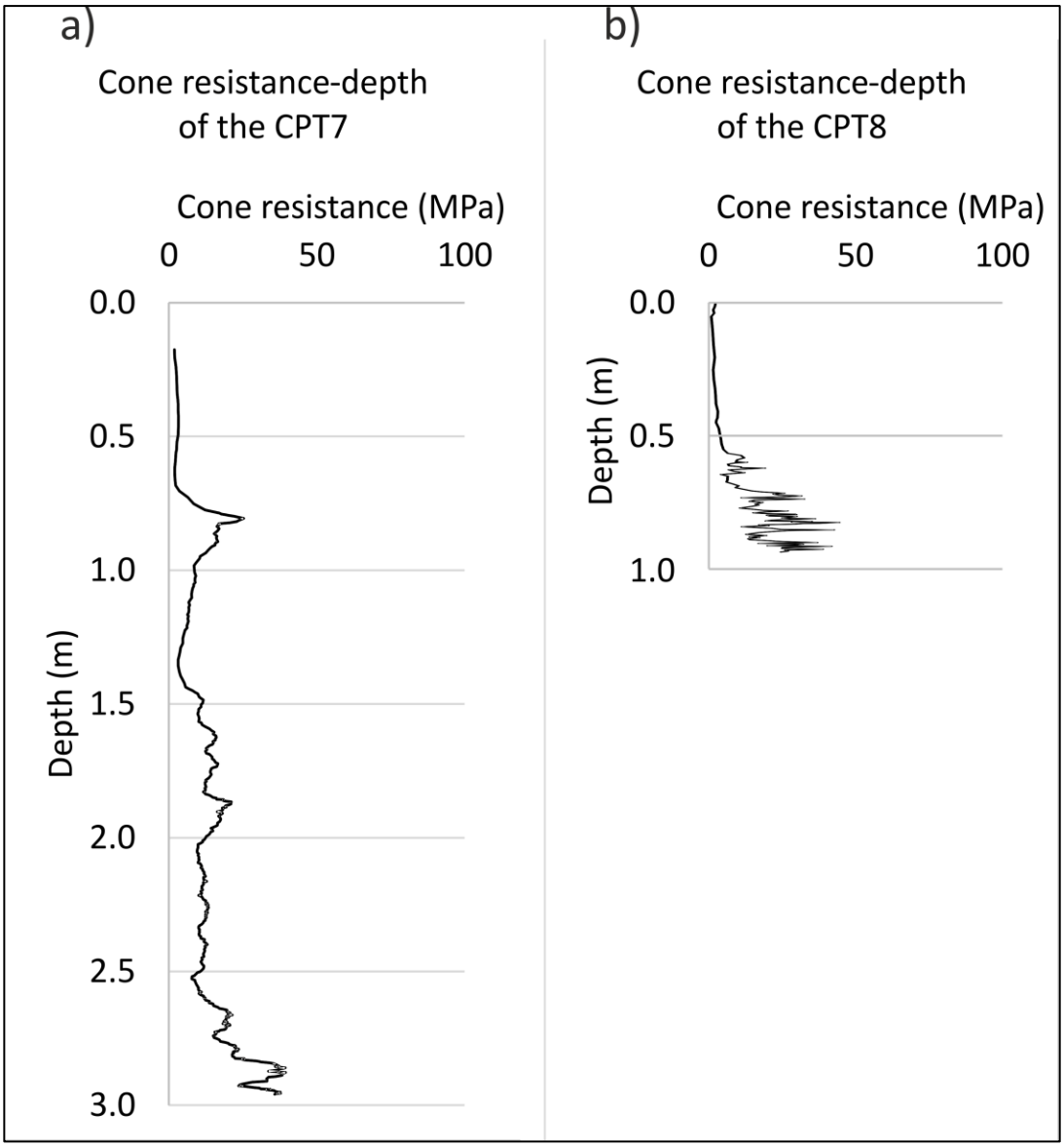

Figure 4-33: Cone resistance - depth profiles of CPT sounding 7 (see Figure 4-31 and Figure 4-32 for location) which penetrated to 3 m bgl and CPT sounding 8 which penetrate less than a metre.

To check that equations 4-1 and 4-2 give reasonable results and to constrain the obtained shear modulus from the Panda 2 data, the CPT's shear modulus was compared with results obtained from the active seismic surveys (MASW, see section 5.2). In this regard, the active seismic records which have had their shear wave velocity - depth profiles estimated at the same position as the CPT soundings (Figure 4-34) were inverted

individually to produce 1D shear wave velocity – depth profile and then shear modulus – depth profiles (Figure 4-35). After that, the shear moduli (the CPT's shear modulus and the MASW's shear modulus) values were then compared; they were found to have good agreement.

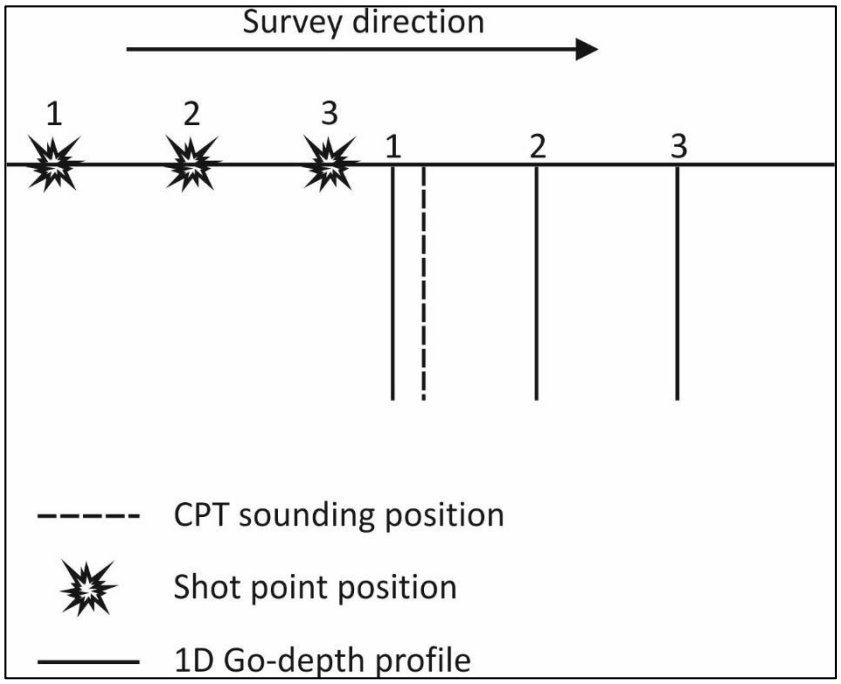

Figure 4-34: Schematic diagram showing the expected position of the Go-depth profile obtained from the active seismic surveys relatively to a CPT sounding position.

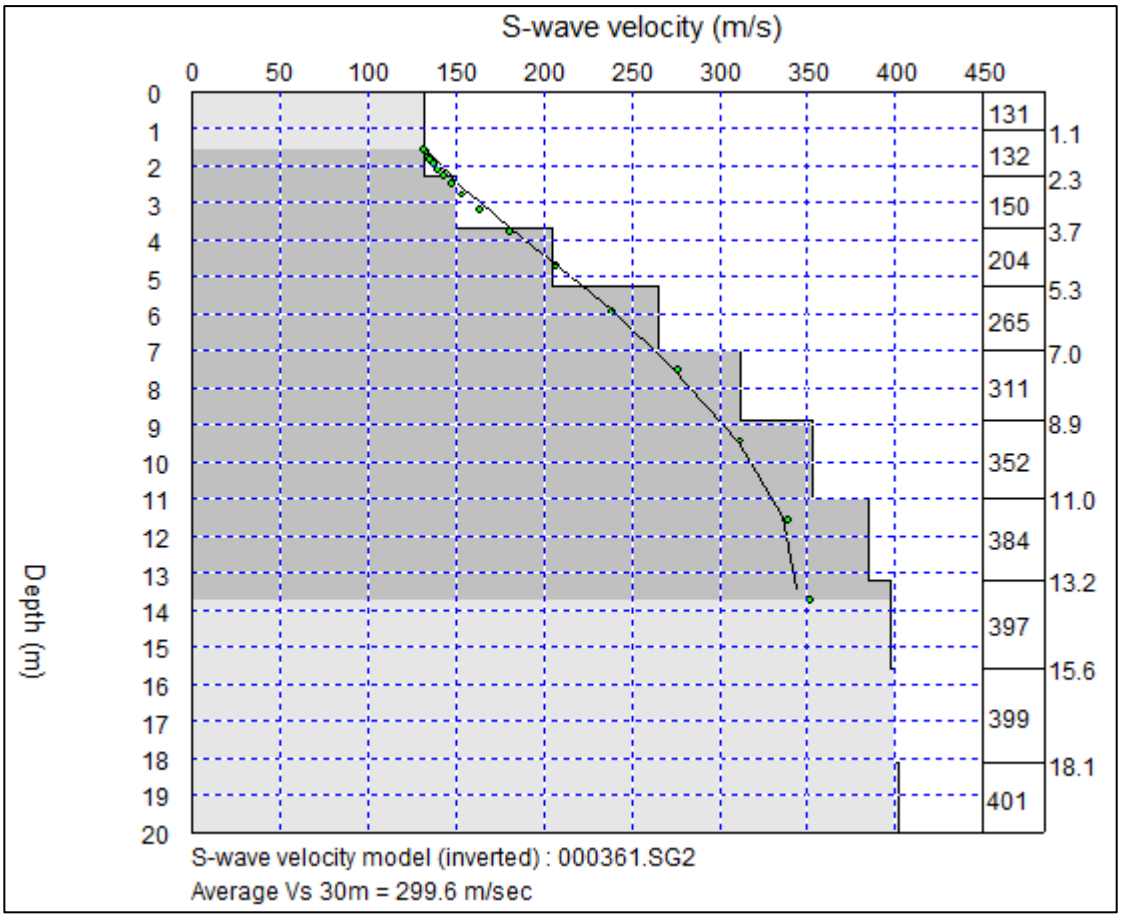

Figure 4-35: 1D shear wave velocity – depth profile of the MASW record located close to the CPT sound no.1 (see Figure 4-25 and Figure 4-26 for location).

From the CPT data, most evidenced different resistances at different depths (with gravel layers causing high values to be recorded) and, therefore, the site's deposits is evidenced to be heterogeneous, both spatially and vertically. In general, gravelly deposits have higher cone resistance compared to more clay-rich deposits.

For each CPT test, all 11 readings of the data set were averaged, and the cone resistance plotted with depth to generate a profile which can be utilized for determining the vertical stratigraphy variation at each sampling location. The cone resistance – depth profiles can then be used to generate a 2D cross section of the studied site, CPT soundings 5-9 were used here (Figure 4-36). See appendix E for all the cone resistance - depth profiles.

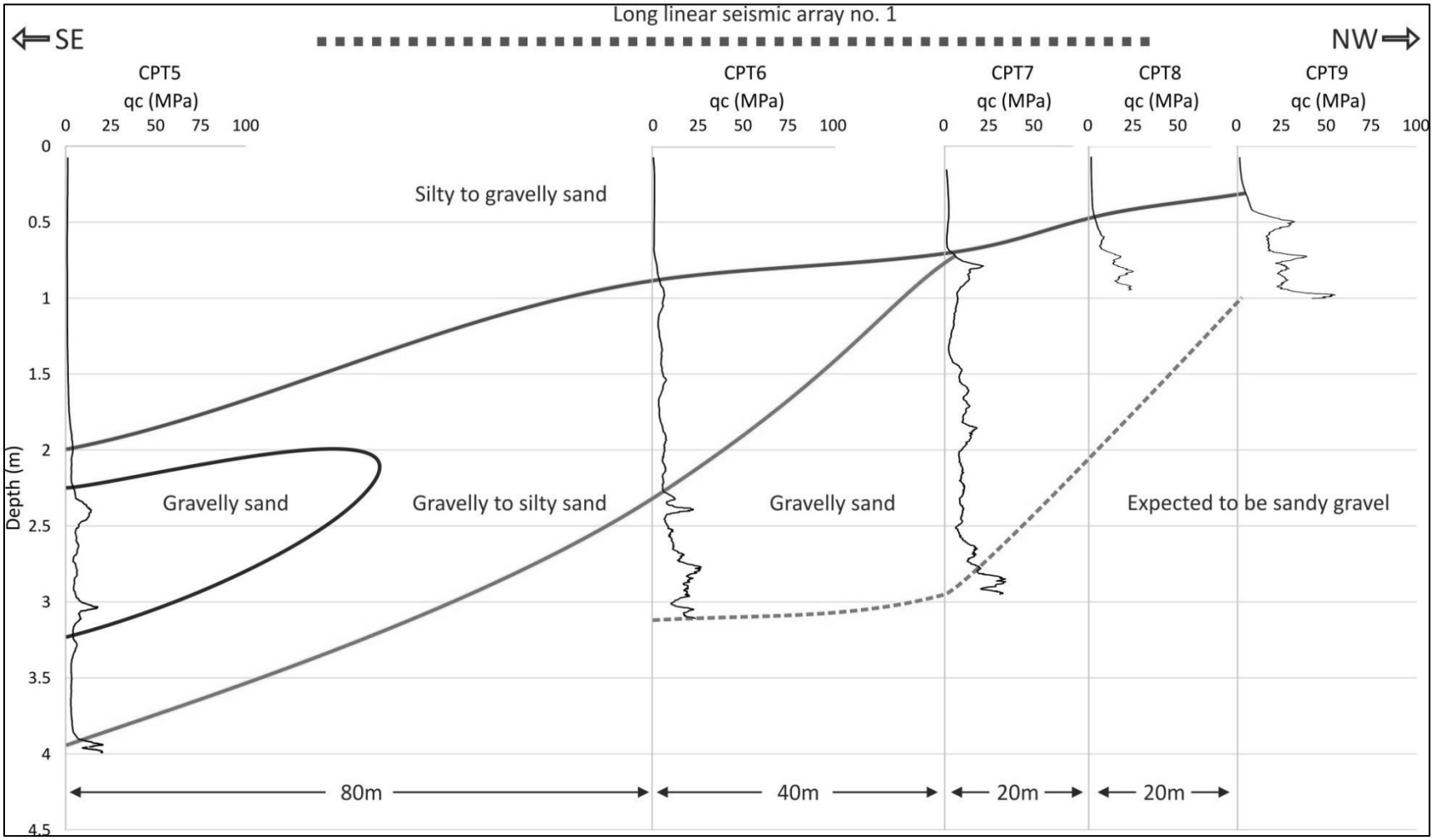

Figure 4-36: An underground expected model across the CPT soundings 5-9 with the position of the long linear seismic array no. 1 (see Figure 4-31, for location).

4.6 Microgravity surveys

To estimate the density of the geomaterials, the thickness variation of the deposits and to determine the deposits-bedrock interface topography, a microgravity survey was performed at the Rugeley site. Three microgravity survey profiles were conducted at the site; the location of the profiles is represented in Figure 4-37 and Figure 4-38.

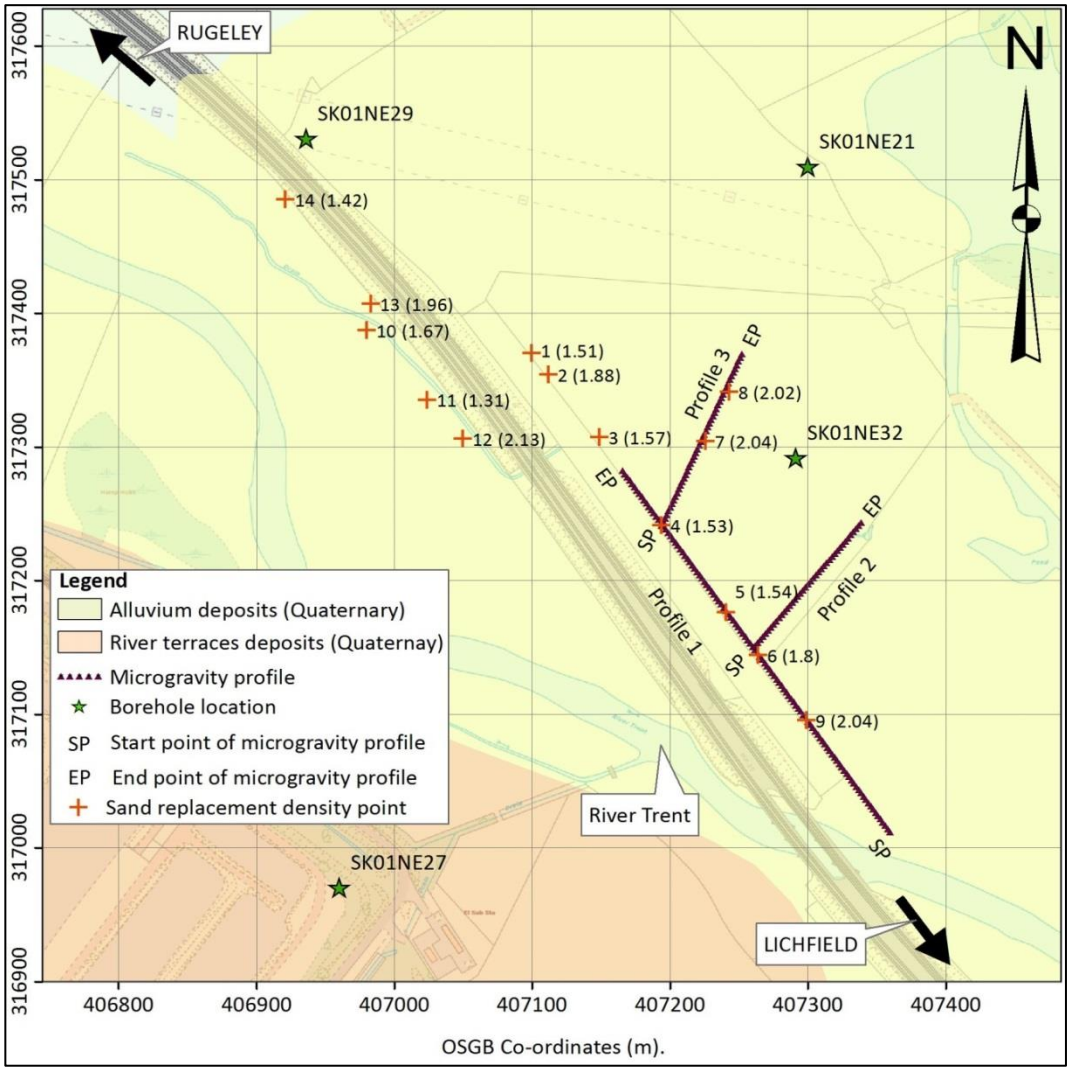

Figure 4-37: Microgravity survey profiles, sand replacement test locations and the obtained density values (values in parentheses) with superficial deposits underlain at the Rugeley. The four borehole positions (green stars) are also shown. Images supplied courtesy of Ordnance Survey/EDINA, 2016.

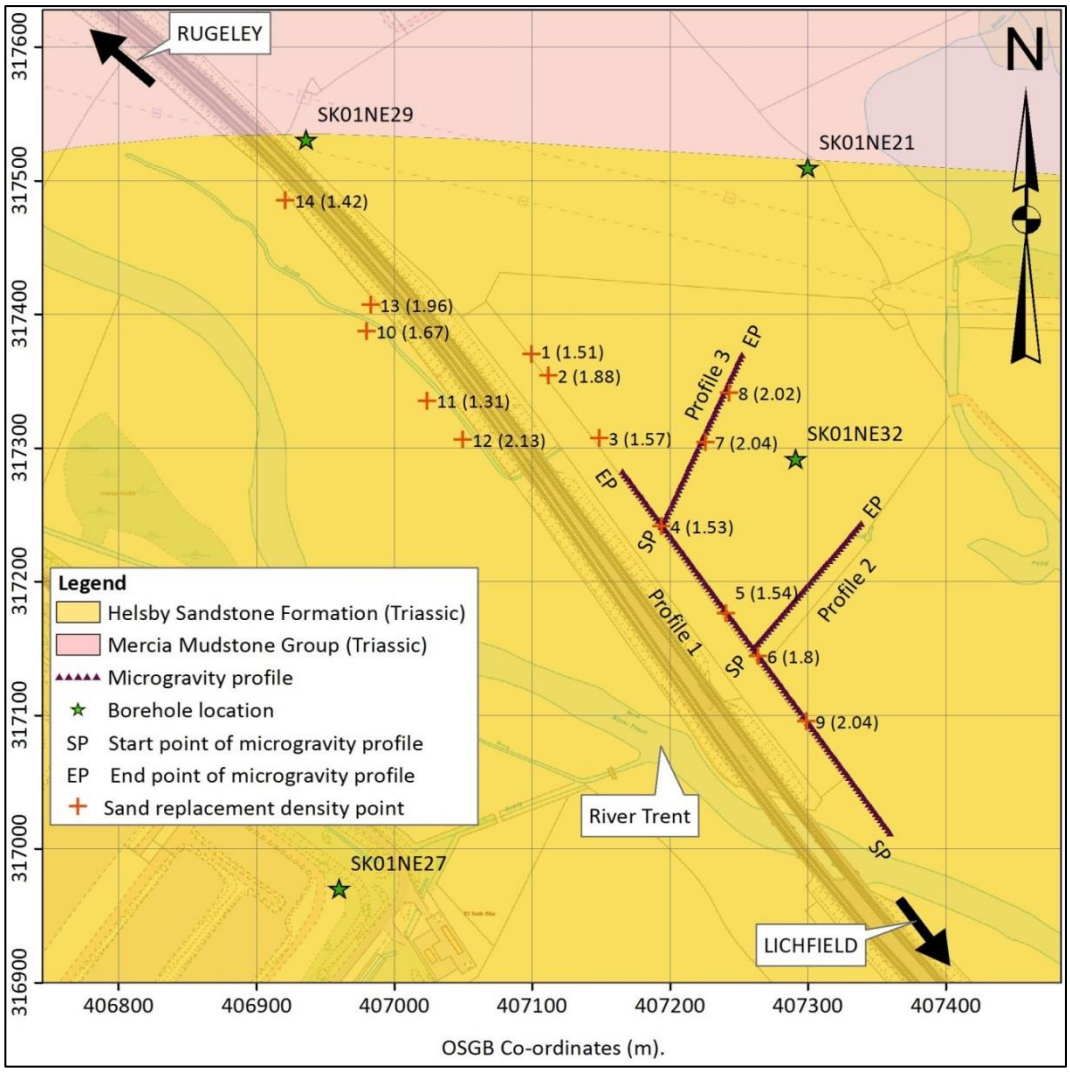

Figure 4-38: Microgravity survey profiles, sand replacement test locations and the obtained density values (values in parentheses) with bedrock underlain at the Rugeley site. The four borehole positions (green stars) are also shown. Images supplied courtesy of Ordnance Survey/EDINA, 2016.

The microgravity measurements need to be corrected to compensate for any increasing or decreasing in the gravitational field caused by background effects such as instrument drift, elevation and latitude variations, as detailed in the following points:

1- Elevation correction, the difference in elevation for the surveyed microgravity stations was found relatively to a local base station (a local base station was taken as a datum point). Then the elevation correction (for free air and Bouguer corrections) was

done following the standard procedure (for example, see, Reynolds, 2011) and as following:

Free air correction: this correction was done using the following equations:

$$\text{Free air correction} = 3.086\ h \text{ g.u.} \quad (4\text{-}3)$$

Where h is height.

Bouguer correction: this correction was done using the following equation:

$$\text{Bouguer correction} = \beta\rho h \text{ g.u.} \quad (4\text{-}4)$$

Where β is a constant (which is 0.4192 g.u. m2 Mg-1), ρ is material density and h is the height.

Then, the elevation correction was determined using the following equation:

$$\text{Elevation correction} = \text{free air correction} - \text{Bouguer correction} \quad (4\text{-}5)$$

The amount of the elevation correction was subtracted from the observed microgravity data.

2- Drift correction:

The drift correction was performed for the observed microgravity data to correct it for the drift of the instrument following the standard corrections and as following:

Repeated microgravity readings were taken at a base station during the survey period. The data observed at the base station was used to determine the drift rate. The drift rate was determined for each reading using the following equation:

$$\text{Drift rate} = \frac{R2-R1}{T2-T1} \quad (4\text{-}6)$$

Where R2 and R1 are reading 2 and reading 1 recorded at time 2 (T2) and time 1 (T1), respectively.

The drift rate was in a range from – 28.8 g.u. to 25.8 g.u.. The drift of the microgravity readings at the base station was used to plot the drift curve (Figure 4-39). The drift correction then performed for all the microgravity readings by subtracting the drift amount from the microgravity reading using the drift curve.

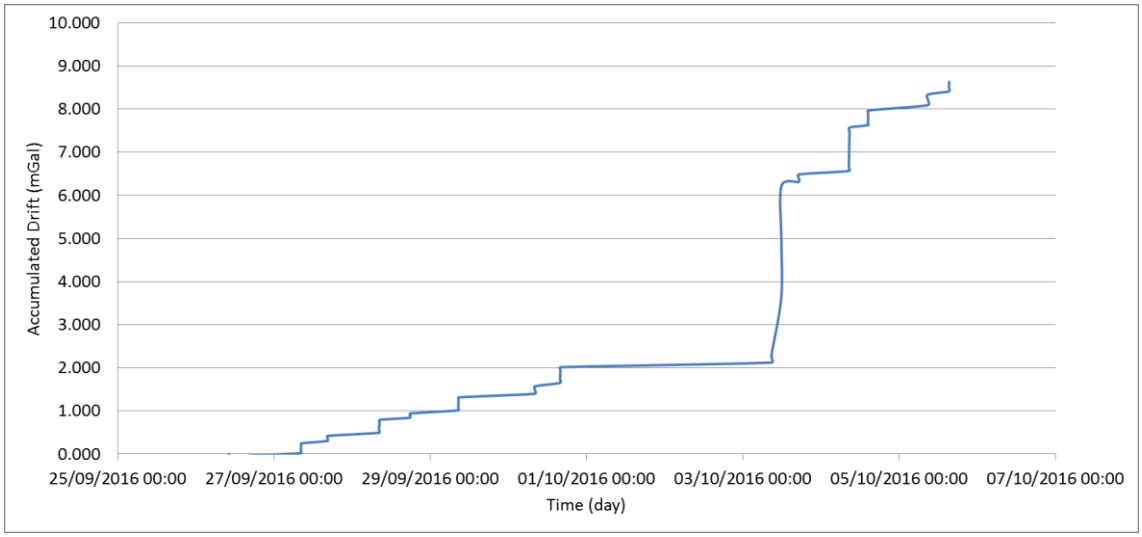

Figure 4-39: An instrument drift curve generated from the repeated microgravity readings at a base station.

The collected data was corrected by subtracting the calculated corrections values from the observed value, by this process, the observed microgravity readings will be reduced to Bouguer anomaly. For Bouguer correction, subsurface density was assumed to be 2.5 g/cm^3. After that, the Bouguer anomaly values were imported into Grav2dc, a free software package dedicated for subsurface numerical modelling using microgravity data.

This package works by presenting the corrected microgravity data and the calculated data as two curves and by finding the best match between these two datasets. In addition, to representing the datasets, the package allows creating subsurface anomalies (positive or negative microgravity anomalies) with certain parameters (shape, size, depth and gravity contrast with the hosting background). The relationship between the observed and the calculated microgravity curves can be changed interactively with any change in one or more of the subsurface anomaly parameters. Based on the best match between the observed and calculated datasets (taking in consideration the non-uniqueness of the microgravity method), an expected model of the studied site can be generated.

The microgravity models from the collected datasets are presented in Figure 4-40, Figure 4-41 and Figure 4-42. The absolute density of the site's deposits, from the microgravity survey, is 1.81 gm/cc and it was found comparable with the average of the deposits' density obtained from sand replacement test (i.e. the average of the sand replacement density is 1.74 gm/cc), (Table 4-4).

Table 4-4: Absolute density of the Rugeley site deposits and bedrock obtained from the microgravity survey.

Profile	Deposits density (gm/cc)	Helsby Sandstone Formation density (gm/cc)	Chester Sandstone Formation density (gm/cc)
Profile 1	1.81	2.02	2.15
Profile 2	1.82	2.06	2.15
Profile 3	1.80	2.05	2.15
Average	1.81	2.04	2.15

The microgravity profile one (Figure 4-40) shows that the deposits' thickness at the SE of the studied site (the SE end of the profile which is close to the River Trent) is much thicker than that at the NW end of the profile. This was interpreted by deepening of the river Trent valley during the last glaciation due to meltwater action. The over-deepened river valley was subsequently backfilled with glacial outwash sediments and then overlaid with post-glacial recent river terrace and alluvium from the River Trent.

The profiles 2 and 3 (see Figure 4-41 and Figure 4-42) represent an inclined deposits-bedrock interface mainly to the SW and the deposits thickness gets thinner towards the NE of the site (away from the over-deepened river valley). More survey profile(s) cross the railway embankment and the river Trent, longer profiles and higher data resolution could also help to image the expected over-deepened channel and to identify the underlying structure of the studied site.

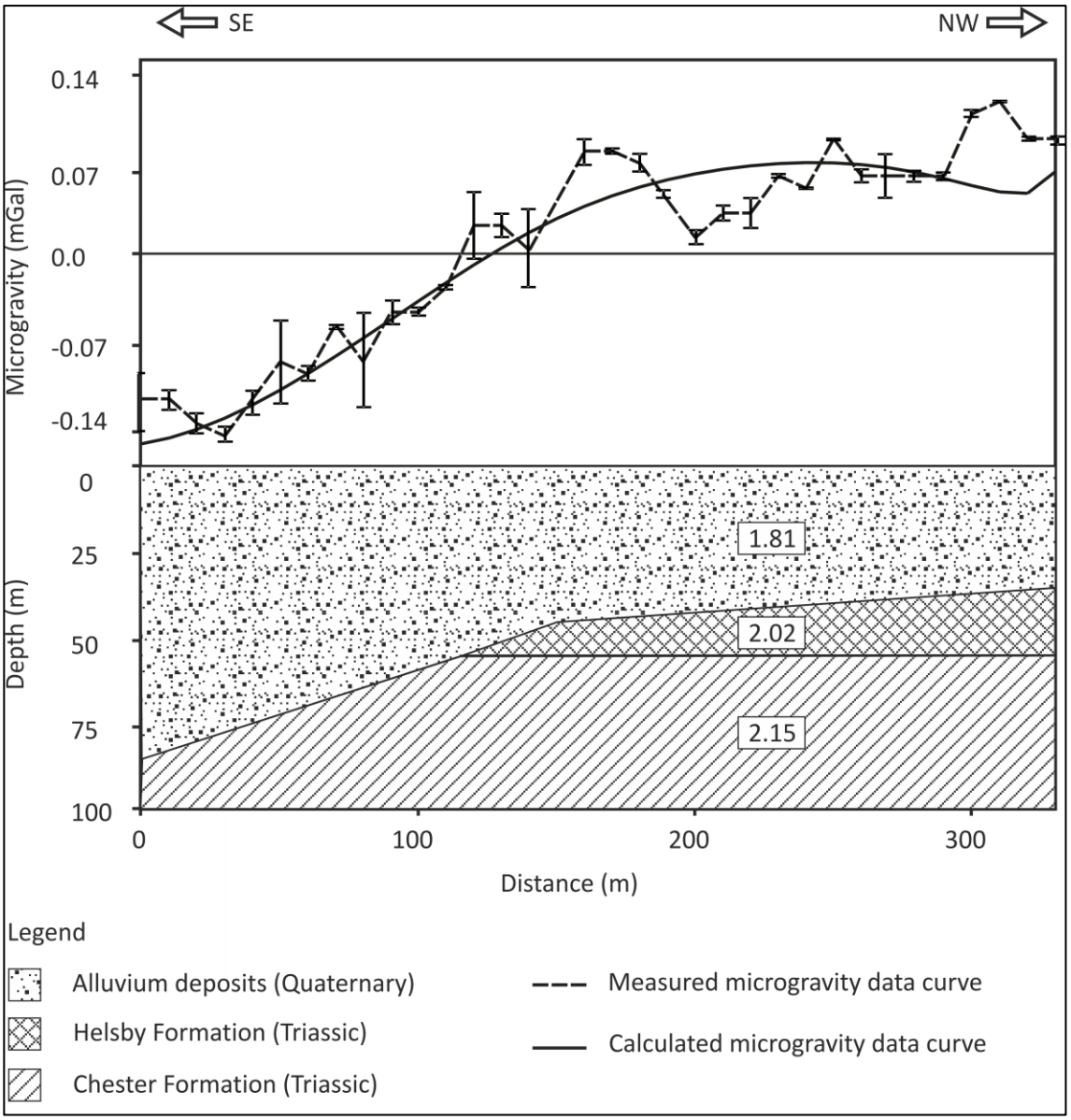

Figure 4-40: The microgravity model obtained from the survey profile one (conducted along the railway embankment, see Figure 4-37 and Figure 4-38 for location), showing the collected data, error bars of the collected data, the interpreted data, the underground geology underneath the profile and the over-deepened river valley. The misfit between the model data and the actual data = 0.29 mGal.

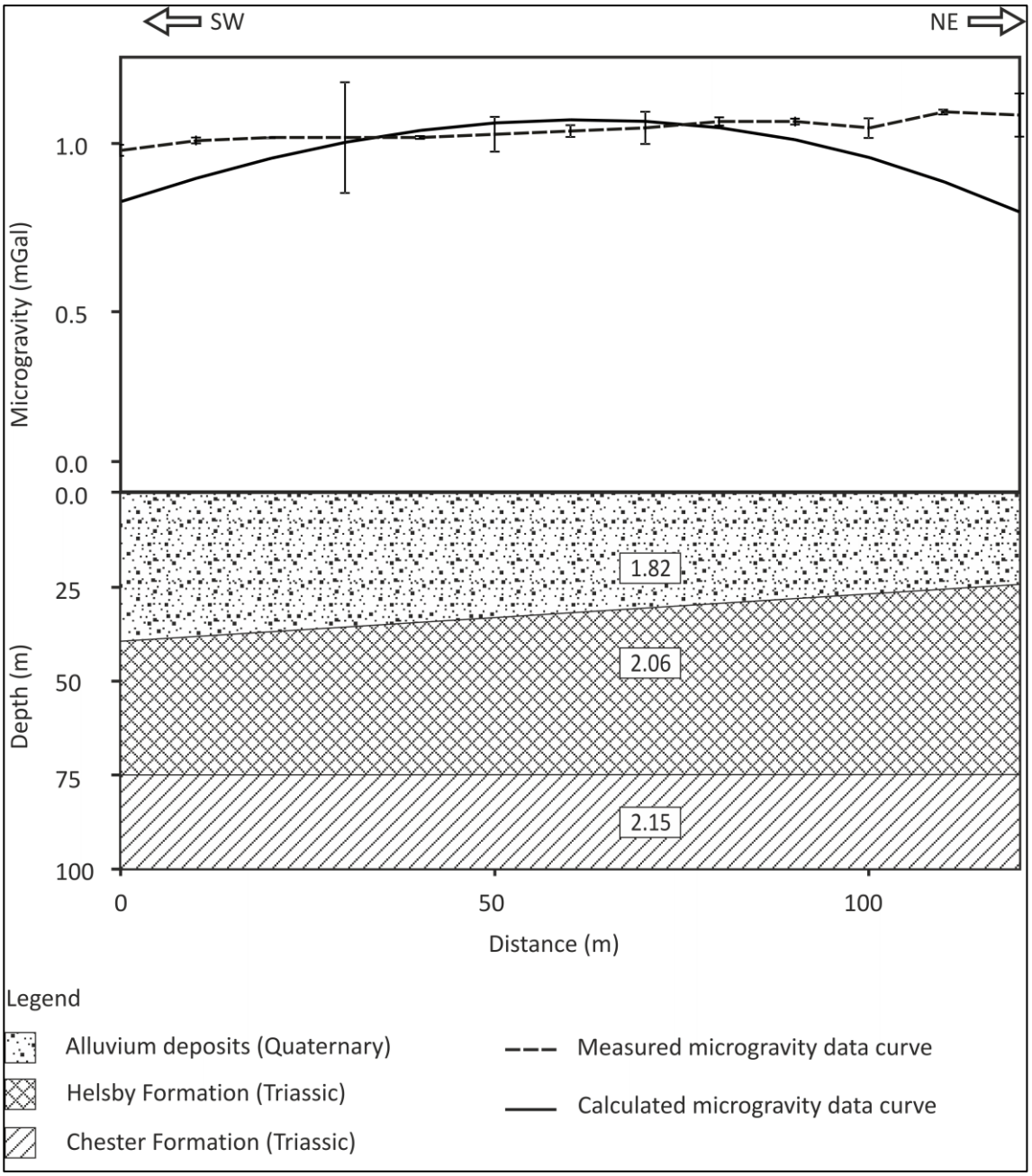

Figure 4-41: The microgravity model obtained from the survey profile two (see Figure 4-37 and Figure 4-38 for location), showing the collected data, error bars of the collected data, the interpreted data and the underground geology underneath the survey profile. The misfit between the model data and the actual data = 1.24 mGal.

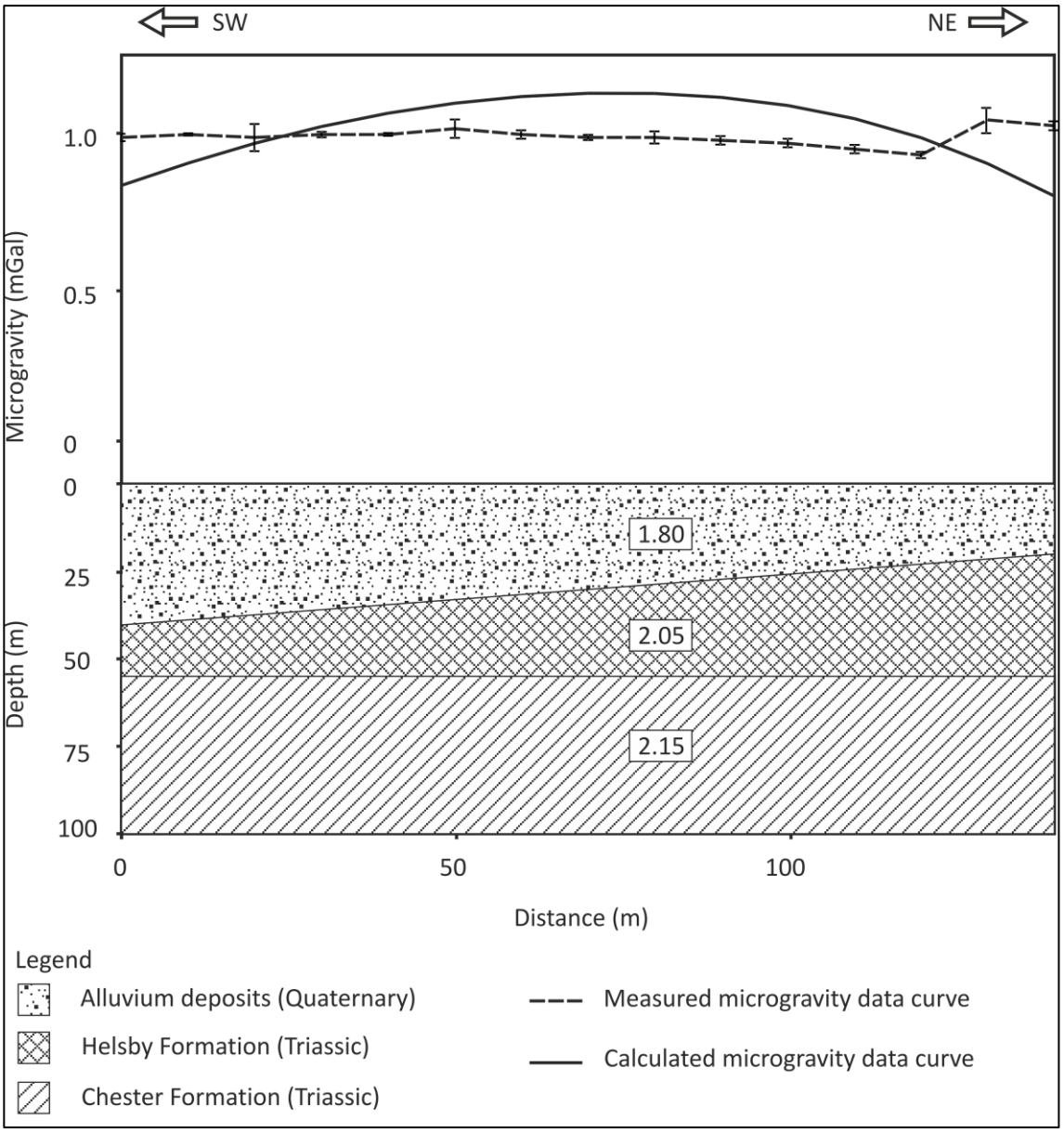

Figure 4-42: The microgravity model obtained from the survey profile three (see Figure 4-37 and Figure 4-38), showing the collected data, error bars of the collected data, the interpreted data and the underground geology underneath the survey profile. The misfit between the model data and the actual data = 1.28 mGal.

4.7 Sand replacement density test

The sand replacement density test was performed for 14 points at the Rugeley site. The test was undertaken to determine the deposits density at different locations around the site. The location of the tested points and the obtained density values are represented in Figure 4-37, Figure 4-38 and Table 4-5. The minimum and the maximum density values were found to be 1.31 gm/cc and 2.13 gm/cc, respectively. The average of the sand replacement density test was found 1.74 gm/cc which is comparable with deposits' density from the microgravity surveys (see Table 4-4 and Table 4-5).

Table 4-5: Density values obtained from the sand replacement density test (see Figure 4-37 and Figure 4-38 for location), with the standard deviation in parentheses.

Point	Density value (gm/cc)
1	1.51
2	1.88
3	1.57
4	1.53
5	1.54
6	1.8
7	2.04
8	2.02
9	2.04
10	1.67
11	1.31
12	2.13
13	1.96
14	1.42
Average	1.74 (SD= 0.3)

The obtained density values from the test represent the wide range of the possible deposits' densities on the ground surface.

4.8 Correlation between geophysical and the conventional datasets

4.8.1 Qualitative correlation

The electrical resistivity (ERT) and seismic MASW datasets of the same subsurface section can be qualitatively correlated. This correlation can give confidence in data interpretation and might highlight key points for shear modulus estimation in 2D cross sections of the resistivity and the MASW datasets.

The resistivity model agreed well with the MASW cross section, the bedrock topography and the top of the deposits were mapped on the cross section from both the surveys cross sections (Figure 4-43). Both show the Helsby Sandstone Formation bedrock at the NW end of respective survey profiles, as a high resistivity anomaly on the ERT and having high seismic wave velocities on the MASW datasets, respectively (Figure 4-43).

On Figure 4-43, in the SE part of the study profile, the ERT images high resistivity anomalies which appear as low seismic wave velocities on the MASW results. On the same figure, another high resistivity patch within the deposits at 96 – 144 m on the resistivity profile, appeared as relatively low wave velocity on the MASW results. The deposits are represented in a way unlike that with the bedrock (Figure 4-43). The differences between the drift soil deposits and the bedrock needed to be interpreted carefully, with other important variables that may be affecting results including moisture content, 'soil' type and density (see Samouelian et al., 2005). The MASW cross section shows more details about the subsurface at the north-west and the south-east ends of the study profile and shows a relatively deeper soil deposits – bedrock interface, particularly at the SE end.

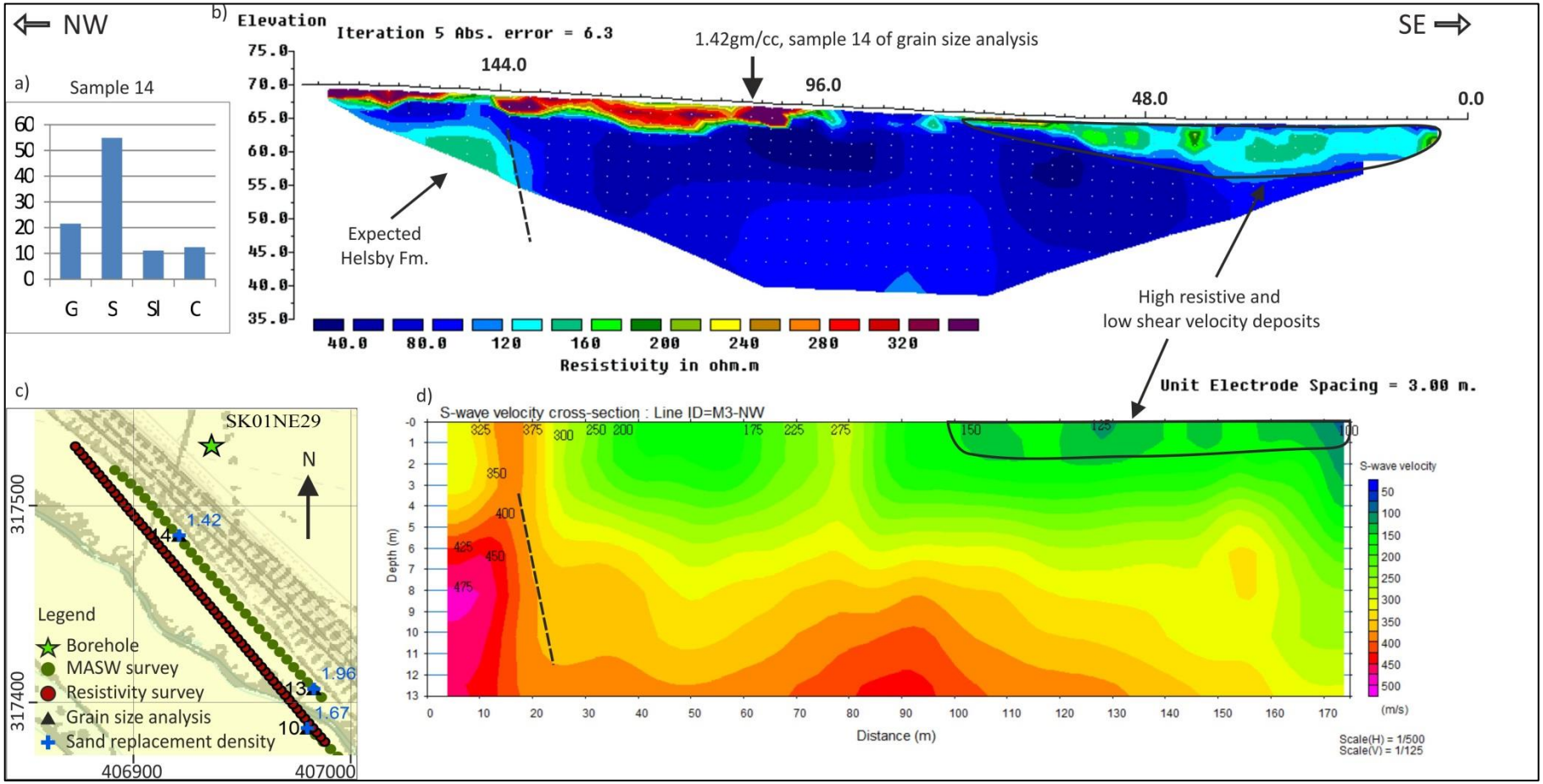

Figure 4-43: a) grain size analysis of sample 14, b) 2D resistivity model of the profile 5-c, c) location map (inset) shows a, b and c respective site locations and d) MASW 2D cross section.

4.8.2 Quantitative correlation

To correlate the datasets quantitatively, the datasets have to be prepared first, for example, combine the CPT's shear modulus with MASW's shear modulus.

4.8.2.1 Full profile of shear modulus

The active seismic surveys and the CPT sounding datasets were used to determine the material shear modulus and to create a full shear modulus - depth profile; from the ground surface down to 15 m bgl. The active seismic survey (MASW) of the M4-NW profile and the CPT sounding no. 6 were employed to create a full shear modulus-depth profile. The CPT sounding can investigate from the ground surface down to 3 m bgl, whilst the active seismic surveys typically resolve from 3 m to 15m bgl (Figure 4-44).

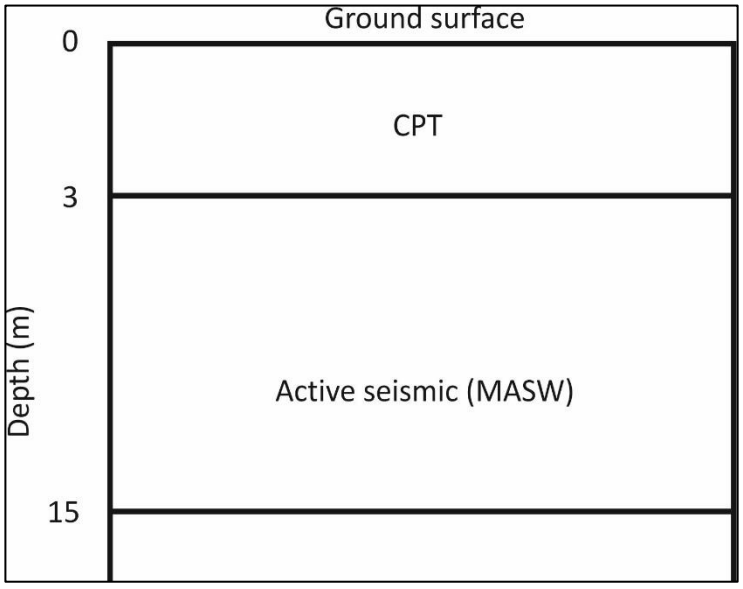

Figure 4-44: Schematic diagram shows how to produce 1D shear modulus – depth by combining both the seismic surveys with CPT sounding datasets.

The active seismic records no.23 and no.24 are close to the centre of the resistivity profile no.8 (see Figure 4-45); these were then processed individually to generate 1D shear wave

velocity-depth profiles (Figure 4-46 and Figure 4-47). Then, the average of the obtained shear wave velocity of the processed records was utilized to generate the full shear modulus – depth and shear wave velocity - depth profiles.

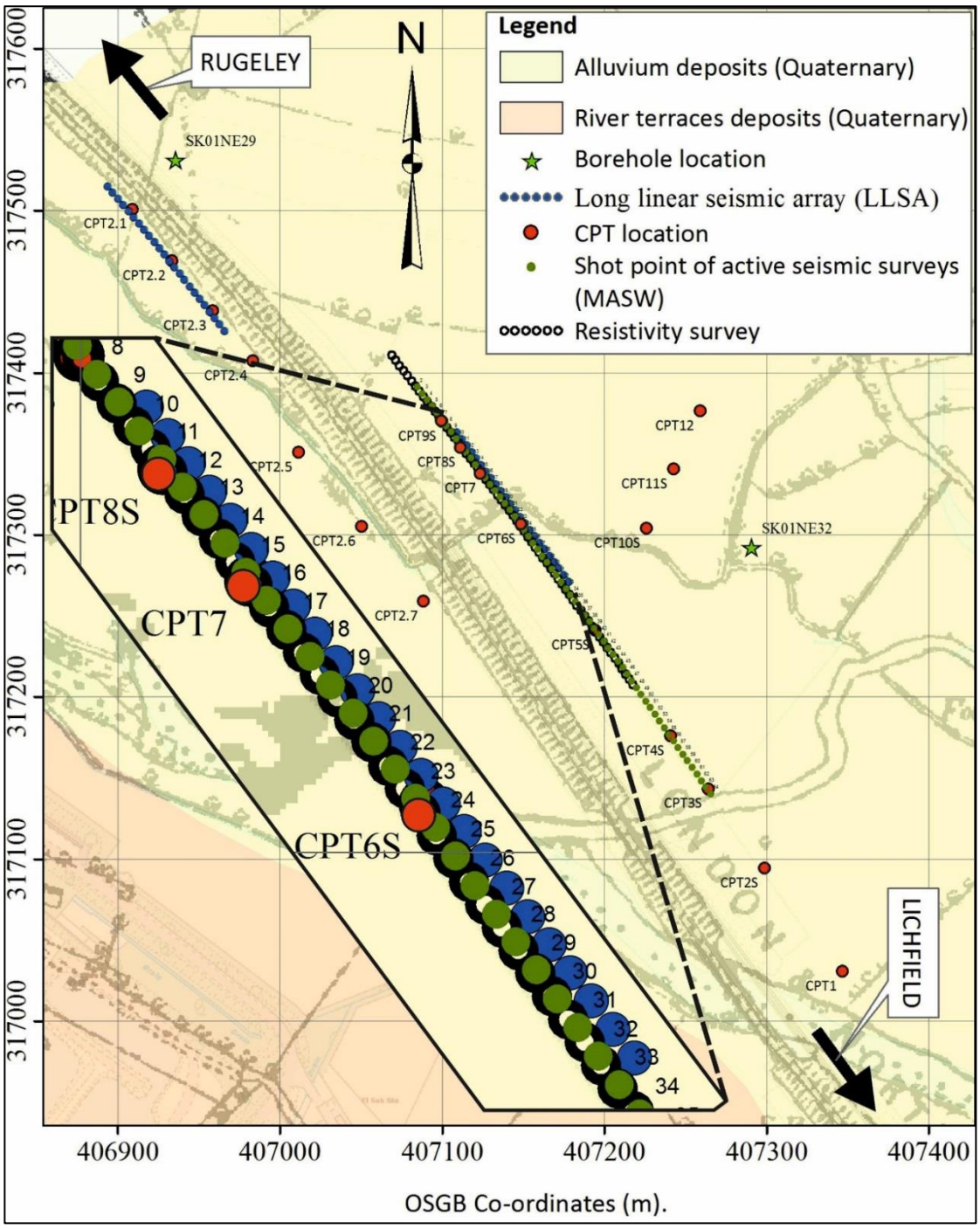

Figure 4-45: The position of the active seismic records that combined with passive seismic survey data to generate the full shear modulus – depth profiles.

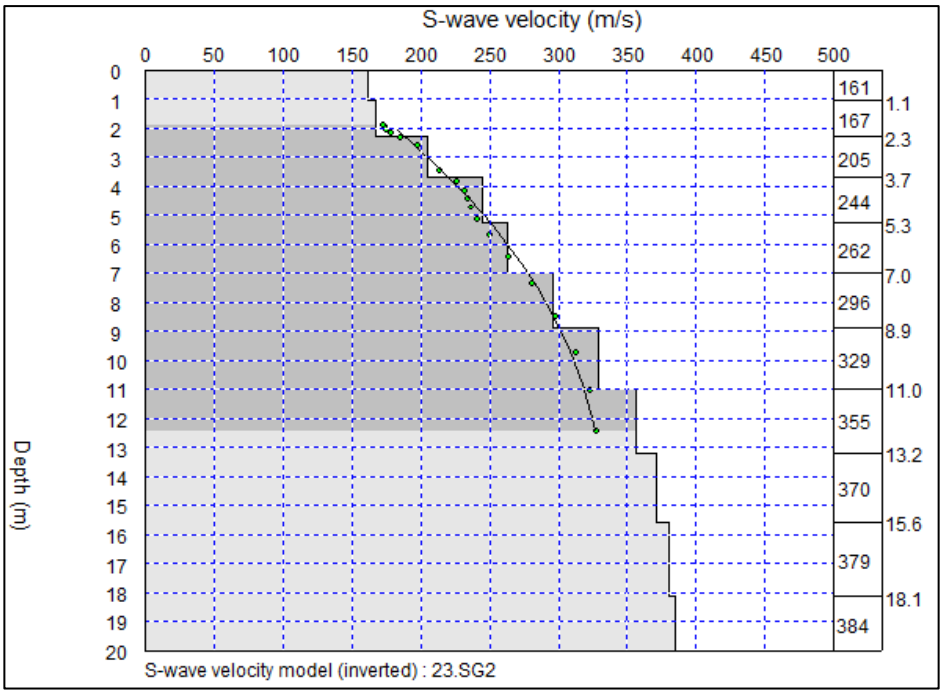

Figure 4-46: 1D shear wave velocity - depth profile of record 23, for shot point location see Figure 4-45.

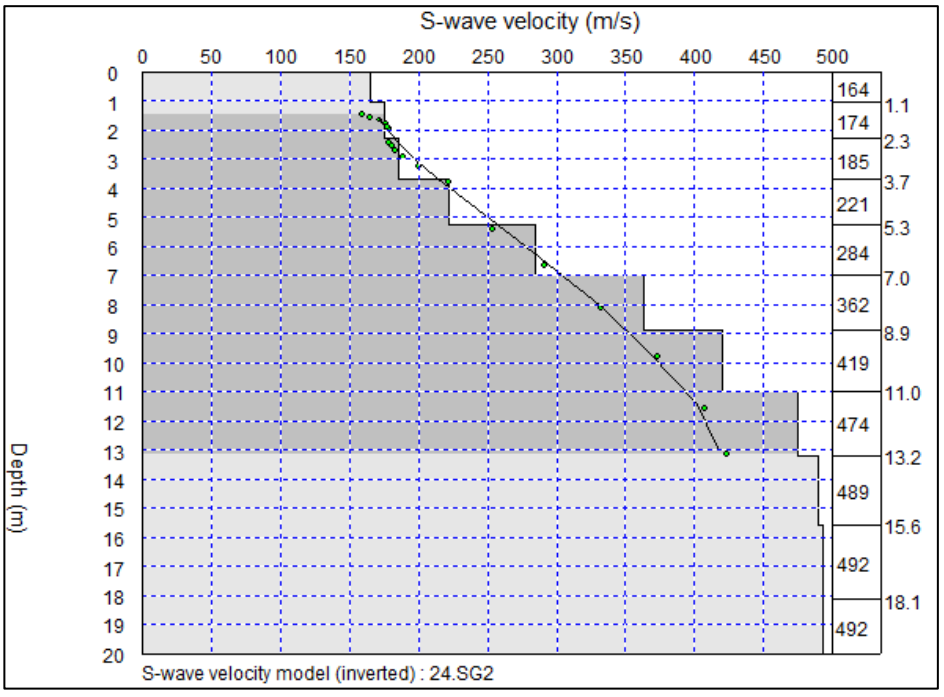

Figure 4-47: 1D shear wave velocity - depth profile of record 24, for shot point location see Figure 4-45.

4.8.2.2 Creating the datasets in a unified data increment

The results from all the surveys (i.e. active seismic, CPT, electrical resistivity and density), which are presented in Table 4-6 are used to find out any possible correlation among these different datasets (i.e. the physical and the geotechnical parameters). These surveys have different resolutions (i.e. readings were measured at different depth intervals), therefore, the datasets were interpolated to prepare it at 1 m increment.

The resistivity data in Table 4-6 was extracted from the inverted resistivity data of profile 8 (Figure 4-23). The depth to each investigated resistivity level (i.e. electrode spacing) was determined using the following equation:

$$depth = Resistivity\ level \times geometric\ factor \times electrode\ spacing \qquad (4-7)$$

Then, the resistivity values for depths located in between the investigated resistivity levels were obtained by averaging the collected resistivity readings.

The density of the materials at the ground surface was obtained from the sand replacement test (see section 5.6). For deeper depths, the SeisImager/SW (of the active seismic datasets) generates a text file that includes the material's density, which is used in the quantitative correlation and interpolated in 1 m increments (Table 4-6).

In addition, the CPT's shear modulus was used to generate the shear wave velocity – depth for the material from the ground surface down to 3 m using the following equation:

$$Go = Vs^2 \times density \qquad (4-8)$$

Where *Go* is shear modulus and V_s is shear wave velocity.

Table 4-6: Shear modulus, material density, shear wave velocity and resistivity readings with depth from the Rugeley site; obtained from seismic, resistivity, CPT and sand replacement density investigations.

Depth (m)	*Go* (Mpa)	Density (gm/cc)	Shear wave velocity (m/sec)	Resistivity (Ohm.m)
1	14.33	1.74	90.75	98.41
2	23.70	1.77	115.39	98.41
3	41.46	1.79	151.77	99.22
4	98.79	1.81	233.44	100.04
5	98.79	1.81	233.44	101.16
6	136.82	1.82	273.79	102.29
7	136.82	1.82	273.79	107.49
8	201.90	1.84	329.47	112.68
9	201.90	1.84	329.47	105.50
10	263.89	1.85	374.50	98.32
11	263.89	1.85	374.50	83.17
12	328.17	1.86	415.09	68.02
13	328.17	1.86	415.09	65.44
14	352.23	1.86	430.11	62.87
15	352.23	1.86	430.11	62.83

Now, the obtained data can be correlated to each other and represented graphically, as follow:

4.8.2.3 Shear modulus – depth relationship

The shear modulus – depth correlation is presented in Figure 4-48 and has a linear relationship such that the shear modulus increases linearly with depth. The increase in shear modulus with depth can be interpreted as being due to increasing material density with depth (Figure 4-49). Material at specific depths can be exposed to higher compaction due to the load of the overlying material, evidenced by increasing shear wave velocity on the 1D shear wave velocity profiles (Figure 4-46 and Figure 4-47) and the 2D cross

sections (Figure 4-29). The following empirical relationship was obtained for shear modulus – depth correlation:

$$Go = 26.793\, d - 24.8 \qquad (4-9)$$

Go is the shear modulus and *d* is depth.

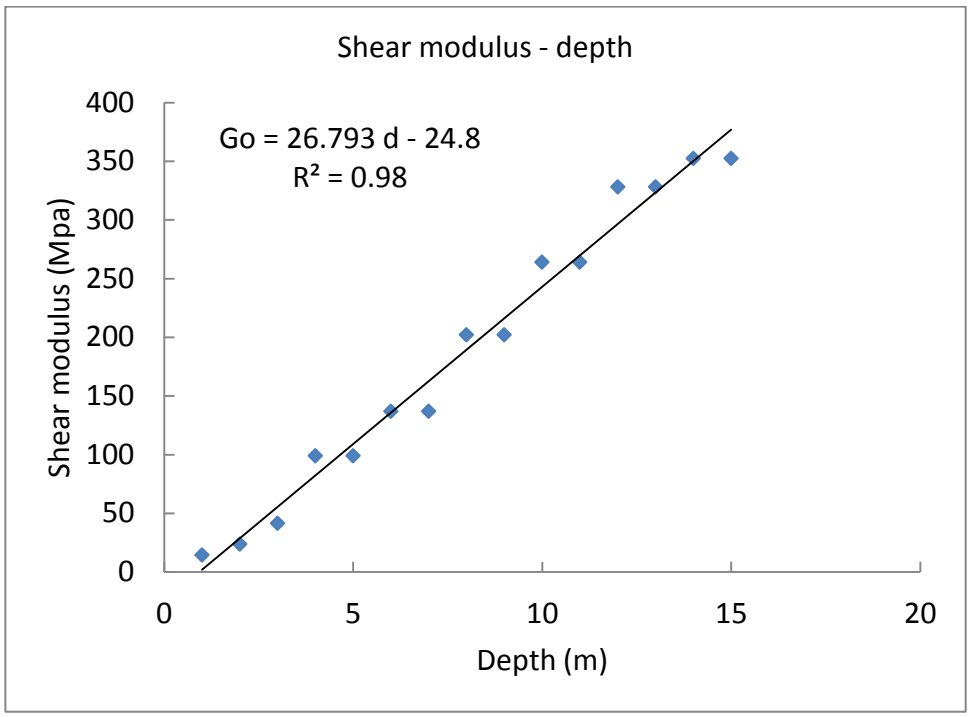

Figure 4-48: Shear modulus – depth correlation, the shear modulus was extracted from the CPT and MASW datasets.

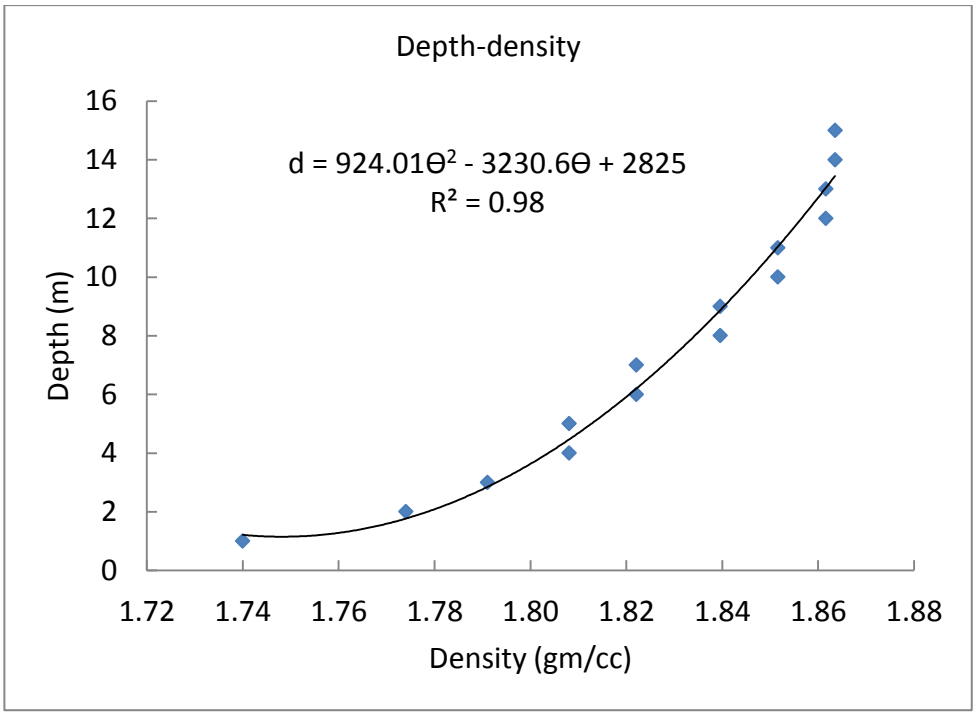

Figure 4-49: Depth - material's density relationship. Density was extracted from the sand replacement test and the active seismic (MASW) survey.

4.8.2.4 Shear modulus – density relationship

Figure 4-50 shows the exponential relationship between shear modulus and material density. The mathematical equation of the relation is:

$$Go = 28263\theta^2 - 99226\theta + 87102 \qquad (4-10)$$

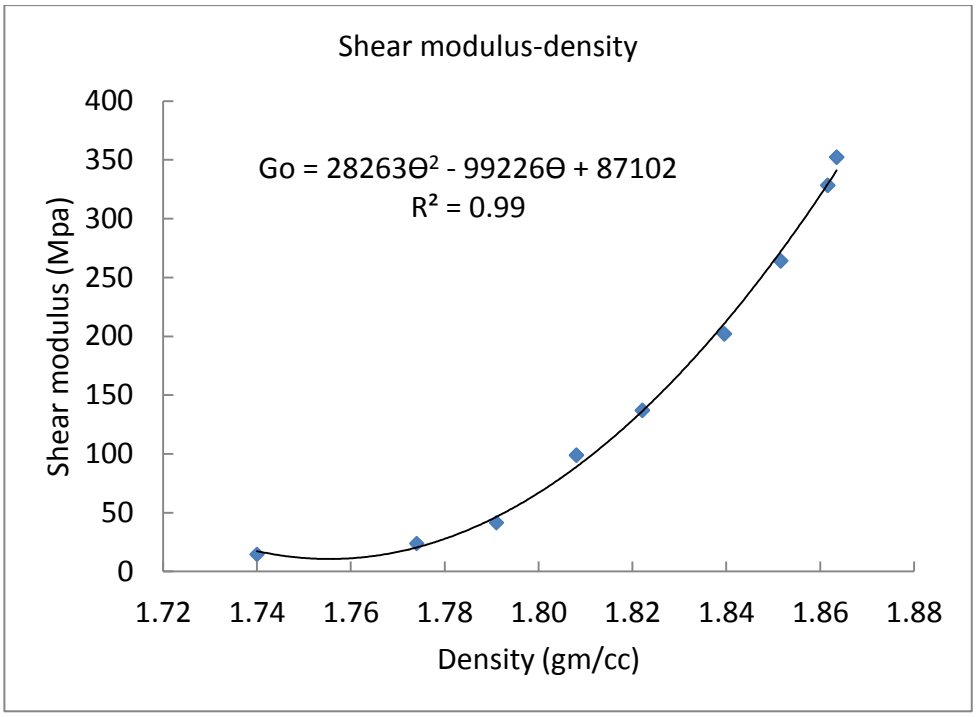

Figure 4-50: Shear modulus - density relationship from the Rugeley site. Shear modulus has been obtained from the CPT and the active seismic surveys.

4.8.2.5 Material density - resistivity and depth – resistivity relationships

Another relationship can be obtained from the material density and resistivity datasets (Figure 4-51). The figure shows two different linear relationships and that interpreted due to site conditions, for example, water content and material type effects on the obtained results.

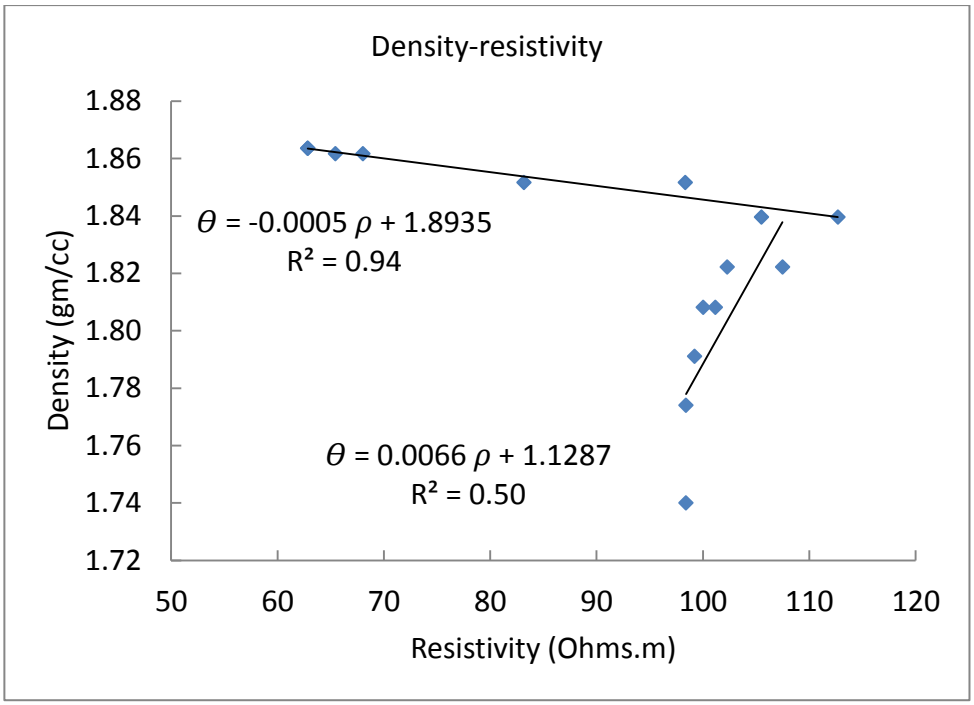

Figure 4-51: Density - resistivity correlation from the Rugeley site. Density data was obtained from the sand replacement test and the active seismic surveys.

Figure 4-52 shows the relationship between investigated depth and resistivity. The slight increasing in resistivity readings from close to the ground surface to about 7 m depth can be interpreted due to the existence of the unsaturated gravel-rich layer which produce high resistivity readings compared with material below it. The low resistivity readings between 7 – 15 m depth are obtained, very likely, due to saturation conditions (i.e. below the regional groundwater table) and less to its higher density.

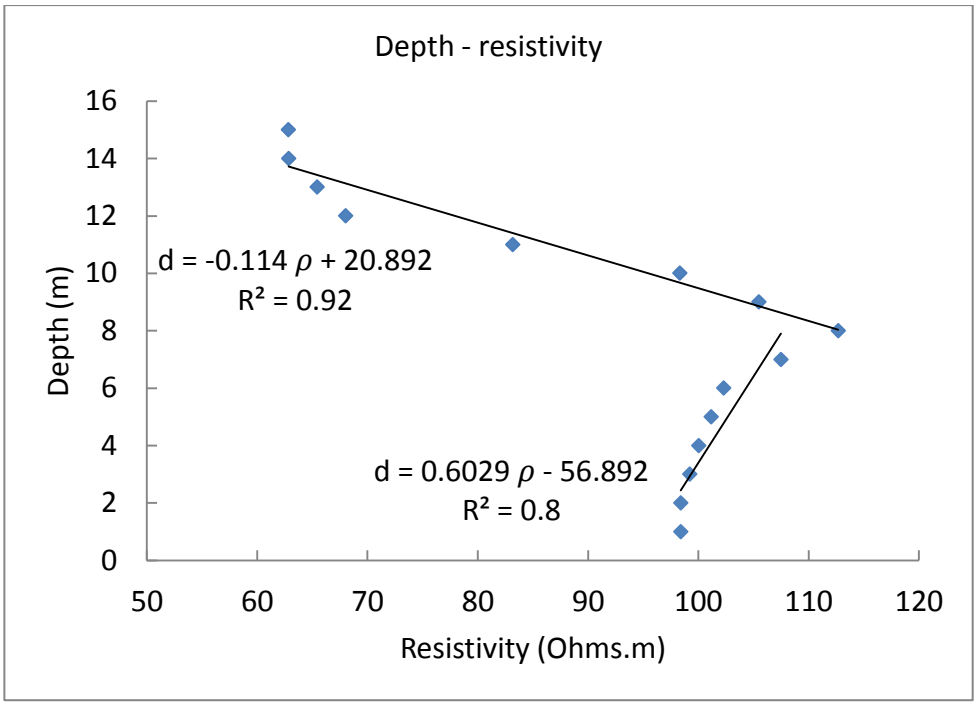

Figure 4-52: Resistivity – depth correlation from the Rugeley site.

4.8.2.6 Shear wave velocity – resistivity relationship

In a trial to demonstrate a quantitative correlation between the shear wave velocity and the resistivity datasets of the investigated site, Figure 4-53 shows two different relationships between the wave velocity and resistivity datasets. Site conditions, the existence of the gravel-rich layer and saturation conditions, have important roles on the resistivity surveys for geotechnical site investigation. The correlation supported by the findings from the qualitative correlation.

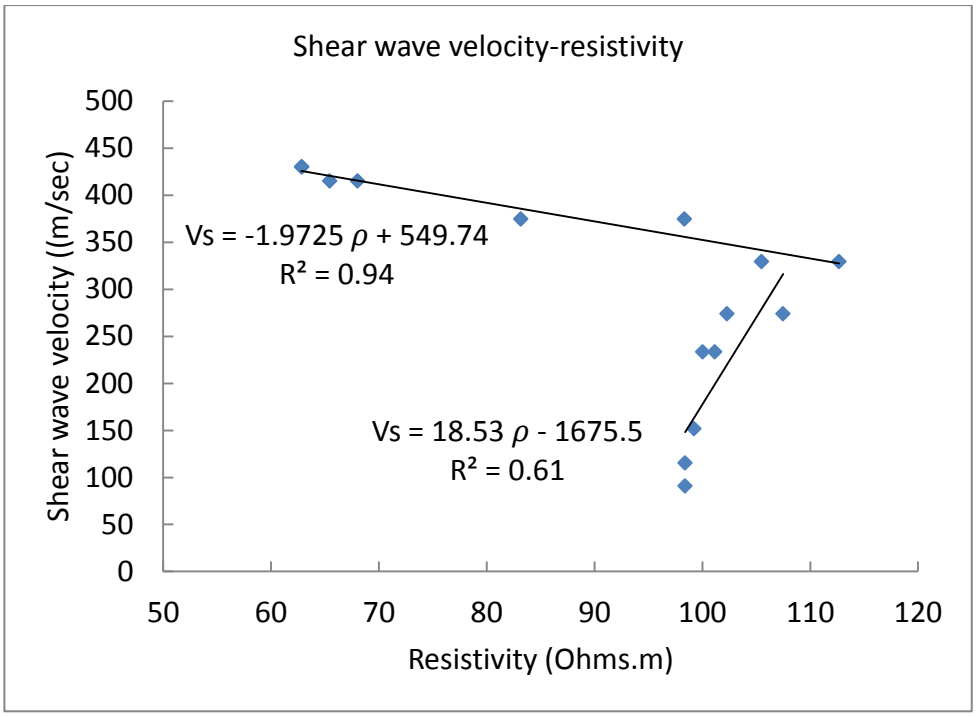

Figure 4-53: Shear wave velocity - resistivity linear relationship from the Rugeley site. Shear wave velocity was obtained from the CPT sounding and the active seismic surveys.

4.8.2.7 Shear modulus – resistivity relationship

The correlation between shear modulus and resistivity datasets appears to be quite similar to the wave velocity – resistivity relation (Figure 4-54). The shear modulus is directly related to shear wave velocity; ultimately the shear modulus can be related to electrical resistivity, almost, in a similar relation.

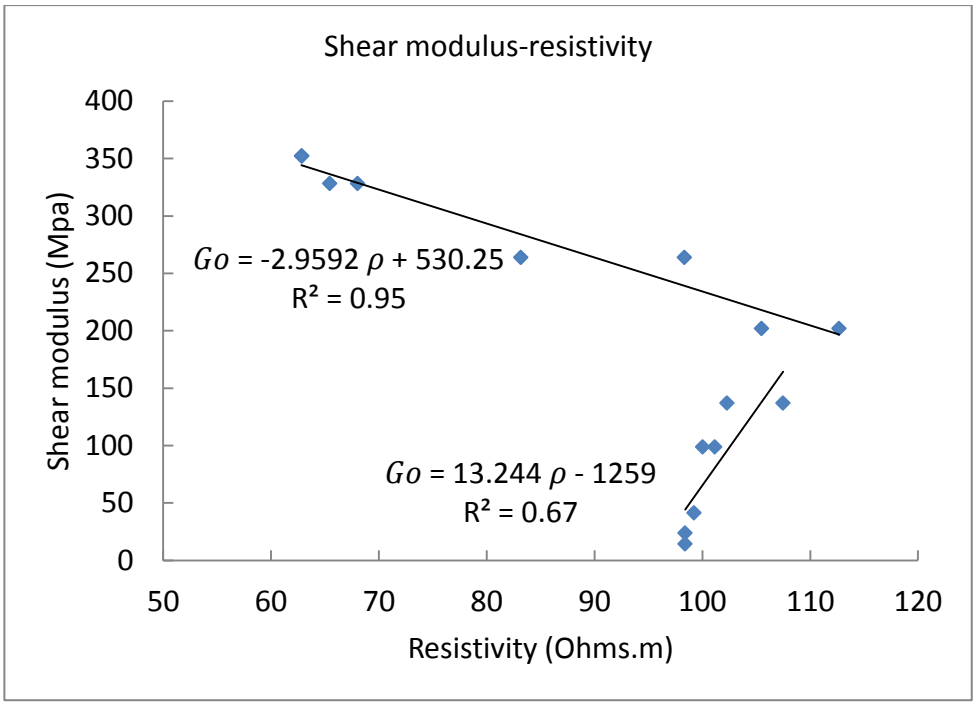

Figure 4-54: Shear modulus – resistivity relationship from the Rugeley site. Shear modulus data was obtained from the CPT sounding and from the active seismic surveys (MASW).

4.9 Summary

Site characterisation is a crucial stage for any construction project. It can be performed by conventional tests (e.g. CPT) and/or using geophysical methods (e.g. seismic and resistivity methods). Combining conventional and geophysical methods help to avoid either method limitation, deliver more constrained model of a studied site by using join interpretation and site investigation can be performed in more than 1 dimension (e.g. 2D cross sections, 3D blocks and time-lapse surveys).

In this study, a site was subjected to conventional and geophysical surveys as a case study site and in order to prepare a site for performing a passive seismic study using train-induced vibrations as passive seismic waves. Therefore, active seismic (MASW), resistivity and microgravity surveys alongside with CPT soundings, grain size analysis and sand replacement test are conducted at the site.

The microgravity survey shows that the deposits-bedrock interface is inclined and suggests an over-deepened and backfilled river channel is existed underneath the current river Trent and that can be confirmed partly by the available borehole data. Material density suggested by the microgravity surveys agrees with that determined from the sand replacement test.

Shear wave velocity-depth cross sections are generated from the active seismic surveys using the MASW method. These cross sections represent the general increasing in shear wave velocity with depth. The resistivity surveys locate the regional and some perched ground water tables and more importantly the existence of gravely layer shallower than the ground water table. Location of the buried mill leetes are imaged by the resistivity and the seismic cross section. Most of the north and north east parts of the site are

covered by coarse deposits whilst the south and south west parts are covered by almost fine deposits as determined from the grain size analysis and it matches with resistivity surveys.

The CPT soundings investigate the shallow deposits (from the ground surface down to about 4 m), it shows the spatial and vertical variations in the site deposits. Shear wave velocity and shear modulus of the shallow deposits were determined from the CPT soundings and piled with those generated from active seismic surveys to investigate upward the ground surface.

The qualitative correlation between the resistivity and active seismic cross sections shows that these two methods differently imaged the same investigated subsurface section and highlights that the resistivity data should carefully interpreted and other parameters (e.g. moisture content and clay content) should be taken in consideration in such surveys.

Chapter five: Train-induced vibrations analysis and application for site characterisation using the Refraction Microtremor method (ReMi) – Rugeley, Staffordshire, UK

Seismic surface waves can be generated by moving trains (see, for example, Gunn et al., 2015b). Kim and Lee (2000) and Kouroussis et al. (2014) state that the Rayleigh waves are the chief component of train-induced vibrations compared to body waves (P- and S-waves). Whilst train-induced vibrations are potentially problematic along railway routes (see, e.g., Krylov, 1994; Madshus and Kaynia, 2000; Motazedian *et al.*, 2011; Sanayei et al., 2014; Gunn *et al.*, 2015b; Fu, 2016; Ma *et al.*, 2016), they could, in fact, be useful as passive seismic sources for seismic surveys for site characterisation. In the published literature, few studies have been published utilizing train-induced vibrations as passive seismic waves for site characterisation and to produce shear wave velocity- depth profiles (although see Nakata et al., 2011; Quiros et al., 2016; and Fuchs et al., 2017).

This study aims to (1) define the optimum survey parameters to collect train-induced vibrations (i.e. array location and orientation to the railway), (2) determine how the geology affects train-induced vibrations characteristics, and (3) to assess the feasibility of using trains as passive seismic sources to characterise the local site's geology by determining shear wave velocity-depth profiles. The study objectives will be (1) to collect a series of ReMi seismic survey datasets using different sized linear (with different orientations to the railway) and 2D arrays, (2) three components ground motion is recorded (vertical (V), horizontal parallel to the railway (HP) and horizontal orthogonal to the railway (HO)), and (3) the results from different seismic components, and different train directions will be compared.

5.1 Site selection criteria

The Rugeley site is a rural area that is relatively geophysically quiet (i.e. away from urban noise sources) except the West Coast Line railway that between Rugeley and Lichfield train stations (Figure 4-1). The train line, built in the middle 19th century (Clark, 1967), is electrified for higher speed trains (although diesel engine trains also use the line) and is on a raised earthen embankment running northwest-southeast across the site. The embankment height decreases northward and enters a cutting beyond the site in order to maintain the track 'at grade'. The site was chosen for several reasons: (1) train traffic is frequent enough with about 30 trains per day passing the site, (2) different types of train pass the site, passenger trains (i.e. Pendolino electrical, Pendolino diesel, and Midland passenger trains) and heavy goods freight trains, (3) non-horizontal bedrock geology helps to assess any directionality effects (i.e. different results from opposite trains travel directions) on the vibrations.

5.2 Methodology and field deployment

The methodology used for data collection, survey parameters, seismic array locations, and field deployment for linear and 2D arrays are now detailed and represented in the following subsections.

5.2.1 Survey consideration

Passive seismic surveys using the refraction microtremor (ReMi) technique were performed using linear arrays (see Louie, 2001) and 2D arrays, for example, L-shape arrays, (see Foti et al., 2015). The 2D arrays are more useful as the true velocity for any obliquely incident waves can be determined using trigonometric functions. Only apparent velocity can be determined for obliquely incident waves for the linear array, which is its main drawback. Therefore in this work, both linear and 2D array configurations were used for data collection.

The data was collected for all passing trains (i.e. passenger and freight trains) and for trains travelling in both directions. This helps to compare the train-induced vibration velocity-depth profiles generated by each train type and to evaluate how the site geology can affect the propagated passive seismic wave vibrations.

5.2.2 Survey parameters

In this research, a seismic receiver station has a vertical polarized geophone and two horizontal polarized geophones. One of the horizontal geophones was oriented to be parallel to the railway embankment, whilst the second was orientated orthogonally. This deployment manner helps to build up three-component seismic data sets (Figure 5-1).

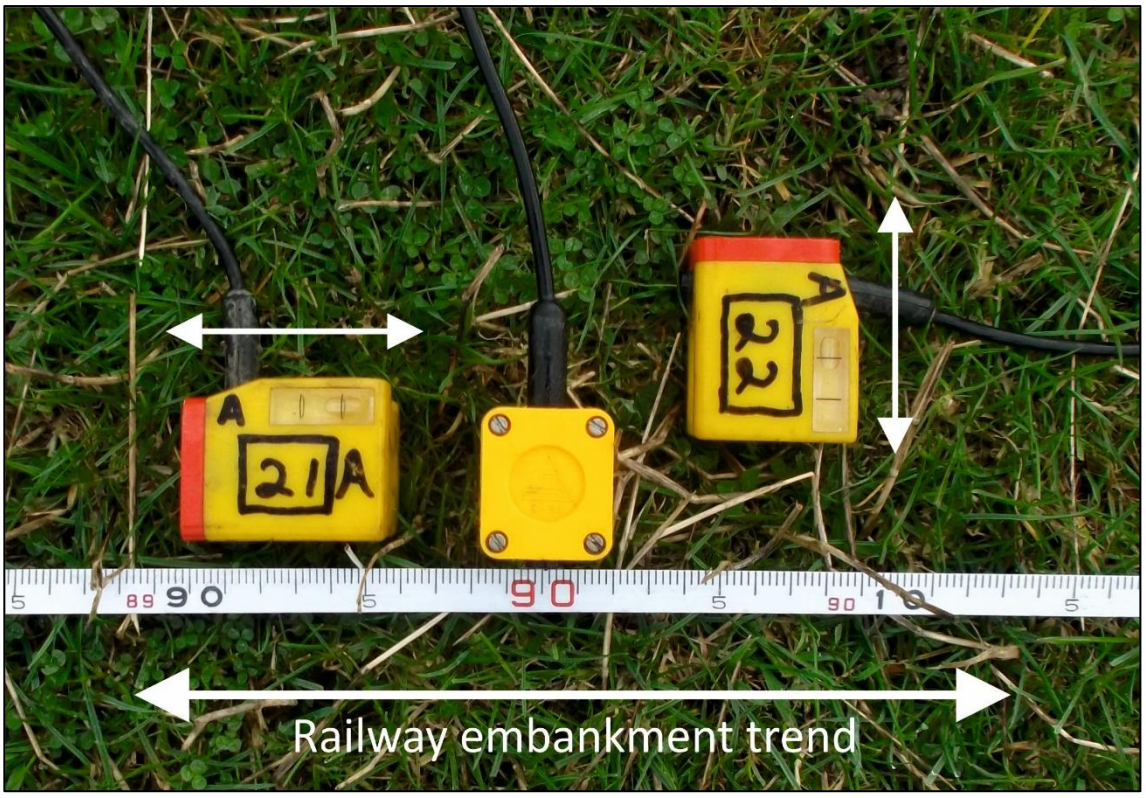

Figure 5-1: A seismic receiver station at the Rugeley study site, showing the orientation of the geophones, a vertical geophone (middle), and the two surrounding orthogonal horizontal geophones.

5.2.2.1 Long linear arrays survey parameters

Two long linear arrays were used at the site; the orientation of the array was parallel to the railway embankment. Each single array had 24 three-component seismic stations (Figure 5-1), using a 5 m seismic station spacing and set geophone frequency of 4.5 Hz (Figure 5-2).

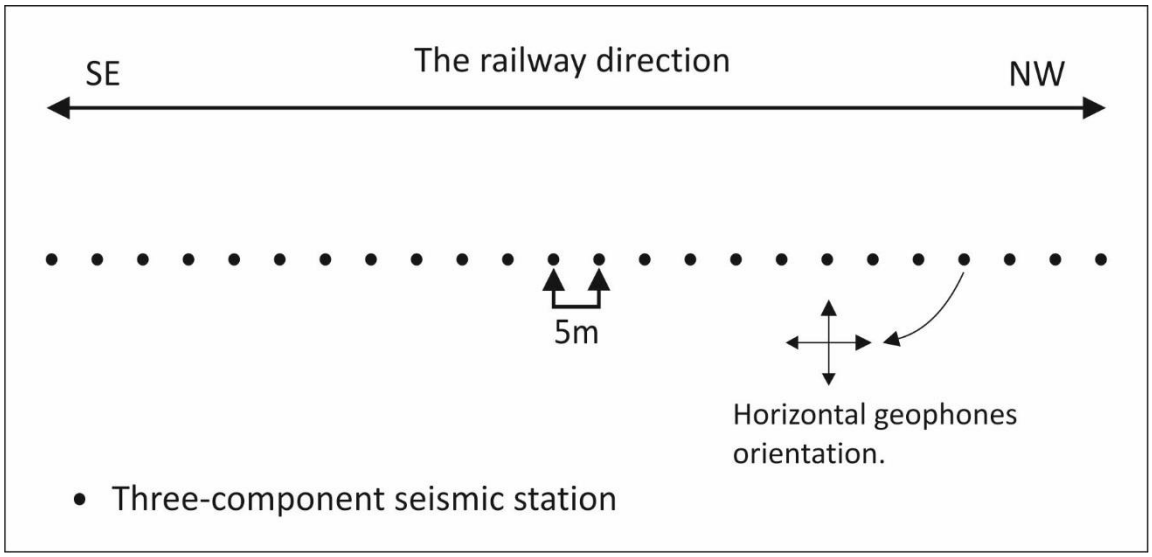

Figure 5-2: Configuration of the long linear seismic array used for data collection at the Rugeley study site.

5.2.2.2 Manual configuration array survey parameters

The term manual array refers to any particular seismic array geometry that does not conform to any of the standard geometries (e.g. linear, triangle, circle and L-shape geometries) supported by the SeisImager/SW and its geometry can be specified by the researcher. Four manual seismic arrays were used at the Rugeley site. The short side of the manual array was orientated parallel to the railway embankment and the long side of the array was orientated orthogonal to the railway embankment. Seismic stations spacing here was 4 m. The manual arrays had 9 three-component seismic stations at the short side and 12 three-component seismic stations at the long side; the station at the manual array corner is shared between the two sides (Figure 5-3).

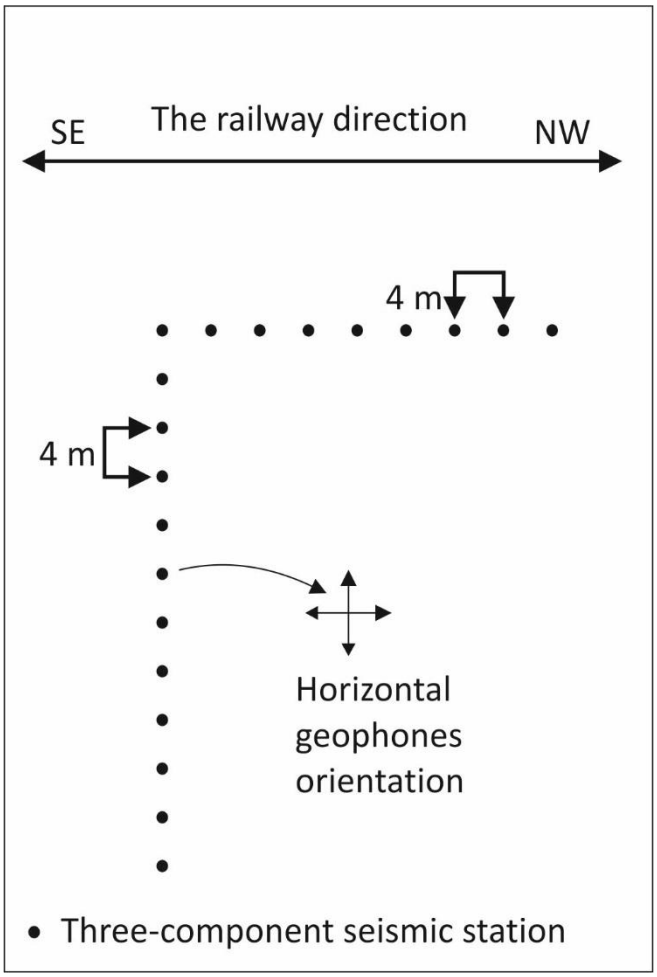

Figure 5-3: The manual seismic array configuration used for data collection at the Rugeley study site.

The collected data at the seismic stations of the long side of the manual array could be extracted and used as a linear array data set with 12 seismic stations (i.e. seismic traces) as shown in Figure 5-4. To differentiate between the linear arrays, linear arrays parallel to the railway are called long linear seismic arrays (LLSA) and the linear array from the long side of the manual arrays are called short linear seismic arrays (SLSA) which are orientated orthogonal to the railway embankment.

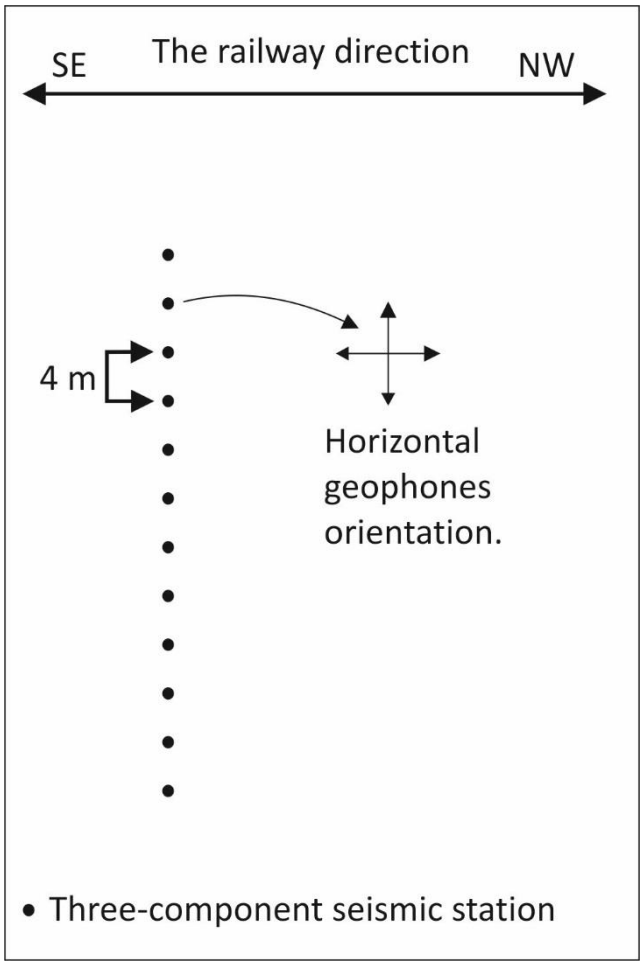

Figure 5-4: The short linear seismic array (extracted from the long side of the manual array) at the Rugeley study site.

Table 5-1: The survey parameters for all the seismic arrays at the Rugeley study site.

Survey Parameter / Array type	Array number	Seismic component	Seismic stations	Array length	Seismic station spacing
Manual array	4	3	20	32 m short side, 44 m long side	4 m
Long linear array	2	3	24	115 m	5 m
Short linear array	4	3	12	44 m	4 m

5.2.3 Field deployment

The fieldwork was undertaken in collaboration with the British Geological Survey (BGS). The arrays position, orientation, and location to the superficial deposits and bedrock lithology of the long linear arrays and short linear arrays are presented in Figure 5-5 and Figure 5-6 respectively. The manual arrays are presented in Figure 5-7 and Figure 5-8. Figure 5-9 shows fieldwork deployment at the Rugeley study site for trains-induced vibrations data collection.

Base on the site accessibility, the LLSA no.1 and the manual arrays no. 1-3, on the east side of the railway, were deployed at about 30 m from the railway embankment. The LLSA no.2 and the manual array no.4, on the west side, were deployed at 6 m from the railway embankment.

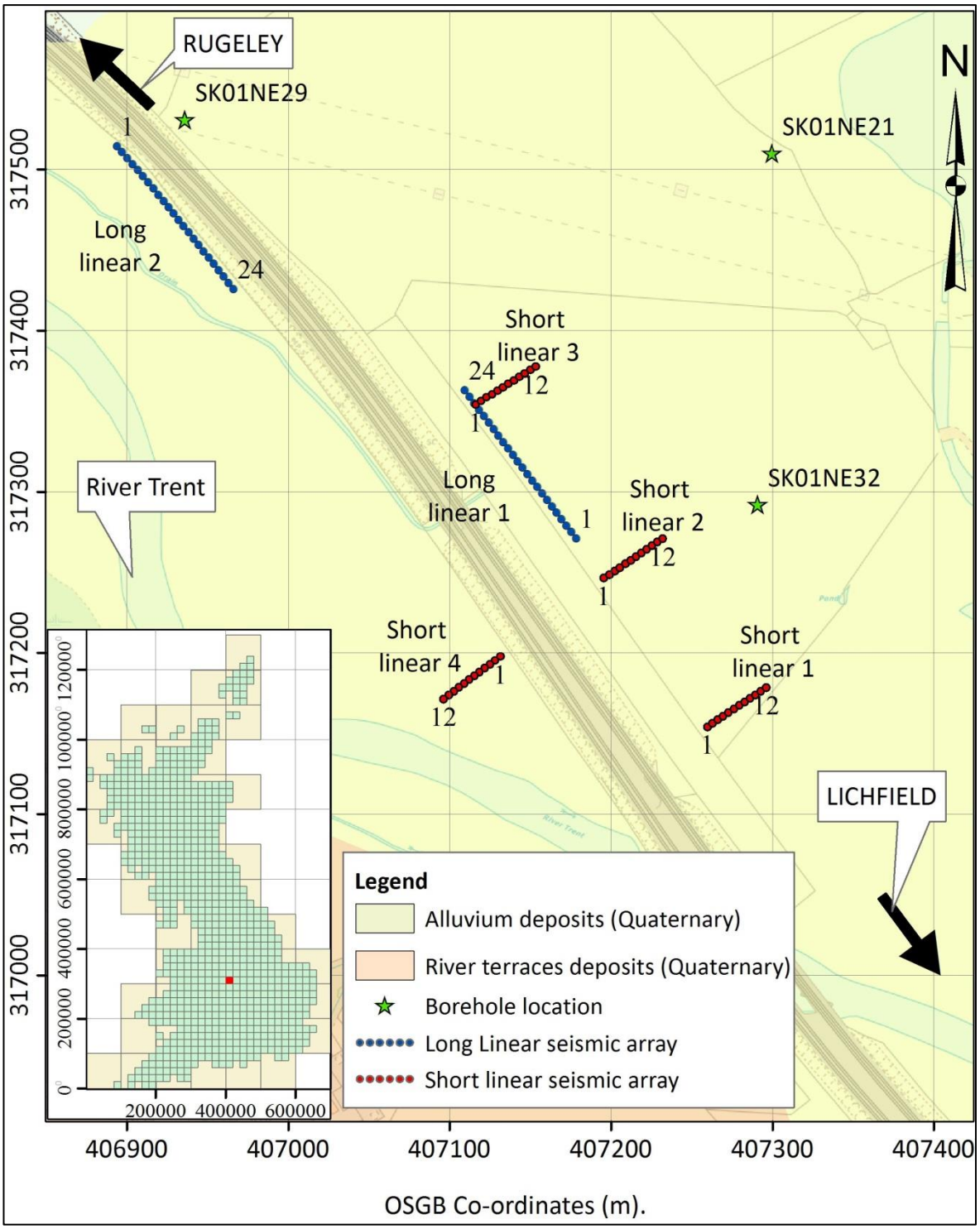

Figure 5-5: Long linear and short linear arrays position at the Rugeley study site, relative to the superficial deposits and orientation to the railway embankment. Borehole information (green stars denote location) shown in Figure 4-4. Images supplied courtesy of Ordnance Survey/EDINA, 2016. Numbers at the start and the end of each array are refer to the first and the last seismic station.

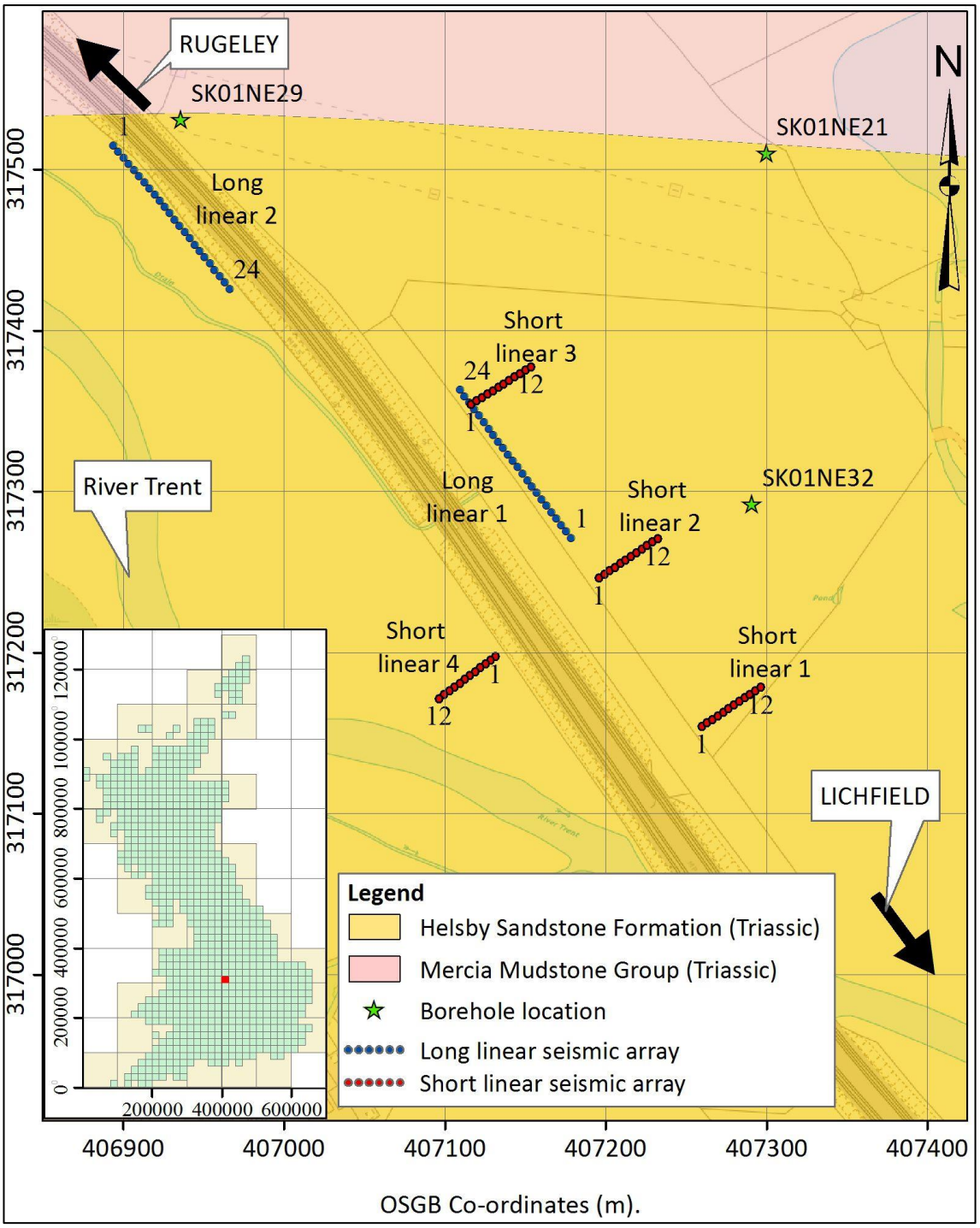

Figure 5-6: Long linear and short linear arrays position at the Rugeley study site, relative to the bedrock and orientation to the railway embankment. Borehole information (green stars denote location) shown in Figure 4-4. Images supplied courtesy of Ordnance Survey/EDINA, 2016. Numbers at the start and the end of each array are refer to the first and the last seismic station.

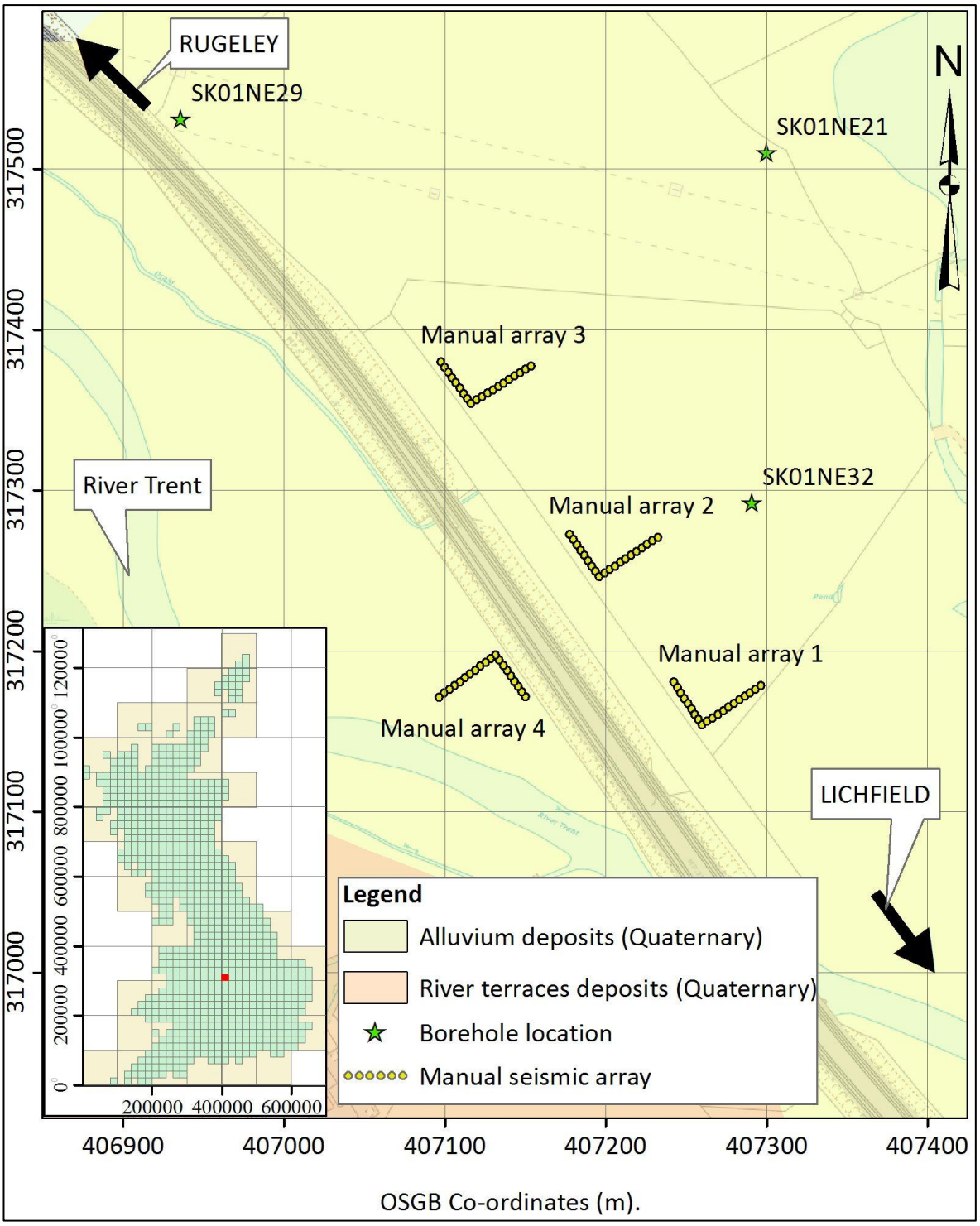

Figure 5-7: Manual arrays position relative to the superficial deposits and the orientation of the array sides to the railway embankment at the Rugeley study site. Borehole information (green stars denote location) shown in Figure 4-4. Images supplied courtesy of Ordnance Survey/EDINA, 2016.

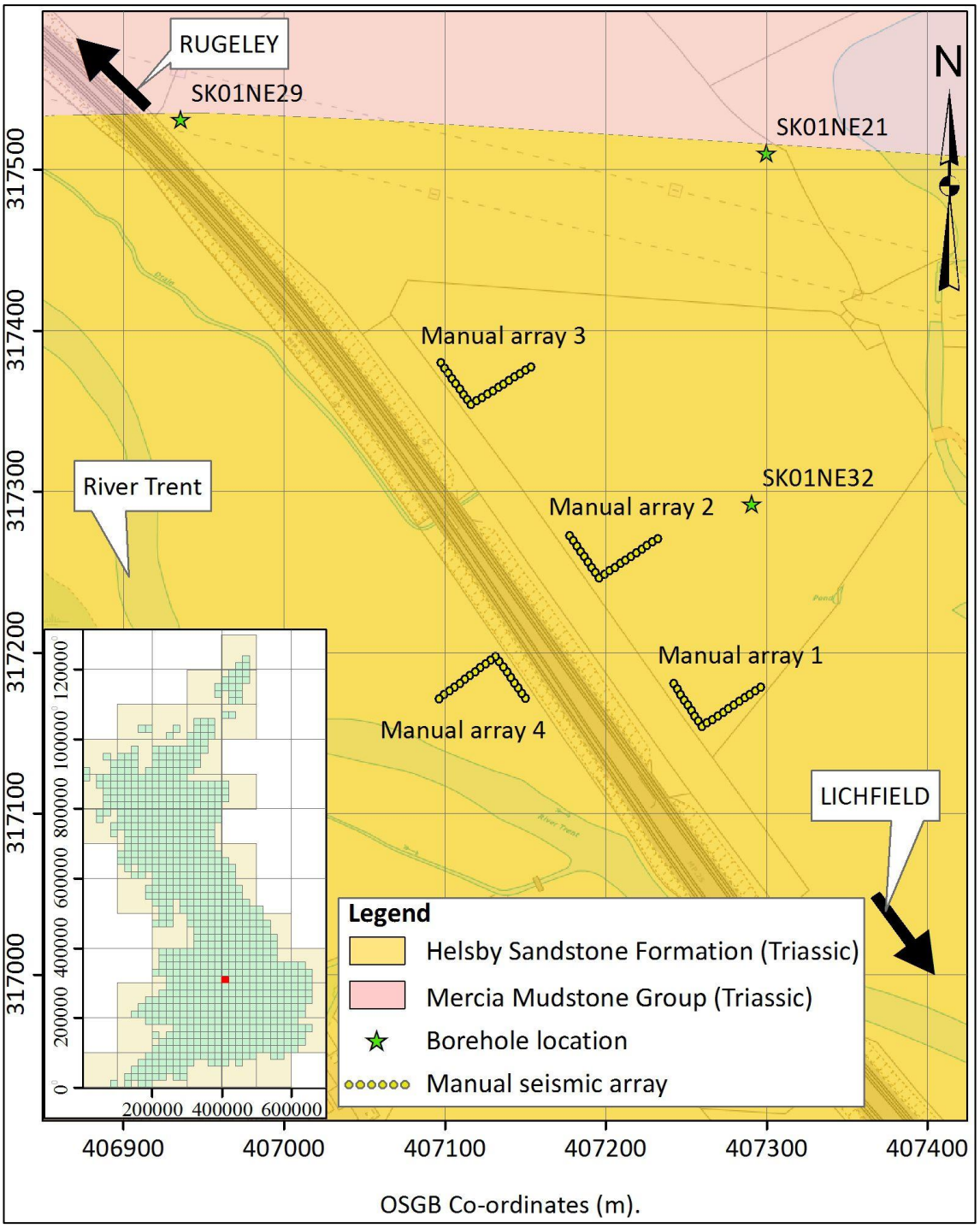

Figure 5-8: Manual array positions relative to the bedrock and the orientation of the array sides to the railway embankment at the Rugeley study site. Borehole information (green stars denote location) shown in Figure 4-4. Images supplied courtesy of Ordnance Survey/EDINA, 2016.

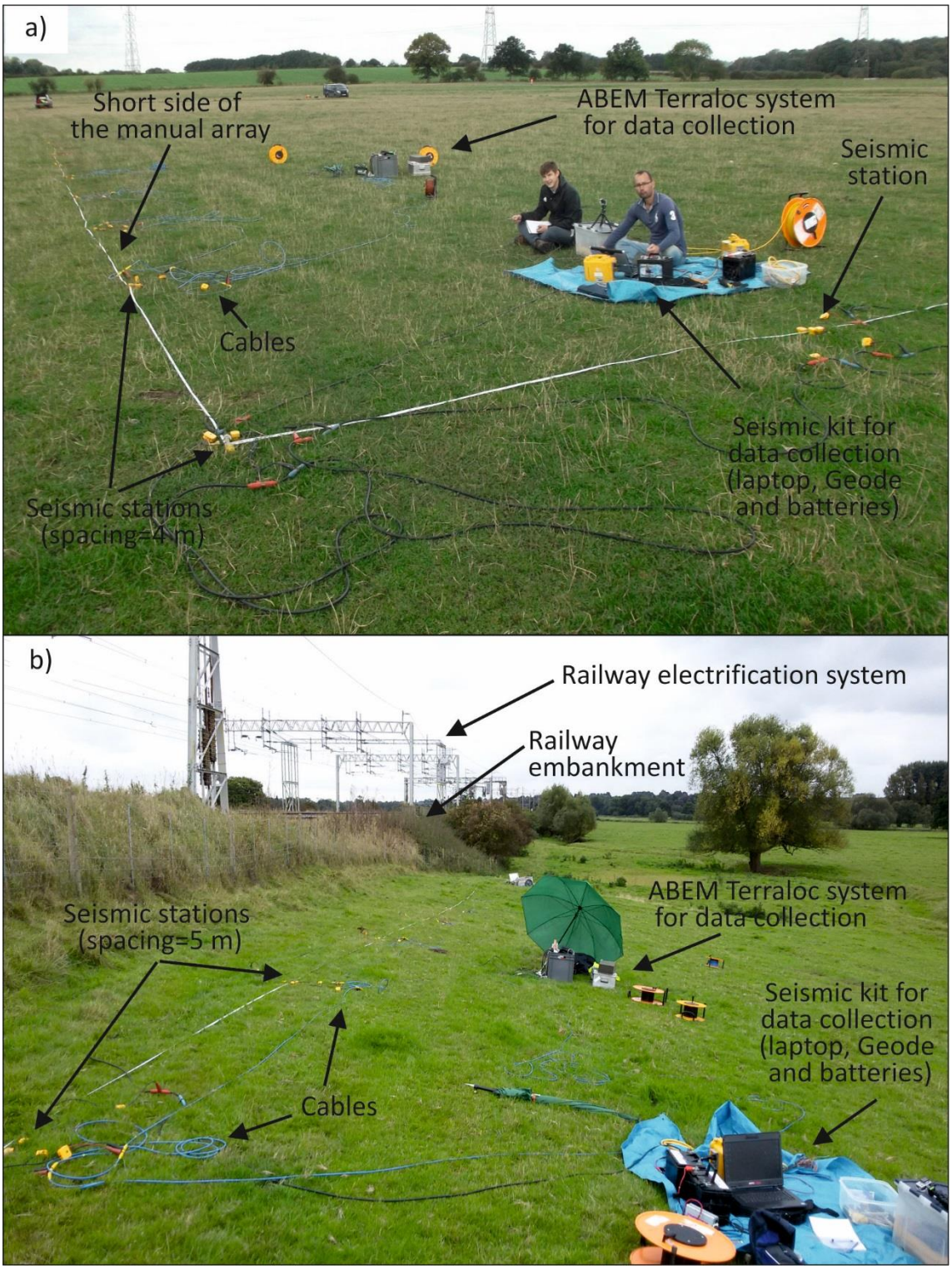

Figure 5-9: Fieldwork deployment to collect train-induced vibrations datasets at the Rugeley study site, a) shows the manual array no. 1 at the east side of the railway embankment, b) shows Long linear array no.2 at the west side of the railway embankment.

5.3 Data preparation

ReflexW^{TM} v.8.1 (Sandmeier geophysical research) software was used for seismic data preparation. It was used to extract seismic traces into three different components, vertical, horizontally orthogonal (HO) to the railway, and horizontal parallel (HP).

Data acquisition commented of the collection of train-induced vibrations from all passing trains from the 3rd to the 7th of October 2016.

The collected data was separated into three groups depending upon the train's direction of travel, see Table 5-2 and Table 5-3. Therefore, the groups were named as NW trains group which means passive seismic records collected for trains coming from the NW and going in the SE direction. Another group was created for trains coming from the SE and going to the NW and named the SE trains group. The third group named the "All trains" group, refers to the combined records from the two previous groups. The collected datasets are then subdivided into nine groups depending upon the seismic component (V, HP and HO) and trains groups (all trains, NW trains and SE trains).

Two different recording systems, based on the available equipment, were applied for data collection; the Geode (Geometrics, OYO corporations, USA) and the ABEM Terraloc (ABEM instrument). Therefore, the ReflexW software was applied to check the collected data and to combine it in final records.

Table 5-2: Specifications of the trains that use the railway at the Rugeley site and their vibrations were recorded in this study. * Based on the wagon type.

Train type	Number of wagons/cars	Car/wagon length	Train length	Estimated train speed
Pendolino Virgin passenger	11	24 m	264 m	170 km/h
Pendolino Virgin passenger	9	24 m	216 m	170 km/h
Diesel Virgin passenger	5	24 m	120 m	170 km/h
Midland passenger	4	22.5 m	90 m	130 km/h
Heavy goods freight	About 30	About 20* m	600 m	100 km/h

Table 5-3: The numbers of trains and destination were recorded for each array and their vibrations were processed (i.e. inverted) to determine the site's shear wave velocity in this study. P11 is Pendolino Virgin passenger with 11 cars, P9 is Pendolino Virgin passenger with 9 cars, D5 is Diesel Virgin passenger with 5 cars, M4 is Midland passenger with 4 cars and F is freight train. * In case of two trains (named M* in the table), one travelling NW->SE and the second travelling SE->NW, passing the site during the recording time, that certain seismic record was not involved in NW->SE and SE->NW groups but it was involved in all train group. In number of trains column, numbers to the left for trains travelling SE->NW; numbers to the right for trains travelling NW->SE.

Array	Number of trains						Total number of trains in each group		
	P11	P9	D5	M4	F	M*	NW->SE	SE->NW	All trains
Manual array 1	2/5	2/0	1/1	2/0	1/2	1	8	8	17
Manual array 2	6/4	3/2	2/2	2/1	1/2	2	11	14	27
Manual array 3	7/3	3/4	2/0	2/0	2/1	0	8	16	24
Manual array 4	6/7	3/2	1/1	2/2	1/4	2	16	13	31
Long linear seismic array 1	3/5	4/1	2/0	0/0	2/4	2	10	11	23
Long linear seismic array 2	8/2	1/3	0/0	1/1	2/2	4	8	12	24

For the manual arrays, the respective seismic array positions above the superficial deposits and the bedrock at the site are illustrated in Figure 5-7 and Figure 5-8 respectively. All the collected datasets using manual arrays (i.e. the 4 manual arrays, the 3 seismic components and the 3 train groups) were prepared into two ways: 1) they had 11

seismic traces (extract 11 seismic traces to generate datasets as collected using L-shape arrays) or 2) had 20 seismic traces. The first trial with 11 seismic traces matched the seismic record with the SeisImager/SW software options, whereas trace no. 6 was kept at the corner of the L-shape, the second trial had 20 seismic traces as the data was collected at the site, the L-shape arrays no. 1-4 location is coincident with that of the manual arrays (see, Figure 5-7, for location). Figure 5-10 shows how the array configuration will look like after preparing the observed data.

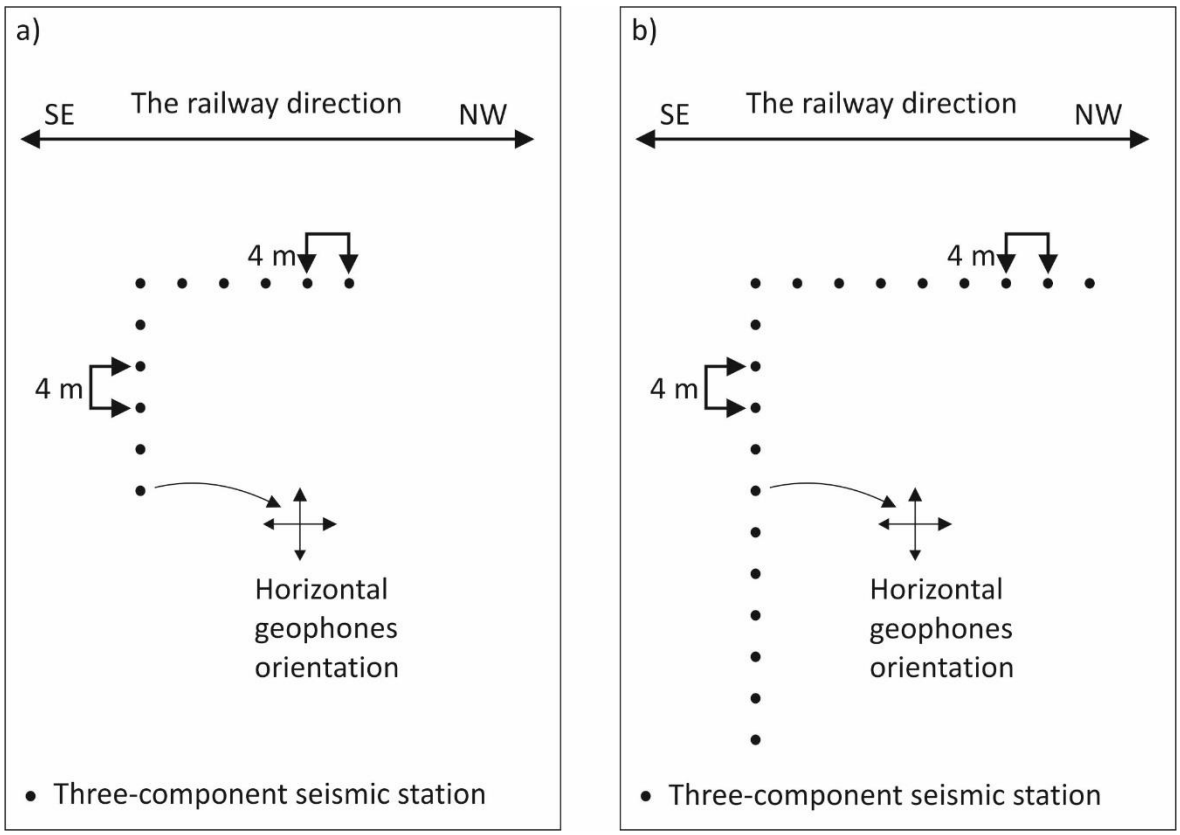

Figure 5-10: 2D arrays configuration, a) shows the extracted 11 seismic traces to generate L-shape array datasets, and b) shows manual arrays configuration with 20 seismic traces.

5.4 Results of trains-induced vibration datasets

5.4.1 Train-induced vibration comparison from different trains and travelling in different directions

The data were collected for the three different trains (Pendolino and Midland passenger and heavy goods freight trains) and for both directions of travel (see Table 5-2 and Table 5-3). Figure 5-11 shows the vertical component of typical seismic traces for the three different trains coming from the SE direction.

The freight train takes longer than the other trains to travel over the study site due to its longer length (about 30 wagons) and slower speed. In addition, the freight trains caused measurably larger vertical displacement of seismic waves, when compared to the passenger trains, most probably due to their heavier weight. Moreover, the amplitude spectrum of the trains (the passenger and freight trains) shows that there were significant energy between 4.5 Hz (the geophone frequency set of the vertical geophones) and 20 Hz (Figure 5-12, Figure 5-13 and Figure 5-14). For the Matlab scripts used in this study, see appendix F, included on the CD, inside the back cover.

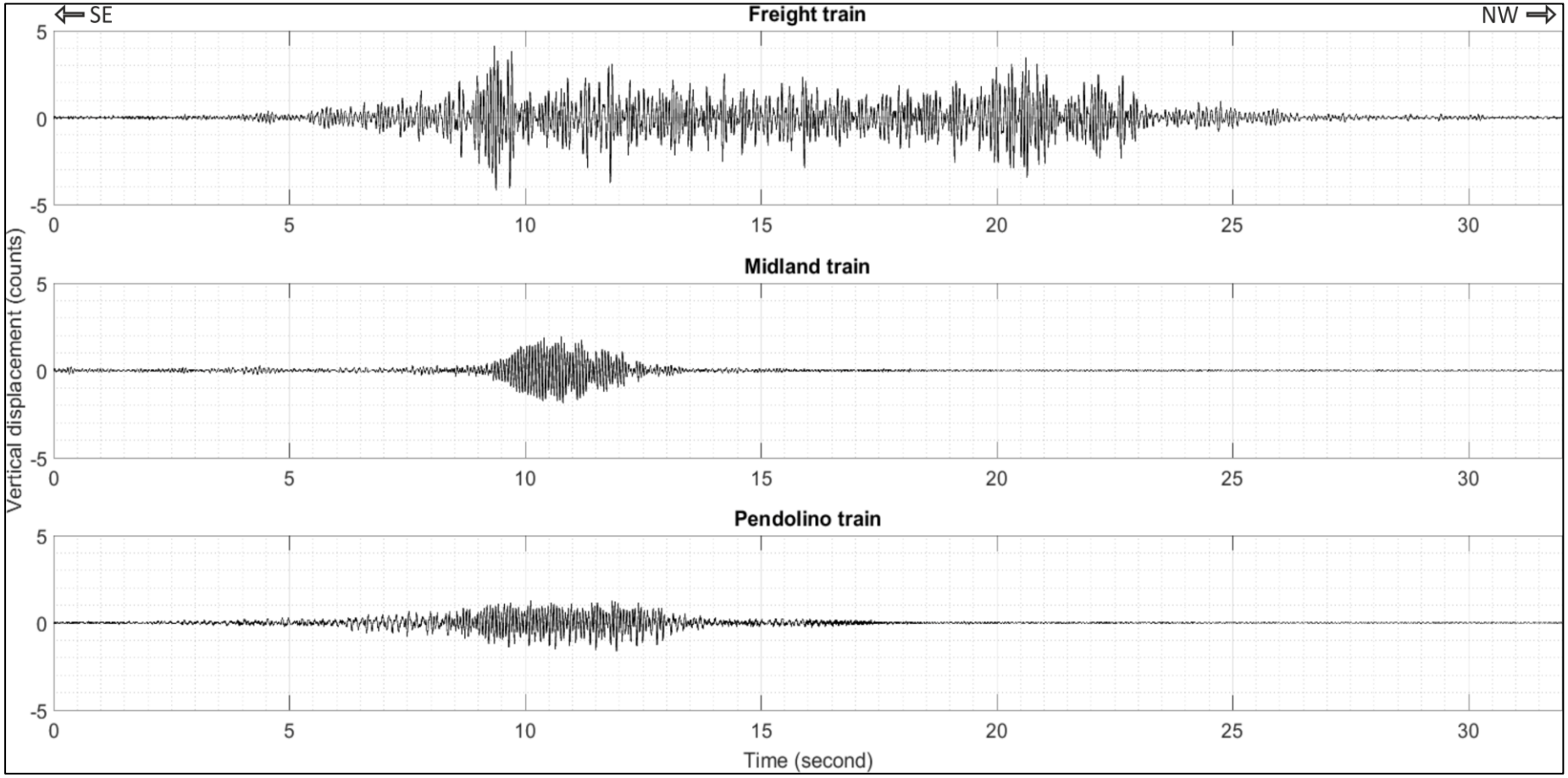

Figure 5-11: Typical seismic traces of the vertical component of the train-induced vibrations recorded at the Rugeley study site, top) heavy goods freight train, middle) Midland passenger train and bottom) Pendolino passenger train, the train's direction of travel is SE->NW.

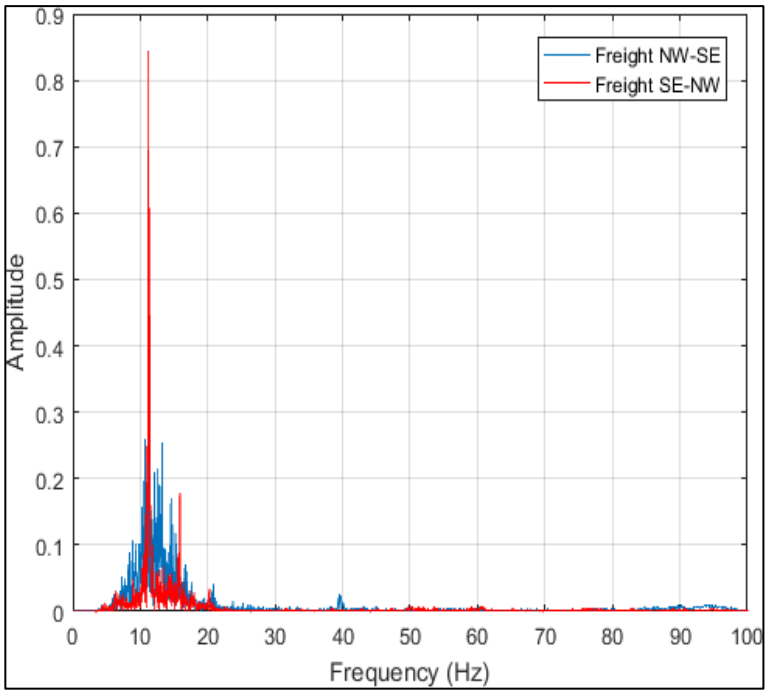

Figure 5-12: Amplitude spectrum of heavy goods freight trains coming from either direction (see key), data collected at the manual array 2 (see Figure 5-7 for location in the study site).

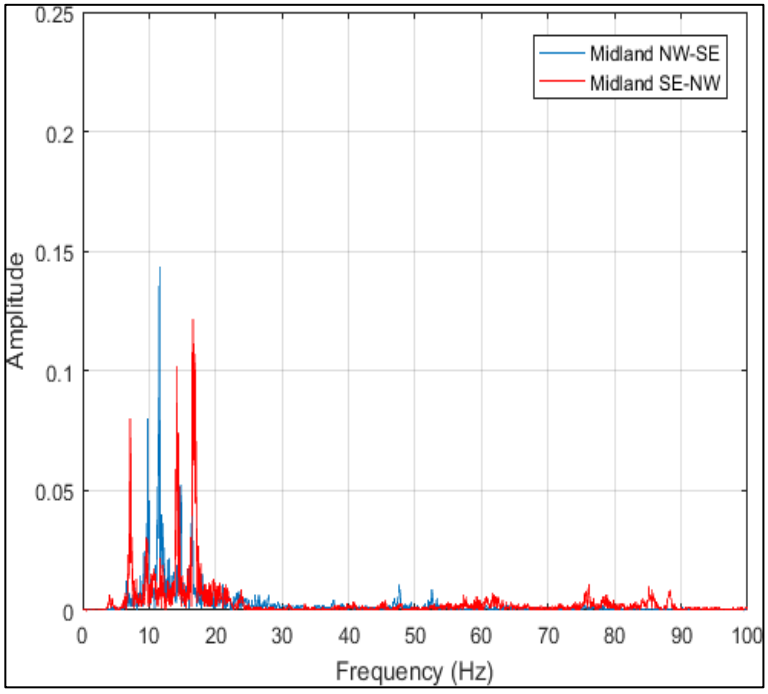

Figure 5-13: Amplitude spectrum of Midland passenger trains coming from either direction (see key), data collected at the manual array 2 (see Figure 5-7 for location in the study site).

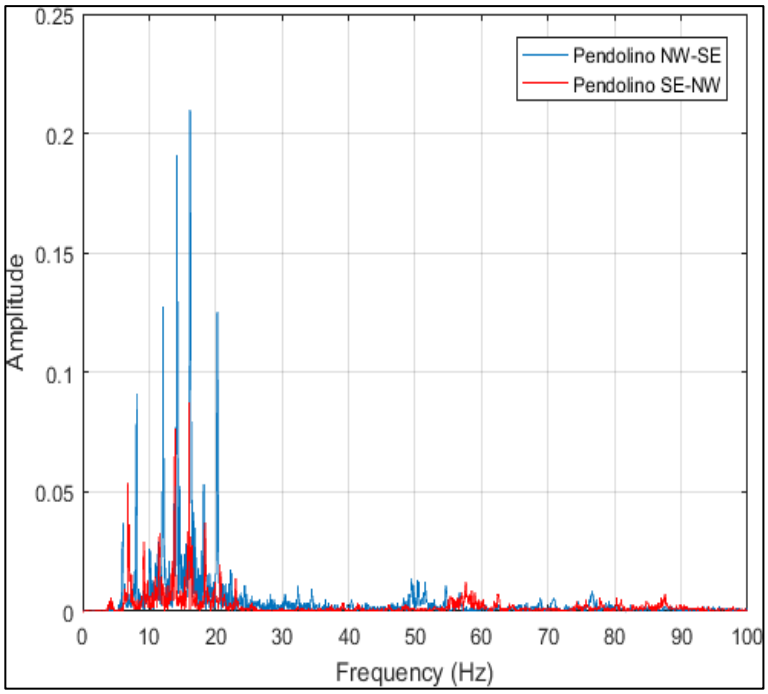

Figure 5-14: Amplitude spectrum of Pendolino passenger trains coming from either direction (see key), data collected at the manual array 2 (see Figure 5-7 for location in the study site).

5.4.2 Comparison of Rayleigh wave content from different trains

The ReflexW software was also used to generate particle motion plots to investigate if the recorded vibrations were consistent with Rayleigh waves. The particle motion plots of the combined heavy goods freight, Pendolino and Midland passenger trains are represented in Figure 5-15, Figure 5-16 and Figure 5-17 respectively; x axis is parallel to the railway, y axis is orthogonal to the railway and z is the vertical axis. The elliptical shape of the particle motion plots of Pendolino and Midland passenger trains indicates that the collected vibrations are consistent with Rayleigh waves, but the heavy goods freight trains are not.

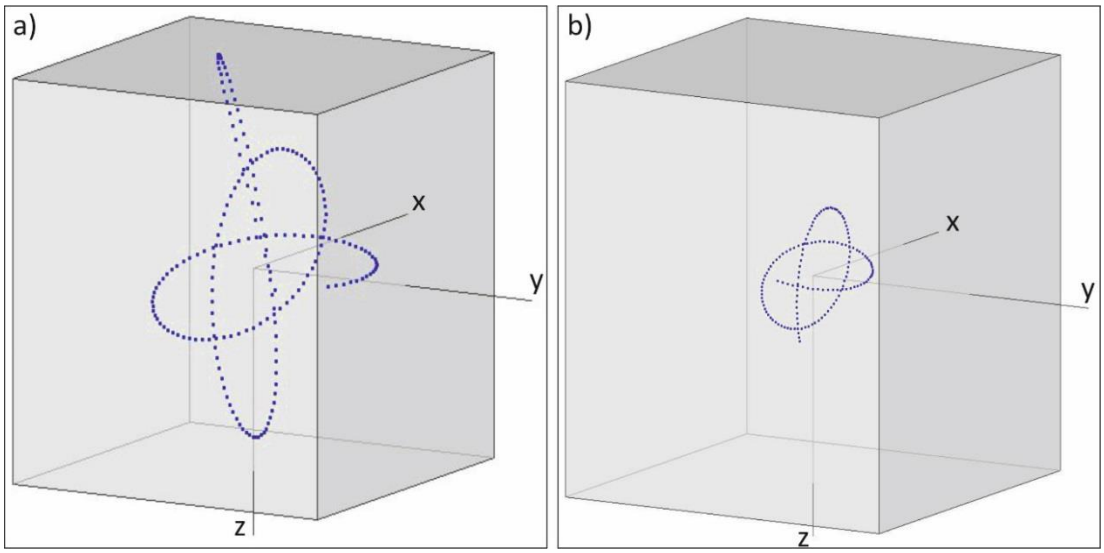

Figure 5-15: Particle motion plot of heavy goods freight train-induced vibrations. a) data used was collected at short linear seismic array no. 4, the farthest seismic station from the railway embankment (see Figure 5-5). Train direction was NW->SE; b) collected data from the short linear seismic arrays no. 1, the closest seismic station from the railway embankment (see Figure 5-5), train direction was SE->NW. 300 samples were used for these plots.

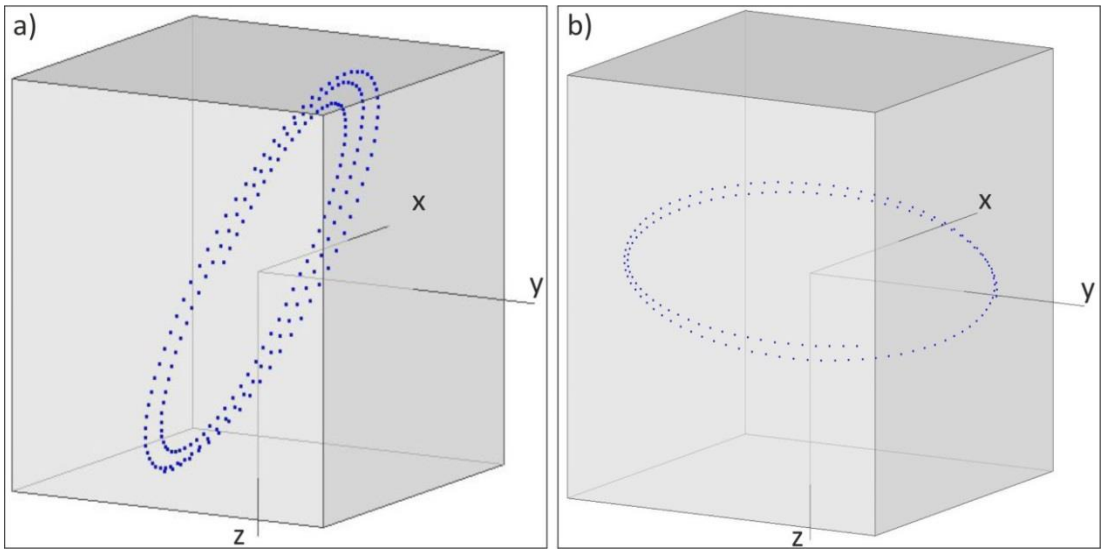

Figure 5-16: Particle motion plot of Pendolino passenger train-induced vibrations. a) data used was collected at short linear seismic array no. 4, the farthest seismic station from railway embankment (see Figure 5-5). Train direction was SE->NW; b) collected data from the short linear seismic array no. 2, the closest seismic station from the railway embankment (see Figure 5-5), train direction was NW->SE. 300 samples were used for these plots.

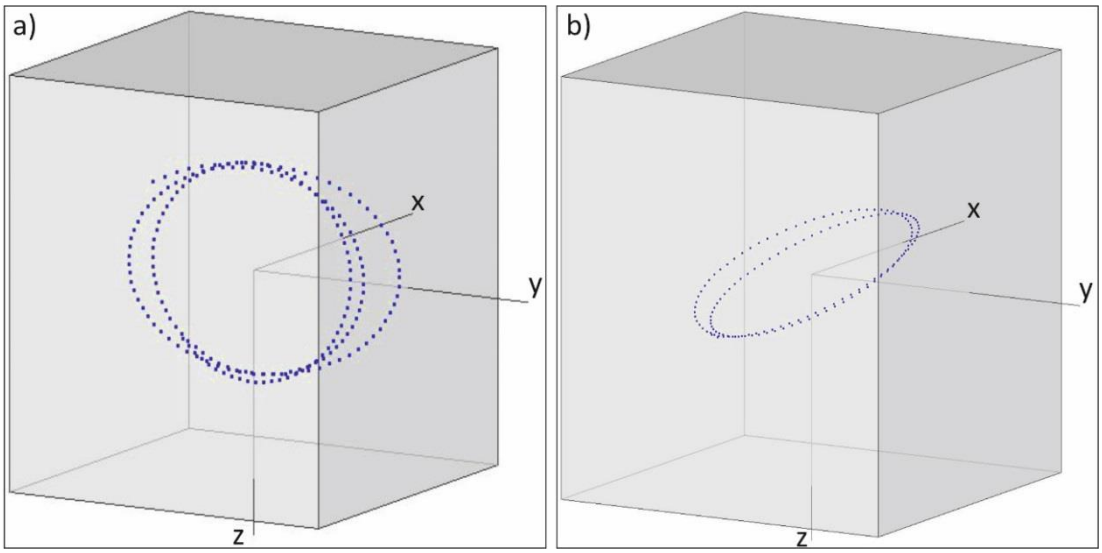

Figure 5-17: Particle motion plot of Midland passenger train-induced vibrations. a) data used was collected at short linear seismic array no. 4, the farthest seismic station from railway embankment (see Figure 5-5). Train direction was SE->NW; b) collected data from the short linear seismic array no. 2, the closest seismic station from the railway embankment (see Figure 5-5), train direction was NW->SE. 300 samples were used for these plots.

Other particle motion plots were prepared, using MatLab software, to determine the manner (i.e. prograde or retrograde) of the wave propagation. Figure 5-18 shows the yz view (y is orientated horizontal orthogonal to the railway and z is the vertical axis) of Pendolino passenger train induced-vibration that travelled in SE->NW directions, data was collected at the short linear seismic array no.1 at the east side of the railway (see, Figure 5-5 for location). The plot shows that the generated waves propagated in a retrograde elliptical manner characteristic of Rayleigh waves. Figure 5-19 shows particle motion plot of Pendolino passenger train induced-vibrations, the train travelled in a NW->SE direction, and the data used in this plot was collected at the short linear seismic array no.1 at the east side of the railway. The plot shows the retrograde propagation of Rayleigh waves.

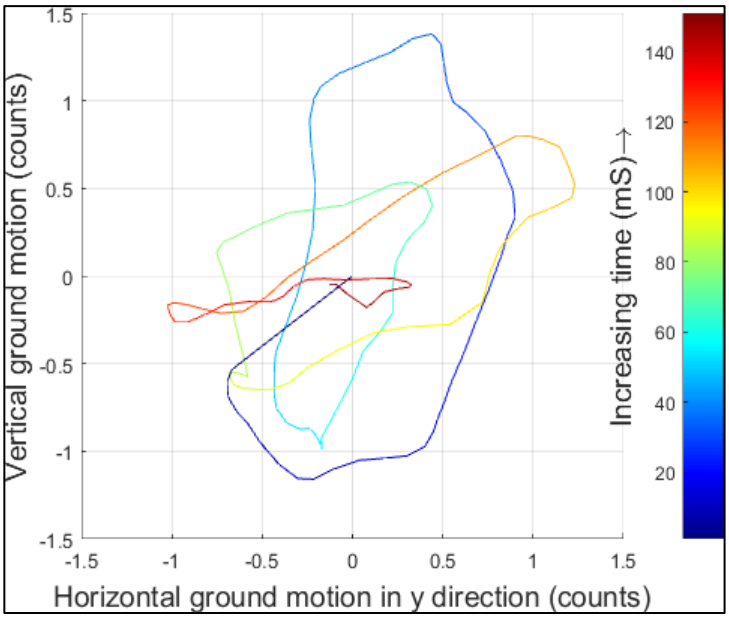

Figure 5-18: Particle motion plot of Pendolino passenger train travelling in SE->NW direction, yz view; y direction is orientated orthogonal to the railway embankment. Data used for this plot was collected at short linear seismic array no. 1, the closest seismic station from the railway embankment (see Figure 5-5 for location), 150 samples were used for the plot.

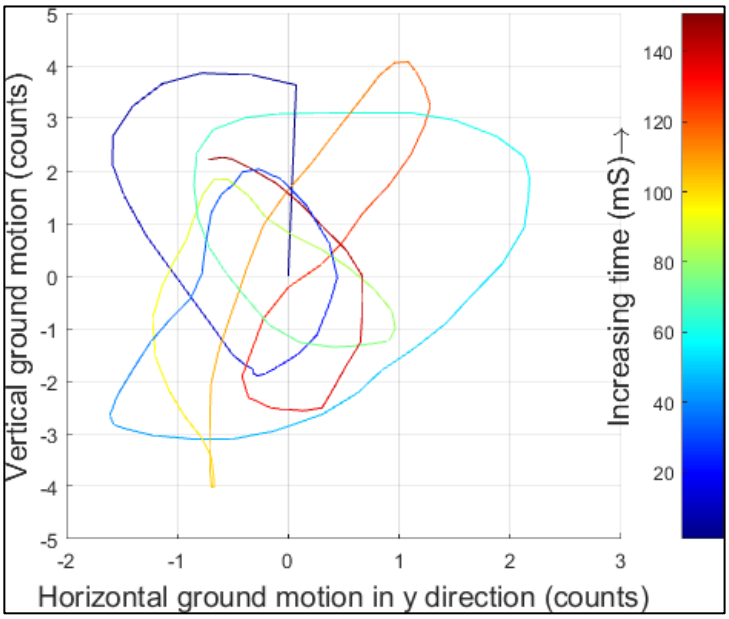

Figure 5-19: Particle motion plot of Pendolino train in NW- SE direction, yz view, y directions is orthogonal to the railway embankment. Data used for this plot was collected at short linear seismic array no. 1, the closest seismic station from the railway embankment (see Figure 5-5 for location). 150 samples were used for these plots.

The particle motion plots for the different train types (i.e. heavy goods freight trains and Pendolino/Midland passenger trains) represented in Figure 5-15, Figure 5-16 and Figure 5-17 show significant differences. Passenger trains produce vibrations more consistent with a simple Rayleigh-wave source when compared to vibrations generated from freight trains. When passenger trains are approaching and receding from the seismic array they effectively act as point sources, only behaving as complex multiple sources at each axle as the train is adjacent to the array. The freight trains being longer, and with a lower dominant frequency, behaves as a complex multiple sources for a greater range of distances.

Therefore, particle motion plots were produced to analyze a train's vibrations when the train was approaching, adjacent to, and receding from the monitoring seismic stations. This analysis was undertaken for Pendolino and Midland passenger trains travelling in both directions (i.e. NW->SE and SE->NW). The analysis shows that the train-induced vibrations, when the train was receding, propagated in the opposite way compared with when the train was approaching. The Pendolino and Midland passenger trains had the same characteristics in this regard; Figure 5-20 shows a Pendolino passenger train travelling NW->SE and Figure 5-21 shows a Pendolino passenger train travelling SE->NW. Figure 5-22 and Figure 5-23 represent Midland passenger trains travelling from NW->SE and SE->NW respectively.

The changes in the seismic wave propagation direction when the train approaches and recedes should happen when the train was adjacent to the seismic array. When the train was adjacent to the seismic array, each train wheel should be expected to work as a

seismic point source (i.e. the train works as a multiple point seismic source rather than as a single point seismic source). Therefore, during the time when the train was adjacent to the array, the vibrations would be expected to be more complex compared to when the train was approaching and receding the seismic array. After that, when the train goes past the array, the train should revert to represent a single source and generate vibrations more dominated from one direction, and the vibrations' propagation direction might change during this time and reversed to be opposite to that when the train was approaching the seismic array.

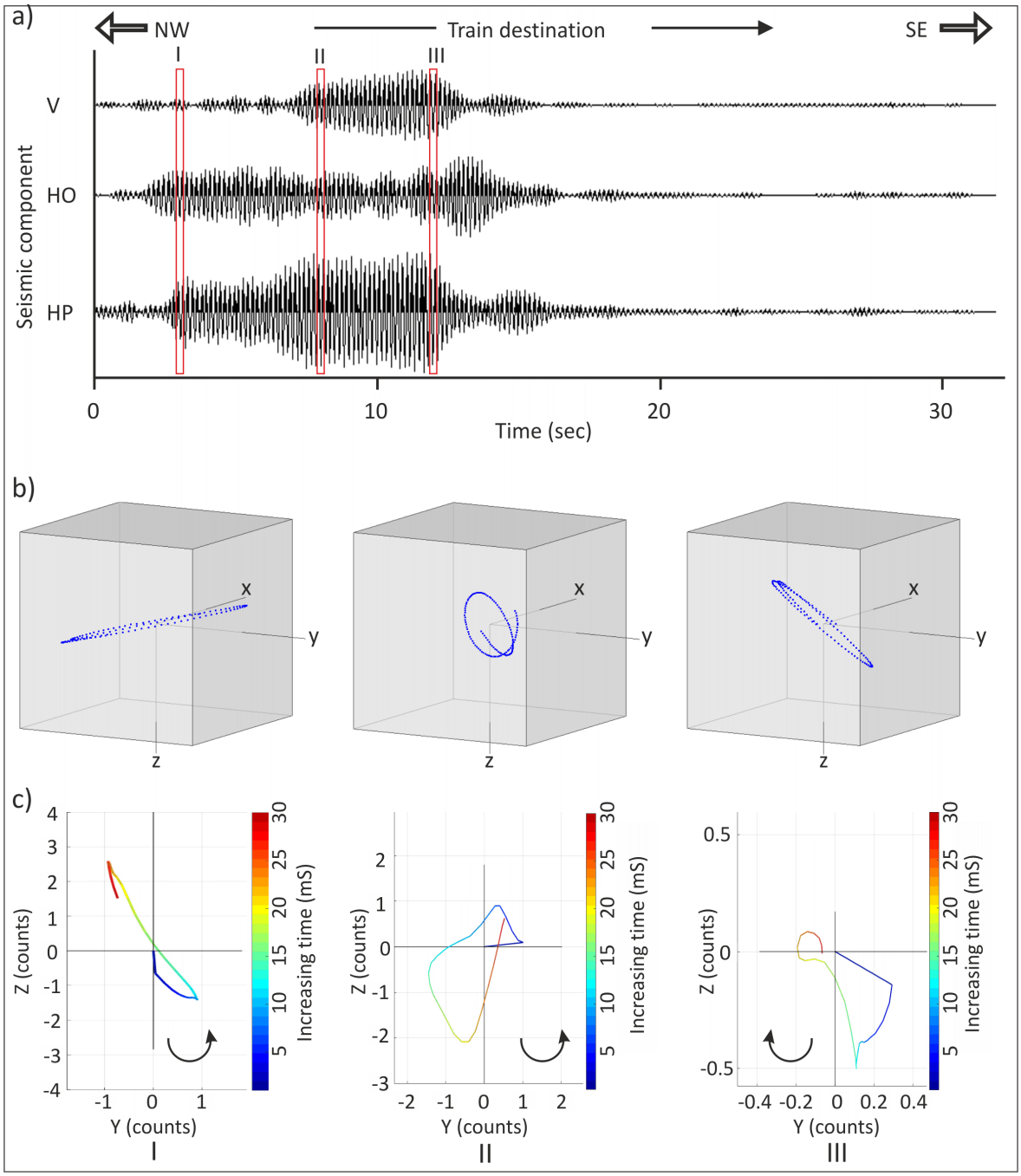

Figure 5-20: Particle motion plots for a Pendolino passenger train travelling in NW->SE direction, a) three components seismic traces with red rectangles representing the selected analysis window, b) particle motion plots using Reflex, c) particle motion plots using Matlab showing propagation direction when the train is I) approaching, II) adjacent and III) receding from the seismic station respectively.

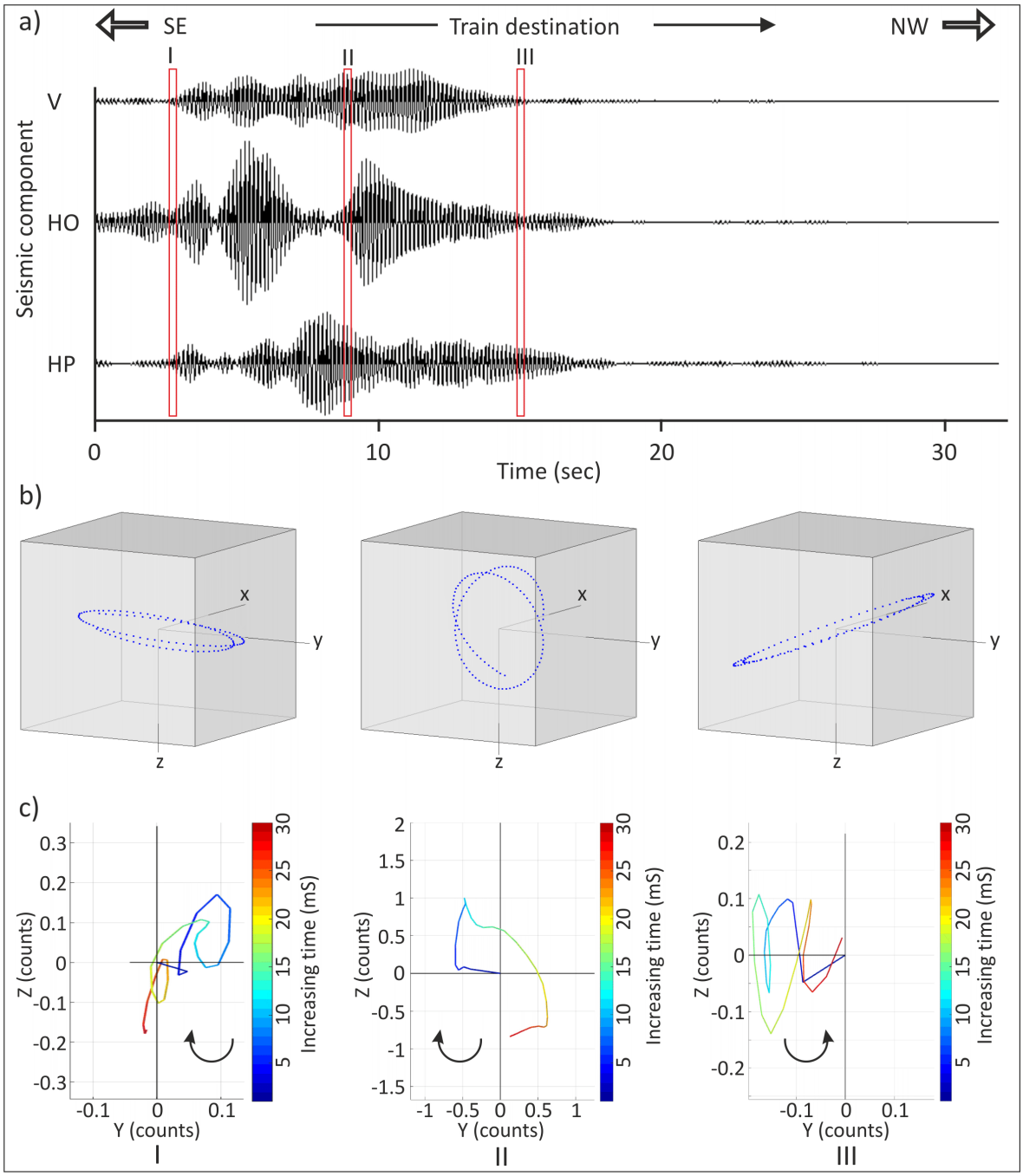

Figure 5-21: Particle motion plots for a Pendolino passenger train travelling in SE->NW direction, a) three components seismic traces with red rectangles representing the selected analysis window, b) particle motion plots using Reflex, c) particle motion plots using Matlab showing the propagation direction when the train is I) approaching, II) adjacent and III) receding from the seismic station, respectively.

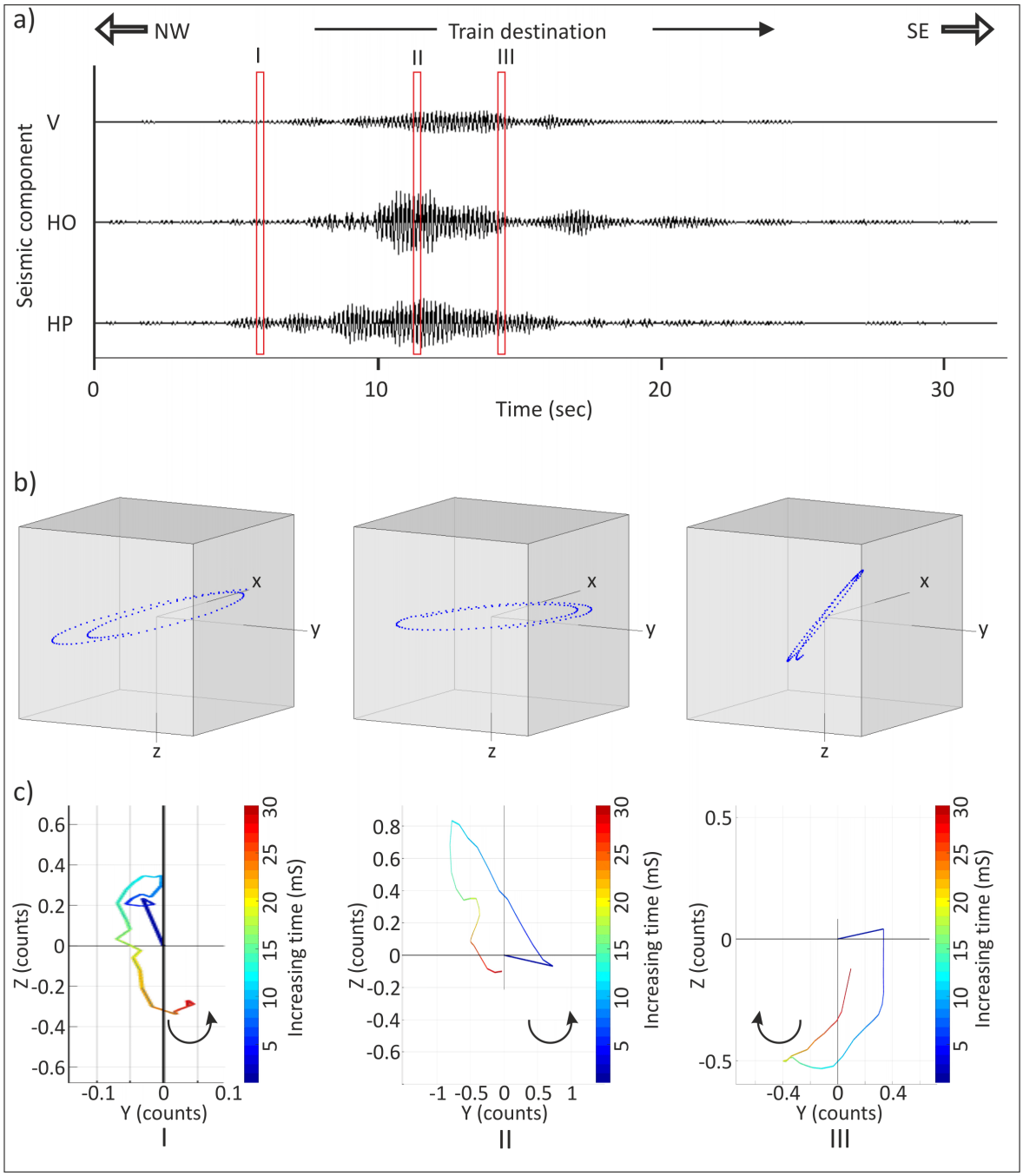

Figure 5-22: Particle motion plots for a Midland passenger train traveling in NW->SE direction, a) three components seismic traces with red rectangles representing the selected window, b) particle motion plots using Reflex, c) particle motion plots using Matlab showing the propagation direction when the train is I) approaching, II) adjacent and III) receding from the seismic station respectively.

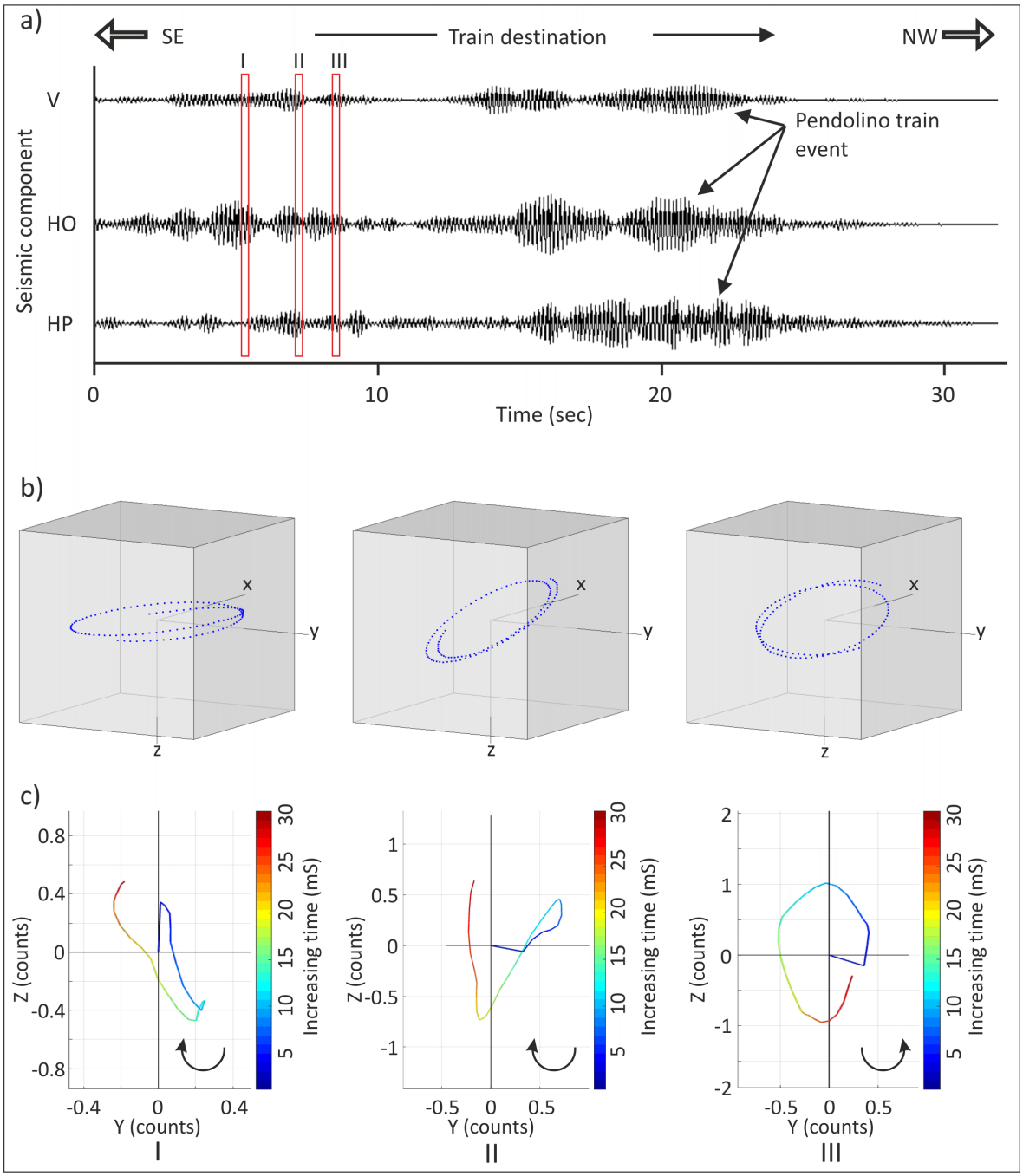

Figure 5-23: Particle motion plots for a Midland passenger train travelling in SE->NW direction, a) three components seismic traces with red rectangles representing the selected window, b) particle motion plots using Reflex, c) particle motion plots using Matlab showing the propagation direction when the train is I) approaching, II) adjacent and III) receding from the seismic station respectively.

5.4.3 Particle displacement on the vertical and horizontal seismic components

The maximum and minimum seismic wave vertical component amplitudes were measured on all 24 geophones on the LLSA no.1 array, all being at a distance 30 m northeast from the embankment, with channel 1 being located at the southeast end of the array (Figure 5-5 and Figure 5-6).

Figure 5-24 shows the maximum and minimum seismic wave amplitude values on vertical components from trains travelling to the NW were smaller than those trains travelling to the SE, even when the shorter distance from the array to the bound train was taken into account. This was also true for data collected from the SLSA no.4 located at the southwest side of the train track, even though NW bound trains use that side of the train track. In addition, the maximum seismic amplitude value of the vertical component for SE bound trains increased to the SE, whilst for NW bound trains, the maximum seismic wave amplitude value on the vertical component remains fairly constant across the array (Figure 5-24).

These results were interpreted as being due to an effect of the thickness variation of superficial deposits which increase in thickness towards the SE, as suggested by the microgravity survey. For more details about the microgravity surveys see chapter four, section 4.6. These results contrast with the findings of Quiros *et al.* (2016) who record similar vibrations from trains travelling in opposite directions at their site.

Another interpretation is that it might be that the vibrations propagate through different material when approaching each geophone, when the trains travel either destination.

This is particularly true when near the River Trent. Train speed and train load might also have another effect on the varying wave amplitudes.

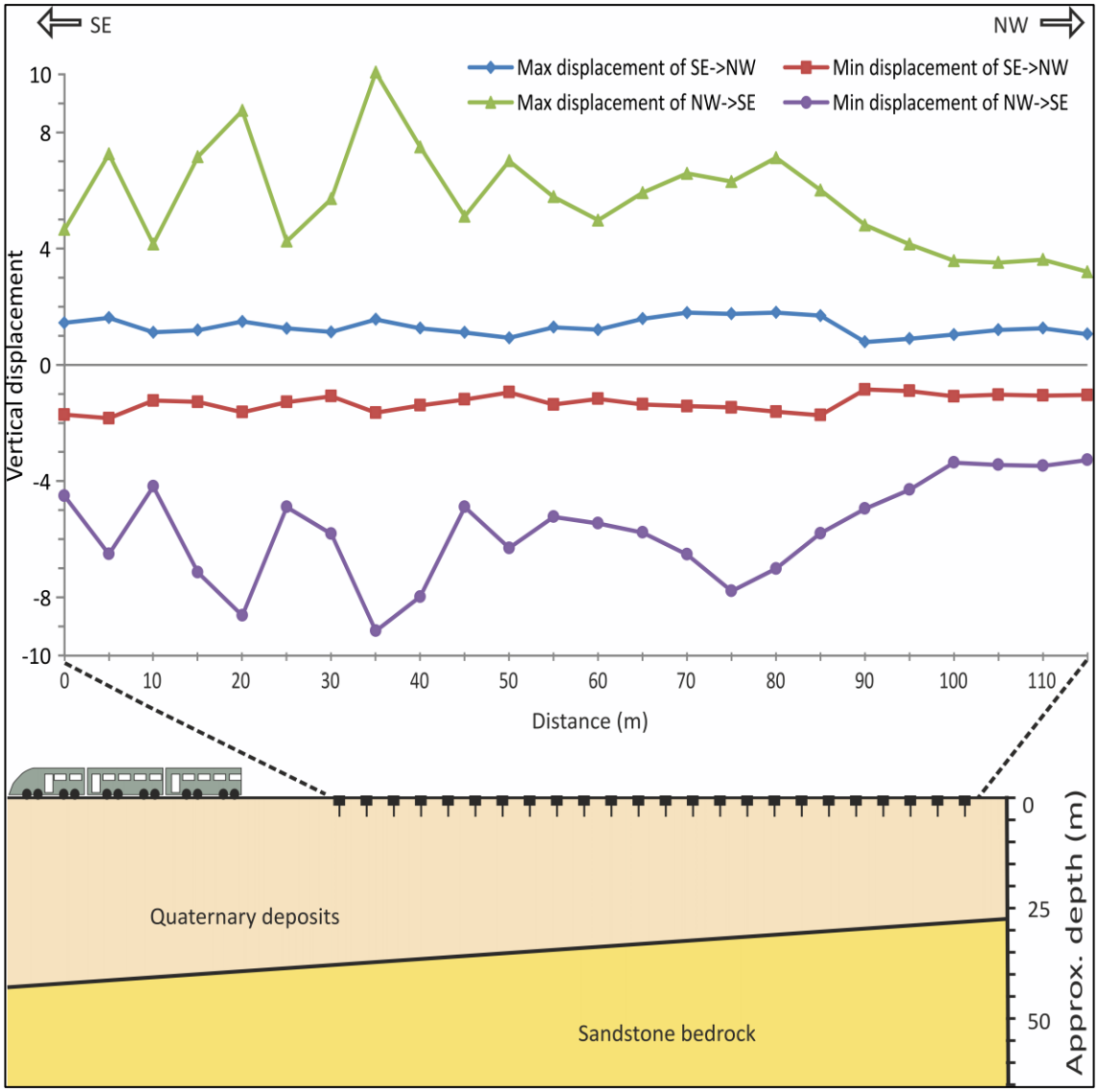

Figure 5-24: Maximum, minimum and best-fit linear correlation lines of vertical particle displacement when passenger train (Pendolino) passing the site either direction. Displacement values represented in the figure are averaged for three passing trains (i.e. records). Geophones were spaced 5 m apart.

Another particle motion displacement analysis was performed for the vertical and the horizontal components using the data from the SLSA no.1 array (see Figure 5-5 for location). The analysis was performed to analyse the vibrations' attenuation away from the railway embankment (Figure 5-25). The analysis shows that the vertical component had relatively larger particle motion displacement when compared to the horizontal component data, which might be related to Rayleigh propagation. Analysing all three component datasets, SE-bound trains generated relatively larger particle motion vibration displacements when compared to NW-bound trains. The vibrations' attenuation could also be seen with distance away from the railway (Figure 5-25).

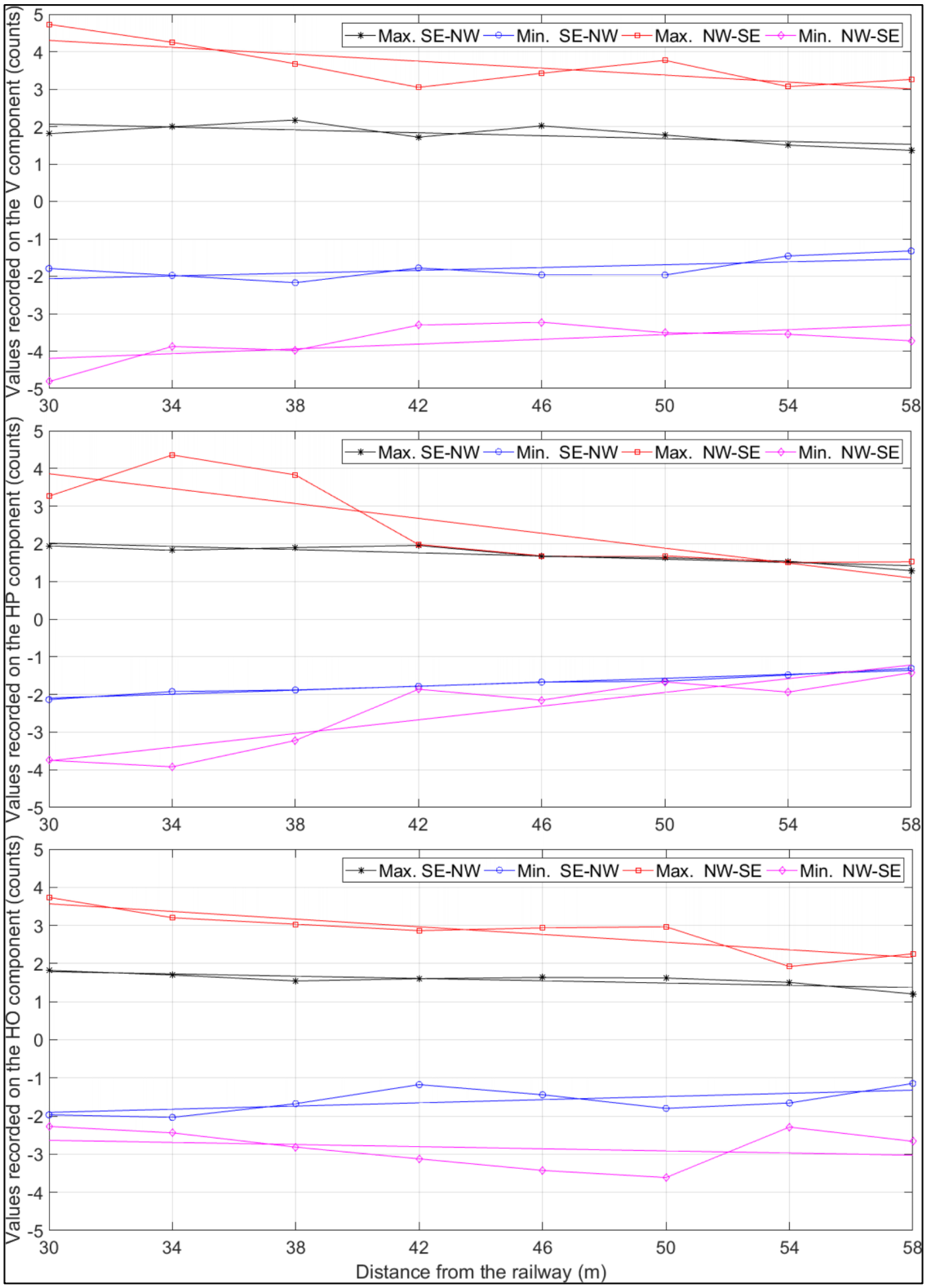

Figure 5-25: Particle motion displacement analysis for the vertical and horizontal displacements in an orthogonal orientation to the railway embankment, using the vibrations from the SLSA no.1 array (see Figure 5-5 for location).

5.4.4 Doppler Effects

The train-induced vibrations are generated by moving sources, therefore, the observed vibrations would be expected to display a Doppler Effect which might be observable on the spectrograms, *i.e.,* a shift to higher frequencies with an approaching train and lower frequencies as it recedes. Fuchs *et al*. (2018) undertook a Doppler analysis for a fixed point at 300 m from the train track in their study using the following equation:

$$f_{obs}(t) = \frac{f_{source}}{(1 - \left[\frac{v}{c * \sqrt{1 + \frac{d^2}{v^2 * t^2}}}\right])} \qquad (5-1)$$

Where f_{obs} is the observed frequency, f_{source} is the emitted frequency from the source, t is time, v is the source velocity (the train in this study), c is the wave velocity and d is the offset between the source and the receiver.

The travelling train speed and the soil wave velocity were determined as the key site parameters, with a frequency shift found to be up to 2 Hz at the recording station between the approaching and receding train.

In this study, vibrations were observed at 30 m from the track; therefore, a theoretical Doppler Effect was analysed for points located at different distances from the track using the equation above. At 20 Hz, train speed was 40 m/sec and soil wave velocity was 1000 m/sec, the Doppler Shift was found to be approximately ±0.8 Hz with the transition being smoother with increasing offset from the track (see Figure 5-26).

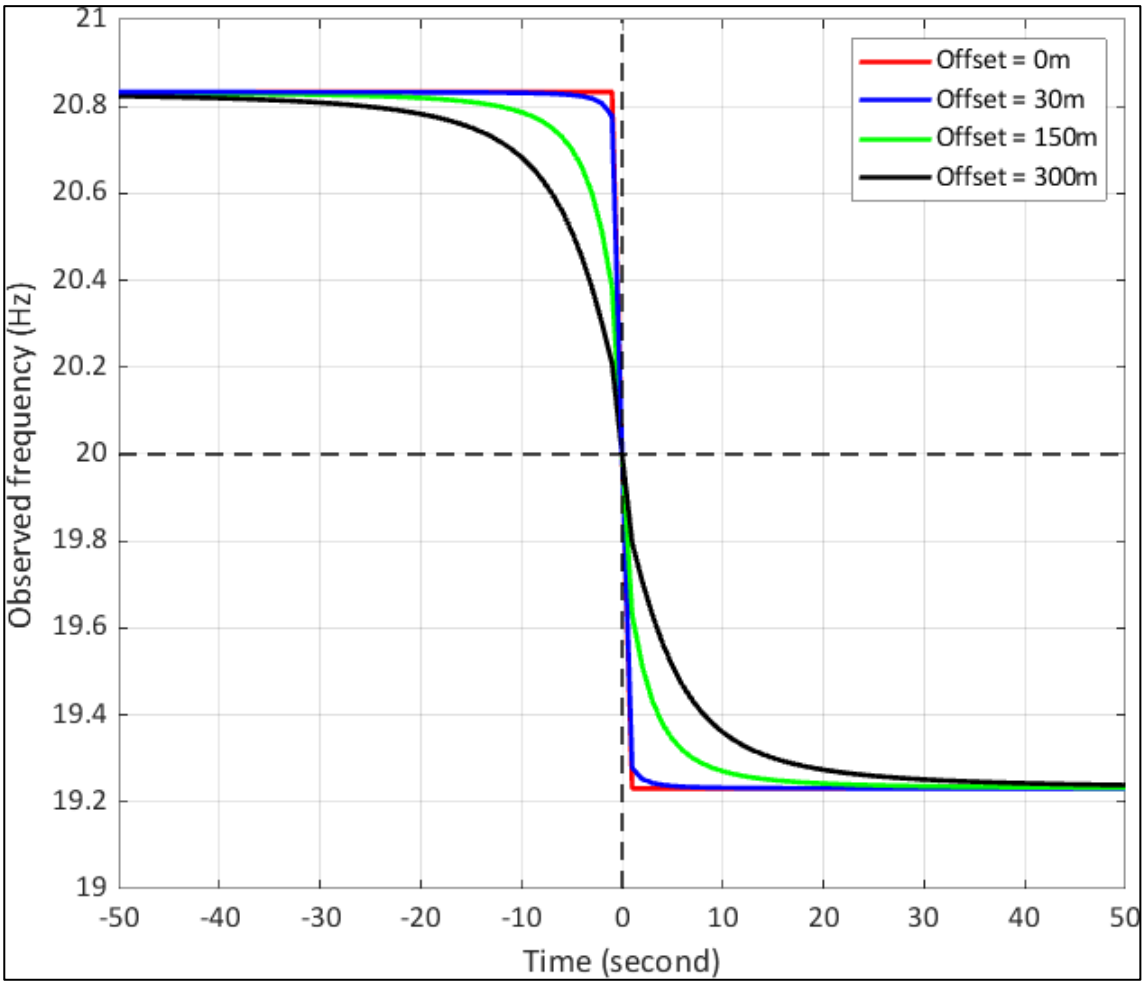

Figure 5-26: Expected Doppler shifts at 4 different distances from the track (see key), with train speed at 40 m/s, soil wave velocity of 1000 m/s and the emitted frequency of 20 Hz.

However, this theoretical frequency shift is not particularly noticeable above the noise on the recorded spectrograms (Figure 5-27). The spectrograms were performed for all train types (Pendolino and Midland passenger and heavy goods freight trains) travelling in both directions (i.e. SE->NW and NW->SW) and for each of the three seismic components. Consequently, it is unlikely that Doppler effects will influence shear wave velocity profile determination (Figure 5-27). For the full recorded spectrograms, see appendix G.

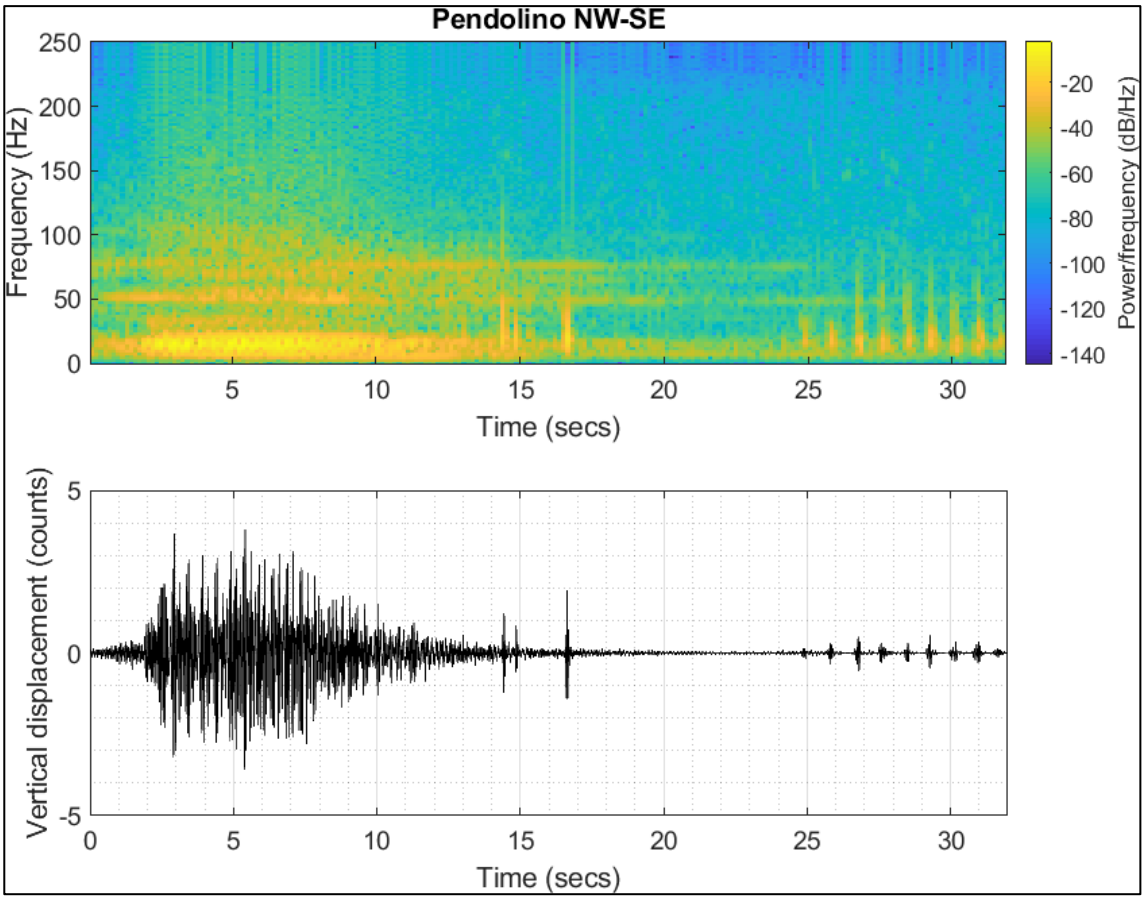

Figure 5-27: top) spectrogram of a NW->SE travelling Pendolino passenger train looking at the vertical component, bottom) seismic trace of the observed vibration, using the vibrations from the SLSA no.2 (see Figure 5-5 for location).

5.4.5 Comparison of seismic surveys from passing trains travelling in different directions

5.4.5.1 Comparison of the effective investigated depth range

The datasets from the three seismic components were processed to produce 1D shear-wave velocity-depth profiles for all trains, divided into SE->NW travelling trains and NW->SE travelling trains. Generally, the long straight seismic arrays (LLSA no.1 & LLSA no.2) datasets for all the trains had a greater range of effective investigated depth than the short arrays as would be expected (see Figure 5-28, Figure 5-29 and Figure 5-30) for the

LLSA no.1 dataset examples. Figure 5-31 shows an example of frequency-phase velocity curve of the horizontal orthogonal component, data acquired from LLSA no.1. The differences in the investigated depth between the long and short arrays are related to the length of the deployed arrays, the longer array the deeper investigated depth and, therefore, the investigated depth of the long arrays cannot be compared with the investigated depth of the short arrays. The comparison, mainly, would be among the investigated depth from different seismic components of the same seismic array. The short linear seismic arrays typically gave results that were not consistent with known ground conditions; see Figure 5-32, Figure 5-33 and Figure 5-34. Figure 5-35 represent the frequency-phase velocity curve of the horizontal orthogonal component of the SLSA no.1. The frequency-phase velocity curves were generated using the SeisImager/SW software; uncertainty analysis of the generated curves could not been determined due to the limited functions of the software. Other algorithms, for example, MuLTI (Multimodel Layered Transdimensional Inversion) can be utilized for the uncertainty analysis and for the joint inversion as well using another data set. For more details about the MuLTI joint inversion tool, see Killingbeck et al., (2018). For the shear wave velocity-depth profiles of LLSA no.2 array and SLSA no.2-4 see appendix H, for the rest of the frequency-phase velocity curves, see, appendix I. The valid depth range of shear-wave velocities for all the collected data sets of the long and short linear arrays are summarized in Table 5-4.

Table 5-4: Depth range bgl of valid shear wave velocity determinations for all the collected data sets, depths measured in metres; V is the vertical component, HP is the horizontal parallel component and HO is the horizontal orthogonal component.

Array	All trains group			SE->NW trains			NW->SE trains		
	V	HP	HO	V	HP	HO	V	HP	HO
LLSA no.1	10-60	8-50	8-40	10-65	10-50	8-38	15-55	10-55	7-40
LLSA no.2	10-50	8-35	7-30	10-50	10-35	7-30	10-50	10-40	7-30
SLSA no.1	6-14	6-14	5-17	6-18	7-13	7-18	6-13	6-15	6-17
SLSA no.2	7-11	8-16	6-14	8-10	7-15	614	7-12	6-16	6-15
SLSA no.3	6-18	8-15	8-17	6-17	8-15	8-16	6-19	8-15	6-17
SLSA no.4	6-22	7-16	6-17	6-22	11-15	6-16	7-22	7-16	6-16

The investigated depth bgl ranges for the vertical component of datasets recorded from the LLSA no.1 and LLSA no.2 was greater than the investigated depth range bgl for the horizontal components (Table 5-4). For all the datasets the horizontal parallel component resolved velocities deeper than the horizontal orthogonal component. This confirms that low frequency Rayleigh waves are best recorded on vertical component geophones, and they are better recorded as coherent waves as the train is approaching or receding the geophone on the horizontal parallel component than on the horizontal orthogonal component when the train is adjacent to the array as the Rayleigh waves are less incoherent. There was little observable difference between SE->NW and NW->SE travelling trains datasets.

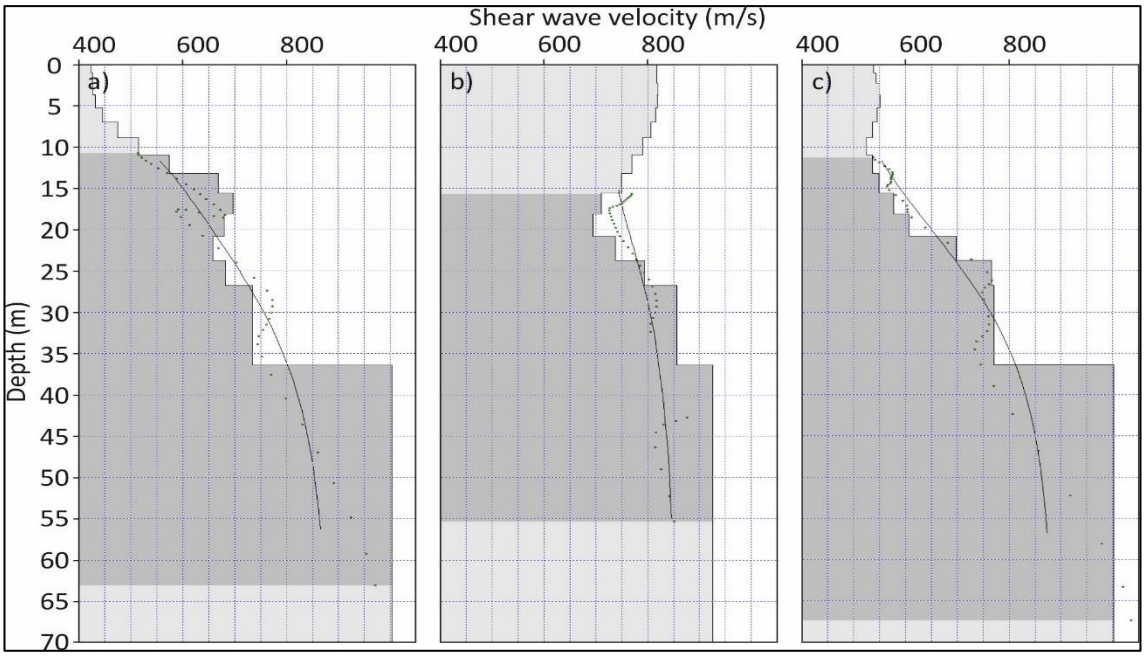

Figure 5-28: Shear-wave velocity-depth profile from vertical component data acquired from LLSA no.1 array (see Figure 5-5 for location), a) for all trains, b) for NW->SE travelling trains, and c) for SE->NW travelling trains. Dots on profiles show results generated using one third wavelength method; the curve on the profile represents the theoretical dispersion curve. The dark grey area shows the effective investigated depth.

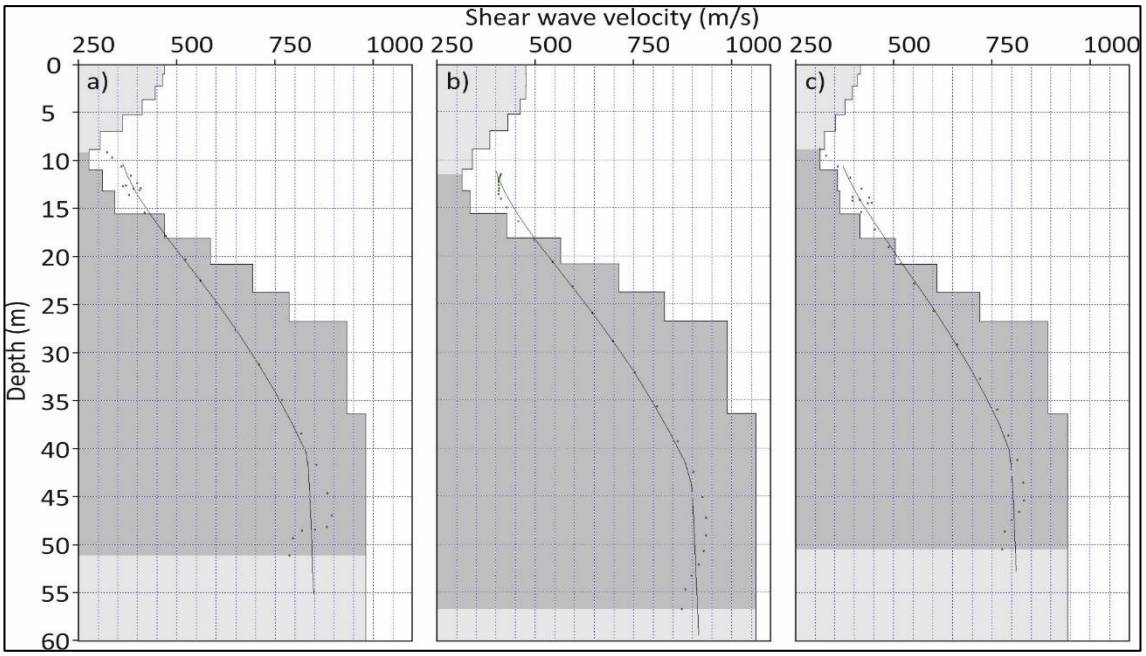

Figure 5-29: Shear-wave velocity-depth profile from horizontal component parallel to the railway embankment, data acquired from the LLSA no.1 array (see Figure 5-5 for location), a) for all trains, b) for NW->SE travelling trains, and c) for SE->NW travelling trains. Dots on the profile show results generated using one third wavelength method; the curve on the profile represents the theoretical dispersion curve. The dark grey area shows the effective investigated depth.

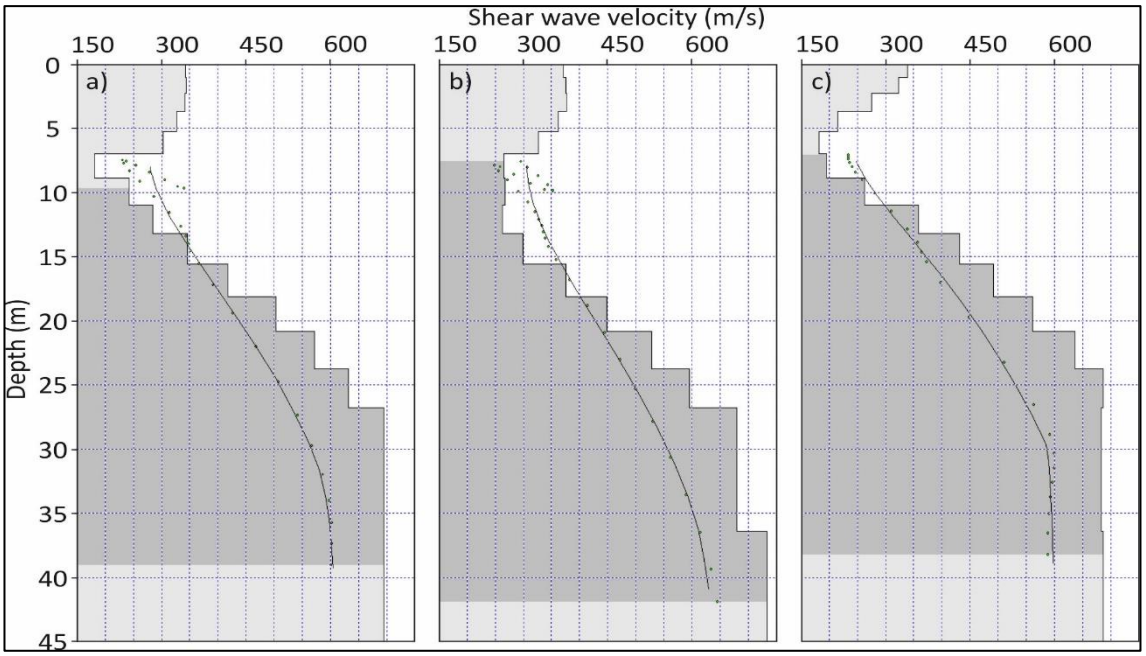

Figure 5-30: Shear-wave velocity-depth profile from the horizontal component orthogonal to the railway embankment, data acquired from the LLSA no.1 array (see Figure 5-5 for location), a) for all trains, b) for NW->SE travelling trains, and c) for SE->NW travelling trains. Dots on the profile show results generated using one third wavelength method; the curve on the profile represents the theoretical dispersion curve. The dark grey area shows the effective investigated depth.

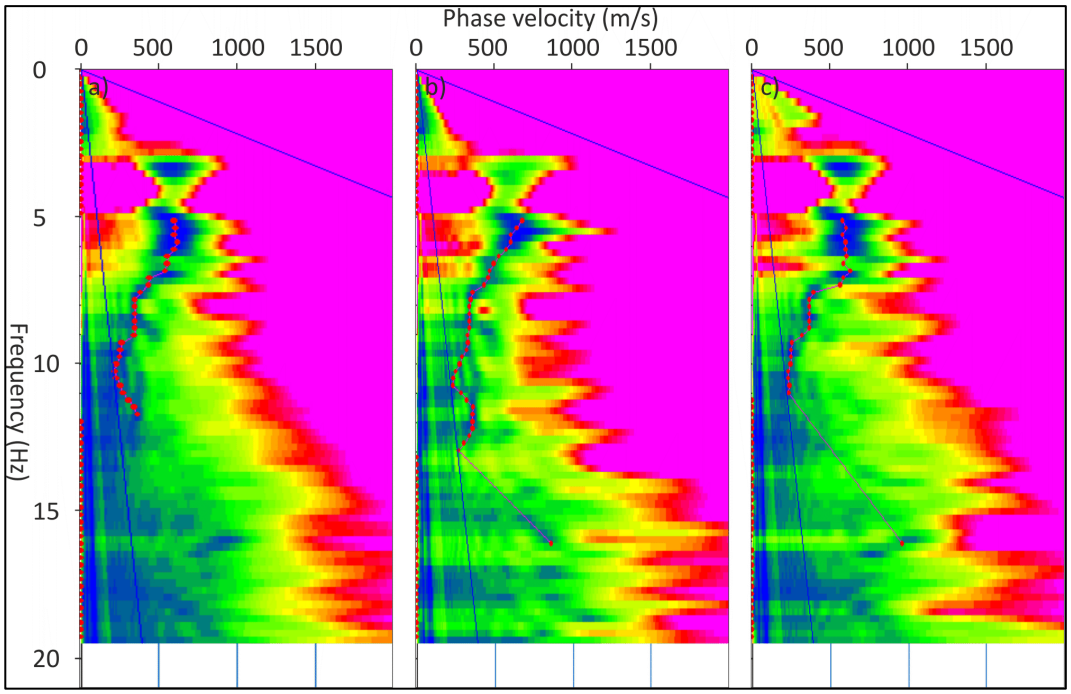

Figure 5-31: Frequency – phase velocity profile from horizontal orthogonal component, data acquired from LLSA no.1 array, a) for all trains, b) for NW->SE travelling trains, and c) for SE->NW travelling trains, using the vibrations from Rugeley site, see Figure 5-5 for location.

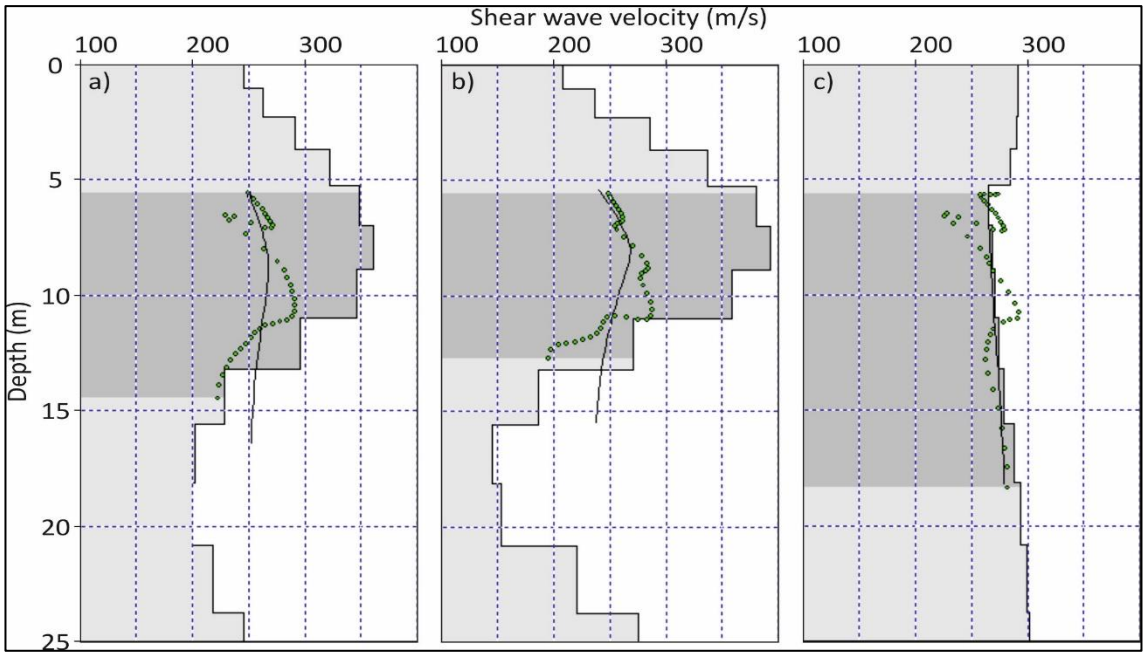

Figure 5-32: Shear-wave velocity-depth profile from the vertical component, data acquired from the SLSA no.1 (see Figure 5-5 for location), a) for all trains, b) for NW->SE travelling trains, and c) for SE->NW travelling trains. Dots on the profile show results generated using one third wavelength method; the curve on the profile represents the theoretical dispersion curve. The dark grey area shows the effective investigated depth.

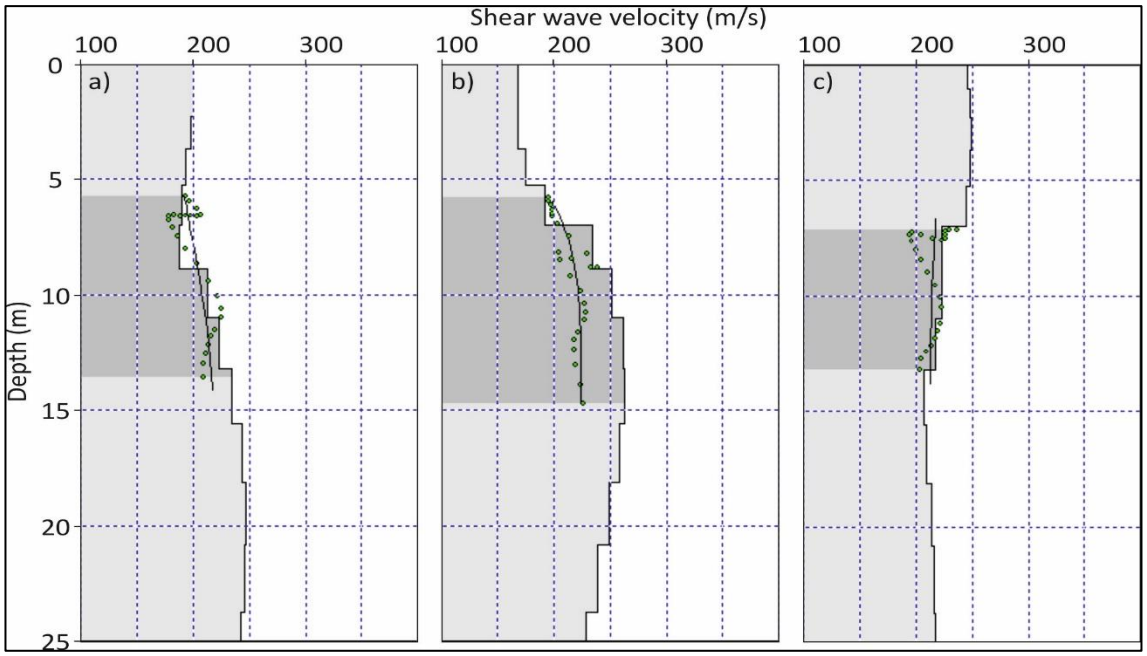

Figure 5-33: Shear-wave velocity-depth profile from the horizontal parallel to the railway component, data acquired from the SLSA no.1 (see Figure 5-5 for location), a) for all trains, b) for NW->SE travelling trains, and c) for SE->NW travelling trains. Dots on the profile show results generated using one third wavelength method; the curve on the profile represents the theoretical dispersion curve. The dark grey area shows the effective investigated depth.

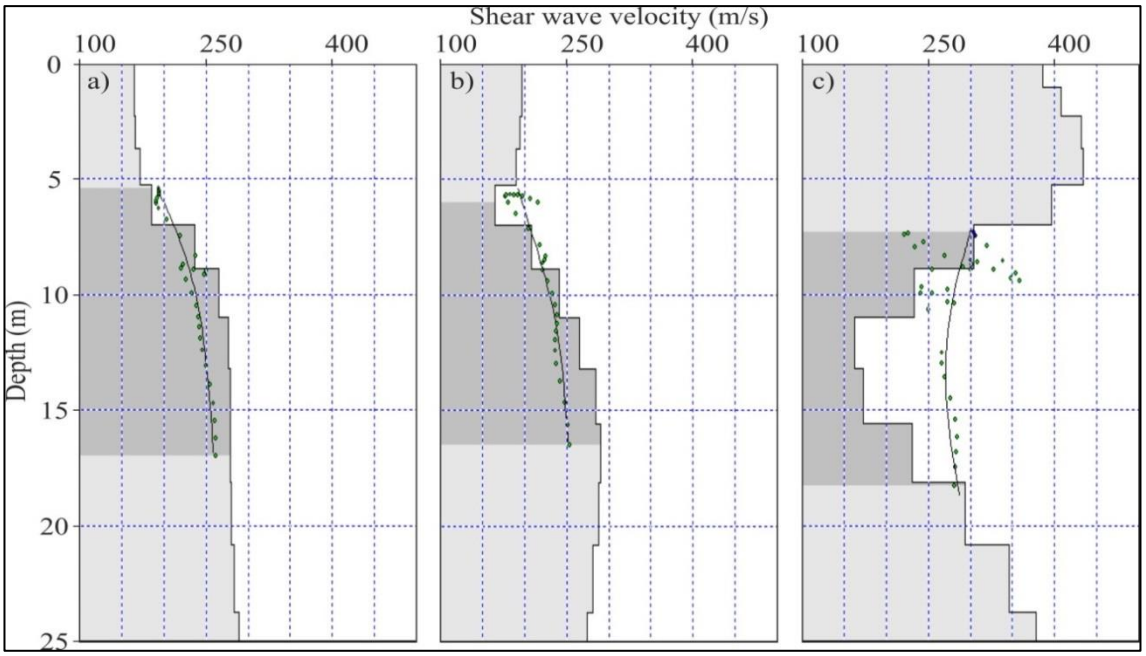

Figure 5-34: Shear-wave velocity-depth profile from the horizontal orthogonal to the railway component, data acquired from the SLSA no.1 (see Figure 5-5 for location), a) for all trains, b) for NW->SE travelling trains, and c) for SE->NW travelling trains. Dots on the profile show results generated using one third wavelength method; the curve on the profile represents the theoretical dispersion curve. The dark grey area shows the effective investigated depth.

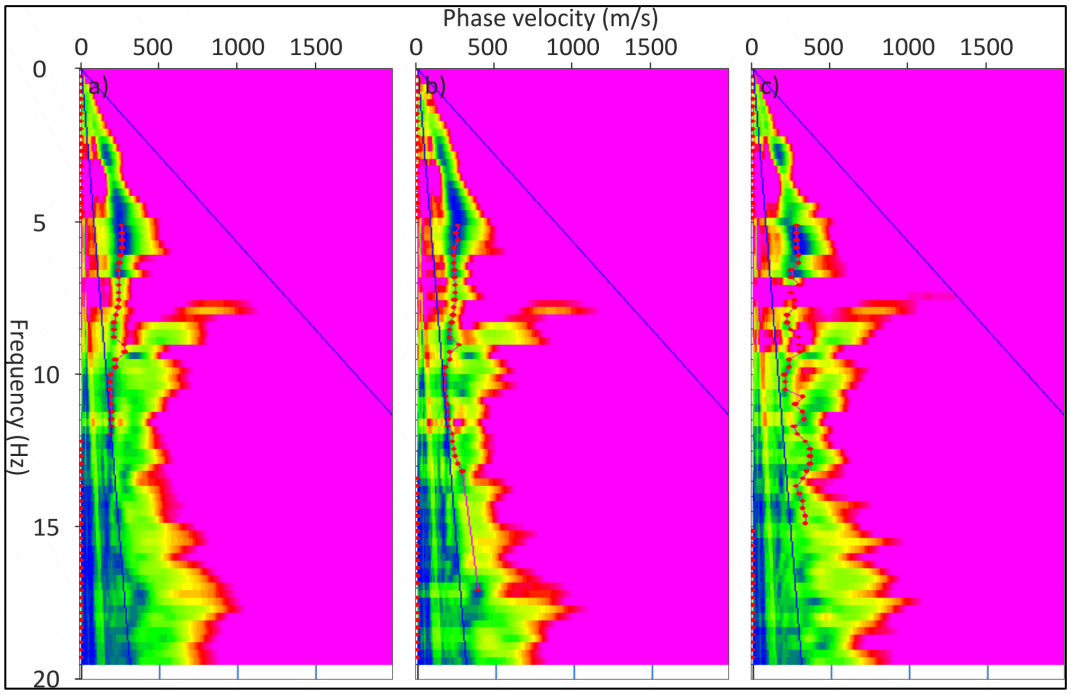

Figure 5-35: Frequency – phase velocity profile from horizontal orthogonal component, data acquired from SLSA no.1 array, a) for all trains, b) for NW->SE travelling trains, and c) for SE->NW travelling trains, using the vibrations from Rugeley site, see Figure 5-5 location and.

5.4.5.2 Comparison of shear-wave velocity profiles

Because the long linear seismic arrays resulted in deeper effective investigated depths bgl, the resulting shear wave velocity-depth profiles from the arrays will be used to compare wave velocities from different seismic components and different train groups. The shear-wave velocity-depth profiles obtained from the SLSA no.1-4, the manual arrays no. 1-4 and the L-shape arrays 1-4 will not be compared (but see appendix H).

The vertical component data produce different shear-wave velocity-depth profiles from different train directions, e.g. see the LLSA no.1 array datasets (Figure 5-36 and Figure 5-37). The horizontal components (both HP and HO) show good agreement

between velocities obtained from the three directions for trains groups. However, the velocities determined at a particular depth were lower for the HO component than they were for HP, and neither particularly matched the velocity profiles from the vertical component (Figure 5-36).

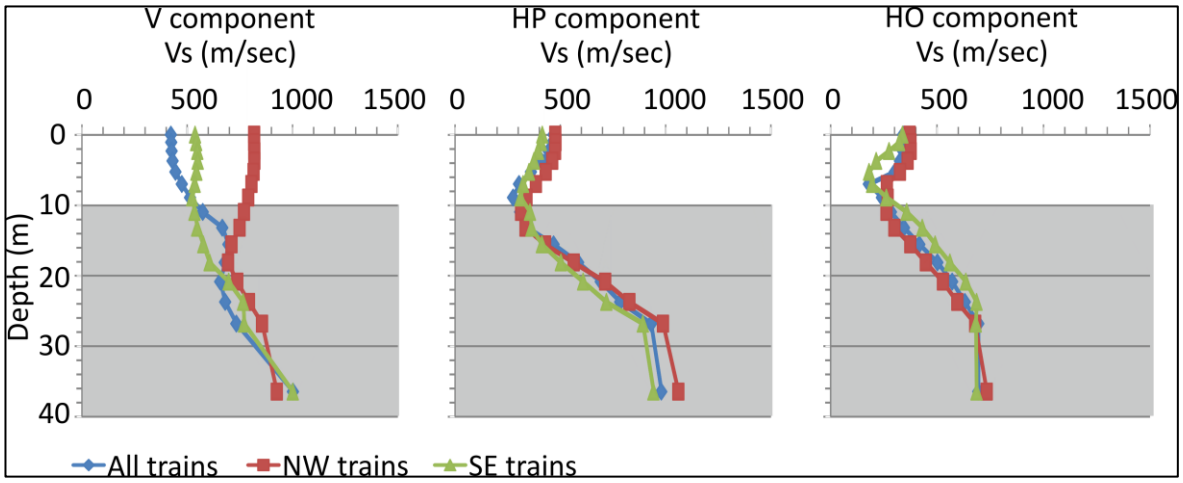

Figure 5-36: Shear wave velocity comparison based on the seismic components using data from the long linear seismic array no.1 (see Figure 5-5 for location), showing the three components and using data from all passing trains.

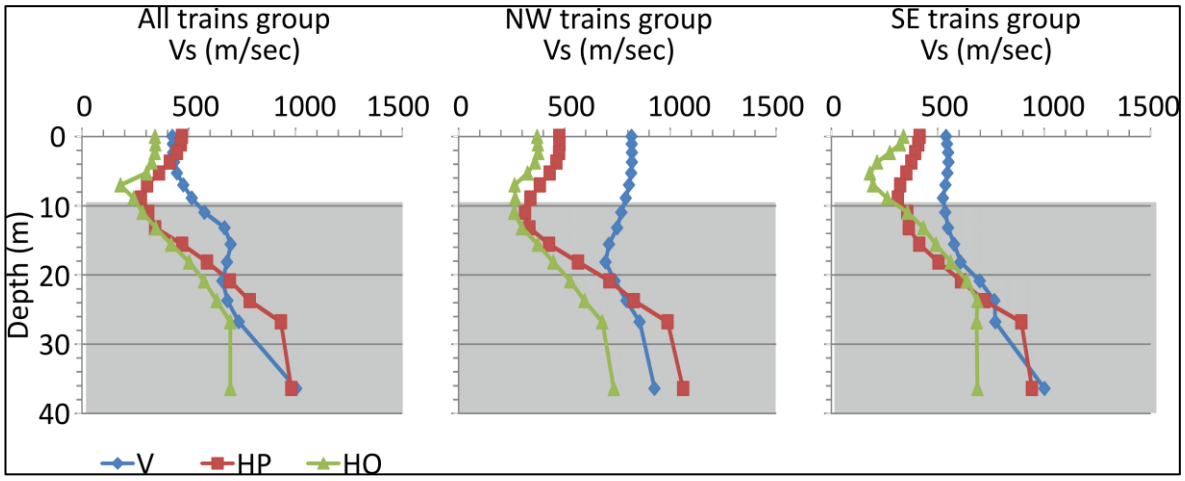

Figure 5-37: Shear wave velocity comparisons based on the train groups using data from the long linear seismic array no.1 (see Figure 5-5 for location), showing three components and using data from all passing trains.

Comparison of the shear wave velocity-depth profiles, on different seismic components and different trains groups, from data recorded from the LLSA no.2 array had almost the same results as from the LLSA no.1 array (see Figure 5-5 for location), see Figure 5-38 and Figure 5-39.

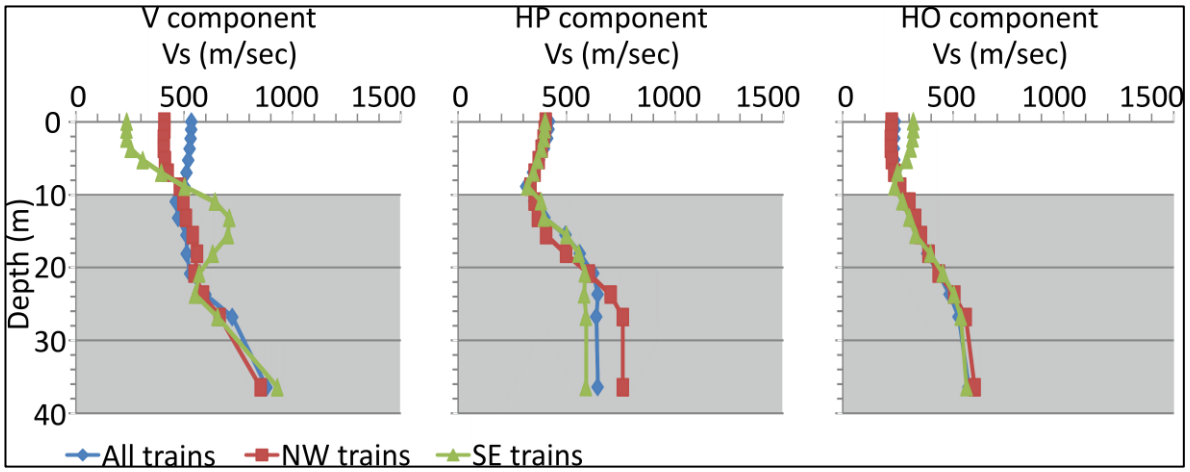

Figure 5-38: Shear wave velocity comparisons based on the seismic components using the data from the long linear seismic array no.2 (see Figure 5-5 for location), showing three components and using data from all passing trains.

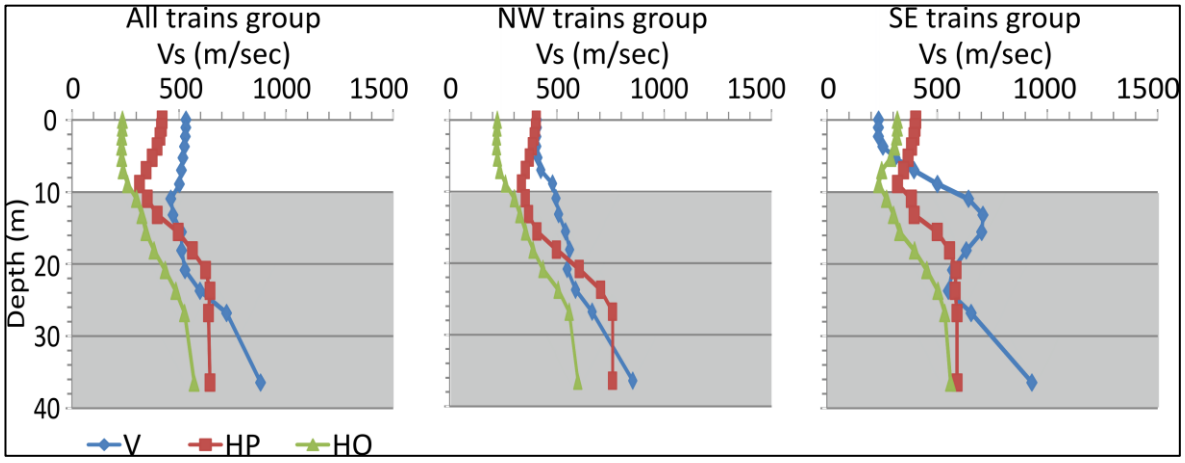

Figure 5-39: Shear wave velocity comparisons based on the train groups using the data from the long linear seismic array no.2 (see Figure 5-5 for location), showing three components and using data from all passing trains.

Comparing the frequency-phase velocity curves from the LLSA no.1 array (see Figure 5-5 for location), it was found that, for a given frequency, it had apparently different phase velocities on different seismic components (Figure 5-40 and Figure 5-41).

This result is inconsistent as it would appear that the shear-wave velocity-depth profile determined for the same area was significantly different for different components of ground motion and for the direction of travel of the passing trains; without a drilling and testing programme there is no way of determining which profile best matches true ground conditions, or indeed if none of them do.

Frequency-phase velocity comparisons for data acquired from the LLSA no.2 (see Figure 5-5 for location), on different seismic components and using different passing trains, also shows the same findings as from the LLSA no.1 (Figure 5-42 and Figure 5-43). For the frequency-phase velocity obtained from the LLSA no.1-2, SLSA no.1-4, the manual arrays no.1-4 and the L-shape arrays no.1-4 see appendix I.

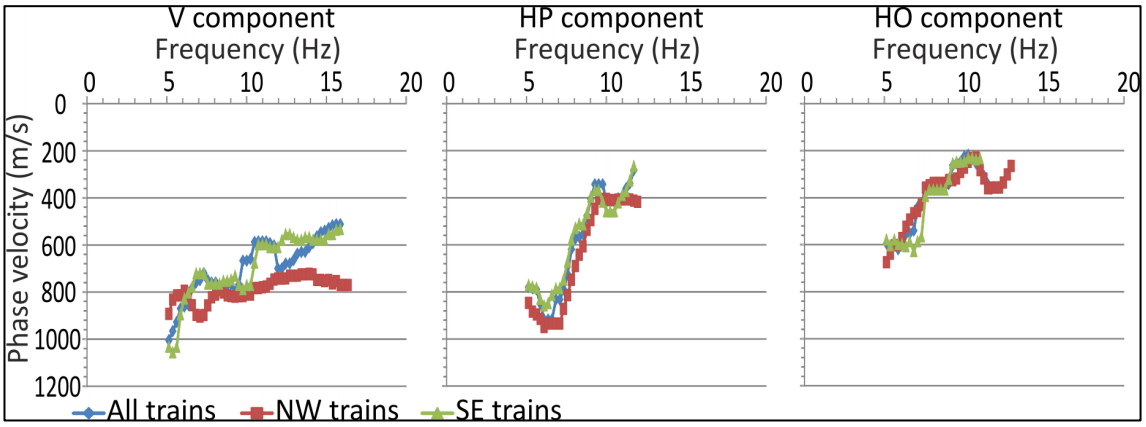

Figure 5-40: Frequency-phase velocity curve from the LLSA no.1 array datasets (see Figure 5-5 for location), using the three seismic components and the three groups of passing trains (see key), based on the seismic components shown.

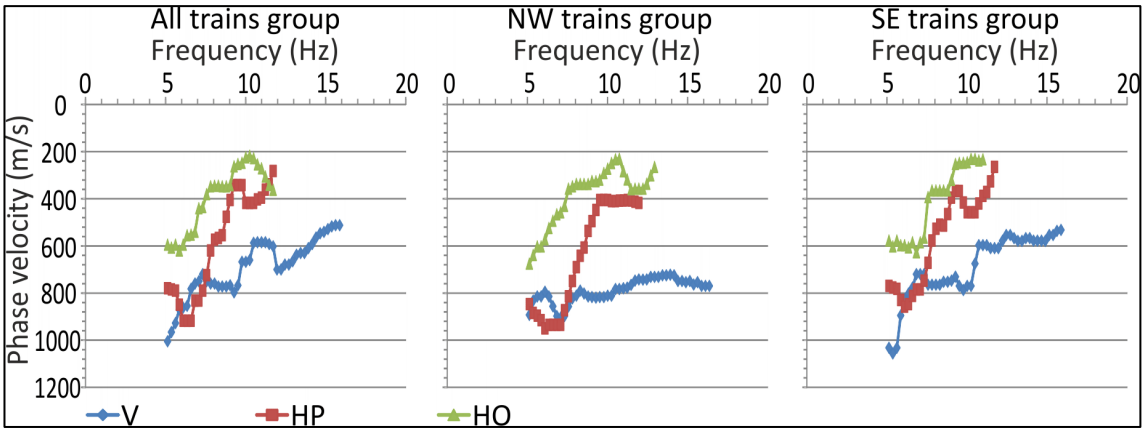

Figure 5-41: Frequency-phase velocity curve from the LLSA no.1 datasets (see Figure 5-5 for location), using the three seismic components and three groups of passing trains (see key), based on the train groupings.

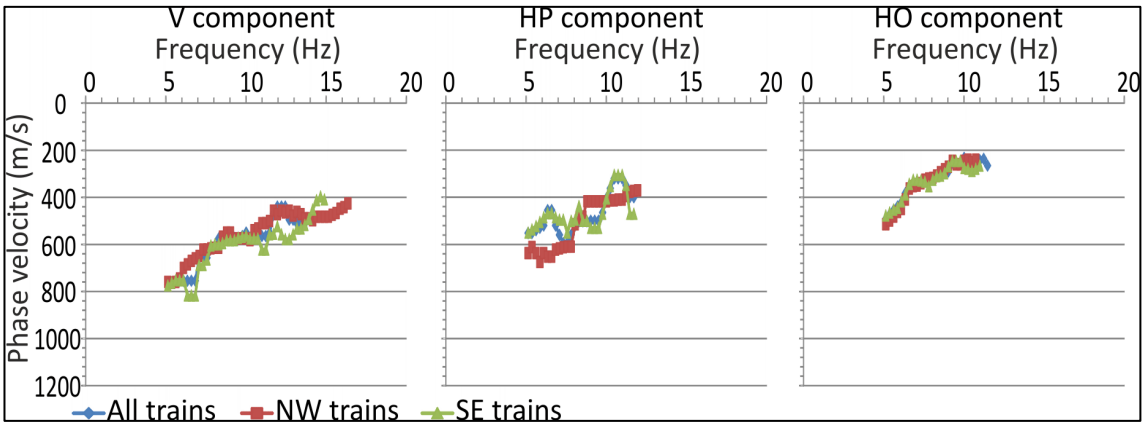

Figure 5-42: Frequency-phase velocity curve from the LLSA no.2 datasets (see Figure 5-5 for location), using the three seismic components and the three groups of passing trains (see key), based on the seismic components shown.

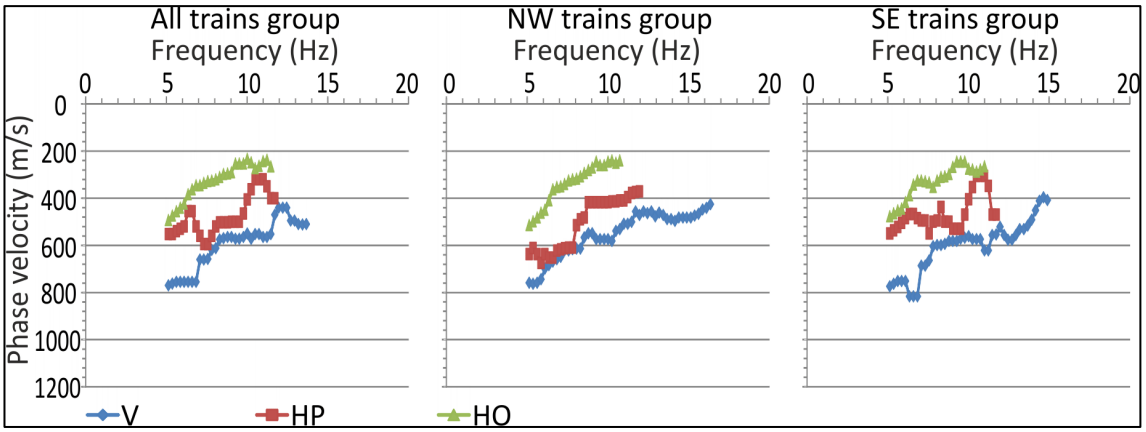

Figure 5-43: Frequency-phase velocity curve from the LLSA no.2 array datasets (see Figure 5-5 for location), using the three seismic components and three groups of passing trains (see key), based on the train groupings.

To check the different apparent wave velocities, on different seismic components, frequency-wavenumber analysis was carried out; 1) to check if apparent wave velocities were recorded by comparing the positive part of the f-k transform with the negative part of the f-k transform, and 2) to inspect if refracted body waves were observed alongside with observed surface waves, as this analysis was applied in previous studies, see, for example, Quiros *et al*., 2016.

The frequency-wavenumber (f-k) analysis of raw recorded vibrations generated by Pendolino passenger train travelling either destination (i.e. NW->SE and SE->NW) and from vertical, horizontal parallel and horizontal orthogonal components was carried out for the different train positions (i.e. train approaching, adjacent and receding). Due to the short recording time (32 seconds for the whole seismic record) and due to the even smaller recording time window for the approaching, adjacent and receding parts, the f-k analysis was not informative enough to deliver a robust interpretation. Figure 5-44 shows

the f-k analysis for a Pendolino passenger train traveling in NW->SE direction and when the train approaching the site, recording time window was 4 seconds. The asymmetry between the positive and the negative parts of the f-k transform indicates to the apparent wave velocity was recorded. When the train is adjacent to the seismic array, most the generated vibrations are approaching broadside the array which means, as long as the train is parallel to the array, an infinite wave velocity might be recorded (Figure 5-45). On the f-k transform, when the train receding (Figure 5-46), the propagated energy appears more on the negative part of the transform which indicate for recording apparent wave velocity, For the rest of the f-k transforms, see appendix J.

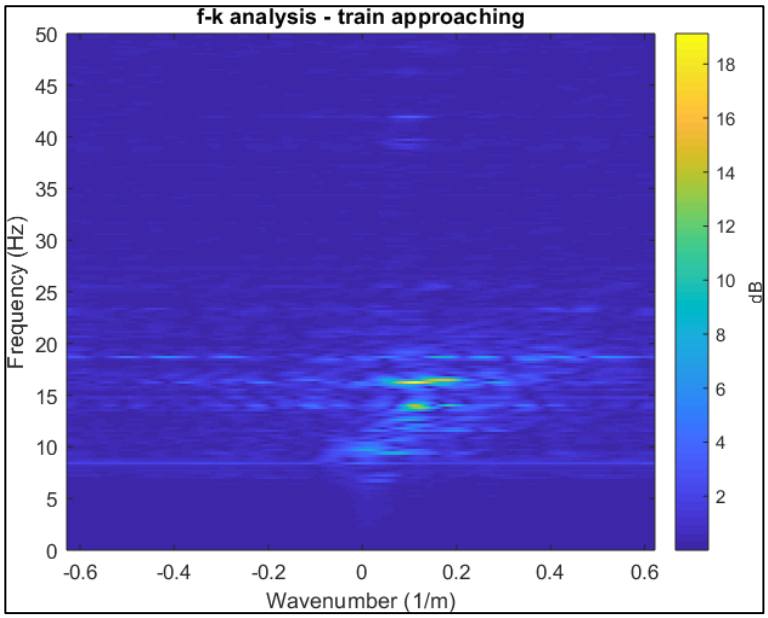

Figure 5-44: f-k analysis for a Pendolino passenger train travelling in NW->SE direction, when the train is approaching the array, data used was collect at long linear seismic array no. 1, (see Figure 5-5 for location). Time window here is 4 seconds.

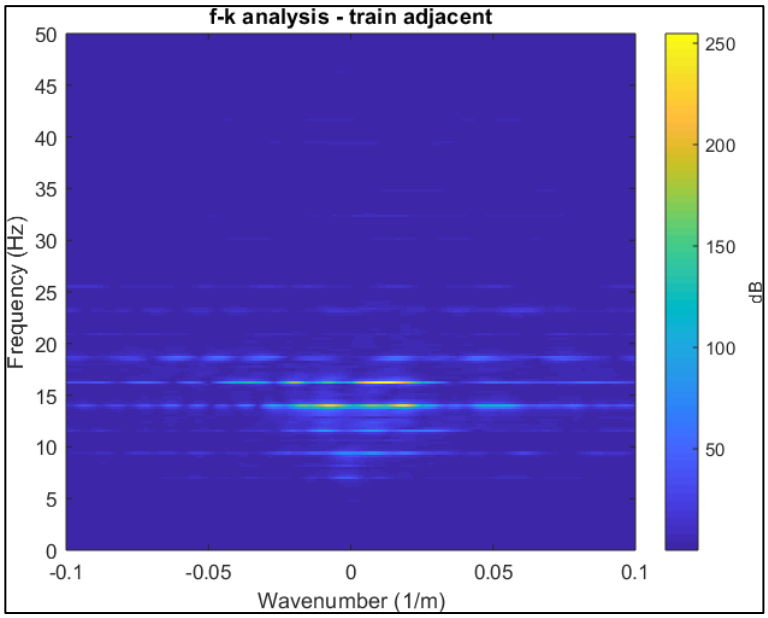

Figure 5-45: f-k analysis for a Pendolino passenger train travelling in NW->SE direction, when the train is adjacent to the array, data used was collect at long linear seismic array no. 1, (see Figure 5-5 for location). Time window here is 4 seconds.

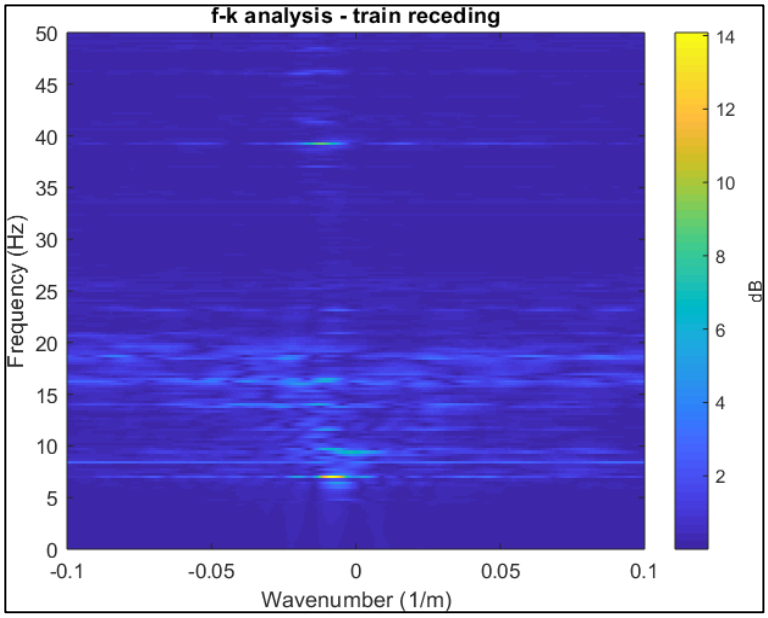

Figure 5-46: f-k analysis for a Pendolino passenger train travelling in NW->SE direction, when the train is receding, data used was collect at long linear seismic array no. 1, (see Figure 5-5 for location). Time window here is 4 seconds.

Another possible reason for the different shear wave velocities on different seismic components might be, related to the site's heterogeneity and observing Love waves on the horizontal components and Rayleigh waves on the vertical component. Safani *et al*. (2005) found different shear wave velocities, at the same investigated depth, from inverting Rayleigh and Love wavefields collected at same site and time. At 17m depth, shear wave velocity calculated using Rayleigh wave was found nearly double of that calculated using Love wave. The variations of the measured shear wave velocity were interpreted due to the site anisotropy.

Vibrations from a moving train can be generated by two different vertical and horizontal excitation mechanisms; the vertical vibrations are produced by vertical loading of the underlying physical sleepers under the railway track, whereas horizontal vibrations may come from train wheel-railway track interactions (Li *et al*., 2017). Song et al. (1989) state that Love wave can be observed using horizontal geophones oriented orthogonal to the array length, which are similar to the horizontal orthogonal component (HO) in this study. Ultimately, the observed vibrations on the horizontal parallel (HP) and horizontal orthogonal (HO) components can be more consistent with Love waves rather than Rayleigh waves; the horizontal vibrations were observed and could be seen on the particle motion plots, see, Figure 5-22 - b- II (train adjacent) and Figure 5-23 - b – I (train approaching). Because the moving trains, as a seismic source, kept moving during the recording time and the seismic array deployed at a side of the railway (i.e. the seismic source is not in line with the array), therefore, not one of the three deployed seismic components can be totally consistent with the generated vibrations and it might be that

the seismic components have different sensitivity to the generated Love and Rayleigh waves during recording time (Figure 5-47) and (Table 5-5).

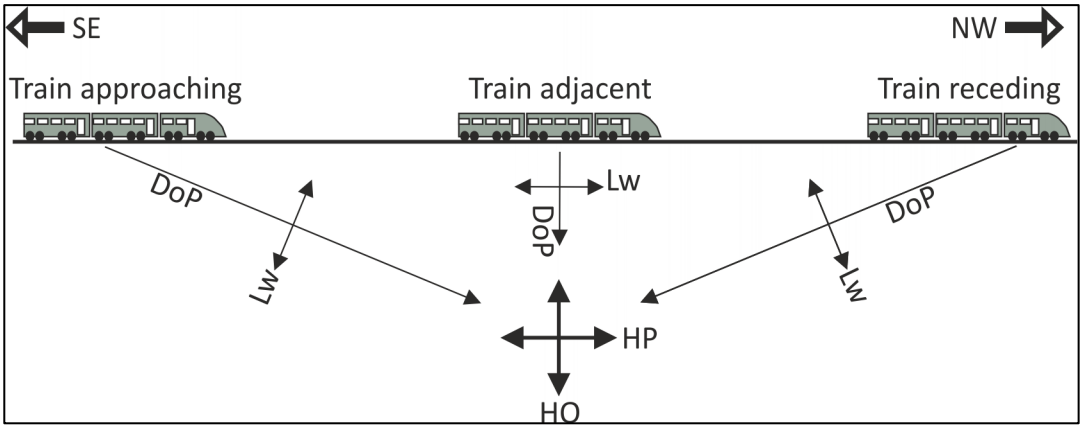

Figure 5-47: Schematic diagram shows how the generated Love wave approach the horizontal parallel (HP) and the horizontal orthogonal (HO) components when the train approaching, adjacent and receding, DoP is the Direction of Propagation and Lw is Love wave.

Table 5-5: The three seismic components compatibility with generated Love and Rayleigh waves during recording time. Wave type in parentheses indicates to less response between that certain wave type and that seismic component.

Train position	Vertical component	Horizontal parallel component	Horizontal orthogonal component
Train approaching	Rayleigh	Rayleigh (Love)	Love (Rayleigh)
Train adjacent	Rayleigh	Love (Rayleigh)	Rayleigh (Love)
Train receding	Rayleigh	Rayleigh (Love)	Love (Rayleigh)

Based on this analysis, in this study, if the difference in shear wave velocities between the horizontal parallel and the horizontal orthogonal components are ignored, the difference between the wave velocity on vertical component (i.e. inverting Rayleigh wave) and the wave velocity on the horizontal components (i.e. inverting Love wave) might be related to the site's heterogeneity.

Other studies have also shown that the railway embankment has noticeable effects on the vibrations, for example, the frequency range and the waveguide effects (e.g. see Ditzel and Herman, 2004; Connolly *et al.*, 2013). The embankment's waveguide effect may also help to generate variations in shear wave velocities from different seismic components.

5.4.6 Shear wave velocity obtained from the manual arrays

The obtained shear wave velocity-depth profiles of the manual and the L-shape arrays (both configurations) did not show reasonable results and were not consistent with the site's geology. The inversion process could not generate shear wave velocity-depth profiles for most of the L-shape arrays with 11 seismic traces. Figure 5-48 shows an example of the obtained results of the manual arrays with 20 seismic traces and (Figure 5-49) represent the shear wave velocity from the L-shape arrays with 11 seismic traces.

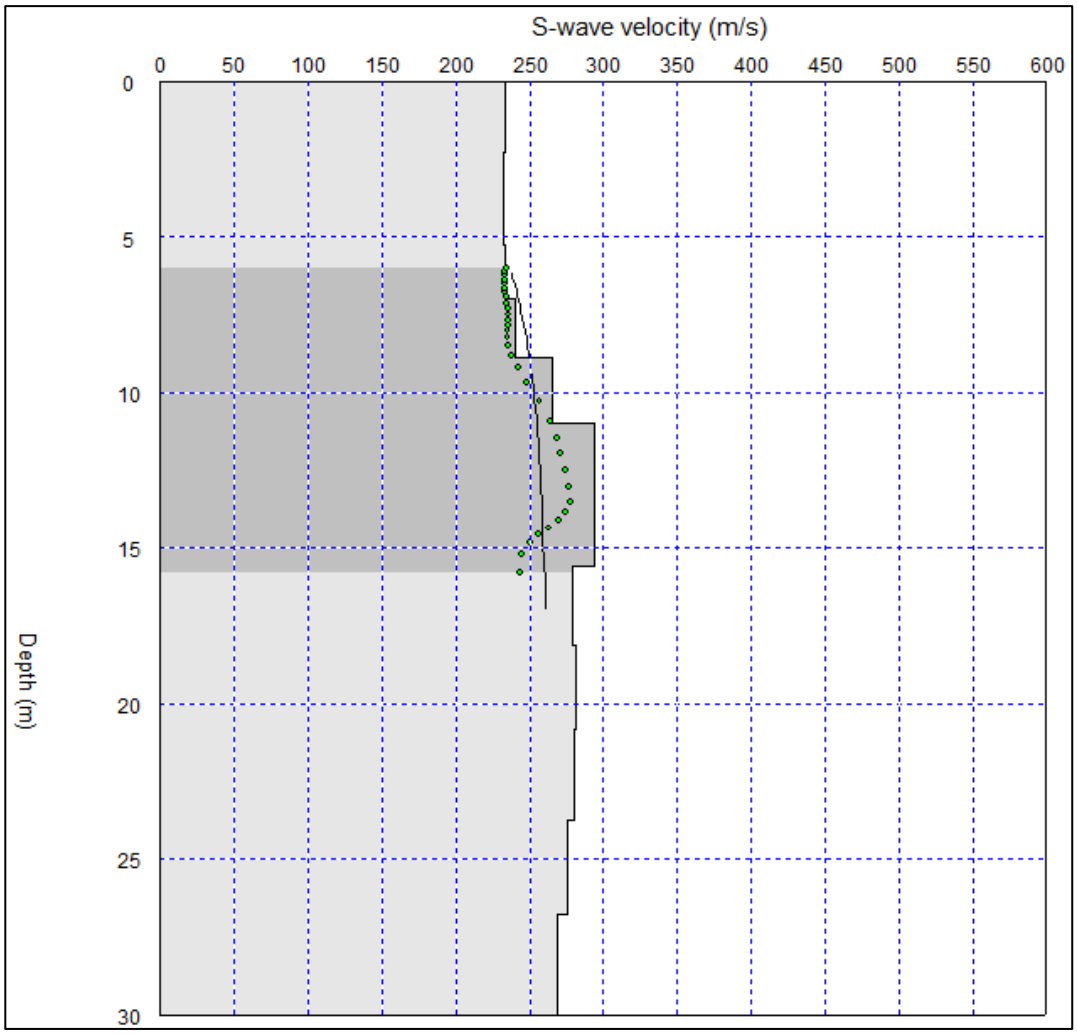

Figure 5-48: Shear wave velocity-depth profile of manual array no.1 (see Figure 5-7 for location), using data from the vertical seismic component, all passing trains and with 20 seismic traces.

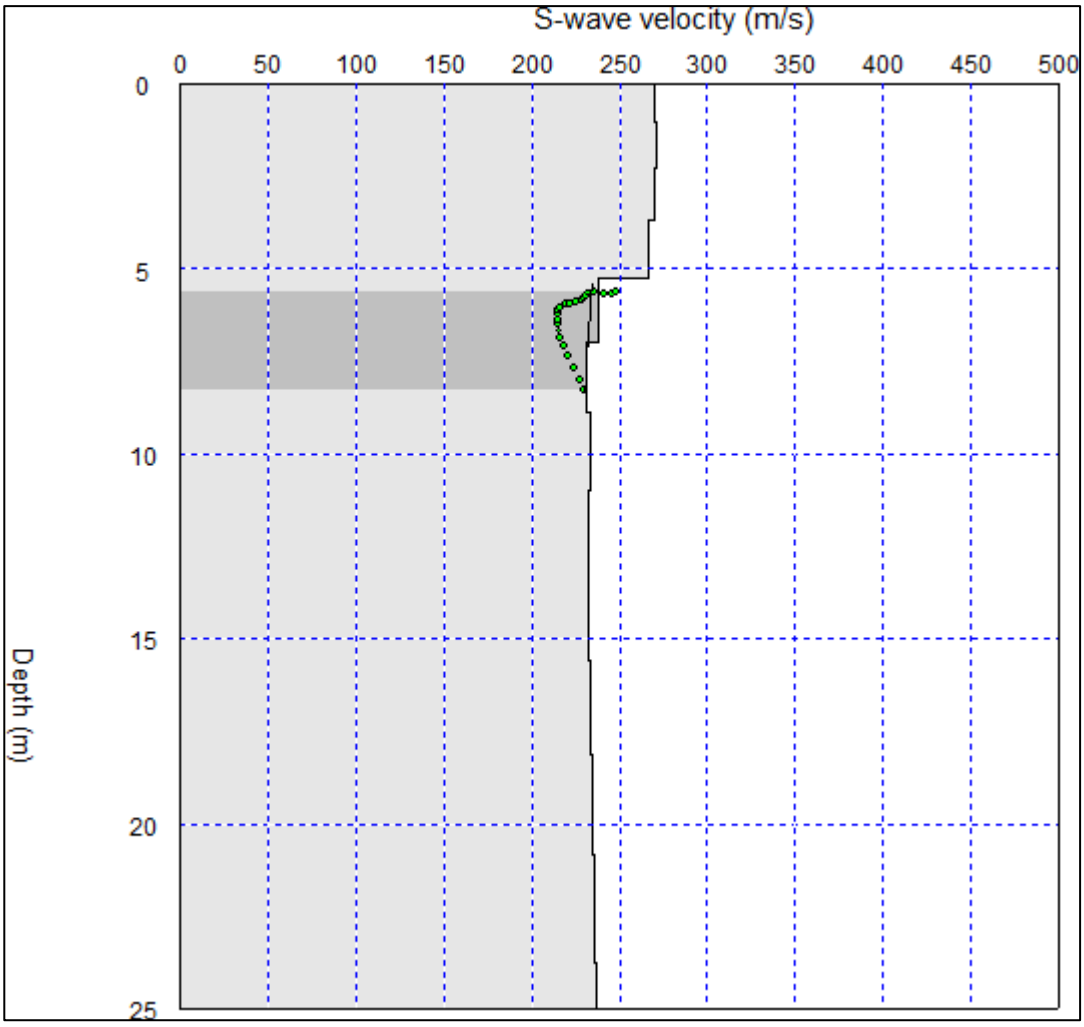

Figure 5-49: Shear wave velocity-depth profile of L-shape array no.1 (see Figure 5-7 for location), using data from the vertical seismic component, all passing trains and with 11 seismic traces.

The poor shear wave velocity-depth profiles from the observed train-induced vibrations using the manual and the L-shape arrays were interpreted to be due to the source characteristics and to the software's ability to extract the true phase velocity of the observed vibrations. A moving train, as a seismic source used in this study, keeps changing location with time when the train crossed the site. This means that the arrival angle of the generated vibrations kept changing during the recording time. The

SeisImager/SW software is designed to process surface waves that is collected by 2D arrays (e.g. the L-shape) and generated by a stationary seismic source by applying trigonometric functions. Therefore, the SeisImager/SW software could not find the true phase velocity, even using trigonometric functions, from the collected train-induced vibrations. For the rest of the shear wave velocity-depth profiles from the manual and the L-shape arrays see appendix H.

5.5 Summary

Ground vibrations generated by moving passenger and freight trains (moving on earth-raised embankments) were observed using linear and 2D seismic arrays and three-component geophones for trains moving in both directions. The refraction microtremor method was utilized to record the vibrations. The site's geological setting was that it consisted of Quaternary and river traces deposits overlying sandstone bedrock, with an inclined unconsolidated deposits-bedrock interface.

Particle motion plots shows that the observed vibrations are consistent with Rayleigh waves. The vibrations are slightly effected by Doppler Effect, based on a theoretical analysis; however, it cannot be noticed on the spectrograms (time-frequency analysis) of the observed vibrations.

The vertical component amplitude of trains travelling SE->NW are smaller than those of trains travelling NW->SE. The vertical component of trains travelling NW->SE was found to increase to the SE, whilst for trains travelling SE->NW was found to be fairly constant. This was interpreted to be due to the inclined deposits-bedrock interface and to the increasing in the thickness of the deposits to the SE. Another possible reason, the vibrations might be propagated through different materials when the trains are travelling in different directions, particularly near the River Trent.

The vibrations observed by the linear seismic arrays, oriented parallel to the railway line, produced better shear wave velocity-depth profiles (i.e. covered wider effective investigated depth and increasing in shear wave velocity with depth) than those

generated from linear seismic arrays oriented orthogonal to the railway and the manual arrays (the 2D arrays).

The resolved shear wave velocity-depth profiles from different seismic components showed different shear wave velocities with depth. The vertical component resolved the largest wave velocity, whilst the horizontal orthogonal to the railway component resolved the smallest wave velocity, which cannot be the case for the same piece of ground. The differences in the resolved wave velocities were interpreted due to the poor alignment between the deployed array and the seismic source (the trains). Therefore, most of the generated vibrations will be approaching the arrays obliquely and/or broadside and apparent wave velocities were observed rather than true wave velocities. This interpretation can be confirmed by the frequency-wavenumber analysis.

Another possible interpretation might be due to observing Rayleigh wave on the vertical component and Love wave on the horizontal components. Inverting Love wave and Rayleigh wave using same software package (the SeisImager/SW) which has no certain option to differently process Rayleigh wave from Love wave.

Chapter six: Discussion

In chapter one, the main stated goal was to test different geophysical techniques for both site characterisation and for brownfield redevelopment investigation. The electrical resistivity method was utilized to determine the location of a buried foundation in a brownfield site. Although resistivity has been used by other researchers to locate foundations (see, for example, Cardarelli et al., 2007; Khan et al., 2012), there is still uncertainty on the optimal electrical array configuration for buried foundations detection. This research highlights key practical issues and specifies the best electrode configurations and survey parameters for buried foundation surveys.

Train-induced vibrations have been previously used as passive seismic wave sources for shear wave velocity – depth profile determination (see, for example, Quiros *et al.,* 2016). Previous research has observed train-induced vibrations on one (usually the vertical) seismic component geophones being recorded. There has not been a study using train-induced vibrations to characterise a site, especially using three seismic component geophones and a geologically complex site. This research does this using the refraction microtremor method (for more details about the method, see Louie, 2001).

Finally, this study demonstrates the necessity of acquiring geophysical surveys alongside conventional tests for geotechnical site investigation as others have discussed (see, for example, McCann *et al.,* 1997). The importance of an integrated approach for a confident interpretation is demonstrated. These findings will now be discussed in this chapter.

6.1 Electrical resistivity arrays comparison for locating buried foundations

Aim 1: To determine differences in resistivity models of different electrode configurations (arrays) for eliminating a target from the host background and to demonstrate the usefulness of local traffic-induced vibrations for site investigation.

As shown in chapter 3, the electrical resistivity method was successfully applied to determine the location of a buried foundation from the host background, as has been found by other researchers (e.g. Khan *et al.,* 2012; Vargemezis *et al.,* 2013; Arjwech *et al.,* 2013; Lysdahl *et al.,* 2017). The target anomaly was successfully imaged on the resistivity models in this study, depending on the array type (see later). Although the target position was known (i.e. the target dimensions/location/depth, the construction materials of the target, the geology and the material of the host background), a reconnaissance survey was still undertaken to assess site accessibility and survey parameters following best practice (see, for example, Reynolds, 2011).

The resistivity data inversion process generated large differences between the background and the test site resistivities, 10-≈1000 Ω.m and 10^2-10^8 Ω.m, respectively. However, this study has shown that the same subsurface anomaly (i.e. the foundation target) could still be imaged differently using different resistivity array configurations. Among the four utilized arrays (Wenner, dipole-dipole, pole-dipole and pole-pole types), the Wenner and dipole-dipole were found to be optimal to delineate the target in terms of its spatial location, and to some extent, its dimensions. The Wenner array was found to be an accurate electrode configuration for lateral target discrimination, which is contrary to the perception that the array is relatively poor to detect vertical changes in the

subsurface (see, for example, Loke, 2015). It was judged that the pole-pole array was the most affected array by electrical noise and had many poor data points (e.g. zero values) recorded, as have been mentioned by others (see, for example, Loke, 2015). This ultimately will influence the performance of the array and will result in generating less accurate resistivity model for a certain target, the buried foundation in this study.

It was found that the inversion algorithm utilised had a significant effect, the least-squares smoothness-constraint inversion could image the brick foundation but the robust inversion could not, see Geotomo™ software (2004) for more information. However, they were relatively poor to delineate the foundation wall base from the host background. This was, most probably, due to the blocking effect of the target itself. Therefore, it is suggested to use a variety of algorithms to determine which one would be optimal to detect the target.

The survey design, in this study, highlighted the importance of appropriate survey design (e.g. minimum electrode spacing (0.25 m), array type, position and orientation of the survey profile (parallel and orthogonal to the wall direction)) to the target specifications (e.g. its dimensions and location), see Reynolds (2011) for more information. A survey profile (EW 2) parallel to the length of the foundation wall was deployed at a distance (0.75 m) bigger than the minimum electrode spacing (0.25 m), but could still be imaged clearly on the Wenner and dipole-dipole array datasets.

Finally, the effective investigated depth from shear wave velocity profiles using traffic-induced vibrations resolve from about 3 m down to about 11 m. Therefore, it is suggested to use active seismic surveys and/or conventional tests to investigate shallower than 3 m.

An integrated interpretation of geophysical and conventional tests

Aim 2: To perform a multi-geophysical technique site investigation using active and passive geophysical techniques with in-situ direct tests.

This case study, as shown in chapter 4, utilizes non-invasive geophysical surveys with *in situ* direct tests, it shows the integrated interpretation advantages for site characterisation and for utilizing different surveys/tests to overcome the limitation(s) of one method alone, as others have undertaken (see, for example, Vargemezis *et al.,* 2013; Cardarelli *et al.,* 2014) and for site/earthwork infrastructure investigation (see, for example, Oyedele and Olorode, 2010; Gunn *et al*., 2018).

The site deposit's stratigraphy was mapped by utilizing CPT soundings and with near-surface geophysical surveys. The CPT soundings show that the top of the gravel-rich layer get shallower toward the NW, hence, the readings were not able to be collected at even less than 1 m depth bgl in this area. In other parts of the area, the maximum investigated CPT depth bgl was 4 m (i.e. the maximum depth that can be studied using the Panda 2 data acquisition equipment). Therefore, the geophysical methods, for example, the ERT surveys and the microgravity surveys, were powerful techniques to investigate deeper depths and to fill the gaps between the CPT sounding sample positions. The ERT surveys showed high resistivity deposits down to about 7 m bgl, which was confirmed by a gravelly layer being exposed on the River Trent bank at the west side of the study area. The microgravity data is not depth restricted and allowed the mapping of the deposits-bedrock interface and the over-deepened and backfilled river valley.

The active seismic surveys, using the MASW method, were undertaken to generate 1D shear wave velocity- depth profiles and 2D shear wave velocity – depth cross sections. From these results, the variation of the site's shear wave velocity was mapped and the site's shear modulus (as a soil stiffness parameter) was determined, as others have done (see, for example, Pegah and Liu, 2016). Due to the effective investigated depth being related to the frequency range generated by the active seismic source (a sledge hammer in this study), CPT soundings datasets were used to generate the shear wave velocity – depth profile and shear modulus for shallower depths (1 m -3 m bgl).

Grain size distribution analysis showed higher coarse grain size content on samples taken from the northern parts of the studied site which confirm the high resistivity anomalies observed on the ERT models. The deposits density using a sand replacement test showed good agreement with the density obtained from the microgravity data.

Qualitative correlations between MASW and ERT datasets showed that the ERT method should be used carefully if practitioners want to use it for geotechnical site investigation (determining shear wave velocity and shear modulus). Other physical parameters, for example, soil moisture content, material type and density, should be involved in the resistivity data interpretation, as other previous studies have shown (see, for example, Sudha *et al*., 2009; Apuani *et al.*, 2015). The 2D MASW was more informative than the ERT at deepest investigated depths.

Quantitative correlations showed that the depth - density and shear modulus – density have an exponential relationship. Based on the site conditions (e.g. ground water table

location), the resistivity data have different relationships (an inverse and direct linear relationships) with shear wave velocity, shear modulus and density.

6.2 Train-induced vibrations analysis using refraction microtremor method (ReMi)

Aim 3: To test train-induced vibrations for seismic surveys to characterise a site in three dimensions.

As shown in chapter 5, ground vibrations, generated by moving trains on an earthen embankment, were collected using three-component seismic stations and different array configurations (i.e. 1D linear, and 2D L-shape and manual type arrays). The survey results indicated that the optimal survey type configuration was the linear arrays, oriented parallel to the railway embankment, the LLSA no. 1-2 in this study, which confirmed what other researchers have used (see, for example, Quiros *et al.*, 2016). The linear arrays, oriented orthogonal to the embankment (as named SLSA in this study), and the 2D arrays (i.e. the L-shape and manual types) were found to be the least useful, where the calculated shear wave velocity-depth profiles did not agree with the studied site's observed subsurface geology.

The particle motion plots, generated from ground vibrations caused by different passing train types (Pendolino and Midland passenger trains and heavy goods freight trains), showed different results when compared to standard Rayleigh wave propagation theory. The Pendolino and Midland passenger trains generated consistent ground vibrations with standard Rayleigh waves, as found by other researchers (e.g. Kim and Lee, 2000;

Motazedian *et al.,* 2011), but the heavy goods freight trains' ground vibrations did not; it works as a complex multiple sources for greater range of distance.

Observed shear wave velocities, collected using vertical geophone component, was found to have the largest velocity, in contrast to shear waves collected on the horizontal geophone orthogonal component that was found to have the smallest wave velocity. The trains direction of travel did not affect measured shear wave velocity. Observing different apparent wave velocities, on different seismic components, might be the main reason for the variation in shear wave velocity. Observing an apparent wave velocity is one of the ReMi method limitations, as has been discussed in previous studies (see, for example, Louie, 1002; Strobbia and Cassiani, 2011; Strobbia *et al.*, 2015). Other possible causes, might be the site's geological heterogeneity as others have found (see, for example, Safani *et al*., 2005). The wave guide effect of the railway embankment might also contribute to the differences in measured shear wave velocity (see, for example, Ditzel and Herman, 2004).

Doppler Shift analysis was undertaken in this study for the train-induced vibrations observed on different seismic components, different train types and for trains travelling in either destination. Analysis of results suggests that they do not represent a clear evidence of Doppler Shift, which confirms other researcher findings (see, for example, Quiros *et al*., 2016; Fuchs *et al*., 2017). A theoretical Doppler Shift analysis, for points located at different distances from the track, shows that the observed vibrations can be slightly effected by Doppler Shift which were deemed not important, this finding agrees with previous studies (see, for example, Fuchs *et al*., 2017).

The specific site geology, with variations in drift deposit thickness, was found to have an important effect on the recorded train-induced vibrations, the vibrations having relatively larger vibration magnitudes when propagating through thicker drift deposits, in comparison to those recorded through relatively thinner deposits. This finding was in contrast to the Quiros *et al.* (2016) study. Another reason could be that the energy travelling in different directions would travel through different material, notably crossing the River Trent and associated deposits when approaching from the SE direction, which may account for this difference.

6.3 Study limitation

Despite desk studies and reconnaissance surveys, some limitations were still encountered during fieldwork and data processing during the study of this thesis.

In chapter 3, in the buried foundation surveys, study test site constraints caused some difficulties to set out the remote electrodes for the pole-pole and pole-dipole resistivity arrays. The trees surrounding the test site prevented some survey profiles to be deployed at optimal distances. Finally conductive cabling from nearby buildings generated local electrical noise which affected the resistivity datasets, especially when the electrode configurations that needed remote potential and/or current electrode placements (see Reynolds, 2011 for more detail).

In chapter 4, as a comparative case study, the geophysical surveys and conventional tests both had specific limitations. The CPT soundings were conducted using the Panda 2 equipment which is limited to investigate down to 4 m depth bgl. Some of the CPT soundings were stopped at very shallow depths, even less than 1 m, for example for CPT 8, therefore, other CPT equipment, for example, an anchored drill-rig, would have been better to investigate deeper bgl. The Panda 2 also has no seismic sensor at the cone, therefore, shear wave velocity and shear modulus for the shallow depths could not be straightforwardly determined.

The resistivity surveys were conducted using the Campus™ Tigre with 64 electrodes. Large ERT surveys have to use wide horizontal electrode spacing so suffered from relatively low lateral resolution. Because of the railway electrification system, the Wenner array was

used due to its good signal:noise ratio, but has comparatively smaller horizontal coverage with depth when compared to other array types, which resulted in poor base resolution at depth. Finally the active MSAW seismic surveys were collected using a 24 geophone land streamer with 1 m geophone spacing. This will have limited the maximum investigated depth due to it being related to half of the total length of the seismic array. However, the minimum effective investigated depth relates to the highest frequency generated by the sledge hammer which was about 2 m bgl. This indicates the need of using higher frequency seismic source or a direct test, for example, seismic CPT, to better investigate beneath the ground surface.

In chapter 5, the train-induced vibrations experiment, few passing train types was the main issue, thus very few seismic records were observed from passing Midland passenger and heavy goods freight trains, when compared to passing Pendolino passenger trains. Therefore, there was not enough data to divide results based on train type and consequently prevent comparing shear wave velocity-depth profiles from different train types, even when being onsite and recording for 5 days. Also not enough passing train traffic meant that there were fewer than optimal seismic records for the passive seismic experiment. Some parts of the site were not accessible, for example, the strip field along the embankment on the east side of the train track prevented seismic arrays to be laid down close to the embankment. Equipment was also an issue, for example, available geophone frequency was 4.5 Hz which constrained depths of investigation. Seismic cable lengths were also not enough to observe vibrations that may be observed by longer arrays or indeed by smaller geophone spacings. Finally, the data was not continuously

observed using automatic seismic recorders (see, for example, Quiros *et al*., 2016), therefore, not all passing trains were able to be recorded which was unfortunate.

Chapter seven: Conclusions and future work

In this study, different geophysical techniques were utilized to perform geotechnical site characterisation. The electrical resistivity method was used to detect and to characterise a buried foundation and to test the optimal electrode configuration which can be used for buried foundation surveys redeveloped brownfield sites. In addition, non-invasive geophysical surveys were performed alongside conventional direct *in situ* CPT tests for an integrated interpretation for geotechnical site characterisation. In this conclusion chapter, the main results of the thesis are summarized and a set of recommendations for further studies are given. The passive train-induced vibrations were analysed and used to generate shear wave velocity-depth profiles from vibrations observed on different seismic components and from passing trains from both track directions.

7.1 Main findings

7.1.1 Buried foundation detection by the electrical resistivity method

For brownfield site redevelopment, the electrical resistivity method is a good non-invasive survey technique to detect buried foundations. Trialling different electrode configurations can determine the optimal array configuration to both detect and characterise near-surface buried objects. The Wenner and dipole-dipole arrays represent the best electrode configurations for buried foundation surveys, the Wenner was found to be more sensitive to resolving the target foundation base and vertical edges, whilst the dipole-dipole was found to be more accurate at resolving the foundation top. The pole-pole array was the least useful configuration due to its sensitivity to electrical noise at the

studied site; which is probably the case for most urban sites. The survey parameters and design were found to be as important as the array type. The survey profile orientated parallel to the length of the buried foundation, even set at a distance from the foundation bigger than the minimum electrode spacing, was found to produce better results when compared to the orthogonal surveys. This is most probably due to the foundation having a bigger side area and therefore looks to be a bigger subsurface anomaly. The 25 cm electrode spacing used in this study over the scaled-model, was found to be adequate to detect the buried target. For targets with bigger dimensions than the target in this study, a wider electrode spacing could be utilized.

It was found that inverting the resistivity data using different inversion algorithms generated some differences on the resulting target's anomaly in the 2D images. The least-square smoothness-constraint algorithm detected the brick wall foundation from the gravel volume when compared to the robust algorithm. In contrast, the robust inversion could discriminate the whole test site as an obvious high resistive target, with more accurate dimensions and with narrower resistivity contouring when compared with the least-square smooth-constrained algorithm data.

Passive seismic waves, generated almost by local traffic, can resolve a limited effective investigated depth range; the range was about 3 -11 m (the array size should be taken in consideration). Active seismic surveys and/or conventional tests will be needed to investigate upward to the ground surface.

7.1.2 The potential HS2 site characterisation: as a case study

Near-surface geophysical methods, such as active seismic (1D and 2D MASW surveys), electrical resistivity tomography and microgravity, along with conventional *in situ* CPT tests were collected for geotechnical investigation of a potential HS2 development site. In this case study, the effectiveness of the geophysical methods was suggested to fill a gap between the conventional geotechnical site tests and using desk study 1D borehole information.

The 1D and 2D active seismic surveys (MASW) showed that the measured shear wave velocities vary both laterally and vertically in the study site. The wave velocity of the drift deposits close to the ground surface was about 100 m/s and increased with depth (≈ 12 m) to about 400 m/s. The 2D shear wave velocity-depth cross sections, obtained by using 5 m shot point spacings, generate suitable resolutions to detect local variation in the site's recent deposits.

The site's drift deposit heterogeneity was confirmed by the electrical resistivity surveys. A high resistivity deposit (gravel-rich) layer was interpreted to be present from close to the ground surface down to about 7 m depth bgl, observed exposed on the eastern bank of the river Trent at the west side of the site. The sharp reduction on resistivity values at depths below this most probably indicated the groundwater table at the site. There were some local perched water tables present onsite, as shown on resistivity profiles that bisected the buried stream locations. The electrode spacings used in this case study were 2 m, 3 m and 4 m, the general site characteristics were detected using those electrode spacings.

The microgravity surveys, and their associated numerical model solutions, suggested the site to be an over-deepened and backfilled river valley, most probably from the last glaciation, and showed an increasing drift deposit thickness towards the south west of the study site. The determined geomaterial density, from the microgravity surveys, agreed well with the average density obtained from the sand replacement tests.

The CPT site data showed different cone resistances at different depths down to 4 m bgl and at different locations, which indicated the variation in the site top soil layer deposits as would be expected in a heterogeneous site.

The density of the material has an exponential relationship with depth and with shear modulus of the studied site, whilst resistivity data has two different linear relationships (direct and inverse) with density, shear modulus and shear wave velocity and that was based on the site conditions.

Combining the results from different surveys (i.e. geophysical and/or conventional site investigations) in an integrated survey assists in better site data interpretation and overcomes the limitations of individual method.

7.1.3 Train-induced vibration analysis using the refraction microtremor method (ReMi)

The refraction microtremor method was performed to observe train-induced vibrations for geotechnical site characterisation. 1D (i.e. linear) and 2D (i.e. manual and L-shape) arrays were utilized for observing train-induced vibrations when trains passed the site and in either direction.

The resulting data plots of particle motions showed that the vibrations generated by Pendolino and Midland passenger trains are consistent with Rayleigh waves and the vibrations generated by heavy goods freight trains were found not to be consistent. The inconsistency of vibrations from heavy goods freight trains was interpreted due to the trains acting as a complex multiple source for greater range of distance.

The effective investigated depth range which was resolved by the shear wave velocity calculations had a range between 10 m – 50 m bgl. The effected investigated depth is a function of the observed frequency range, the higher the frequency the shallower investigated depths. This study highlights the need for active seismic surveys to be carried out alongside passive seismic surveys (i.e. the train-induced vibrations) to investigate the top 10 m bgl, or indeed another technique (e.g., CPT surveys, etc.).

The linear arrays, orientated parallel to the railway, were found to be the optimal survey configuration to observe train-induced vibrations. The linear arrays, oriented orthogonal to the railway, and 2D array configurations (i.e. the manual and L-shape arrays), were found to be relatively poor to observe train-induced vibrations, due to both the limited investigated depth bgl and the unlikely shear wave velocity values calculated for the study site.

Although the linear arrays, oriented parallel to the railway, were found to be the best survey configuration, different shear wave velocities were determined from the three seismic components which was not physically possible. The vertical component resolves the greatest shear wave velocity, whilst the horizontal orthogonal resolves the smallest. The differences in shear wave velocity might be from observing different apparent wave

velocities, on different seismic components. The apparent wave velocity is calculated from a moving source (the trains) passing the deployed array in a transverse direction (i.e. the moving train is not in-line with the seismic array) and most of the generated vibrations were thus approaching obliquely and/or broadside the array's orientation.

The geological heterogeneity of the site may be another reason for different shear wave velocities, based on the survey configuration, inverting Love waves (on the horizontal seismic components) and Rayleigh waves (on the vertical component) can suggest and indicate the site's heterogeneity. Another possible reason might be the embankment waveguide effect contributes to the shear wave velocity differences.

The considerable difference in shear wave velocities on different seismic components, therefore, is regarded as the main limitation for using the train-induced vibrations, as passive seismic waves, for geotechnical site characterisation. In addition, passive seismic surveys close to railway routes, are suggested to be carried out when there is no moving train passing the site during the recording time.

The Doppler shift could not be seen on the spectrograms of the observed vibrations from the three seismic components, different types of trains (Pendolino and Midland passenger trains and heavy goods freight trains) and for trains travelling in either direction. The theoretical Doppler shift analysis shows that the expected shift in the observed vibrations is about 0.8 Hz at 20 Hz observed frequency. Furthermore, the transition, in Doppler shift, would be smoother with increasing distance away from the railway.

In contrast to previous studies, this study shows that the trains vibrations have increasing magnitudes with increasing drift deposit thicknesses and/or trains vibrations might be passed through different material for trains travel either destination.

7.2 Recommendations for future work

7.2.1 Buried foundation detection surveys

It is recommended that these surveys should be acquired over a bigger target which may be buried at different depths bgl. Different sites with different backgrounds and conditions, for example, moisture content, are recommended to be tested to determine what effect these variations will have on target discriminations in electrical resistivity datasets. Other electrode configurations could be tested, especially those less sensitive to the electrical noise encountered here in this 'urban' site. True 3D datasets might also generate better representation of the target, take in consideration the available equipment and data resolution (i.e. the higher resolution the more equipment will be needed). Other geophysical methods, for example, ground penetrating radar, might be worth testing to determine optimal detection techniques for buried foundations.

7.2.2 The potential HS2 site characterisation: as a case study

It is recommended to undertake closer-spaced CPT soundings for better horizontal data resolution and more detailed investigations for the shallow site depths bgl (i.e. < 4 m). Using an anchored drill-rig CPT should help to investigate deeper and even penetrate through the gravelly layer which was not possible in this study. Performing seismic CPT soundings would also facilitate shear wave velocity determination and, ultimately, shear modulus as a stiffness parameter. Conducting CPT soundings as a grid would also help to understand the deposits' architecture variation in 3D.

Smaller electrode spacings for the resistivity surveys and smaller shot points spacing for the 2D MASW surveys are suggested to generate higher resolution 2D profiles for more

detailed investigations. Applying longer seismic arrays (for the 1D and 2D MASW) should also result in deeper penetration depths. Seismic refraction surveys would also help to determine the deposits-bedrock interface location and confirm the microgravity data interpretations. Collection more microgravity data using longer survey profiles, higher resolution datasets and most importantly, survey profile(s) cross the railway embankment and the river Trent would also help to identify the deposits-bedrock interface and to image the expected over-deepened river channel. Collecting soil samples from a certain depth (say 1 m) bgl would help to determine the estimated moisture content using the resistivity data. Drilling a borehole(s) should not only contribute to get more direct data but also can facilitate the geophysical data interpretation for better ground truthing.

More sophisticated algorithms for the active seismic (MASW) data processing, are recommended, especially algorithms based on joint inversion, for example, the “MuLTI” algorithm, which not only constrains investigated depth by another external dataset but also can assess the reliability of the obtained model, for more details about the “MuLTI” algorithm, see Killingbeck et al. (2018).

7.2.3 Train-induced vibration analysis

It is suggested to collect more ReMi datasets using linear arrays that are oriented parallel to the railway embankment, with datasets generated by Pendolino and Midland passenger trains. The observed data should be then sorted based on the train type, and then inverted separately to determine shear wave velocity against depth for each dataset (i.e. based on the train type). Manual comparison of shear wave velocity profiles would help to work out the train type effect on the shear wave velocity profiles.

It is recommended to collect train-induced vibrations using the seismic interferometry method using three-component seismic station surveys. Then, inverting the datasets, separately, to find out if the wave velocities are consistent from different seismic components. This experiment should help to figure out if it is possible to have different apparent wave velocities on different seismic components.

It is recommended to collect some ReMi datasets using lower frequency geophones (i.e. <4.5 Hz) to determine if the effective investigated depth can increase from that determined in this study. This might also help to determine the differences in shear wave velocities at deeper depths (i.e. deeper than the ≈ 50 m depth determined on the LLAS no. 1-2 in this study).

Another suggested experiment would be collecting at different distances from the railway line/embankments using the three-component seismic stations. Although the ground underneath each array would be expected to be different and have a specific shear wave velocity-depth profile, this experiment would help to determine an optimum distance away from the railway lines, or if there is a correlation of vibration with distance.

It is recommended to use more functional software package for inverting the train-induced vibrations rather than the SeisImager/SW. Vibrations observed on the horizontal components are recommended to be inverted using specific packages/algorithms that already designed to invert Love wave.

7.3 Concluding remarks

Non-invasive geophysical techniques represent an excellent tool for geotechnical site characterisation surveys. Electrical resistivity tomography was shown to detect buried foundations in brownfield sites, with Wenner and dipole-dipole arrays being optimal electrode configurations. Performing desk studies and understanding the buried foundation and background site conditions should assist the design of the optimal survey parameters such as survey orientation and electrode spacing.

Integration of different geophysical survey technique(s), coupled with conventional site tests should provide the best approach for a robust site investigation and ground truthing.

Passing passenger trains on study sites generate ground vibrations that are consistent with simple Rayleigh waves and the vibrations generally span low frequencies. These can be utilized to extract shear wave velocity-depth profiles, but different wave velocities can be measured in different seismic components, which may be problematic.

This study highlights that there is a need for further studies into resistivity surveying over buried foundations using different electrode configurations, and for bigger foundation dimensions and different background hosting material. More research is needed into train-induced vibrations, for example, using different sites such as earth-cutting and at-grade rail-lines and varying distance of surveys from railway lines.

References:

Abbiss, C.P. (1981). Shear wave measurements of the elasticity of the ground. *Géotechnique*, 31 (1), 91-104.

Adewoyin, O.O., Joshua, E.O., Akinyemi, M.L., Omeje, M. and Joel, E.S. (2017). Application of 2D electrical resistivity imaging and cone penetration test (CPT) to assess the hazardous effect of near surface water on foundation in Lagos Nigeria. *Journal of Physics*, conference series 852 012033, doi :10.1088/1742-6596/852/1/012033.

Aggour, M.S., Tawfiq, K.S., and Amini, F. (1987). Effect of frequency content on dynamic properties of cohesive soils. In: Cakmak, A.S. (Ed). *Soil Dynamics and Liquefaction*, vol. 42 of Developments in Geotechnical Engineering. Elsevier Publ. Co., New York, 31-39.

Aizebeokhai, A.P. (2010). 2-D and 3-D geoelectrical resistivity imaging: theory and field design. *Scientific Research and Assays*, 5 (23), 3592–3605.

Akawwi, E., Al-Zoubi, A., Abu-Alades, A. and Al-Rzouq, R. (2014). Using vertical electrical for locating static water level and geological feature in Aqaba area, Jordan. *Research Journal of Environmental Sciences*, 8 (1), 39-48.

al Hagrey, S. A. and Petersen, T. (2011). Numerical and experimental mapping of small root zones using optimized surface and borehole resistivity tomography. *Geophysics*, 76, G25-G35.

Allied associates geophysics Ltd. (2006). Tiger resistivity meter user's manual. [Available online]: http://www.allied-associates.co.uk/pdfmanuals/Manual-Tigre.pdf. [Accessed 28th Feb. 2016].

Amoroso, S., Gaudiosi, I., Tallini, M., Giulio, G. and Milana, G. (2018). 2D site response analysis of a cultural heritage: the case study of the site of Santa Maria di Collemaggio Basilica (L'Aquila, Italy). *Bull. Earthquake Engineering*, https://doi.org/10.1007/s10518-018-0356-2.

Apuani, T, Giani, G.P., d'Attoli, M., Fischanger, F., Morelli, G., Ranieri, G., and Santarato, G. (2015). Assessment of the efficiency of consolidation treatment through injections of expanding resins by geotechnical tests and 3D electrical resistivity tomography. *The Scientific World Journal*, article ID 237930, 1-13.

Archie, G.E. (1942). The electrical resistivity log as an aid in determining some reservoir characteristics. *Trans. AM. Inst. Min. Metall. Pet. Eng*. 146, 54-62.

Ardestani, V.E. (2013). Determination of the relative soil compactness in the foundation condition by microgravity. *Bollettino di Geofisica Teorica ed Applicata*, 54(2), 129-124.

Ardestani, V.E. and Ashena, Z.B. (2018). Detecting and modelling the collapsed zone around a shaft in a dam site by microgravity data. *Bollettino di Geofisica Teorica ed Applicata,* 59(1), 107-116.

Arjwech, R., Everett, M.E., Briaud, J.L., Hurlebaus, S., Medina-Cetina, Z., Truker, S. and Yousefpour, N. (2013). Electrical resistivity imaging of unknown bridge foundations. *Near Surface Geophysics*, 11, 591-598.

Arneson, L.A., Zevenbergen, L.W., Lagasse, P.F. and Clopper, P.E. (2012). Hydraulic engineering circular No. 18: Evaluating scour at bridges: final report. U.S. Department of Transportation, Federal Railroad Administration, pages 1-340. Available at: https://www.fhwa.dot.gov/engineering/hydraulics/pubs/hif12003.pdf [Accessed 22 July 2018].

Asfahani, J. (2011). Application of a directional geoelectrical resistivity square configuration for anisotropy estimation in Haramoun region, southern Syria. *JAKU: Earth Sci*., 22 (1), 77-98.

Atkinson, J. (2014). *Fundamentals of Ground Engineering*. Boca Raton: CRC Press, p. 220.

Banham, S.G. and Pringle, J.K. (2011). Geophysical and intrusive site investigations to detect an abandoned coal-mine access shaft, Apedale, Staffordshire, UK. *Near Surface Geophysics*, 9, 483-496.

Barnes, G. (2010). *Soil Mechanics: Principles and Practice*. 3nd edition. Great Britain: Palgrave Macmillan, p. 493.

Barnes, G. (2016). *Soil Mechanics: Principles and Practice*. 4th edition. Great Britain: Palgrave Macmillan, p. 560.

Bazin S. and Pfaffhuber A.A. (2013). Mapping of quick clay by electrical resistivity tomography under structural constraint. *Journal of applied geophysics*, 98, 280-287.

Beckman Coulter Inc. (2011). Coulter LS series: product manual. [Availabe online]: https://www.beckmancoulter.com/wsrportal/techdocs?docname=4237214EA.pdf. [Accessed 12/05/2016].

Beff, L., Gunther, T., Vandoorne, B., Couvreur, V. and Javaux, M. (2013). Three-dimensional monitoring of soil water content in a maize field using Electrical Resistivity Tomography. *Hydrology and Earth System Science*, 17, 595-609.

Behm, M., Leahy, G.M., and Snieder, R. (2014). Retrieval of local surface wave velocities from traffic noise – an example from the La Barge basin (Wyoming). Geophysical Prospecting, 62, 223-243.

Bentley, L.R. and Gharibi, M. (2004). Two- and three-dimensional electrical resistivity imaging at a heterogeneous remediation site. *Geophysics*, 69 (3), 674–680.

Beresenv, I.A., Hruby, C.E. and Davis, C. A. (2002). The use of multi-electrode resistivity imaging in gravel prospecting. *Journal of Applied Geophysics*, 49, 245-254.

Bishop, A.W. and Hight, D.W. (1977). The value of Poisson's ratio in saturated soils and rocks stressed under undrained conditions. *Geotechnique*, 27(3), 369-384.

Blahova, K., Ševelova, L. and Pilařova. P. (2013). Influence of water content on the shear strength parameters of clayey soil in relation to stability analysis of a hillside in Brno region. *ACTA universitatis agriculturae et silviculturae mendelianae brunensis*, LXI (6), 1583-1588.

Boncio, P., Amoroso, S., Vessia, G., Francescone, M., Nardone, M., Monaco, P., Famiani, D., Di Naccio, D., Mercuri, A., Manuel, M., Galadini, F. and Milana, G. (2018). Evaluation of liquefaction potential in an intermountain quaternary lacustrine basin (Fucino basin, central Italy). *Bulletin Earthquake Engineering*, 16, 91-111.

Brillante, L., Mathieu, O., Bois, B., van Leeuwen, C. and Leveque, J. (2015). The use of soil electrical resistivity to monitor plant and soil water relationships in vineyards. *Soil*, 1, 273-286.

Brunet P., Clement R., and Bouver, C. (2010). Monitoring soil water content and deficit using electrical resistivity tomography (ERT)-A case study in the Cevennes area, France. *Journal of hydrology*, 380, 146-153.

BS 1377 (1990). *British Standard Methods of Test for Soils for Civil Engineering Purposes, part 2: Classification Test*. B.S.I. London.

Butler, D.K. (1984). Microgravimetric and gravity gradient techniques for detection of subsurface cavities. *Geophysics*, 49(7), 1084-1096.

Calamita, G., Brocca, L., Perrone, A., Piscitelli, S., Lapenna, V., Melone, F. and Moramarco, T. (2012). Electrical resistivity and TDR methods for moisture content estimation in central Italy test-sites. *Journal of Hydrology*, 454-455, 101-112.

Cardarelli, E., Cercato, M. and De Donno, G. (2014). Characterization of an earth-filled dam through the combined use of electrical resistivity, P- and SH-wave seismic tomography and surface wave data. *Journal of Applied Geophysics*, 106, 87-95.

Cardarelli, E., Cercato, M., Cerreto, A. and Di Filippo, G. (2010). Electrical resistivity and seismic refraction tomography to detect buried cavities. *Geophysical Prospecting*, 58, 685–695.

Cardarelli, E., Cercato, M., Di Filippo, G. (2007). Assessing foundation stability and soil-structure interaction through integrated geophysical techniques: a case history in Rome (Italy). *Near Surface Geophysics*, 5, 141–147.

Carpenter, E.W. and Habberjam, G.M. (1956). A tri-potential method of resistivity prospecting. *Geophysics*, XXI (2), 445-469.

Cassidy, N. (2001). *The application of mathematical modelling in the interpretation of near-surface archaeological ground-penetration radar.* Ph.D. thesis, Keele University.

Celano G., Palese, A.M., Ciucci, A., Martorella, E., Vignozzi, N., and Xiloyannis, C. (2011). Evaluation of soil water content in tilled and cover-cropped olive orchards by the geoelectrical technique. *Geoderma*, 163, 163-170.

Cha, Y.H., Kang, J.S, and Jo, C. (2006). Application of linear-array microtremor surveys for rock mass classification in urban tunnel design. *Exploration Geophysics*, 37, 108-113.

Chai, G. and Roslie, N. (1998). The Structural Response and Behavior Prediction of Subgrade Soils using Falling Weight Deflectometer in Pavement Construction. In: Proceedings of the 3rd International Conference on Road and Airfield Pavement Technology. In: Lamas-Lopez, F., Cui, Y.J., D'Aguiar, S.C. and Calon, N. (2016). Geotechnical auscultation of a French conventional railway track-bed for maintenance purposes. *Soils and Foundations*, 56(2), 240-250.

Chambers, J.E., Wilkinson, P.B., Weller, A.L., Meldrum, P.I., Ogilvy, R.D. and Caunt, S. (2007). Mineshaft imaging using surface and crosshole 3D electrical resistivity tomography: A case history from the East Pennine Coalfield, UK. *Journal of Applied Geophysics*, 62, 324-337.

Chen, Q., Li, I., Li, G., Chen, L., Peng, W., Tang, Y., Chen, Y. and Wang, F. (2004). Seismic features of vibration induced by trains. *Acta Seismologica Sinica*, 17 (6), 715-724.

Chrétien, M., Lataste, J.F., Fabre, R. and Denis, A. (2014). Electrical resistivity tomography to understand clay behavior during seasonal water content variations. *Engineering Geology*, 169, 112-123.

Clark, P. L. (1967). Railways. In: Greenslade, M. W. and Jenkins, J. G. (Eds.). A history of the county of Stafford: volume II. Oxford University Press (London), 312-334.

Clayton, C.R.I. (2011). Stiffness at small strain: research and practice. *Geotechnique*, 61 (1), 5-37.

Clayton, C.R.I., Matthews, M.C. and Simons, N.E. (1995). *Site Investigation*. Blackwell science, Oxford, p. 584.

Coakley, J.P. and Syvitski, J.P. (1991). SediGraph technique. In: Syvitski, J.P. (Ed). Principles, methods, and application of particle size analysis. Cambridge University press, 129-142.

Connolly, D., Giannopoulos, A. and Frode, M.C. (2013). Numerical modelling of ground brone vibration from high speed rail lines on embankment. *Soil Dynamics and Earthquake Engineering*, 46, 13-19.

Connolly, D.P., Kouroussis, G., Woodward, P.K., Costa, P.A. and Verlinden, O. (2014). Field testing and analysis of high speed rail vibrations. Soil Dynamics and Earthquake Engineering, 67, 102-118.

Cosenza, P., Marmet, E., Rejiba, F., Cui, Y., Tabbagh, A. and Charlery, Y. (2006). Correlations between geotechnical and electrical data: a case study at Garchy in France. *Journal of Applied Geophysics*, 60, 165–178.

Craig, R. F. (1997). *Soil Mechanics*. 6th edition. Great Britain: E and FN Spon, p. 485.

Craig, R.F., (2004). *Craig's Soil Mechanics*. 7th edition. Spon Press- Taylor and Francis Group, p. 447.

Crawford, M.M. and Bryson, S. (2018). Assessment of active landslide using field electrical measurements. *Engineering Geology*, 233, 146-159.

Dahlin, T. (2000). Short note on electrode charge-up effects in DC resistivity data acquisition using multi electrode arrays. *Geophysical Prospecting*, 48, 181-187.

Dahlin, T. (2001). The development of DC resistivity imaging techniques. *Computers and Geosciences*, 27, 1019-1029.

Dahlin, T. and Zhou, B. (2004). A numerical comparison of 2D resistivity imaging with 10 electrode arrays. *Geophysical prospecting*, 52, 379-398.

Dannowski, G. and Yaramanci, U. (1999). Estimation of water content and porosity using combined radar and geoelectrical measurements. *Eur. J. Environ. Eng. Geophys*., 4, 71-85.

Das, B.M, (2006). *Principles of Geotechnical Engineering.* 7th edition. United State of America: Cengage learning, p. 666.

Das, B.M. and Ramana, G.V. (2011). *Principles of Soil Dynamics*. 2nd edition, United State of America: Cengage learning, p. 673.

Deceuster, J., Delgranche, J. and Kaufmann, O. (2006). 2D cross-borehole resistivity tomography below foundations as a tool to design proper remedial actions in covered karst. *Journal of Applied Geophysics*, 60, 68-86.

Dick, H., Pringle, J., Soane, B., Carver, J., Wisniewski, K., Haffenden, A., Porter, S., Roberts, D., and Cassidy, N. (2015). Detection and characterisation of black death burials by multi-proxy geophysical methods. *Journal of Archaeological Science*, 59, 132-141.

Dick, J., Tetzlaff, D., Bradford, J. and Soulsby, C. (2018). Using repeat electrical resistivity surveys to assess heterogeneity in soil moisture dynamics under contrasting vegetation types. *Journal of Hydrology*, 559, 684-697.

Ditzel, A. and Herman, G.C. (2004). The influence of a rail embankment on the vibrations generated by moving trains. *Journal of Sound and Vibration*, 271, 937-957.

Dobrin, M.B. and Savit, C.H. (1988). *Introduction to Geophysical Prospecting*. 4th edition. Singapore: Geology Series, McGrow-Hill International, p. 867.

Doll, W.E., Miller, R.D. and Bradford. J. (2012). The emergence and future of near – surface geophysics. *The Leading Edge*, 31, 684-691.

Donohue, S., Gavin, K. and Tolooiyan, A. (2011). Geophysical and geotechnical assessment of a railway embankment failure. *Near Surface Geophysics*, 9 (1), 33–44.

Edwards, L.S. (1977). A modified pseudosection for resistivity and IP. *Geophysics*, 42 (5), 1020-1036.

Elawadi, E., Salem, A. and Ushijima, K. (2001). Detection of cavities and tunnels from gravity data using a neural network. *Exploration Geophysics*, 32, 204-208.

Emsley, S.J. and Bishop, I. (1997). Application of the microgravity technique to cavity location in the investigations for major civil engineering works. In: McCann, D.M., Eddleston, M., Fenning, P.J. and Reeves, G.M. (Eds). *Modern geophysics in engineering geology*. Geological Society Engineering Geology Special Publication No. 12, 183-192.

Everett, M.E. (2013). *Near Surface Applied Geophysics*. 1st edition. Cambridge University Press, p. 403.

Fallah-Safari, M., Hafizi, M.K. and Ghalandarzadeh, A. (2013). The relationship between clay geotechnical data and clay electrical resistivity. *Bollettino di Geofisica Teorica ed Applicata,* 54 (1), 23-38.

Fischanger, F., Morelli, G., Ranieri, G., Santarato, G., and Occhi, M. (2013). 4D cross-borehole electrical resistivity tomography to control resin injection for ground stabilization: a case study history in Venice (Italy). *Near Surface Geophysics*, (11), 41-50.

Fleisch, D. and Kinnaman, L. (2015). *A Student's Guide to Waves*. 1st edition. United Kingdom. Cambridge University Press, p. 219.

Foti, S., Lai, C.G., Rix, G.J. and Strobbia, C. (2015). *Surface Wave Methods for Near Surface Site Characterization*. CRC press, p. 467.

Fu, C. 2016. Dynamic behaviour of a simply supported bridge with a switching crack subjected to seismic excitations and moving trains. *Engineering Structures*, 110, 59-69.

Fuchs, F. and Bokelmann, G. (2017). Equidistant spectral lines in train vibrations. *Seismological Research Letters*, https://dx.doi.org/10.1785/0220170092.

Gabriel, K. (2001). What's on the agenda?. *Ground Engineering*, 34 (7), 22-23.

Gamal, M.A. and Pullammanappallil, S. (2011). Validity of the refraction microtremors (ReMi) method for determining shear wave velocities for different soil types in Egypt. *International Journal of Geosciences*, 2, 530-540.

Garman, K. and Purcell, S. (2004). Three-dimensional electrical resistivity surveys to identify buried karst features affecting road projects, subsurface evaluation, Inc. [Availabe online]: http//www.dot.state.fl.us/statematerialsoffice/geotechnical/conference/materials//garman-pursel.pdf. [Accessed 09/02/2016].

Gassenmeier, M., Sens-Schonfelder, C., Delatre, M., and Korn, M. (2015). Monitoring of environmental influences on seismic velocity at the geological storage site for CO2 in Kertzin (Germany) with ambient seismic noise. Geophysical Journal International, 200, 524-533.

Geometrics, Inc. (2009). SeisImager/SW™ manual: windows software for analysis of surface waves.

Geotomo™ Software (2004). RES2DINV version 3.54 user's manual.

Gouveia, F., Fonseca, A., Gomes, R.C. and eves-Costa, P. (2018). Deeper Vs profile constraining the dispersion curve with the ellipticity curve: A case study in Lower Tagus Valley, Portugal. *Soil Dynamics and Earthquake Engineering*, 109, 188-198.

Griffiths, D.H. and Barker, R.D. (1993). Two-dimensional resistivity imaging and modelling in areas of complex geology. *Journal of Applied Geophysics*, 29, 211-226.

Griffiths, D.H. and Kings, R.F. (1981). *Applied Geophysics for Geologists and Engineers: the Elements of Geophysical Prospecting*. 2nd edition. Great Britain: Pergamon press, p. 230.

Gunn, D., Williams, G., Kessler, H. and Thrope, S. (2015b). Rayleigh wave propagation assessment for transport corridors. In: *Proceedings of the institution of civil engineers – Transport*. 168 (6), 487-498.

Gunn, D.A., Chambers, J.E., Dashwood, B.E., Lacinska, A., Dijkstra, T., Uhlemann, S., Swift, R., Kirkham, M., Milodowski, A., Wragg, J. and Donohue, S. (2018). Deterioration model and condition monitoring of aged railway embankment using non-invasive geophysics. *Construction and Building Material*, 170, 668-678.

Gunn, D.A., Chambers, J.E., Uhlemann, S., Wilkinson, P.B., Meldrum, P.I., Dijkstra, T.A., Haslam, E., Kirkham, M., Wragg, J., Holyoake, S., Hughes, P.N., Hen-Jones, R., Glendinning, S. (2015a). Moisture monitoring in clay embankments using electrical resistivity tomography. *Construction and Building Material*, 92, 82-94.

Hanson, C. E., Jason, P.E., Ross, C., David, A. and Towers, P.E. (2012). High-speed ground transportation noise and vibration impact assessment: final report. Washington, District of Columbia: U.S. Department of Transportation, Federal Railroad

Administration, Office of Railroad Policy and Development, pages 1-248. Available at: http://purl.fdlp.gov/GPO/gpo48309 [Accessed 28 April 2018].

Hardin, B.O. and Black, W.L. (1968). Vibration modulus of normally consolidated clay. Journal of the Soil Mechanics and Foundations Division, the American Society of Civil Engineers, SM2, 353-369.

Hencher, S. (2012). *Practical Engineering Geology*. Taylor and Francis, p. 450.

Heymann, G. (1998). *The stiffness of soils and weak rocks at very small strains*. Ph.D. thesis, University of Surrey.

Hunter, J.A., Benjumea, B., Harris, J.B., Miller, R.D., Pullan, S.E., Burns, R.A. and Good, R.L. (2002). Surface and downhole shear wave seismic methods for thick soil site investigations. *Soil Dynamics and Earthquake Engineering*, 22, 931-941.

Imai, T, Sakayama, T. and Kanemori, T. (1987). Use of ground-probing radar and resistivity surveys for archaeological investigation. *Geophysics*, 52(2), 137-150.

Karabulut, S. (2018). Soil classification for seismic site effect using MASW and ReMi methods: A case study from western Anatolia (Dikili-İzmir). *Journal of Applied Geophysics*, 150, 254-266.

Kaufmann, G., Romanov, D. and Nielbock, R. (2011). Cave detection using multiple geophysical methods: Unicorn cave, Harz Mountains, Germany. *Geophysics*, 76(3), B71-B77.

Keary, P., Brooks, M. and Hill, I. (2002). *Introduction to Geophysical Exploration*. 3rd edition. The United Kingdom: Blackwell publishing, p. 262.

Keller G.V. and Frischknecht F.C. (1966). E*lectrical Methods in Geophysical Prospecting*. 1st edition. Oxford: Pergamon Press Inc., p. 519.

Khalil, M.A. and Santos F.A.M. (2009). Influence of degree of saturation in the electric resistivity–hydraulic conductivity relationship. *Surv Geophys*, 30, 601–615.

Khan, M.S., Hossain, M.S., Hossain, J. and Kibria, G. (2012). Determining Unknown Bridge Foundation Depth by Resistivity Imaging Method. In: Proceedings Geo-Congress, Oakland, CA.

Khazri, D. and Gabtni, H. (2018). Geophysical methods integration for deep aquifer reservoir characterization and modeling (Side Bouzid basin, central Tunisia). *Journal of African Earth Sciences*, 138, 289-308.

Killingbeck, S.F., Livermore, P.W., Booth, A.D. and West, L.J. (2018). Multimodel layered transdimensional inversion of seismic dispersion curves with depth constraints. *Geochemistry, Geophysics, Geosystems*, 19. https://doi.org/10.1029/2018GC008000

Kim, D., and Lee, J. (2000). Propagation and attenuation characteristics of various ground vibrations. *Soil Dynamics and Earthquake Engineering*, 19, 115-126.

Kouroussis, G., Connolly, D.P., and Verlinden, O. (2014). Railway-induced ground vibrations – a review of vehicle effects. *International Journal of Rail Transportation*, 2 (2), 69-110.

Krylov, V.V. (1994). On the theory of railway-induced ground vibrations. *Journal De Physique IV*, 4, C5 769-C5 772.

Krylov, V.V. (1995). Generation of ground vibrations by superfast trains. *Applied Acoustic*, 44, pp. 179-164.

Krylov, V.V. (2001). Generation of ground vibration boom by high-speed trains. In: Krylov, V.V. (Ed). Noise and vibration from high-speed trains. Thomas Telford, 252-283.

Kumar, R., Tiwari, A.K., Yadav, G.S. and Singh, N.S. (2014). Geohydrological investigation using vertical electrical sounding at Banaras Hindu University campus, Varanasi, U.P, India. *International Journal of Research in Engineering and Technology*, 03, (9).

Lancellotta, R. (2009). *Geotechnical Engineering*. 2nd edition. London and New York: Taylor and Francis, p. 499.

Lane, J.W., Haeni, F.P. and Watson, W.M. (1995). Use of a square-array direct-current resistivity, method to detect fractures in crystalline Bedrock in New Hampshire. *Ground Water,* 33, 476-485

Lane, V. (2009). *An evaluation of the MCSM (Multi-Component Seismic Microtremor) method for determining the engineering properties of the shallow sub-surface*. Ph.D. thesis, Keele University.

Langton, D.D. (1999). The panda lightweight penetrometer of soil investigation and monitoring material compaction. *Ground Engineering*, (September), 33-37.

Li, P., Ling, X., Zhang, F., Li, Y. and Zhao Y. (2017). Field testing and analysis of embankment vibrations induced by heavy haul trains. *Shocks and Vibrations*, vol. 2017, Article ID 7410836, 14 pages, 2017. https://doi.org/10.1155/2017/7410836.

Loke, M.H. (2014). Tutorial 2-D and 3-D electrical imaging survey. [Available online]: www.geotomosoft.com.

Loke, M.H. (2015). Tutorial 2-D and 3-D electrical imaging survey. [Available online]: www.geotomosoft.com.

Loke, M.H. and Barker, R. D. (1995). Least-square deconvolution of apparent resistivity pseudosections. *Geophysics*, 60 (6), 1682-1690.

Loke, M.H. and Dahlin, T. (2002). A comparison of the Guass-Newton and quasi-Newton methods in resistivity imaging inversion. *Journal of Applied Geophysics*, 49, 149-162.

Loke, M.H., Wilkinson, P.B. and Chambers, J.E. (2010). Fast computation of optimized electrode arrays for 2D resistivity surveys. *Computers and Geosciences*, 36, 1414-1426.

Loke, M.H., Wilkinson, P.B., Uhlemann, S.S., Chambers, J.E. and Oxby, L.S. (2014). Computation of optimized array for 3-D electrical imaging surveys. *Geophysical Journal International*, 199, 1751-1764.

Loke, M.H.; Acworth, I. and Dahlin, T. (2003). A comparison of smooth and blocky inversion methods 2D electrical imaging surveys. *Exploration geophysics*, 34, 182-187.

Louie, J.N. (2001). Faster, better: shear-wave velocity to 100 meters depth from refraction microtremor arrays. *Bulletin of the Seismological Society of America*, 91 (2), 347-364.

Lowrie, W. (2007). *Fundamental of Geophysics*. 2nd edition. New York, USA: Cambridge University Press, p. 381.

Lunne, T., Robertson, P.K. and Powell, J.J.M. (1997). *Cone Penetration Testing: In Geotechnical Practice*. New York: Blackie Academic/Chapman-Hall Publishers, p. 312.

Lysdahl, A.K., Bazin, S., Christensen, C., Ahrens, S., Günther, T. and Pfaffhuber, A. (2017). Comparison between 2D and 3D ERT inversion for engineering site investigation – a case study from Oslo Harbour. *Near Surface Geophysics*, 15, 201-209.

Ma, M., Liu, W., Qian, C., Deng, G., and Li, Y. (2016). Study of the train-induced vibration impact on a historic Bell Tower above two spatially overlapping metro lines. *Soil Dynamics and Earthquake Engineering*, 81, 58-74.

Madshus, C., and Kaynia, A.M. (2000). High-speed railway lines on soft ground: dynamic behaviour at critical train speed. *Journal of Sound and Vibration*, 231 (3), pp. 689-701.

Mantlík, F., Matias, M., Lourenco, J., Grangeia, C. and Tareco, H. (2009). The use of gravity methods in the internal characterization of landslides – a case study. *Journal of Geophysics and Engineering,* 6, 357-364.

Martys, N.S. (1999). Diffusion in partially-saturated porous materials. *Materials and Structures/Materiaux et Constructions*, 32, 555-562.

Massoud, U., Khalil, M.M., Tokunaga, T. and Santos, F.A.M. (2016). Preliminary hydrogeophysical investigation at the 10th of Ramadan city, Egypt, by 1D and 2D inversion of VES data. *Near Surface Geophysics,* 14(3), 287-297.

Mathews, M. C., Clayton, C. R. I. and Own, Y. (2000). The use of field geophysical technique to determine geotechnical stiffness parameters. *Geotech. Engng* 143, 31-42.

Mathews, M. C., Hope, V. S. and Clayton, C. R. I. (1996). The use of surface waves in the determination of ground stiffness profiles. In: *Proceeding of ICE - Geotechnical Engineering.* [online] 119(2), 84-95. Accessed at 26/10/2015.

Mathews, M. C., Hope, V. S. and Clayton, C. R. I. (1997). The geotechnical value of ground stiffness determined using seismic methods. *Engineering Geology Special Publication,* (12), 113-123.

Matias, H.C., Santo, F., Ferreira, F., Machado, C. and Luzio, F. (2006). Detection of graves using the micro-resistivity method. *Annals of geophysics*, 49, (6), 1235-1244.

Mayne, P.W. (2007). Cone Penetration Testing: A Synthesis of Highway Practice. Project 20-5. Transportation research board, Washington, D.C. NCHRP synthesis 368, p. 118.

McCann, D.M., Culshaw, M.G. and Fenning, P.J. (1997). Setting the standard for geophysical surveys in site investigation. In: McCann, D.M., Eddleston, M., Fenning, P.J. and Reeves, G.M. (Eds). *Modern geophysics in engineering geology*. Geological Society Engineering Geology Special Publication No. 12, 3-34.

McDowell, P., Barker, R.D., Butcher, A., Culshaw, M., Jackson, P., McCann, D., Skipp, B., Matthews, S., Arthur, J. (2002). *Geophysics in engineering investigations*. Ciria, London, p. 252.

Metwaly, M., El-Qady, G., Massoud, U., El-Kenawy, A., Mastsushima, J. and Al-Arifi, N. (2009). Integrated geoelectrical survey for groundwater and shallow subsurface evaluation: a case study at Siliyin spring, El-Fayoum, Egypt. *Springer*, 99, 1427-1436.

Michot, D., Benderitter, Y., Dorigny, A., Nicoullaud, B., King D. and Tabbagh, A. (2003). Spatial and temporal monitoring of soil water content with an irrigated corn crop cover using surface electrical resistivity tomography. *Water Resour. Res*., 39 (5), p. 20.

Milsom, J. (2003). *Field Geophysics: The geological field guide series*. 3rd edition, England: John Wiley and Sons Ltd, p. 232.

Milsom, J. and Eriksen, A. (2011). *Field geophysics*. 4th edition. John Wily and Sons, p. 287.

Miyazakai, T. (2006). *Water Flow in Soils*. 2nd edition. London: Taylor and Francis Group, p. 418.

Mochales, T., Cases, A.M., Pueyo, E.L., Pueyo, O., Román, M.T., Pocoví, A., Soriano, M.A. and Ansón, D. (2008). Detection of underground cavities by combining gravity, magnetic and ground penetrating radar surveys: a case study from the Zaragoza area, NE Spain. *Environmental Geology*, 53, 1067-1077.

Mohamed, A.M.E, AI Ata, A.S.A., Azim, F., and Taha, M.A. (2013). Site-specific shear wave velocity investigation for geotechnical engineering application using seismic refraction and 2D multi-channel analysis of surface waves. *NRIAG Journal of Astronomy and Geophysics*. 2, 88-101.

Moro, G.D. (2015). *Surface Waves Analysis for Near Surface Applications*. Elsevier Inc., p. 244.

Motazedian, D., Hunter, J.A., Sivathayalan, S., Pugin, A., Pullan, S., Crow, H., and Banab, K.K. (2011). Railway train induced ground vibrations in a low Vs soil layer overlying a high Vs bedrock in eastern Canada. *Soil Dynamics and Earthquake Engineering*, doi:10.1016/j.soildyn.2011.02.008.

Mucciarelli, M., Gallipoli, M.R., Giacomo, D., Nota, F., and Nino, E. (2005). The influence of wind on measurements of seismic noise. Geophysical Journal International, 161, 303-308.

Murthy, V.N.S. (2002). *Geotechnical Engineering: Principles and Practices of Soil Mechanics and Foundation Engineering*. Marcel Dekker Incorporation, New Your, p. 1029.

Mussett, A.E. and Khan, M.A. (2000). *Looking Into the Earth: An Introduction to Geological Geophysics*. Cambridge, Cambridge University Press, p. 470.

Nabighian, M.N, Ander, M.E., Grauch, V.J.S, Hansen, R.O., LaFehr, T.R., Li, Y., Pearson, W.C., Peirce, J.W., Phillips, J.W. and Ruder, M.E. (2005). *Geophysics*, 70(6), 63ND-89ND.

Nakata, N., Snieder, R., Tsuji, T., Larner, K., and Matsouka, T. (2011). Shear wave imaging from traffic noise using seismic interferometry by cross-coherence. *Geophysics*, 76 (6), SA97-SA106.

Narayan, S., Dusseault, M.B. and Nobes, D.C. (1994). Inversion techniques applied to resistivity inverse problems. *Invers Problems*, 10, 669-686.

Nyquist, J.E. and Roth, M.J.S. (2005). Improved 3D pole-dipole resistivity surveys using radial measurement pairs. *Geophys. Res. Lett*., 32, L21416, p.4.

Ofomola, M.O. (2018). Geophysical assessment for contaminant hydrology in Ujevwu. *Journal of African Earth Sciences*, 138, 177-191.

Okada, H. (2003). The Microtremor Survey Method, Society of Exploration Geophysicists, *Geophysical Monograph Series*, Number 12.

Okpoli, C. (2013). Sensitivity and resolution capacity of electrode configurations. *International Journal of Geophysics*. Article ID 608037, p. 12.

Önal, A. Ö., Demirbilek, D. and Demir, V. (2013). Geo-environmental site investigation for Tunceli, Turkey municipal solid waste disposal site. *Engineering Geology*, 159, 76-82.

Orfanos, C. and Apostolopoulos, G. (2011). 2D-3D resistivity and microgravity measurements for the detection of an ancient tunnel in the Laverion area, Greece. *Near Surface Geophysics*, 9, 449-457.

Osella, A., de la Vega, M. and Lascano, E. (2005). 3D electrical imaging of an archaeological site using electrical and electromagnetic methods. *Geophysics*, 70(4), G101-G107.

Osinowo, O.O. and Falufosi, M.O. (2018). 3D electrical resistivity imaging (ERI) for subsurface evaluation in pre-engineering construction site investigation. *NRIAG Journal of Astronomy and Geophysics*, xx, pp. xx-xx.

Oyedele, K.F. and Olorode, D.O. (2010). Site investigation of subsurface condition using electrical resistivity method and cone penetration test at Medina Estate, Gbagada, Lagos, Nigeria. *World Applied sciences Journal*, 11(9), 1097-1104.

Padín, J., Martín, A. and Anquela, A. (2012). Archaeological microgravimetric prospection inside don church (Valencia, Spain). *Journal of Archaeological Science*, 39, 547-554.

Park, C., Miller, R. and Xia, J. (1997). *Multi-channel analysis of surface waves (MASW), "A summary report of technical aspects, experimental results, and perspective"*. [online]: Kansas geological survey, p.2. Available at: http://citeseerx.ist.psu.edu/viewdoc/download?doi=10.1.1.530.5257&rep=rep1&type=pdf [Accessed 10th Aug. 2016].

Park, C.B., Miller, R.D. and Xia, J. (1999). Multichannel analysis of surface waves. *Geophysics*, 64(3), 800-808.

Park, Y.H, Doh, S.J. and Yun, S.T. (2007). Geoelectric resistivity sounding of riverside alluvial aquifer in an agricultural area at Buyeo, Geum River watershed, Korea: an application to groundwater contamination study. *Environmental Geology,* 53, 849-859.

Pegah, E. and Liu, H. (2016). Application of near-surface seismic refraction tomography and multichannel analysis of surface waves for geotechnical site characterization: A case study. *Engineering Geology*, 208, 100-113.

Perez-Santisteban, I., Garcia-Mayordomo, J., Martin, A., and Carbo, A. (2011). Comparison among SASW, ReMi and SP-logging techniques: Application to a railway embankment. *Journal of Applied Geophysics*, 73, 59-64.

Pringle, J.K. and Jervis, J.R. (2010). Electrical resistivity survey to search for a recent clandestine burial of a homicide victim, UK. *Forensic Science International*, 202, e1-e7.

Pringle, J.K., Jervis, J.R., Roberts, D., Dick, C.H., Wisniewski, K.D, Cassidy, N.J. and Cassela, J.P. (2016). Longterm geophysical monitoring of simulated clandestine graves using electrical and ground penetrating monitoring simulated clandestine graves using electrical and ground penetrating radar methods;4-6 years. *Journal of Forensics sciences*, 61(2), 309-321.

Pringle, J.K., Styles, P., Howell, C.P., Branston, M.W., Furner, R. and Toon, S.M. (2012). Long-term time-lapse microgravity and geotechnical monitoring of relict salt, Marston, Cheshire, U.K.. *Geophysics,* 77 (6), B287-B294.

Quiros, D.A, Brown, L.D, and Kim, D. (2016). Seismic interferometry of railroad induced ground motions: body and surface wave imaging. *Geophysical Journal International*, 205, 301-313.

Rahman, M.Z. Kamal, A.S.M. and Siddiqua, S. (2018). Near-surface shear wave velocity estimation and V_S^{30} mapping for Dhaka, Bangladesh. *Natural Hazards*, https://doi.org/10.1007/s11069-018-3266-3.

Raines, M.G., Gunn, D.A., Morgan, D.J.R., Williams, G., Williams, J.D.O. and Caunt, S. (2011). Refraction microtremor (ReMi) to determine the shear-wave velocity structure of the near surface and its application to aid detection of a backfilled mineshaft. *Quarterly Journal of Engineering Geology and Hydrogeology*, 44, 211-220.

Rao, V.V., Raju, S., Rao, B.S., and Rao, P. (2004). Bed rock investigation by seismic refraction method-a case study. *J. Ind. Geophys Union*, 8 (3), 223-228.

Rassam, D.W., Fellows, C.S., De Hayr, R., Hunter, H. and Bloesch, P. (2006). The hydrology of riparian buffer zones; two case studies in an ephemeral and a perennial stream. *Journal of Hydrology,* 325, 308-324.

Ravindran, A. and Prabhu, M. (2012). Groundwater exploration study using Wenner-Schlumberger electrode array through W-4 2D Resistivity Imaging systems at Mahapallipuram, Chennai, Tamilanadu, India. *Research Journal of Recent Sciences,* 1 (11), 36-40.

Reynolds, J.M. (1998). *An Introduction to Applied and Environmental Geophysics*. 1st edition, John Wiley and Sons Ltd, p. 796.

Reynolds, J.M. (2011). *An Introduction to Applied and Environmental Geophysics*. 2nd edition, John Wiley and Sons Ltd, p. 696.

Rix, G.J. (2005). Near-surface site characterization using surface waves. In: Lai, C.G. and Wilmanski, K. (Eds). Surface waves in surface waves in geomechanics: Direct and inverse modelling for soils and rocks, CISM Series, Number 481, Springer, Wien, New York, NY, 1–46.

Robertson, P.K. (2009). Interpretation of cone penetration tests- a unified approach. *Canadian Geotechnical Journal*, 46, 1-19.

Robertson, P.K. and Cabal, K.L. (2015). *Guide to Cone Penetration Test for Geotechnical Engineering*. 6th edition. Gregg Drilling and Testing, Inc., p. 133.

Rosenblad, B.L. and Li, J. (2009). Performance of active and passive methods for measuring low-frequency surface wave dispersion curves. *Journal of Geotechnical and Geoenvironmental Engineering*, 135 (10), 1419–1428.

Roy, K.K. (2008). *Potential Theory in Applied Geophysics*. Springer, p. 651.

Rubio-Melendi, D., Gonzalez-Quirós, A., Roberts, D., García, M., Domínguez, A.C., Pringle, J.K. and Fernández-Álvarez, J. (2018). GPR and ERT detection and characterization of

a mass burial, Spanish Civil War, Northern Spain. *Forensic Science International*, 287, e1-e9.

Safani, J., O'Neill, A., Matsuoka, T. and Sanada, Y. (2005) Applications of Love Wave Dispersion for Improved Shear-wave Velocity Imaging. Jo*urnal of Environmental and Engineering Geophysics,* 10 (2), 135-150. doi: https://doi.org/10.2113/JEEG10.2.135.

Salehin, M., Packman, A. and Paradis, M. (2004). Hyporheic exchange with heterogeneous streambeds: Laboratory experiments and modeling. *Water Resources Research*, 40, W11504.

Salem, H.S. (2001). The influence of clay conductivity on electric measurements of glacial aquifers. *Energy Sources*, 23, 225-234.

Samouelian, A., Cousin, I., Tabbagh, A., Bruand, A. and Richard, G. (2005). Electrical resistivity survey in soil science: a review. *Soil & Tillage Research*, 83, 173-193.

Sanayei, M., Kayiparambil, A., Moore, J.A., and Brett, C.R. (2014). Measurement and prediction of trains-induced vibrations in a full-scale building. *Engineering Structures*, 77, pp. 119-128.

Schön, J.H. (2015). *Physical Properties of Rocks: Fundamentals and principles of Petrophysic.* 2nd Edition. Elsevier, 496 P.

Sharma, S. and Verma, G.K. (2015). Inversion of electrical resistivity data: A review. *International Journal of Environmental, Chemical, Ecological, Geological, and Geophysical Engineering*, 9(4), 392-398.

Shearer, P. M. (2009). *Introduction to Seismology*. 2nd edition. Cambridge university press, 396 P.

Sherlock, M.D., McDonnell, J.J. (2003). A new tool for hillslope hydrologists: spatially distributed groundwater level and soilwater content measured using electromagnetic induction. *Hydrological Processes*, 17, 1965–1977.

Simons, N., Menzies, B. and Matthews, M. (2002). *A Short course in: Geotechnical Site Investigation*. Thomas Telford publishing, London, p. 353.

Smith, G.N. and Smith, I.G.N., (1998). *Elements of Soil Mechanics*. 7th edition. Blackwell Science, p. 494.

Smith, I. (2006). *Smith's Elements of Soil Mechanics*. 8th edition. Blackwell publishing, p. 538.

Song, Y.Y., Castagna, J.P., Black, R.A. and Knapp, R.W. (1989). Sensitivity of near-surface shear-wave velocity determination from Rayleigh and Love waves. Expanded abstract of the 59th Annual meeting of the Society of Exploration Geophysicists, Dallas, Texas, 509-512.

Soupios, P.M., Georgakopoulos, P., Papadopoulos, N., Saltas, V., Andreadakis, A., Vallianatos, F., Sarris, A., and Makris, J.P. (2007). Use of engineering geophysics to investigate a site for a building foundation. *Journal of Geophysics and Engineering*, 4, 94-103.

Stephenson, W.J., Louie, J.N., Pullammanappallil, S., Williams, R.A. and Odum, J.K. (2005). Blind shear-wave velocity comparison of ReMi and MASW results with boreholes to 200 m in Santa Clara valley: implications for earthquake ground-motion assessment. *Bulletin of the Seismological Society of America*, 95 (6), 2506-2516.

Strobbia, C. and Cassiani, G. (2011). Refraction microtremor: Data analysis and diagnostics of key hypotheses. *Geophysics*, 76 (3), MA11-MA20.

Strobbia, C., Boaga, J. and Cassiani, G. (2015). Double-array refraction microtremors. *Journal of Applied Geophysics*, 121, 31-41.

Styles, P., McGrath, R., Thomas, E., and Cassidy, N. (2005). The use of microvity for cavity characterization in karstic terrains. *Quarterly Journal of Engineering Geology and Hydrogeology*, 38 (2), 155-169.

Sudha, K., Israil, M., Mittal, S. and Rai, J. (2009). Soil characterization using electrical resistivity tomography and geotechnical investigation. *Journal of Applied Geophysics* 67, 74-79.

Szalai, S. and Szarka, L. (2008). On the classification of surface geoelectric arrays. *Geophysical Prospection*, 56, 159-175.

Tabbagh, A., Dabas, M., Hesse, A. and Panissod, C. (2000). Soil resistivity: a non-invasive tool to map soil structure horizonation. *Geoderma*, 97, 393-404.

Tejero-Andrade, A., Cifuentes, G., Chávez, R.E., López-González, A.E. and Delgado-Solórzano, C. (2015). L- and CORNER-arrays for 3D electric resistivity tomography: an alternative for geophysical surveys in urban zones. Near Surface Geophysics, 13, 355-367, doi:10.3997/1873-0604.2015015.

Telford, W,M., Geldart, L.P. and Sheriff, R.E. (1990). *Applied Geophysics*. 2nd edition. Cambridge University press, p. 770.

Thompson, D. (2009). *Railway Noise and Vibration: Mechanisms, Modelling and Means of Control*. 1st edition, Great Britain: Elsevier Ltd., p. 518.

Topp, G.C., Davis, J.L. and Annan, A.P. (1980). Electromagnetic determination of soil water content: measurements in coaxial transmission lines. *Water Resources Research*, 16 (3), 574–582.

Tuckwell, G., Grossey, T., Owen, S. and Stearns, P. (2008). The use microgravity to detect small distributed voids and low-density ground. *Quaternary Journal of Engineering Geology and Hydrogeology,* 41, 371-380.

Turesson, A. (2006). Water content and porosity estimated from ground-penetration radar and resistivity. *Journal of Applied Geophysics*, 58, 99-111.

Vargemezis, G., Diamanti, N., Fikos, I., Stampolidis, A., Makedon, T. and Chatzigogos, N. (2013). Ground penetrating radar and electrical resistivity tomography for locating

buried building foundations: a case study in the city centre of Thessaloniki, Greece. *Bulletin of the Geological Society of Greece*, XLVII (3), 1355-1365.

Vargemezis, G., Tsourlos, P., Giannopoulos, A and Trilyakis, P. (2015). 3D electrical resistivity tomography technique for the investigation of a construction and demolition waste landfill site. *Stud. Geophys. Geod*., 59, 461–476.

Weissmann, G.S. and Fogg, G.E. (1999). Multi-scale alluvial fan heterogeneity modeled with transition probability geostatistics in a sequence stratigraphic framework. *Journal of Hydrology,* 226, 48-65.

Wilun, Z. and Starzewski, K. (1975). *Soil Mechanics in Foundation Engineering*. 2nd edition. Great Britain: Surry University press, p. 252.

Wood, D. M. (2004). *Geotechnical Modeling*. 1st edition. Spon press, p. 488.

Wu, T.X. and Thompson, D.T. (2001). Vibration analysis of railway track with multiple wheels on the rail. *Journal of Sound and Vibration*, 239(1), 69-97.

Xia, J., Miller, R., and Park, C. (1999). Estimation of near-surface shear-wave velocity by inversion of Rayleigh waves. *Geophysics*, 64, (3), 691-700.

Yalcinkaya, E., Alp, H., Ozel, O., Gorgun, E., Martino, S., Lenti, L., Bourdeau, C., Bigarre, P. and Coccia, S. (2016). Near-surface geophysical methods for investigating the Buyukcekmece landslide in Istanbul, Turkey. *Journal of Applied Geophysics*,134, 23-35.

Yan, M., Miao, L. and Cui, Y. (2012). Electrical resistivity features for compacted expansive soils. *Marine Georesources and Geotechnology*, 30, 167-179.

Yang, Y.B., Hung, H.H. and Chang, D.W. (2003). Train-induced wave propagation in layered soils using finite/infinite element simulation. *Soil Dynamics and Earthquake Engineering*, 23, 263-278.

Yang. Y.B. and Hung, H.H. (2009). *Wave Propagation for Train-Induced Vibrations*. World Scientific Publishing Co, p. 471.

Yi, S., Ma, H., Zheng, C., Zhu, X., Wang, H., Li, X., Hu, X. and Qin, J. (2012). Assessment of site conditions for disposal of low – and intermediate – level radioactive wastes: A case study in southern China. *Science of the Total Environment*, 414, 624-631.

Yilmaz, ö. (2001). Doherty, S.M. (ed), *Seismic Data Analysis. Investigation in Geophysics, Volume 1. Society of Exploration Geophysics*. 2nd edition. Tulsa, OK, USA.

Yong, R. and Warkentin, B. (1975). *Soil Properties and Behaviour*. Elsevier scientific publishing company, Amsterdam, p. 449.

Zhu, J., Currens, J.C. and Dinger, J.S. (2011). Challenges of using electrical resistivity method to locate karst conduits – A field case study in the Inner Bluegrass Region, Kentucky. *Journal of Applied Geophysics*, 75, 523-530.

Appendices

- *Appendix A: Constrained resistivity models using least-square smoothness-constrained inversion of the test site at Keele University.*
- *Appendix B: Constrained resistivity models using robust inversion of the test site at Keele University.*
- *Appendix C: Grain size distribution curves of soil samples collected from Rugeley site.*
- *Appendix D: 2D cross section of the 2D MASW of Rugeley site.*
- *Appendix E: Cone resistance-depth profiles of the CPT soundings from Rugeley site.*
- *Appendix F: Matlab codes used in the thesis.*
- *Appendix G: Doppler Shift analysis (time-frequency spectrograms) of the train induced vibrations, Rugeley site.*
- *Appendix H: Shear wave velocity-depth profiles for 1D (i.e. long and short linear) and 2D (i.e. manual and L-shape) arrays, of the train induced vibrations, Rugeley site.*
- *Appendix I: Frequency – phase velocity curves for 1D (i.e. long and short linear) and 2D (i.e. manual and L-shape) arrays, of the train induced vibrations, Rugeley site.*
- *Appendix J: Frequency – wavenumber (f-k) analysis of the train-induced vibrations, Rugeley site.*
- *Appendix K: Abstracts of presented posters, presentations and publications.*
- *Appendix L: Raw collected datasets of Keele facility test site and Rugeley site.*

See attached CD for appendices